X-RAY PHOTOELECTRON SPECTROSCOPY
OF SILICATE GLASSES

by

G. WILLIAM TASKER

B.S., Ceramic Science, Pennsylvania State University

1972

SUBMITTED IN PARTIAL FULFILLMENT

OF THE REQUIREMENTS FOR THE

DEGREE OF

DOCTOR OF PHILOSOPHY

IN CERAMICS

at the

Massachusetts Institute of Technology

June 1987

Signature of Author ______________________
Department of Materials Science and Engineering
May 1 , 1987

Certified by ______________
D. R. Uhlmann
Thesis Supervisor

Accepted by ________________
S. M. Allen
Chairman, Departmental Committee on Graduate Students

X-RAY PHOTOELECTRON SPECTROSCOPY
OF SILICATE GLASSES

by

G. WILLIAM TASKER

Submitted to the Department of Materials Science and Engineering on May 1, 1987 in partial fulfillment of the requirements for the Degree of Doctor of Philosophy in Ceramics.

ABSTRACT

X-ray photoelectron spectroscopy (XPS) is a powerful technique capable of providing unique information about the structural chemistry of glasses. However, inappropriate procedures for the preparation of sample surfaces or the lack of reliable methods to overcome electrostatic charging effects during analysis of dielectric materials can cause spurious features to be introduced or intrinsic features to be suppressed in photoelectron spectra which are nominally indicative of bulk phenomena. An adaptation of a biased metal-dot (BMD) energy reference for insulators in XPS to the analysis of fracture surfaces prepared in ultra-high vacuum is described that largely eliminates these difficulties. Based on a study of the charging behavior of SiO_2 glass under conditions of positive and negative bias, a reference of the binding energy scale for an insulator to its surface Fermi level is proposed and shown to be consistent with Schottky barrier formation at metal-insulator interfaces.

The utility of this analytical procedure is demonstrated by comparisons of core and valence level spectra acquired from surfaces of fire-polished SiO_2 glass and vacuum-fractured SiO_2 glass and α-quartz. The similarity of core level spectra obtained from fire-polished and vacuum-fractured surfaces of vitreous SiO_2 supports a view that extensive surface reconstruction of siloxane bonds occurs at fracture surfaces. Since no significant differences in core level spectra are found between crystalline and vitreous samples of SiO_2, it is also suggested that the covalent-ionic nature of the Si-O bond does not change appreciably with the Si-O-Si bridging angle.

A structural investigation by XPS of R_2O-SiO_2 glasses and Na_2O-Al_2O_3-SiO_2 glasses was accomplished by analysis of core level spectra which were acquired from vacuum-fractured surfaces and corrected for charging effects by the BMD method. The O 1s spectrum for SiO_2 glass does not indicate the existence of doubly-bonded oxygens or strained siloxane bonds in detectable concentrations. This result calls into question the assertions of recent crystalline cluster models for glass structure. In accord with earlier XPS work, an analysis of O 1s spectra for R_2O-SiO_2 glasses agrees with conventional theory for the accommodation of alkali atoms in a vitreous silicon-oxygen network at mole fractions of alkali oxide $X_R<0.30$ but departs negatively from this theory for $X_R>0.30$. The merits of various explanations for this discrepancy are critically appraised. Trends in the binding energies and widths of various core level spectra for Na_2O-SiO_2 glasses support a contention that while single-phase R_2O-SiO_2 glasses do not exhibit any long-range order, chemical details of the short-range atomic structure bear a close resemblance to those in R_2O-SiO_2 crystals.

The proportions of various bridging and nonbridging components of O 1s spectra for three series of $Na_2O-Al_2O_3-SiO_2$ glasses are shown to be directly related to glass composition in a predictable and rather general way within two adjacent compositional regions: $0\leq Al/Na\leq 1.0$ and $1.0<Al/Na\leq 1.5$. In contrast to prior XPS studies, an analysis of O 1s spectra for glasses with $0\leq Al/Na\leq 1.0$ gives strong support to the classical model for incorporation of aluminum atoms in tetrahedral sites as network formers. An analysis of O 1s spectra for glasses with $1.0<Al/Na\leq 1.5$ is consistent with Lacy's tricluster model for the incorporation of aluminum atoms in excess of sodium atoms in tetrahedral sites as network formers. Trends in the binding energies and widths of various core level spectra for $Na_2O-Al_2O_3-SiO_2$ glasses lend collateral support to the classical model for $Al/Na\leq 1.0$ and the tricluster model for $Al/Na>1.0$.

Thesis Supervisor: Donald R. Uhlmann
Title: Cabot Professor of Materials

TABLE OF CONTENTS

TABLE OF CONTENTS (Cont'd.)

TABLE OF CONTENTS (Cont'd.)

TABLE OF CONTENTS (Cont'd.)

LIST OF FIGURES

LIST OF FIGURES (Cont'd.)

LIST OF FIGURES (Cont'd.)

LIST OF TABLES

ACKNOWLEDGEMENTS

My pursuit of a doctoral degree at M.I.T. has been a challenging and formative experience as well as an all too enduring one. Lately, I have come to understand that such endeavors in life are not truly undertaken alone but instead involve the generous support and collaboration of family, colleagues, and friends. It is my considerable pleasure to acknowledge such contributions at this time. It is also my hope that this document will vindicate and reward the steadfast confidence of the following persons in the author.

To members of my family, Marcia, Patricia, Harvey, and especially my Mother, your love provided the reserves of fortitude and inspiration without which this Thesis could not have been completed.

To my advisor Professor D. R. Uhlmann, your substantial support of this work, occasional scientific and professional advice, and constructively critical reading of the manuscript are all sincerely appreciated.

To the other members of my Thesis Committee, Professors H.L. Tuller and R. Burns, I extend my gratitude for helpful discussions and suggestions offered during the course of this work.

To Drs. P.I.K. Onorato and R. Wong, special thanks are due for the preparation and chemical analyses of most of the glasses investigated in this Thesis. Also, it is a delight to acknowledge the collaboration of Drs. Onorato, M.N. Alexander, and C.W. Struck in certain aspects of the structural studies on sodium aluminosilicate glasses.

To Dr. R.M. Cannon and Professors M.W. Barsoum and D. P. Birnie, I am indebted for stimulating discussions about metal-insulator junctions, the fracture of brittle solids, and other topics pertinent to this Thesis.

To Mike Barsoum, Rowland Cannon, Joe Dynys, Chas Gasdaska, Akihiro Hishinuma, Pat Kearney, John Martin, Thao Nguyen, Hue Song, and other notable denizens of Building 13 past and present, thank you for your help and friendship but above all for the memories of the times we shared together.

Finally, to Linda Sayegh and John Mara, I wish to express my appreciation for her careful typing of the manuscript and for his outstanding technical artistry.

FOREWORD

This Thesis is organized into three major sections, Chapters 1, 2, and 3, to facilitate their prompt publication as separate scientific papers with a minimum of additional editing. Each of these Chapters is thus a nominally self-contained entity with individual sets of references. However, cross-references between these Chapters are made to illustrate certain points or to clarify the discussion.

Chapter 1 elaborates upon the experimental requirements for acquisition of bulk physicochemical information from insulating samples in X-ray photoelectron spectroscopy. The experimental methods that are demonstrated in Chapter 1 by a photoemission study of crystalline and vitreous SiO_2 are then applied to structural investigations of R_2O-SiO_2 glasses in Chapter 2 and $Na_2O-Al_2O_3-SiO_2$ glasses in Chapter 3. A paper based on the work in Chapter 1 will be submitted for publication to the Journal of Electron Spectroscopy and Related Phenomena. The contents of Chapters 2 and 3 will form companion papers to be submitted to the Journal of Non-Crystalline Solids.

For the convenience of the reader, the conclusions of this Thesis are listed in Chapter 4. Finally, suggestions for future work are given in Chapter 5.

CHAPTER 1

EXPERIMENTAL METHODS FOR XPS OF INSULATORS

1.1. Introduction :

Although X-ray photoelectron spectroscopy (XPS) [1-6] is perhaps best known as a powerful technique for chemical analysis of solid-state surfaces and interfaces, it has increasingly been applied to investigations of bulk physicochemical properties. The often-unique capabilities of XPS for probing electronic energy-levels in solids have contributed substantially to the understanding of crystalline and vitreous silicates from both theoretical and applied perspectives. Several applications of XPS to the study of these materials serve to illustrate both its value and potentially vexing experimental difficulties. The present Chapter focuses attention on such difficulties.

Photoemission spectra of core and valence electronic levels in SiO_2 have been used to establish an empirical framework of self-consistent initial states for the various electronic transitions which are measured in optical reflectance, X-ray absorption and emission, and electron-energy-loss spectroscopies. Comparison of such transitions on a universal energy-level diagram leads to an illuminating overview of the electronic structure for SiO_2, as shown by Griscom [7]. Valence band spectra for silicates have provided useful standards (with allowances made for differing cross-sections for photoemission) by which the relative abilities of diverse theoretical methods to simulate an empirical density of states can be ascertained [7-14]. In principle, the sensitivity of XPS to differences in chemical environment among oxygen atoms in multicomponent silicate glasses enables the relative numbers of bridging oxygens (BO's) and nonbridging oxygens (NBO's) to be determined quantitatively as a function of composition by analysis of the O 1s core level [15,16]. BO's are oxygen atoms in Si-O-Si linkages which impart connectivity to the vitreous silicate network; NBO's are oxygens in Si-O-$\sum_j R_j$ arrangements (e.g., where R is an alkali ion) which break up the connectivity of the network. Such information directly addresses fundamental questions about glass structure as emphasized in this Thesis. It is also important in a practical sense since the compositional dependences of many physical properties for silicate glasses can be correlated with changes in structural parameters such as the fraction of NBO's.

An implicit assumption in each of the examples cited above is that the photoemission spectra are representative of bulk electronic structure and chemistry. For the soft X-ray sources commonly used in XPS (e.g., Mg Kα and Al Kα excitation), the effective sampling depth for core and valence levels in silicates is $\lesssim$ 10 nm. This inherent constraint requires the surface region of a given sample under analysis to have a structural and chemical integrity closely approaching that of the bulk. Methods of surface preparation which are inappropriate for a particular sample can cause spurious features to be introduced or intrinsic features to be suppressed in photoelectron spectra. It follows that models for glass structure which are based upon such data must be viewed with caution.

Spectrometer calibration and electrostatic charging effects for insulating samples in XPS are other important areas of experimental concern. In order to establish a binding energy scale for a sample with realistic separations among electronic energy-levels, it is obvious that the energy scale of the spectrometer must be well defined in magnitude, linear, and accurately positioned with respect to the Fermi level $\equiv$ 0 eV of the instrument. Analysis of silicates poses additional complications due to the tendency of dielectric samples to acquire a positive static charge under X-irradiation. This well-known effect results in a confounding shift of the binding energy scale for an insulator relative to the instrumental zero. Furthermore, differential charging over the surface of an insulator can seriously degrade the energy resolution of photoelectron spectra. These charging effects can act to obscure or distort trends in XPS data upon which chemical and structural interpretations are based. The demonstration of a reliable method to compensate for static charging and to minimize differential charging is thus clearly a collateral if not essential requirement for further elucidation of silicate glass structure by XPS.

This Chapter considers experimental methods for obtaining accurately calibrated XPS data for insulating materials, as typified by SiO_2, which are indicative of bulk physicochemical properties. Previous experience with electrostatic charging of insulators and procedures for surface preparation in XPS are assessed in Section 1.2. Descriptions of the spectrometer used in this work and the methods employed to surmount or mitigate each of the experimental problems mentioned above are given in Section 1.3. The efficacy of these procedures is demonstrated in Section 1.4: first, with the results of an investigation of charging correction by a biased metal-dot (BMD) method for fire-polished surfaces of SiO_2 glass; and second, with photoemission spectra for crystalline and vitreous SiO_2 which were acquired from vacuum-fractured surfaces <u>and</u> corrected for static charging by this BMD method. A model for charging correction by the BMD method is presented in Section 1.5 as well as a critical comparison of this work with earlier photoemission studies of SiO_2. Finally, the major conclusions of this chapter are summarized in Section 1.6.

1.2. Literature Survey:

1.2.1. Charging Correction of Insulators

The Fermi level for a good conductor such as elemental gold is characterized in photoemission studies by the onset of occupied states within the overlapping valence and conduction bands [17]. When such a sample is grounded to the spectrometer in XPS, its Fermi level equilibrates with that of the spectrometer and thus becomes a logical choice for a binding energy reference, as illustrated in Fig. 1.1(a). Hence, the familiar relation in photoelectron spectroscopy

$$\begin{aligned} BE_F &= h\nu - KE'_{VAC} - q\phi_{sp} \\ &= BE'_F \end{aligned} \qquad (1.1)$$

gives the binding energy of an electronic level, e.g. $BE_F(E_{CORE})$, for a conductor with respect to a common Fermi level reference. In Fig. 1.1, $h\nu$=energy of X-ray photons; BE_F=binding energy referred to E_F, the Fermi level of the sample; BE'_F=apparent binding energy referred to E'_F, the Fermi level of the spectrometer (i.e., the instrumental zero); KE_{VAC}=kinetic energy of the photoemitted electrons relative to E_{VAC}, the vacuum level of the sample; KE'_{VAC}=kinetic energy of the photoelectrons measured relative to E'_{VAC}, the vacuum level of the spectrometer; $q\phi$=vacuum work function of the sample; $q\phi_{sp}$=work function of the spectrometer; and, q=magnitude of electronic charge.

In contrast, the location of the Fermi level for a typical insulator like SiO_2 is rather ambiguously defined from an experimental standpoint. Its position is idealized at the middle of a large bandgap, E_g, between the valence band maximum, E_V, and the conduction band minimum, E_C. However, this midgap position can be modified either by the presence of uncompensated impurity or

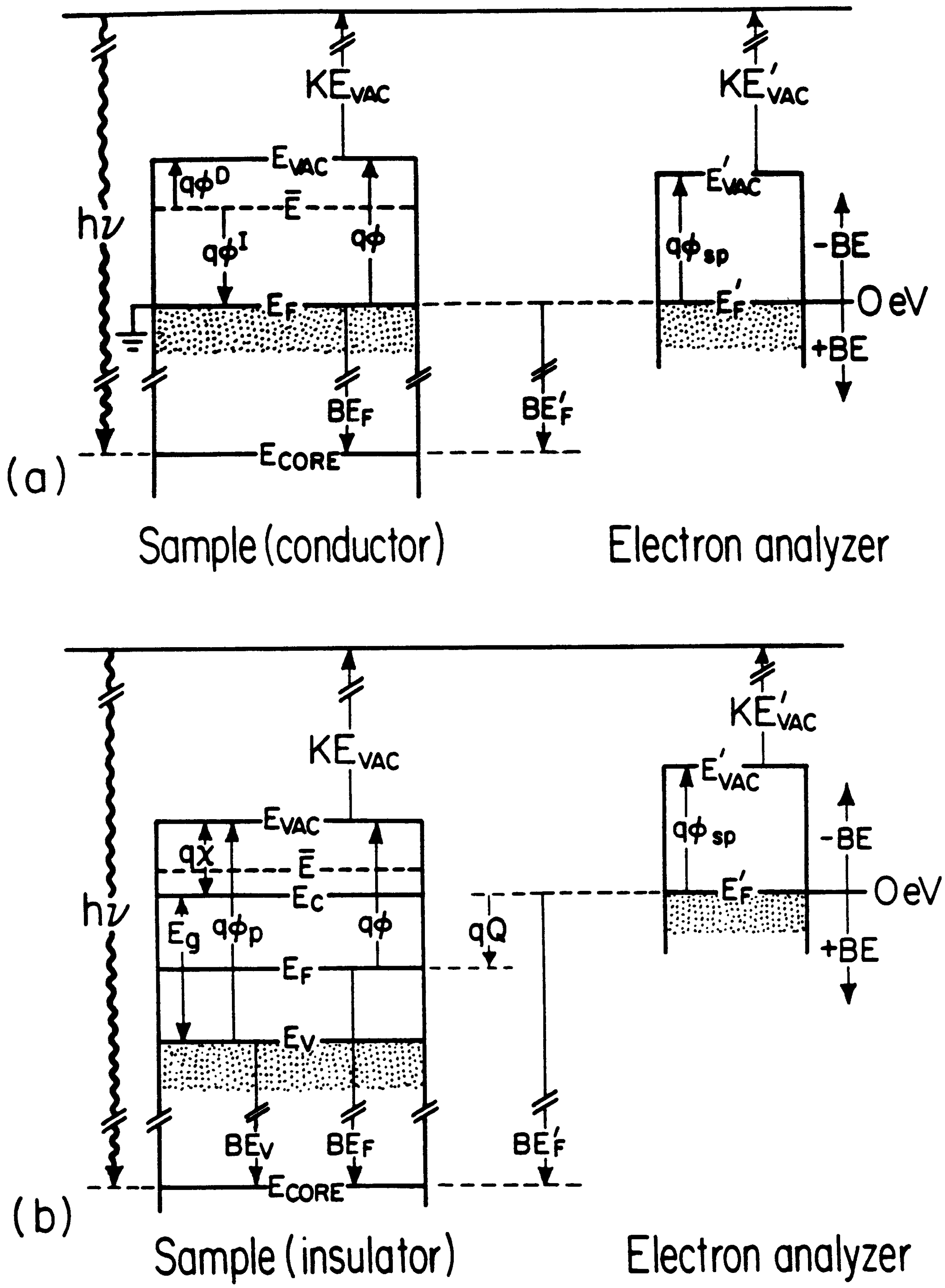

Fig. 1.1: Schematic of XPS experiment: (a) conductor grounded to spectrometer ($BE_F' = BE_F$) and (b) insulator positvely charged ($BE_F' \neq BE_F$). Symbols are defined in text.

defect states within the bandgap, or by band-bending effects near surfaces and interfaces. The negligible electrical conductivity of thick insulating samples in XPS further complicates the specification of an empirical energy reference by giving rise to sample charging effects. When electrostatic charging of the analyzed surface occurs, the Fermi level for an insulator (or an electrically isolated conductor) is offset from the instrumental zero such that

$$\begin{aligned} BE'_F &= h\nu - KE' - q\phi_{sp} \\ &\neq BE_F, \end{aligned} \tag{1.2}$$

as depicted in Fig. 1.1(b). Therefore, only erroneous binding energies BE'_F are observed; and a reliable method of correction for static charging is subsequently required to recover the actual binding energies BE_F.

A fundamental reference for the potential energy scale of a solid is the average internal electrostatic potential, $\overline{E}$. Citran and Hamann [18] have discussed the relation between $\overline{E}$ and two empirically accessible references, E_F and E_{VAC}. For comparisons with theory, the choice between the latter rests upon the relative confidence with which the contributions of the chemical potential, $q\phi^I$, and surface dipole, $q\phi^D$, to $q\phi$ in Fig. 1.1 can be calculated. Construction of an energy scale referred to E_{VAC}, i.e. BE_{VAC}, can be achieved for conductors in Fig. 1.1(a) by adding $q\phi$ to BE_F and for insulators in Fig. 1.1(b) either by adding E_g plus the electron affinity (i.e., the energetic separation between E_C and E_{VAC}), $q\chi$, to binding energies referred to the valence band maximum of the sample, BE_V, or by adding the photoemission threshold, $q\phi_p$, to BE_V. Aside from compilations of vacuum work functions [19,20] for clean elemental metals, $q\phi_M$, however, the necessary data for other materials are generally unavailable.

A reference to E_{VAC} can also be determined directly in X-ray or ultraviolet photoemission experiments by adding $h\nu$ to the secondary electron emission edge [21-24]. The difficulty with this procedure is that delineation of the secondary electron emission edge can be problematic due to truncation errors and other experimentally-related distortions of this feature. Apart from the difficulties in specifying E_{VAC}, the propriety of using this empirical reference to approximate the desired theoretical reference $\overline{E}$ depends on the often-uncertain relative contributions of $q\phi^I$ and $q\phi^D$ to $q\phi$ [25]. Since E_F can be more accurately and routinely accessed than E_{VAC}, BE_F is usually taken as the energy scale for conductors in XPS. The problem to be explored shortly is how the confounding condition of $BE'_F \neq BE_F$ for a charged insulator in Eq. (1.2) can be corrected to the useful condition of $BE'_F = BE_F$ as for a grounded conductor in Eq. (1.1). Before proceeding, it is instructive to summarize prior experience with charging phenomena for insulators in general and silicates in particular.

Electrostatic charging of dielectric samples in XPS is a complex process and has been described in earlier work [22, 26-29] as representing a dynamic equilibrium

$$i_1 = i_2 + i_3 \qquad (1.3)$$

among the following electron currents: i_1 = photo-, Auger, and secondary electrons emitted from the surface of an insulator under X-irradiation; i_2 = slow electrons from the surroundings impinging upon the analyzed surface; and, i_3=electrons flowing from ground to the analyzed surface of the insulator via a bulk or surface conduction mechanism. The magnitudes of these currents are regulated by often-uncontrolled factors including the spectrometer configuration (e.g., monochromatic vs. nonmonochromatic excitation), X-ray intensity and power distribution across the analyzed surface, kinetic energy distributions within currents i_1 and i_2, and the relative photoyield, resistivity, bandgap, and geometry of the sample.

When steady state conditions are established for an insulator under irradiation in XPS, a positive charging potential is typically observed. The displacement of E_F for the insulator with respect to the instrumental zero is the <u>apparent surface potential</u>, Q, which is hypothetically defined in Fig. 1.1(b) as

$$qQ = BE'_F(E_F). \tag{1.4}$$

Attempts to circumvent ambiguities associated with Q by normalization of spectra for a series of silicate glasses to either an arbitrary core level position (e.g., the "bridging oxygen peak" [30]) or a prominent feature in the valence band (e.g., E_V [31]) frequently obscure underlying energetic and structural relationships of interest. Furthermore, instabilities or non-uniformities in the various factors affecting i_1, i_2, and i_3 are capable of producing oscillations or lateral gradients in Q across the analyzed surface of an insulator. This differential charging of the surface is manifest by broadening or in extreme cases by splitting of photoemission lines. The attendant loss of spectral resolution and especially its dependence on surface or bulk resistivity as a function of glass composition can preclude an adequate analysis [32].

Several important conclusions may be drawn from previous investigations of charging effects for insulators in XPS. For thick ($\gtrsim$ 100 nm) samples, i_2 is comparable to i_1 under steady state conditions (see Eq. (1.3)); and these currents are much greater than i_3 [22, 27, 28]. Photoconductivity in the irradiated region corresponding to the penetration depth of X-rays (10^3-10^4 nm) apparently does not play a major role in establishing the charging potential Q for X-ray intensities below a threshold which is thought to increase with E_g of the sample [33]. In the case of nonmonochromatic excitation, secondary electrons emitted from the radiation window between the anode of the X-ray gun and the sample account for a large fraction of i_2 [26]. The absence of such an abundant source of secondary electrons and the confinement of the X-ray flux to the insulator surface when a focusing monochrometer is used often requires an auxiliary source of slow electrons (e.g., a "flood-gun" [29, 34]) to supplement the smaller ambient contribution to i_2. Moreover, it is difficult to achieve exact compensation for the charging current i_1, either by biasing the sample mount [22, 27, 28] or by employing a flood-gun [28, 29] to vary the discharging current i_2, so that Q=0 V during data acquisition. It has been estimated that these currents must be balanced to within ~ 1 pA in order to obtain charging shifts <0.1 eV [27]. Uncorrected spectra for insulators are instead typically characterized by some nontrivial $-10\ \text{V} \lesssim Q \lesssim 10\ \text{V}$ as fixed by the experimental conditions.

Circumstances do exist where the insulator current i_3 is significant. For thin (<< 100 nm) dielectric films on a grounded conductive support, positive charging can be limited by photoinjection [35] or tunneling [36, 37] of electrons from the conductor into the conduction band of the insulator. Negative charging of a ~ 4 nm layer of SiO_2 on a silicon substrate under illumination by a flood-gun is reportedly reduced at sufficiently high flood-gun voltages by hole generation due to impact ionization [38]. These processes can induce appreciable currents within thin films as a consequence of the large electric fields ($\gtrsim 10^6$ V/cm) attained at both extremes of charging behavior in the examples cited.

The standard procedure [39, 40] for rectifying the binding energy scale of a statically charged insulator in XPS involves the use of an electrically isolated calibrant on the analyzed surface to evaluate Q. This procedure is predicated on the following argument: A state of electronic equilibrium exists between the calibrant and insulator (i.e., the respective Fermi levels are coincident), such that the onset in the density of filled states for the calibrant corresponding to E_F enables Q to be monitored through Eq. (1.4). Thus, Q is now operationally defined by the displacement of the <u>common</u> E_F across the calibrant-insulator junction relative to the instrumental zero. However, Q is more readily determined in practice by noting the equivalent offset for a core level of the calibrant with Eq. (1.2), $BE'_F(E_{CORE})$, relative to its position when the calibrant material is grounded to the spectrometer from Eq. (1.1), $BE_F(E_{CORE})$. If gold, platinum, or carbon is employed as a calibrant then Q is specified for each case as follows:

$$\begin{aligned} qQ &= BE'_F(E_{CORE}) - BE_F(E_{CORE}) \\ &= BE'_F(\mathrm{Au}\ 4f_{7/2}) - 84.00\ \mathrm{eV} && (1.5a) \\ &= BE'_F(\mathrm{Pt}\ 4f_{7/2}) - 71.15\ \mathrm{eV} && (1.5b) \\ &= BE'_F(\mathrm{C}\ 1s) - {\sim}284.8\ \mathrm{eV}. && (1.5c) \end{aligned}$$

With Q evaluated in this manner, the erroneous BE'_F scale for a charged insulator in Eq. (1.2) can in principle be corrected to the actual BE_F scale of the sample by

$$\begin{aligned} BE_F &= h\nu - KE'_{VAC} - q\phi_{sp} - qQ && (1.6) \\ &= BE'_F - qQ\ . \end{aligned}$$

Binding energies for an insulator are thus said to have been corrected to the grounded position of a calibrant core level via Eqs. (1.5) and (1.6).

Justification for employing an external calibrant (e.g., adventitious carbon or vacuum-deposited gold or platinum) to monitor Q critically hinges on several criteria:

1. During photoemission experiments, the calibrant must be sufficiently conductive to equilibrate with a charged insulating sample and also with the spectrometer when grounded. In addition, this material must have an accessible core level that is both consistently well defined in shape (see 2) and suitably intense so that its position and hence Q can be determined accurately through Eq. (1.5).

2. Ideally, the calibrant should not chemically react or interdiffuse with the sample, as both of these processes can cause a chemical shift in the positions of core levels for the calibrant and sample. The amount (thickness) of the calibrant should also be sufficient to avoid changes in final states for photoemission due to screening effects by extra-atomic relaxation of electronic charge within the calibrant or polarization of charge across the interface with the sample.

3. It must be demonstrated that corrected binding energies for an insulating sample are invariant over some extended range of Q. This behavior indicates that a stable electronic contact between the calibrant and sample has been established. The positions of E_C, E_V, and the various E_{CORE} for the sample are thus fixed relative to the common E_F at the calibrant-insulator junction under these conditions.

Although adventitious carbon is widely used for correction of static charging in routine surface analytical work [40], serious reservations can be raised regarding its applicability and validity in studies of bulk physicochemical properties by photoemission. The obscure chemical nature of the carbonaceous species contributing to the C 1s photopeak [41-43], the effects of electronic screening on the final states for photoemission [43-45], and the virtual absence of carbon contamination on vacuum-fractured [15,46] surfaces of insulators in UHV (ultra-high vacuum, $\lesssim 10^{-7}$ Pa) systems inveigh against the use of adventitious carbon as a calibrant in more basic work.

On the other hand, the use of noble metals to provide a correction for static charging as practiced in conventional vacuum-deposition procedures [39] is similarly open to strong criticism. The requirement that the metal-insulator junction be characterized by stable electronic properties is often assumed without adequate experimental confirmation. Binding energies of core levels for insulators have been observed to vary relative to the Au $4f_{7/2}$ photopeak with surface coverage or thickness of a gold calibrant [47,48]. The effects of extra-atomic relaxation or polarization of electronic charge, whereby the energetic separation of the Au $4f_{7/2}$ level from the Fermi level is different in small vacuum-deposited gold clusters than in bulk gold, are a likely explanation for this behavior [49]. Although gold tends not to be chemically reactive with oxide materials including silicates, there have been reports to the contrary with halide compounds [49-51]. Assuming surface reactions can be avoided in most cases, the shape of the Au $4f_{7/2}$ photopeak is well defined and its cross-section for photoemission is large in contrast to the C 1s photopeak for adventitious carbon. However, this advantage becomes a liability in conventional practices of "gold decoration", since even if gold is deposited in very small amounts upon the analyzed surface of the insulator, the high background level and intense photopeaks of the calibrant are superimposed on the photoelectron spectrum of the sample. One is reasonably led to conclude that in photoemission studies seeking bulk structural and chemical information for insulators by analysis of clean representative surfaces, a reliance on any external calibrant overlaying the analyzed surface is questionable at best and potentially self-defeating.

Against this generally unsatisfactory state of the science for correction of statically charged dielectric samples in XPS, Stephenson and Binkowski (SB) [52] described a novel biased metal-dot (BMD) method for recovering the binding energy scale BE_F of an insulator. A thick deposit of gold $\sim$1 mm in diameter is vacuum-evaporated onto the surface of an insulating sample, which is then positioned inside the spectrometer such that the gold dot is always irradiated by X-rays. Once the apparent surface potential Q has been evaluated by Eq. (1.5a), the sample is translated slightly so that the gold dot lies just outside the area of analysis. In this way the high background counts and interfering photopeaks of the calibrant are avoided when acquiring spectra for the insulator. Under conditions of negative bias imposed with a flood-gun, SB demonstrated for vitreous SiO_2 that a stable electronic junction between the gold calibrant and insulator is obtained for $-4\ \mathrm{V} \gtrsim Q \gtrsim -10\ \mathrm{V}$. The data of SB also show that broadening of photopeaks due to differential charging is significantly reduced under the above conditions for their monochrometer-equipped instrument--a noteworthy result since spectrometers of this design are notoriously prone to this type of distortion. Furthermore, the final states for photoemission in a thick gold dot match those of bulk gold and hence errors due to screening effects are avoided. The BMD method therefore represents a considerable advance over conventional practice in that it basically meets the three criteria given above for valid use of an external calibrant as well as offering other important advantages.

Several issues regarding the theory and practice of the BMD method remain to be clarified. The energy-level diagram of SB depicting the behavior of a calibrant-insulator junction under successively larger negative biases is reproduced in Fig. 1.2. SB inferred that the binding energy scale obtained through Eq. (1.6) is actually referred to the surface Fermi level, $E_{F(s)}$, and not to the bulk E_F of the insulator. This follows as a consequence of band-bending within the insulator which is required to align the Fermi levels across the junction at thermal equilibrium in Fig. 1.2(d). The amount of band-bending is equal to the difference in work function between a given calibrant and the insulator (i.e., the contact potential, $\Delta q\phi$) at the interface. SB attempted to avoid the implicit reference to $E_{F(s)}$ in Eq. (1.6) by proposing that a unique reference to E_{VAC} is possible through the vacuum work function of the calibrant metal, $q\phi_M$:

$$BE_{VAC} = BE_F + q\phi_M \quad (1.7)$$

This correction is illustrated in Fig. 1.2(f) where the Fermi level of the metal was said to have "pinned" the Fermi level of the insulator (with decidedly unrealistic curvature in the latter). Other workers [29, 53] have made similar but conceptually less rigorous arguments for a reference to E_{VAC} when an isolated metal-insulator junction is illuminated by a flood-gun in XPS.

The validity of Eq. (1.7) is critically examined in this Chapter in the context of what is currently known regarding chemical trends in the formation of Schottky barriers at metal-SiO_2 interfaces. Biasing experiments are conducted which compare the BE_F scales for SiO_2 glass as determined independently for gold and platinum calibrants having nominally distinct vacuum work functions, $q\phi_{Au}$=5.1 eV and $q\phi_{Pt}$=5.65 eV [19]. The conclusions drawn from this analysis are incorporated in a revised energy-level diagram for the BMD method. With these theoretical questions addressed, the feasibility of adapting the BMD method to vacuum-fractured surfaces of insulators for investigation of

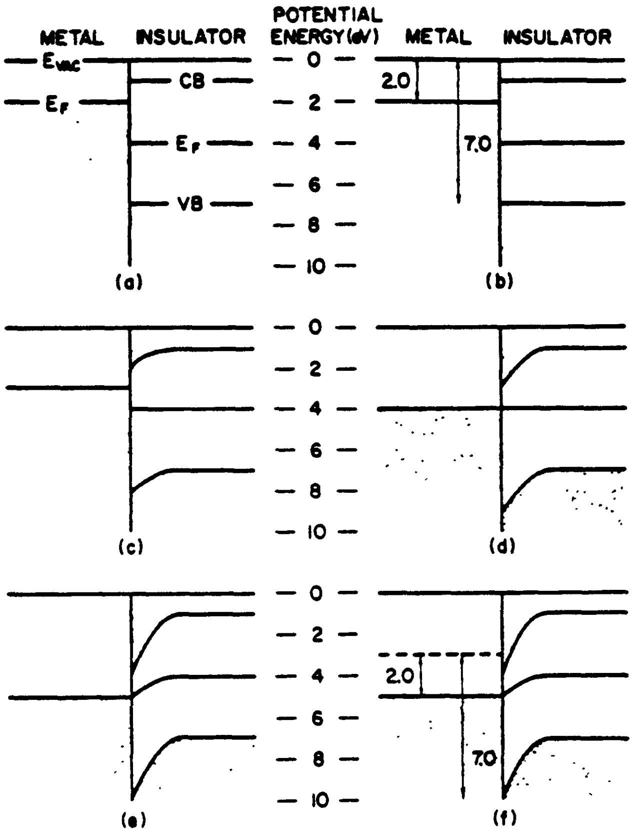

Fig. 1.2: Energy-level diagram of SB for BMD method: (a) legend, (b) zero bias, (c) slight negative bias, (d) exact equilibrium, (e) negatively biased after equilibration, and (f) establishment of reference to E_{VAC} through the vacuum work function of the calibrant. Figure taken from Ref. 52.

bulk properties is ascertained. The rationale for analyzing such surfaces, especially in structural studies of silicate glasses, is reviewed in the next subsection.

1.2.2. Preparation of Insulator Surfaces

In studies of solids by XPS attempting to access bulk physicochemical properties, it is vitally important that the structure and chemistry of the surface region under analysis not be essentially modified relative to the interior. This stringent requirement is imposed by the small mean free paths of electrons in solids for inelastic scattering prior to photoemission. Extrinsic energy losses resulting from inelastic scattering processes occur after photoionization from various electronic levels. For typical electron kinetic energies in XPS (i.e., $KE_{VAC} >> 5$ eV), electron-electron and electron-plasmon scattering are the dominant processes and have strong dependences on energy and material [54-57]. The above extrinsic effects are distinguished from intrinsic energy losses caused by electronic shake-up excitations (e.g., between valence orbitals) or exchange splitting interactions stimulated during photoionization from core levels [25]. These intrinsic effects are thus manifestations of changes in final states for photoemission.

For photoelectrons with a given kinetic energy, the detected photoemission intensity, $I(d)$, originating within some surface layer of thickness d relative to the intensity from an infinitely thick layer, $I(\infty)$, is approximately given by

$$\frac{I(d)}{I(\infty)} = 1 - \exp(-d/\lambda\cos\theta), \tag{1.8}$$

where λ =mean free path for inelastic scattering (IMFP) [58], and θ =emission angle relative to the surface normal. For $\theta=0°$, it follows that if $d = \lambda$, 2λ, 3λ, 4λ, or 5λ, the corresponding fractions of the total photoemission intensity are 0.63, 0.86, 0.95, 0.98, and 0.99. Therefore, the effective sampling depth in photoemission experiments is $\sim 3\lambda$ [59]. Irradiation of SiO_2 with a Mg Kα X-ray source ($h\nu$=1253.6 eV) excites photoelectrons from the O 1s and Si 2p core levels and the valence band region having KE_{VAC} of $\sim$715 eV, $\sim$1145 eV, and 1215-1245 eV, respectively. The IMFP's corresponding to these energies range from $\sim$2.0 to $\sim$4.0 nm in SiO_2 [60-62] with a rough average of 3.3 nm. This gives an effective sampling depth of $3\lambda \lesssim 10$ nm. Using the estimate of λ=3.3 nm in Eq. (1.8), one can more fully appreciate the importance of choosing an appropriate method of surface preparation since 26 % of the signal intensity originates from only a nanometer beneath the surface under conditions most favorable to a bulk analysis (i.e., $\theta \sim 0°$).

Upon first reflection about this result, the very constraints on the photoemission process which make XPS such a powerful technique for surface and interface analysis might appear to rule out the possibility of ever obtaining information characteristic of the bulk. However, Ibach and Rowe [63] have shown for SiO_2 in Fig. 1.3 that the second-derivative of the optical bulk loss function $-\mathrm{Im}\ 1/\varepsilon$, determined from the dielectric functions ε_1 and ε_2 which Philipp [64] calculated from optical reflectance data, agrees reasonably with the second-derivative of their electron-energy-loss spectrum (ELS) from 8 to 20 eV for valence level excitations. This correlation is explained by dielectric scattering theory and implies that the electronic structure probed in the surface region by ELS, where a primary electron energy of 100 eV yields an IMFP of $\sim$0.6 nm and hence $3\lambda \sim 1.8$ nm, is not drastically different from that measured in the bulk by reflectance [23, 24, 63]. Additional ELS results for Si 2p and O 1s core level excitations [65] generally support this interpretation. Further indication of the short-range nature of chemical bonding in silicates is found in the similarity of reflectance spectra for crystalline and vitreous SiO_2 [64].

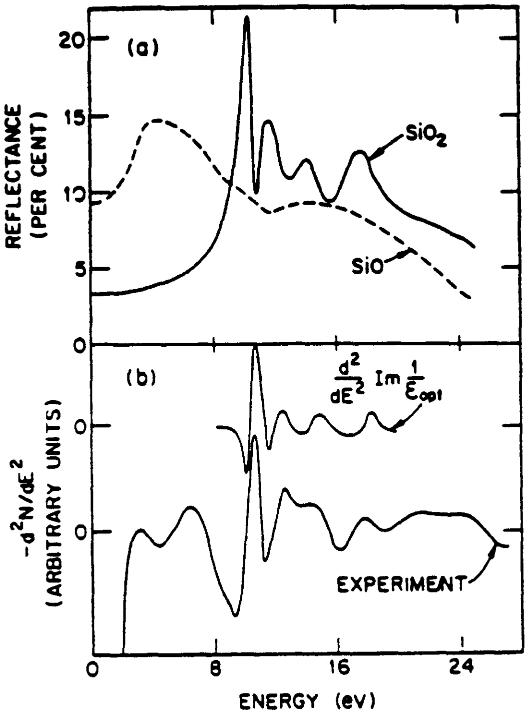

Fig. 1.3: Comparison of optical and ELS spectra for SiO_2: (a) optical reflectance of SiO and SiO_2 films after Philipp [64] and (b) the second-derivative of the ELS spectrum of SiO_2 compared to the second-derivative of the optical bulk loss function. Iback and Rowe [23,24,63] associated the peaks at energies <8 eV with an SiO_x phase and the broad feature centered near 22 eV with surface and bulk plasmons. Figure taken from Ref. 63.

Moreover, molecular orbital computations based on small SiO_4 or Si-O-Si fragments are able to account qualitatively for the density of states in SiO_2 [7]. The argument advanced here for the applicability of XPS to bulk studies of silicates holds, of course, only for surfaces which have not been unduly contaminated, chemically altered, or structurally compromised prior to analysis.

In many earlier investigations of silicates there is evidence which strongly suggests that insufficient attention was directed to the crucial question of what procedures for surface preparation are compatible with the above requisites for a valid bulk analysis. The deleterious effects of preparing glass surfaces by standard practices including mechanical grinding, exposure to solvents, vacuum-heating, ion-sputtering, or combinations thereof have been described by SB [41, 52]. Chemically and physically treated surfaces exhibited large variations in elemental composition from that of a vacuum-milled surface. There exists an opinion that vacuum-milling [16, 52, 66], whereby an abrasive-tipped tool removes a modified or contaminated surface layer, is equivalent to vacuum-fracturing [15, 46] in producing a clean representative glass surface for bulk analysis. However, a comparison of valence band spectra obtained by each method for SiO_2 glass, made later in this Chapter, supports a conclusion to the contrary. Nonetheless, SB effectively emphasize the well-known susceptibility of glass surfaces to gross chemical changes with respect to a nominal bulk composition [67,68] from the vantage provided by XPS.

The unfortunate consequences of employing improper methods for surface preparation are perhaps best demonstrated by spectral artifacts. Structural interpretation of photoemission spectra acquired from glass surfaces which have been "cleaned" by ion-sputtering is particularly tenuous as Bruckner et al [15] have remarked. Asymmetric broadening of core levels in SiO_2 [69,70], as seen for the Si 2p photopeak in Fig. 1.4, denotes that extensive structural and possibly chemical modifications to the Si-O-Si linkages of siloxane bonds are induced by this procedure. Moreover, it has been proposed that lithium silicate glasses contain oxygen atoms in three distinct chemical states [71] based on O 1s spectra for ion-sputtered surfaces such as the one reproduced in Fig. 1.5. In contrast, the O 1s spectrum obtained from a vacuum-fractured surface of a similar $Li_2O \cdot 2SiO_2$ glass [72] upholds only the existence of BO's (O°) and NBO's (O^-) in nearly the same abundances as deduced from Fig. 1.5. The conspicuous absence of the reported (O^{2-}) peak suggests that it represents a spurious feature caused by ion-sputtering. These artifacts make a compelling case against the use of ion-implanted argon as a calibrant for making charging corrections [73] in structural studies of silicate glasses.

Finally, a comparison of O 1s spectra for vacuum-fractured vs. air-fractured surfaces of a sodium silicate glass [74] shows the pronounced effects of hydration in the surface region of the latter. The necessity of preparing and analyzing fracture surfaces in situ under UHV conditions for bulk analysis of reactive or hygroscopic samples by XPS is readily apparent. Although the examples of spectral distortions given here are for silicate glasses, similar caveats apply to a greater or lesser extent for bulk studies of other insulating materials as well.

The mechanism of fracture in quintessentially brittle solids such as silicate glasses can be pictured as the sequential rupture of cohesive bonds along a moving crack front. However, the nature of locally inelastic structural deformation around the crack tip, driven by the nonlinear stress field in a zone of near atomic dimensions, is largely unknown [75].

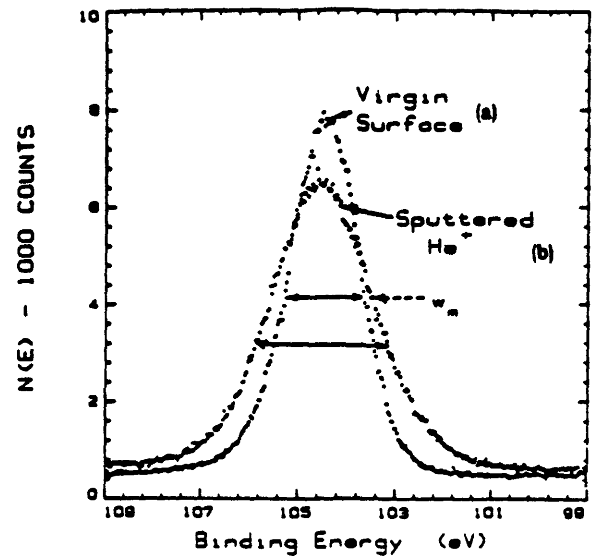

Fig. 1.4; Si 2p core level for thermally grown vitreous SiO_2: (a) chemically etched surface (FWHM=1.73 eV), and (b) surface after ion-sputtering 10 min with 1 keV He^+ ions (FWHM=2.40 eV). Note asymmetric tail at lower energies. Figure taken from Ref. 70.

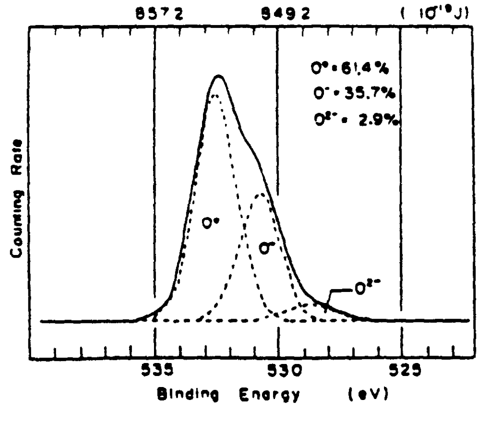

Fig. 1.5: O 1s core level for $0.35\ Li_2O \cdot 0.65\ SiO_2$ glass. Surface prepared by ion-sputtering 120 min with 5 keV Ar^+ ions. Percentages refer to estimates of the fraction of BO's (O°), NBO's (O^{-1}), and oxygens not bonded to silicon (O^{-2}). Figure taken from Ref. 71.

Surface reconstruction in the wake of the crack front by which energetically unfavorable configurations (e.g., dangling bonds) are removed or accommodated is only now beginning to be characterized. During and after fracture of various materials in vacuum, electrons, ions, neutral particles, and photons are emitted from freshly formed surfaces with decay times of microseconds to minutes [76]. These and other observations [77-79] suggest the strain energy which is locally dissipated in the fracture of glass is sufficient to overcome kinetic or topological barriers to reconstruction.

From careful electron spin resonance (ESR) measurements in UHV, Hochstrasser and Antonini [80] have proposed that fracture surfaces of crystalline and vitreous SiO_2 rapidly reconstruct, leaving a residual density of dangling silicon sp^3 bonds (i.e., paramagnetic E'_s centers) $\sim 10^{12}/cm^2$. This represents <1% of the theoretical maximum density of these defects if it is assumed $5 \times 10^{14}/cm^2$ siloxane bonds are broken in the plane of fracture which then yield $2.5 \times 10^{14}/cm^2$ each of dangling silicon bonds and NBO's. The above estimate of the siloxane bond density is concordant with the empirically determined coverage of silonal groups (Si-OH) $\sim 5 \times 10^{14}/cm^2$ on fully hydroxylated surfaces of SiO_2 [81]. Hochstrasser and Antonini believe surface reconstruction occurs by small atomic movements with recombination of ruptured siloxane bonds in possibly strained conformations. Moreover, the elimination of superficial defects in glasses containing significant amounts of alkali is achieved to an even greater extent than for SiO_2 due to the migration of these mobile ions to the surface [80].

Ibach and Rowe [24, 63] attributed the ELS peaks at energies <8 eV in Fig. 1.3 to an SiO_x phase, with a possible SiO chemical state on a less than fully oxidized surface of silicon. However, a later ELS study [82] of vacuum-fractured surfaces of SiO_2 among others suggested these features are indicative of an intrinsic surface state associated with superficial Si=O bonds (i.e., a silicon atom singly bonded to two BO's and doubly bonded to an NBO). It was estimated that the fractional coverage of these NBO's is 5 % to 10 % of a monolayer or $\sim 10^{13}/cm^2$.

Local movement of alkali to the surface has apparently been observed with ion-scattering spectroscopy (ISS) [83] which is sensitive in theory to monolayer coverages. Fracture surfaces of $Na_2O \cdot 3SiO_2$ and especially $K_2O \cdot 3SiO_2$ glasses prepared at $\sim 10^{-6}$ Pa are characterized by enhanced alkali concentrations. However, since these surfaces are inherently sputtered in ISS by ~1 keV ion beams, pertinent questions arise regarding the potential for analytical artifacts even for data acquisition times within 3-5 min [70, 83].

A molecular dynamics (MD) simulation of a vitreous SiO_2 surface under conditions which mimic formation by vacuum-fracture postulates the presence of NBO's with an equivalent surface density $\sim 10^{14}/cm^2$ and strained BO's (apparently in edge sharing tetrahedra) within a depth of 0.5 nm from the surface [84]. Similar computations for $R_2O \cdot 3SiO_2$ glasses where R=Li, Na, and K further predict that a local rearrangement of alkali ions occurs within the same depth and surface segregation increases in the order Li<<Na<K [85] in accord with the ISS results.

It is demonstrated in this Chapter that NBO's are not detected by XPS near vacuum-fractured surfaces of crystalline or vitreous SiO_2. However, a discrepancy in the structural analysis of vacuum-fractured alkali silicate glasses by XPS that is possibly related to surface reconstruction is discussed in Chapter 2. Even if unequivocal empirical confirmation of structural or compositional perturbations near vacuum-fractured surfaces (e.g., movement of alkali to the surface) is obtained (e.g., by angle-resolved photoemission

[86] studies), the spatial extent of such modifications currently seems limited enough that the objective of an accurate bulk analysis by XPS is not seriously compromised for a substantial range of silicate glass compositions. Considering the alternative procedures for surface preparation in XPS, the technique of vacuum-fracture is easily the best choice for basic studies of insulating materials in general and for structural investigations of silicate glasses in particular.

1.3. Experimental Procedures:

1.3.1. Description of Spectrometer, Data Acquisition, and Data Refinement

All photoemission data were obtained using a PHI Model 548 spectrometer [87], equipped with a non-monochromatized Mg Kα X-ray source ($h\nu = 1253.6$ eV) and a double-pass cylindrical mirror analyzer (CMA) [88]. Fig. 1.6 is a schematic showing the principal features and configuration of the test chamber. The surface normal of a sample is inclined 30° to the CMA axis while emitted electrons are detected around a conical surface having an apex angle of 84.6°. For this geometry, the effective emission angle θ in Eq. (1.8) is 41.4° [89,90]. The source diameter focussed by the CMA at high energy resolution is $\sim$2 mm [88]. X-rays were typically generated at a power level of $\sim$400 W.

Convenient access to a six-place sample carousel within the test chamber was facilitated by a turbo-pumped introduction chamber. A fracture stage was constructed that enabled photoemission spectra to be acquired from sample surfaces which were freshly formed in UHV. A flux of low-energy electrons (0-10 eV) at emission currents up to $\sim$0.4 mA for BMD studies was supplied by a flood-gun with its tungsten filament positioned $\sim$10 mm above and behind the analyzed surface. Not shown in Fig. 1.6 is an Ar^+-sputtering gun used to clean metal foils for calibration of the spectrometer energy scale. The ion-pumped test chamber was maintained at a total pressure $\leq 2\times 10^{-7}$ Pa for all experiments. A gas analyzer [91] typically indicated the residuals in the unbaked chamber to be comprised mainly of H_2 and H_2O, with lesser amounts of CO, N_2, and Ar.

The output signal from the spectrometer was digitized, and data acquisition and refinement were facilitated by a mini-computer programmed with MACS V6 software [87]. Survey spectra were obtained with a CMA resolution of 2.0 eV (pass energy = 100 eV), a spectral sampling density

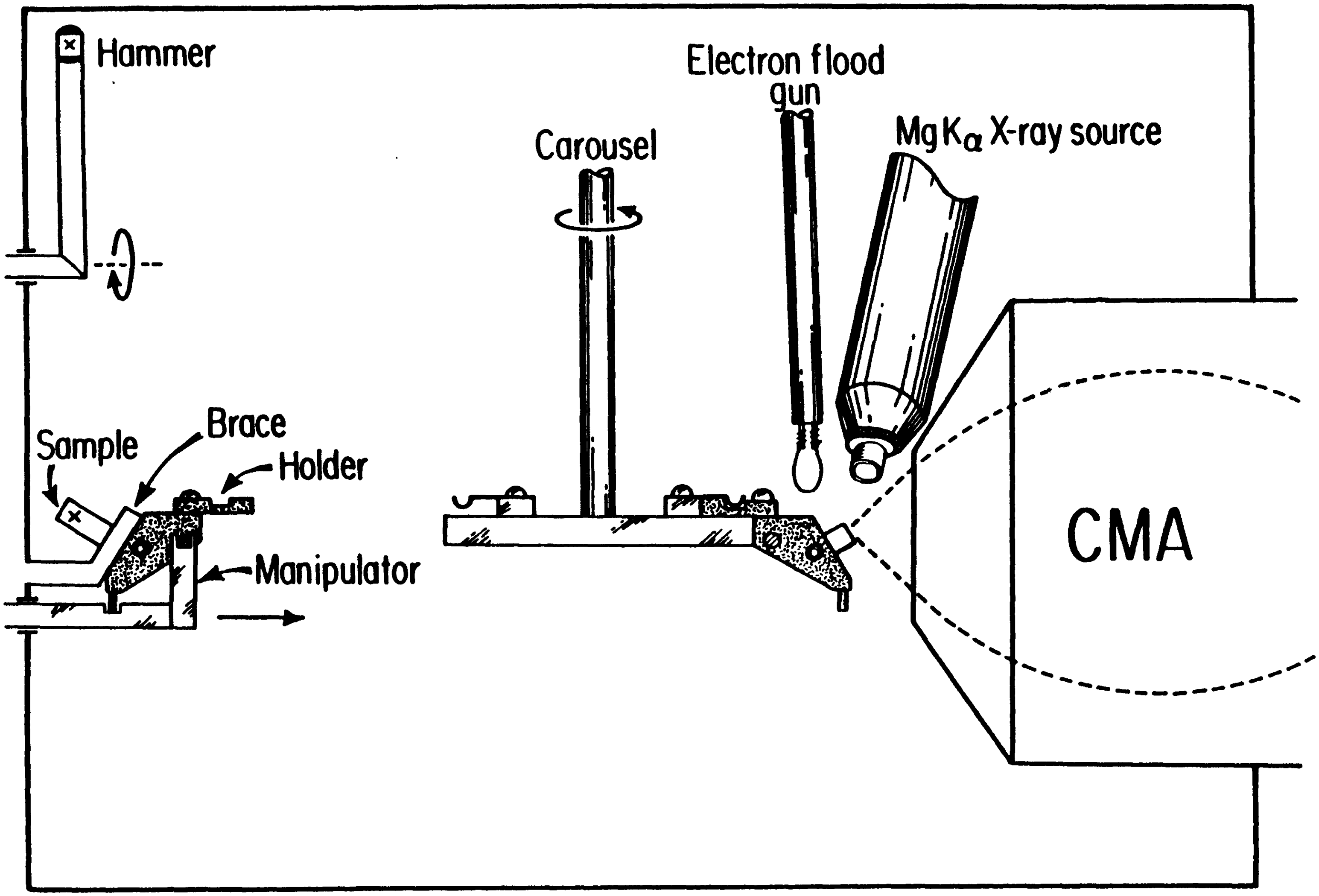

Fig. 1.6: Schematic of test chamber for present work.

of 1.0 eV/channel, and a 50 ms dwell time. High resolution spectra were acquired with a CMA resolution of 0.5 eV (pass energy=25 eV), a spectral sampling density of 0.1 eV/channel, and a 100 ms dwell time. The latter were signal-averaged until signal-to-noise ratios [92] ∿100 for the O 1s and Si 2p core levels and ∿40 for the valence band of SiO_2 were attained.

Refinement of the data was accomplished by appropriate X-ray satellite subtraction, deconvolution, smoothing, and background subtraction routines. Photopeak energies and full widths at half maximum (FWHM) were computed by a curve fitting program. Core level spectra were typically handled in the following sequence: (1) deconvolution of the raw data through five iterations of an algorithm (van Cittert's method [93,94]) to reduce the Mg $K\alpha_2$ component of the source linewidth; (2) two 11-point smoothing operations (Savitsky and Gouley's formula [93]); (3) an inelastic electron scattering correction to the baseline; and (4) a nonlinear least squares fitting analysis to unconstrained mixtures of Gaussian and Lorentzian peak shapes. Valence band spectra were subjected only to a subtraction of the Mg $K\alpha_{3,4}$ satellites from the raw data prior to a base line correction and fitting analysis. The marginal signal-to-noise ratio obtained in this spectral region was a consequence of the nonmonochromatic excitation employed. Conservative treatment of the data deterred further attempts at refinement. Nevertheless, the valence band spectrum of SiO_2 glass measured here is comparable to earlier work and allows several insights of practical importance for XPS of silicates to be developed later in this Chapter.

1.3.2. Spectrometer Calibration

A binding energy scale which is accurately calibrated is fundamental to the integration of photoemission results with other empirical data and to meaningful comparisons with theoretical calculations. Wagner [40] has described a simple procedure for checking the magnitude and linearity of the energy scale and other parameters indicative of spectrometer performance by recording the Cu $2p_{3/2}$, Cu $L_3M_{4,5}M_{4,5}$, and Cu $3p_{3/2}$ lines for Ar^+-sputtered copper sheet. Necessary adjustments to the scale were readily made by manipulation of appropriate potentiometers within the spectrometer-computer interface. The instrumental zero was then established by setting the spectrometer work function, $q\phi_{sp}$, to place the Au $4f_{7/2}$ line for an Ar^+-sputtered gold sheet at 84.00 eV from the spectrometer Fermi level. Using this procedure, calibration of the spectrometer energy scale was routinely maintained in agreement with recently derived data for copper and gold standards [95, 96] as listed in Table 1.1. The Au $4f_{7/2}$ line typically had FWHM's of 1.20 eV and 0.85 eV for raw and deconvoluted data, respectively, which indicate the overall resolution for these measurements. The position, FWHM, and shape of the Au $4f_{7/2}$ line for Ar^+-sputtered gold sheet were unchanged during operation of the flood-gun under the conditions described in Section 1.3.1.

1.3.3. Biased Metal-Dot (BMD) Method

The physical basis for the calibration of insulator binding energies by the BMD method was investigated by comparing the BE_F scales obtained for two different noble metal calibrants on fire-polished surfaces of SiO_2 glass. These samples were prepared by a standard procedure. Rectangular plates of T08 fused quartz [97] (20x10x2 mm) were ultrasonically

Table 1.1: Binding Energies (eV) of Calibration Lines

	This work*	Bird and Swift [95]	Anthony and Seah [96]
Cu $2p_{3/2}$	932.70 (0.02)	932.66 ± 0.06	932.67 ± 0.02
Cu $L_3M_{4,5}M_{4,5}$	334.92 (0.03)	334.96 ± 0.04	334.95 ± 0.01
Cu $3p_{3/2}$	75.13 (0.04)	-	(75.13 ± 0.02)**
Au $4f_{7/2}$	84.00 (0.04)	83.98 ± 0.02	84.00 ± 0.01

---

[*] mean value (standard deviation)

[**] Cu 3p

cleaned in methanol, chemically etched in concentrated HF for 10 min, rinsed in $\sim$18 MΩ H_2O, and dried in a glove bag purged with filtered O_2. The upper surface of a plate, supported on clean platinum foil, was then fire-polished at temperatures >1800°C with a small oxy-hydrogen torch. When cool, this surface was masked with degreased aluminum foil so that a metal calibrant could be vacuum-evaporated onto the sample through a pinhole $\sim$1 mm in diameter. A deposition of gold or platinum, $\gtrsim$100 nm thick, was made in a vacuum-evaporator at $\leq 7\times10^{-4}$ Pa. Samples were placed inside the test chamber $\lesssim$60 min after fire-polishing. Seven fire-polished plates were examined in this study--five with gold and two with platinum calibrants.

The orientation of a sample relative to the CMA for the BMD studies is illustrated in Fig. 1.7(a). The area focussed by the CMA for analysis of the insulator is offset by $\sim$2 mm from the calibrant dot so that spectral interference from the calibrant was avoided. A survey spectrum (1100-0 eV) was acquired initially for each sample. High resolution spectra of O 1s and Si 2p core levels for SiO_2 and the C 1s level from adventitious carbon were then recorded concurrently for apparent surface potentials $+6\ \text{V} \gtrsim Q \gtrsim -10\ \text{V}$ as determined by Eqs. (1.5a) or (1.5b) for gold or platinum calibrants, respectively. By systematically varying the flood-gun voltage, sets of core level spectra were obtained at several values of $Q \lesssim 0$ V for all samples. Additional sets of spectra for $Q > 0$ V were acquired with the flood-gun turned off for some of the samples. In each measurement, Q was determined by focusing the CMA on the calibrant dot before and after the insulator spectra were measured in order to ascertain the stability of the bias imposed at the calibrant-insulator junction. It was generally found that Q was constant to within ± 0.05 eV.

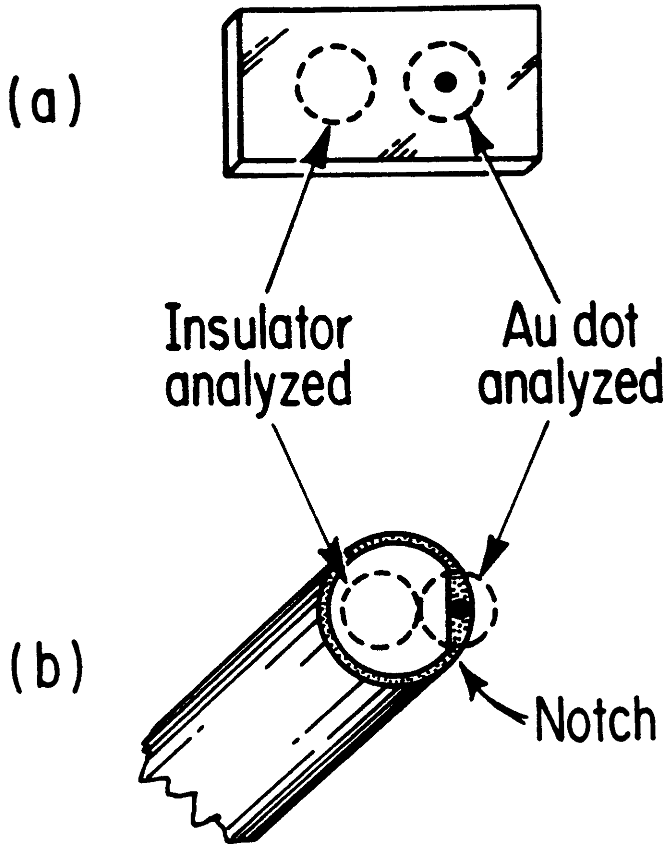

Fig. 1.7: Orientation of sample relative to focal area of CMA; (a) for BMD studies of fire-polished SiO_2 glass plates and (b) for adaptation of BMD method to bulk analysis of vacuum-fractured SiO_2 glass rods.

1.3.4. Adaptation of BMD Method to Vacuum-fractured Surfaces

The BMD method of charging correction was adapted to the analysis of vacuum-fractured surfaces of SiO_2 as follows. Rods of T18 (∿8 ppm OH) and T08 (∿180 ppm OH) fused quartz [97] and T19 (∿1200 ppm OH) fused silica [97] (4 mm in diameter x 20 mm) were radially notched with a diamond wheel to a depth of ∿0.2 mm to promote flat breaks perpendicular to the sample axis. This notch was then deepened to ∿0.5 mm along a section that would become the origin of fracture. Bars of α-quartz (4x4x20 mm), cut from a boule of natural rock crystal [98], were prepared in an analogous manner. After ultrasonic cleaning in methanol, a sample was masked with degreased aluminum foil so that gold could only be vacuum-evaporated onto one side of the deep notch through a pinhole ∿1 mm in diameter. Gold was deposited to a thickness $\gtrsim 100$ nm in a vacuum-evaporator at $\leq 7 \times 10^{-4}$ Pa. Samples were mounted in special holders for these experiments and loaded in sets of up to three onto the carousel inside the test chamber. As indicated in Fig. 1.6, a manipulator is used to transfer a holder from the carousel to the fracture stage. With the notch in the rod or bar level with the top surface of the brace, a pendular hammer is employed to fracture the sample. The holder is then returned to the carousel and rotated into position for analysis. Acquisition of spectra normally commenced <10 min after fracture of a sample. At least seven samples of each type of SiO_2 were examined in order to assess the precision of the BMD method as applied to vacuum-fractured surfaces of insulators.

The orientation of a fracture surface relative to the CMA is illustrated in Fig. 1.7(b). The area focussed by the CMA for analysis of the insulator is once again offset by ∿2 mm from the gold dot to avoid spectral interference. After a survey spectrum, sets of core level spectra were acquired at various values of Q for two samples of T08 fused quartz using the procedure described in Section 1.3.3. All other samples were measured with the flood-gun voltage adjusted to yield values of $Q \sim 10$ V as determined by Eq. (1.5a) for the gold calibrant. The stability of the bias imposed at the calibrant-insulator contact for these measurements was identical to that observed in Section 1.3.3. Following a survey spectrum, a high resolution spectrum of the O 1s core level was obtained prior to the concurrent acquisition of high resolution spectra for the O 1s, Si 2p and C 1s levels. A final survey spectrum completed an analysis. In addition, a high resolution spectrum of the valence band (40-0 eV) was recorded for two samples of T08 fused quartz. Whereas all core level spectra were typically acquired in 1-2 hrs, the valence band spectra required signal averaging over periods of $\sim$20 hrs to attain an adequate signal-to-noise ratio.

1.4. Results:

1.4.1. BMD Studies with Gold and Platinum Calibrants

Survey spectra for fire-polished plates of T08 fused quartz indicated these surfaces were remarkably free of significant contamination by adventitious carbon at the start of an analysis. However, the C 1s signal was found to increase very slowly under X-irradiation during the time of analysis. Binding energies for sets of O 1s, Si 2p, and C 1s core level spectra from seven samples, corrected through Eq. (1.6) with corresponding values of Q from Eqs. (1.5a) and (1.5b), are plotted against Q in Fig. 1.8. The data of SB [52] for a vacuum-milled surface of 7940 (1200 ppm OH) fused silica [99] are also included in Fig. 1.8 for comparison. In the case of the fire-polished surfaces investigated here, BE_F for the core

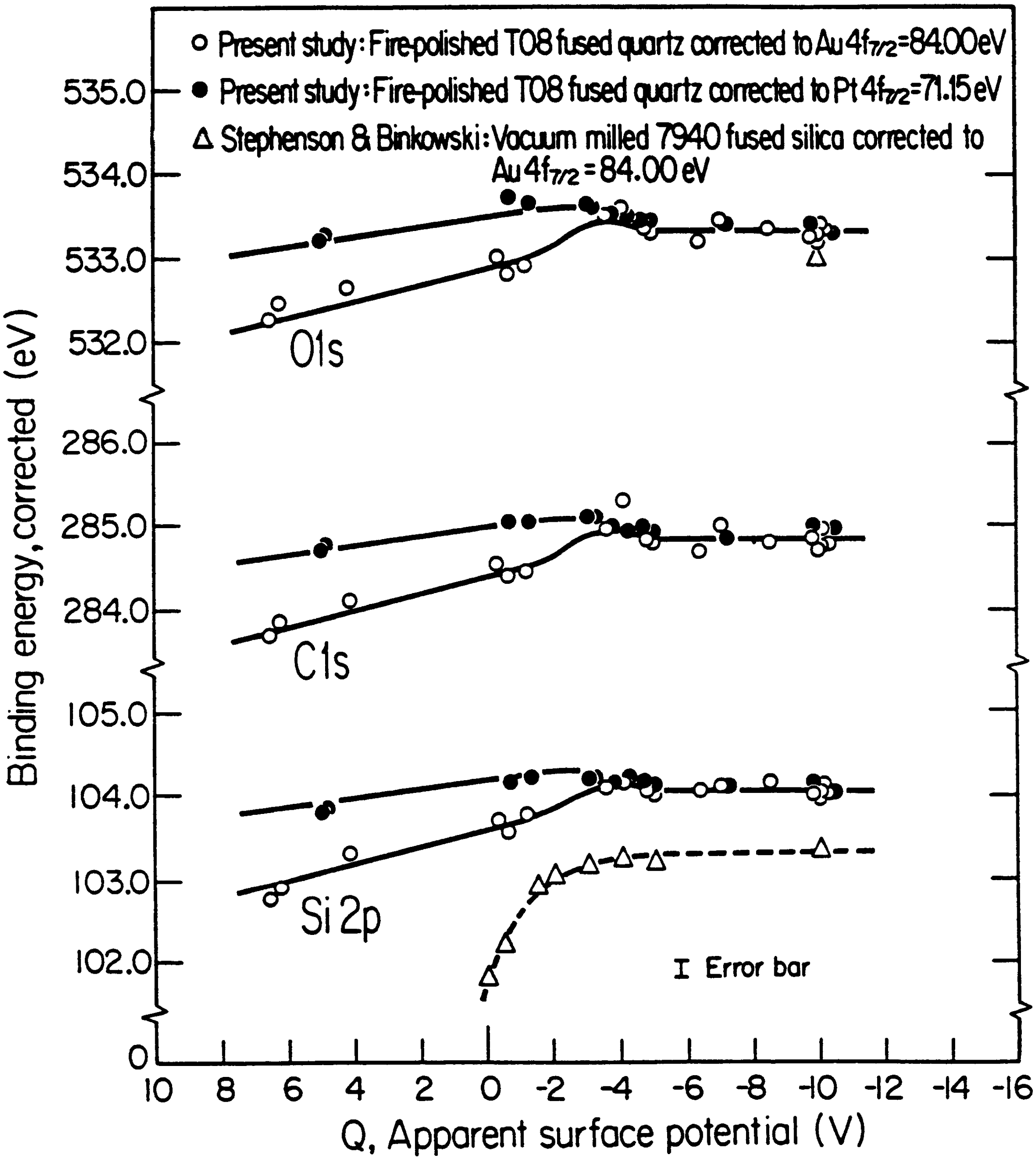

Fig. 1.8: Binding energies, BE_F, corrected by the BMD method vs. the apparent surface potential, Q, for gold and platinum calibrants on fired-polished surfaces of SiO_2 glass. Data of SB [52] included for comparison.

levels are seen to vary with Q for positive, zero, or slightly negative biases. Only for $-4\text{ V}\gtrsim Q\gtrsim -10\text{ V}$ do BE_F become independent of Q, in agreement with the results of SB. Furthermore, each core level is corrected separately by gold and platinum calibrants to an <u>identical</u> BE_F for this range, in contrast to the divergent BE_F observed for $Q>-4$ V. It should also be noted that the position of the C 1s level relative to the O 1s and Si 2p levels of SiO_2 is constant over the entire range of Q investigated in these studies for a given metal calibrant. Moreover, the absolute and relative binding energies of the O 1s and Si 2p levels for the fire-polished surfaces are at variance with SB's data for a vacuum-milled surface (cf at $Q\sim-10$ V in Fig. 1.8).

Typical spectra of the O 1s and Si 2p core levels for fire-polished surfaces of T08 fused quartz are presented in Fig. 1.9. Each level is reasonably described by a single Gaussian peak. Binding energies and widths of these photopeaks for fire-polished surfaces are listed in Table 1.2 along with the position of the C 1s photopeak from adventitious carbon. These data were obtained with a gold calibrant at $Q\sim-10$ V and subsequently corrected by the BMD method of Au $4f_{7/2}$=84.00 eV. Under these conditions, the FWHM for the Au $4f_{7/2}$ line of the calibrant was equivalent to that of grounded gold sheet in Section 1.3.2.

1.4.2. Core and Valence Level Spectra for SiO_2

Survey spectra for a vacuum-fractured surface of T08 fused quartz which correspond to the two orientations of the sample in Fig. 1.7(b) are presented in Fig. 1.10. By offsetting the sample such that the CMA is focussed entirely on the fracture surface, the insulator spectrum in Fig. 1.10(a) is obtained without contaminant lines or spectral interference from the

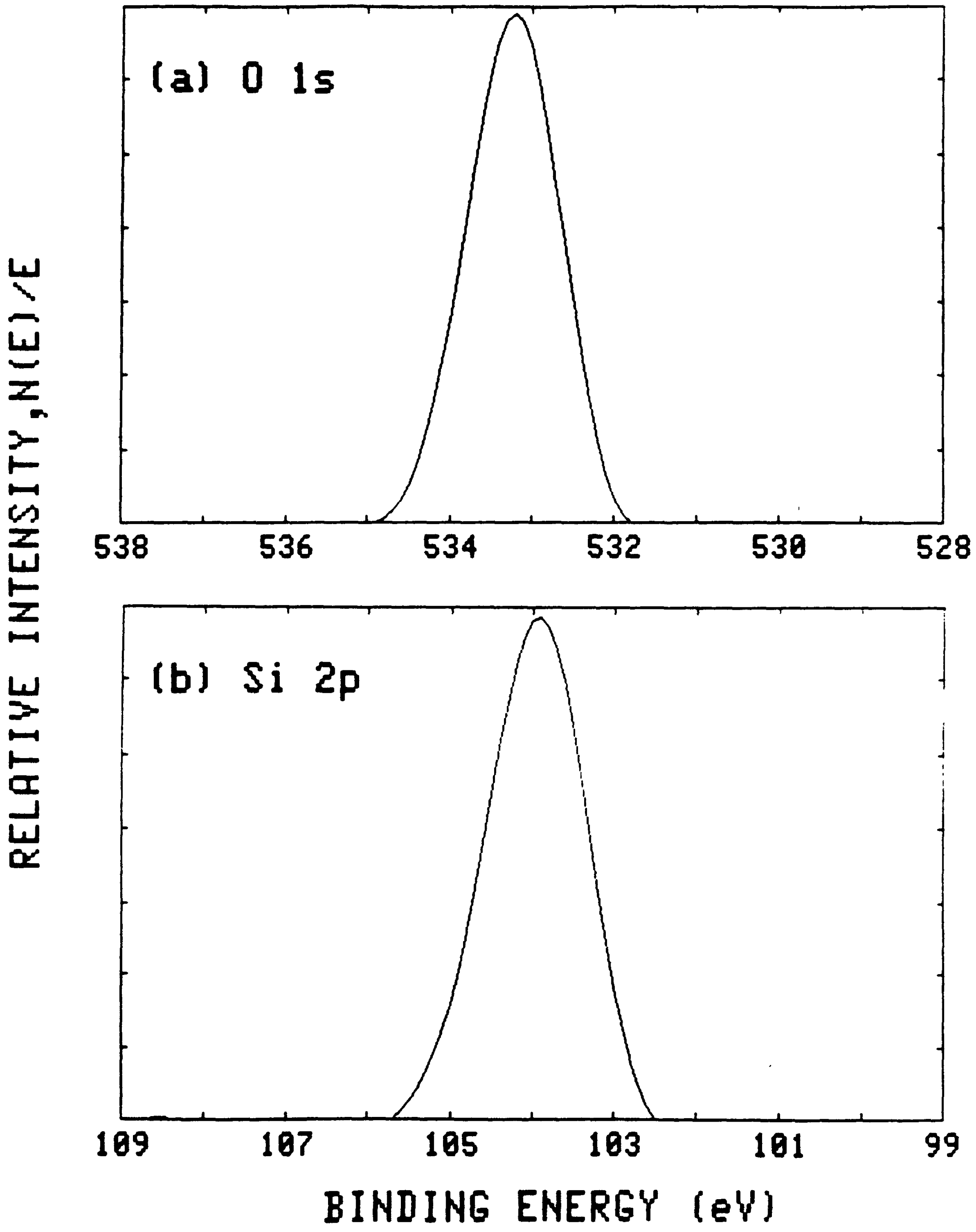

Fig. 1.9: Fire-polished T08 fused quartz: (a) O 1s and (b) Si 2p core levels.

Table 1.2: Binding Energies (eV) and FWHM (eV) of Electronic Levels for SiO_2

	T18* /7/	T08* /13/	T19* /7/	α-quartz* /8/	T08** /5/
E_F		0.00			
UVB:$BE_F(E_V)$		4.80			
:BE_F (peak 1)		7.85			
:BE_F (peak 2)		11.85			
:BE_F (peak 3)		14.65			
: width+		12.00			
LVB:BE_F (peak)		25.20			
:BE_F (shoulder)		∿26.90			
CORE++:BE_F (Si 2p)	103.77(0.16)	103.81(0.15)	103.71(0.10)	103.71(0.15)	104.02(0.06)
:FWHM (Si 2p)	1.40(0.01)	1.39(0.03)	1.39(0.01)	1.39(0.02)	1.37(0.02)
:BE_F(O 1s)	533.00(0.15)	533.04(0.12)	532.93(0.10)	532.97(0.14)	533.29(0.08)
: FWHM (O 1s)	1.34(0.01)	1.33(0.02)	1.33(0.01)	1.34(0.02)	1.29(0.02)
:BE_F (C 1s)	284.74(0.13)	284.82(0.19)	284.65(0.20)	284.92(0.18)	284.85(0.15)

---

[*] vacuum-fractured surfaces

[**] fire-polished surfaces

[+] by extrapolation of leading and trailing UVB edges to baseline

[++] mean value (standard deviation)

// number of samples for core level spectra

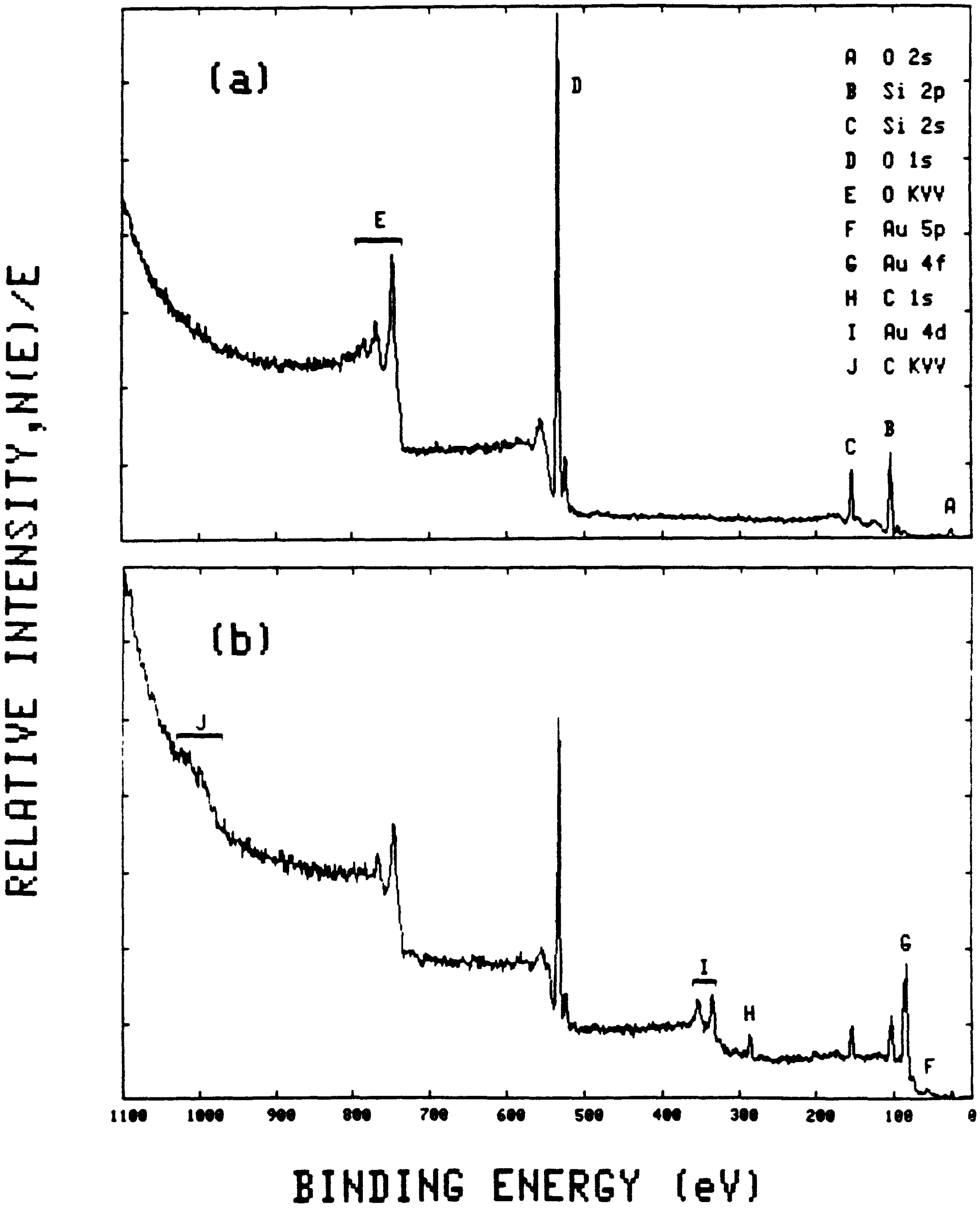

Fig. 1.10: Vacuum-fractured T08 fused quartz: (a) survey spectrum for CMA focused on fracture surface and (b) survey spectrum for CMA focused on gold dot.

calibrant. When the CMA is focussed on the gold dot to determine Q, intense photopeaks and Auger lines from the calibrant and carbon contamination are superimposed on the insulator spectrum in Fig. 1.10(b). As was the case for fire-polished surfaces of SiO_2 glass, the C 1s signal from the fracture surface itself increased very slowly with time under X-irradiation to a level of $\lesssim 1$ atomic % after several hours. Corrected binding energies for sets of core level spectra acquired at $+6\ \text{V} \gtrsim Q \gtrsim -10$ V for two fracture surfaces of T08 fused quartz exhibited similar trends to those described in Section 1.4.1. for fire-polished surfaces.

Typical spectra of the O 1s and Si 2p core levels for vacuum-fractured surfaces of T08 fused quartz are shown in Fig. 1.11. Both levels are again reasonably fit by a single Gaussian peak. No significant differences among the core level spectra for T18, T08, and T19 SiO_2 glasses or α-quartz were observed. Binding energies and widths of the O 1s and Si 2p photopeaks for each of these types of SiO_2 are given in Table 1.2 along with the position of the minor C 1s photopeak from adventitious carbon. All data were acquired from fracture surfaces at $Q \sim -10$ V and subsequently corrected by the BMD method to Au $4f_{7/2}=84.00$ eV. For this sample geometry, the FWHM of the calibrant line was again found to be the same as for the grounded metal.

Valence band spectra from two vacuum-fractured surfaces of T08 fused quartz that have been overlayed to emphasize the reproducibility of these measurements are shown in Fig. 1.12(a). For comparison, the upper valence band (UVB) spectra of vacuum-milled Cab-O-Sil [100], 7940 fused silica, and α-quartz by SB [52] and a thick vitreous SiO_2 film grown from dc-sputtered silicon at 650°C in oxygen by Fischer et al [8] are reproduced

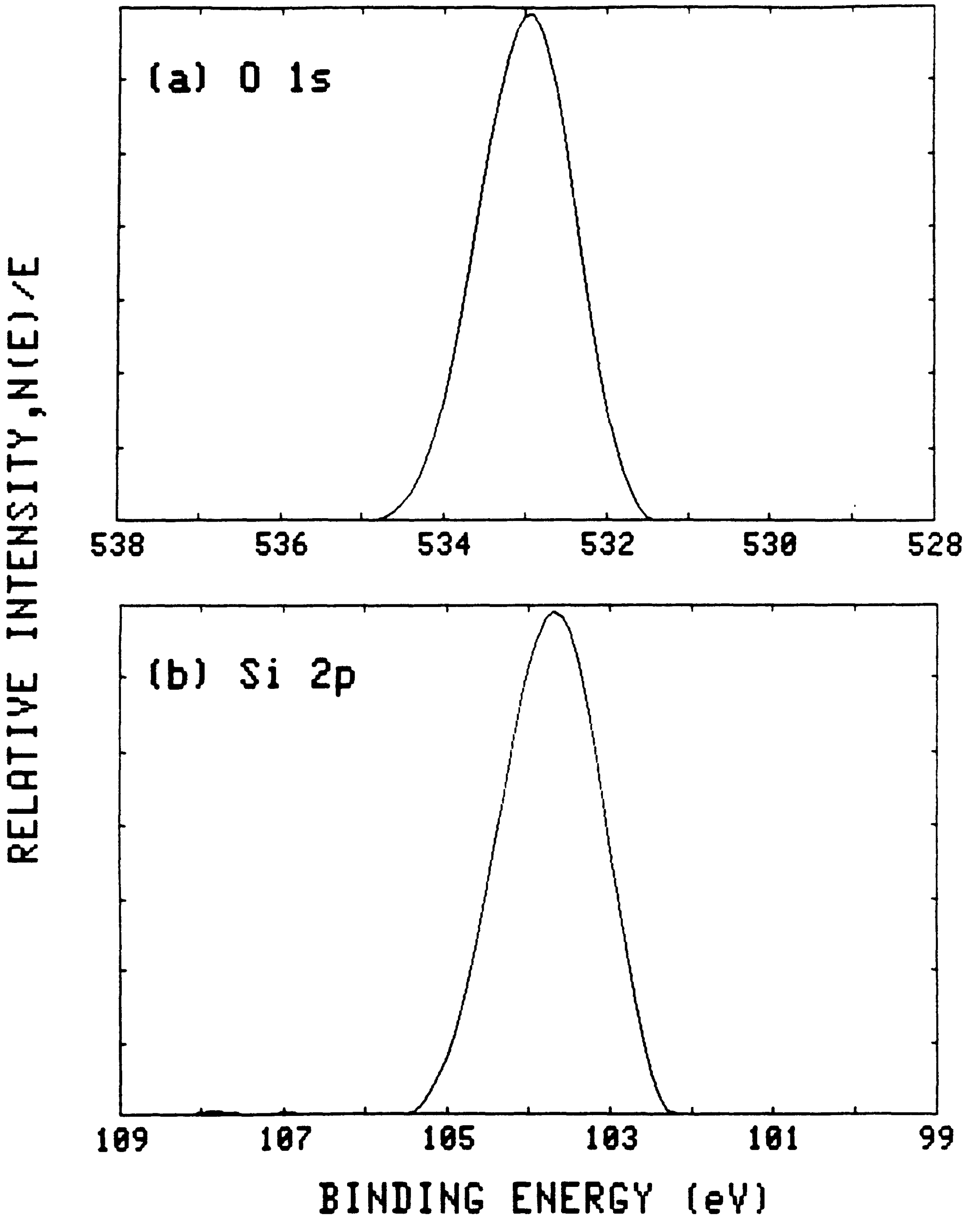

Fig. 1.11: Vacuum-fractured T08 fused quartz: (a) O 1s and (b) Si 2p core levels.

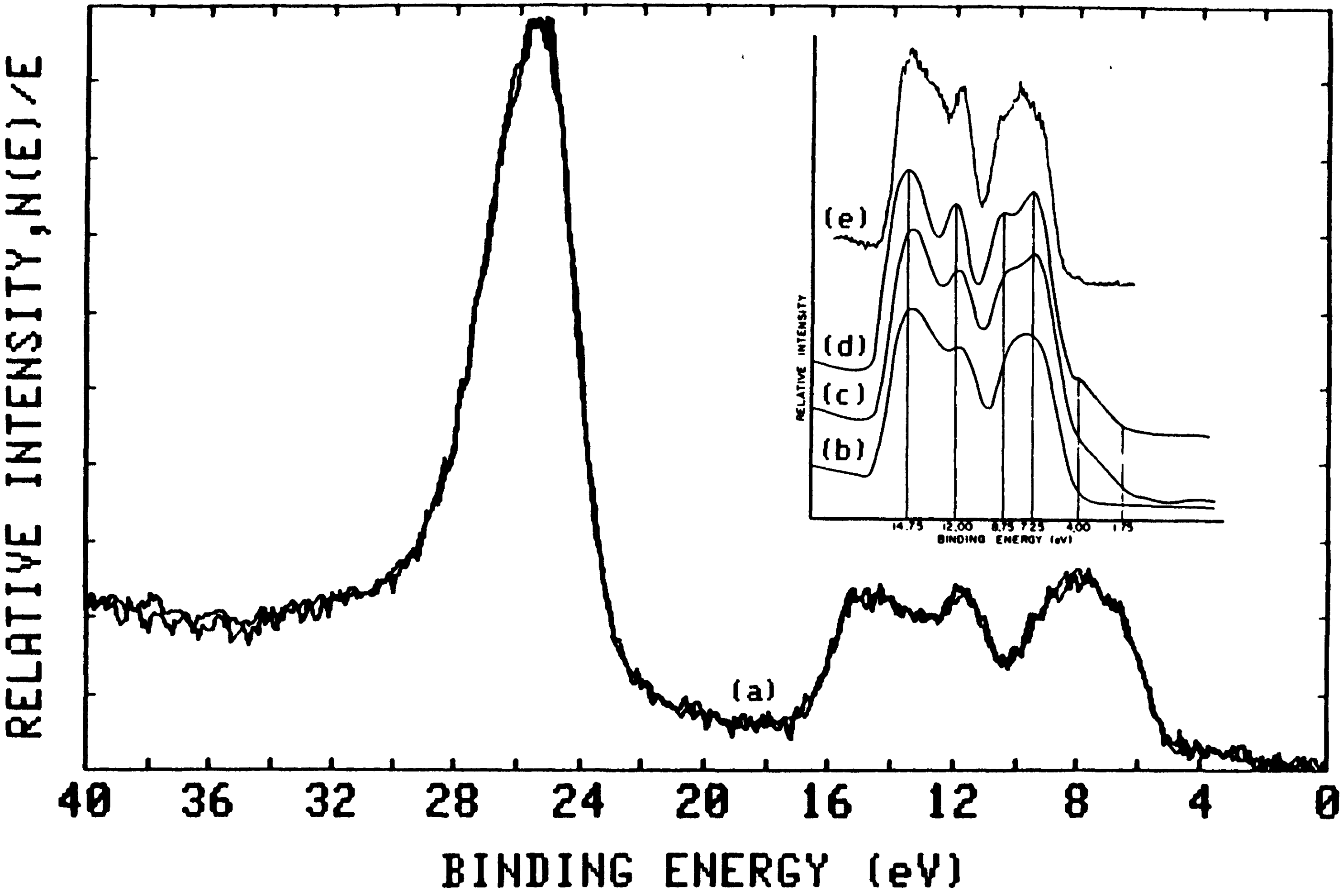

Fig. 1.12: Valence band spectra for SiO_2: (a) vacuum-fractured T08 fused quartz; vacuum-milled (b) Cab-O-Sil, (c) 7940 fused silica, and (d) α-quartz; and, (e) thermally oxidized SiO_2 film. Spectra (b-d) from Ref. 52 and spectrum (e) from Ref. 8.

in Fig. 1.12(b-e), respectively. The spectrum of Fischer et al has been shifted by $\sim$5 eV to higher binding energies in order to align it with the energy scale of the other spectra in Fig.1.12 obtained by the BMD method. For the SiO_2 glass in Fig. 1.12(a), three peaks are resolved in the UVB; while one peak with a broad shoulder at higher binding energies characterizes the lower valence band (LVB). Binding energies of component peaks in the UVB and LVB and the base line width of the UVB are listed in Table 1.2. The three-peak structure of the UVB for vacuum-fractured SiO_2 glass (Fig. 1.12(a)) closely agrees with that for the vacuum-milled particulate SiO_2 (Fig. 1.12(b)) and the thermally-oxidized SiO_2 film (Fig. 1.12(e)). However, this three-peak structure stands in contrast to the five-peak structure that SB reported for vacuum-milled SiO_2 glass (Fig. 1.12(c)) and crystal (Fig. 1.12(d)). Particular attention is called to the feature in the latter spectra at 3.5-4.0 eV whose tail extends $\sim$3.0 eV into the bandgap from an extrapolation of the leading edge for the first major peak in the UVB below E_F=0 eV.

1.5. Discussion:

1.5.1. Metal-Insulator Interfaces

In order to establish a rational basis for applying the BMD method of charging correction to dielectric samples in XPS, some familiarity with the electronic nature of metal-insulator interfaces is necessary. Therefore, the formation of Schottky barriers at metal-semiconductor junctions is first briefly described with the assumption that insulators can be considered as intrinsic semiconductors with large bandgaps. The available data for metal-SiO_2 contacts are then discussed in terms of chemical trends in the formation of Schottky barriers. On this basis, the results of the BMD experiments comparing gold and platinum calibrants are explained and a revised energy-level diagram for the BMD method is proposed in Section 1.5.2.

The general interface potential theory of Cowley and Sze [101, 102] identifies two classic limiting cases for the formation of a rectifying barrier, $q\phi_B$, across a metal-semiconductor interface having coincident Fermi levels at thermal equilibrium. This analysis assumes that the interface between the metal and semiconductor has atomic dimensions and is transparent to electrons, and that the density of surface states is solely a property of the semiconductor surface and does not depend on the metal. In the Bardeen [103] limit, the barrier height is independent of the metal work function, $q\phi_M$, due to stabilization of the Fermi level by surface states within the semiconductor bandgap, E_g. Other theoretical treatments have proposed alternative mechanisms for Fermi level pinning--e.g., by tailing of metal wave functions into the semiconductor bandgap [104], or by narrowing of the bandgap due to differences in electron screening at the metal-semiconductor interface [105]. In the Schottky [106] limit, the barrier height varies linearly with $q\phi_M$ in the absence of surface states. For n-type semiconductors, the barrier to injection of electrons from E_F of the metal to E_C of the semiconductor is

$$q\phi_{Bn} = q(\phi_M-\chi), \tag{1.9a}$$

where $q\chi$ is the electron affinity of the semiconductor. In the case of p-type semiconductors, the barrier to injection of holes from E_F of the metal to E_V of the semiconductor is

$$q\phi_{Bp} = E_g-q(\phi_M-\chi). \tag{1.9b}$$

One of several problems with this formulation of the Schottky limit is the presumption that $q\phi_M$, measured at a metal-vacuum interface, is invariant with respect to the change in boundary conditions when applied to calculations of $q\phi_B$ at metal-semiconductor junctions by Eq. (1.9) [107]. The vacuum work function of a metal in Fig. 1.1(a) consists of two components

$$q\phi_M = q(\phi_M^D - \phi_M^I), \tag{1.10}$$

where $q\phi_M^I$ is the chemical potential (or Fermi level) relative to the average internal electrostatic potential of the bulk, $\overline{E}$, and $q\phi_M^D$ is an additional potential exerted by a surface dipole [20]. The latter component has both intrinsic and extrinsic contributions. The variation in $q\phi_M$ among different crystallographic planes for clean surfaces of single crystals is related to intrinsic differences in atomic surface structure. Extrinsic factors such as the adsorption of electronegative or electropositive contaminants at the metal surface act to increase or decrease $q\phi_M$, respectively. One would thus expect the nature of a metal work function at a metal-semiconductor interface to be quite different from that at a metal-vacuum interface. In fact, it was the anticipation of $q\phi_M^D$ being significantly modified at compound interfaces which led to attempts at correlating $q\phi_B$ with $q\phi_M^I$ through a related bulk property, the electronegativity of the metal [108].

Kurtin et al [109] defined an empirical index which distinguishes between the Bardeen and Schottky limits for electronic barriers at metal-semiconductor interfaces on the basis of the covalent-ionic character of chemical bonding in the semiconductor. The slope S of a straight line, fitted to data for $q\phi_{Bn}$ (e.g., as measured by capacitance-voltage or internal photoinjection techniques [102]) versus the Pauling [110] electronegativity, X, of various metals forming contacts with a particular semiconductor, was reported to be inversely proportional to the degree of Fermi level stabilization. Results for a large number of semiconductors and insulators were interpreted as evidence for a fundamental transition between nearly complete stabilization where $S \underset{\sim}{\sim} 0.1$ for highly covalent materials, and no stabilization when $S \underset{\sim}{\sim} 1.0$ for materials with appreciable ionic bonding character. Although the Bardeen limit is reasonably associated with $S \sim 0$, a statistical reanalysis of Kurtin et al's data by Schluter [111] demonstrated that the covalent-ionic transition toward the Schottky limit is not nearly so well delineated as was claimed in the earlier work. Other theoretical and experimental results [112, 113] have indicated that the Schottky limit occurs for $S \sim 1.5$ rather than unity.

Recent characterizations of the structure and chemistry of metal-semiconductor junctions by surface sensitive spectroscopies have shown the ordered and abrupt boundary, assumed in the above linear interface potential models, is often radically altered in reality. Structural imperfections associated with chemical disordering, interdiffusion, and reactions at typical interfaces are now generally recognized as important if not dominant factors contributing to deviations from simple linear theories for Schottky barriers [114, 115].

With this background, the available data for $q\phi_{Bn}$ by photoinjection [36, 116-121] at various metal-SiO_2 contacts are now scrutinized. The goal here is to understand the nature of the electronic contact between a given calibrant metal and SiO_2 in the present study of the BMD method. Since the mobility of electrons (20-40 $cm^2/V.s$) is much larger than that of holes ($\lesssim 2 \times 10^{-5}$ $cm^2/V.s$) in SiO_2 [122] and $q\phi_{Bn}$ is smaller than $q\phi_{Bp}$ for most metal-SiO_2 contacts, $q\phi_{Bn}$ is the barrier height most readily determined by experiment. A linear regression through the data for $q\phi_{Bn}$ vs. X in Fig. 1.13(a) appears to be a fair description, in accord with barrier-formation approaching the Schottky limit (i.e., $S\sim1.5$). Brillson [123] has contended otherwise that the sigmoidal trend often found in a plot of $q\phi_{Bn}$ vs. the enthalpy of reaction, ΔH_R, for different metals with a given semiconductor more appropriately emphasizes the role of interfacial chemical reactions in determining barrier heights. A graph of $q\phi_{Bn}$ vs. ΔH_R [124-126] in Fig. 1.13(b) for metal-SiO_2 junctions suggests that for palladium, platinum, and gold with $\Delta H_R \gtrsim 3.0$ eV, the barrier height is roughly independent of the metal. For the other metals with $\Delta H_R \lesssim 3.0$ eV, however, the barrier height decreases with increasing reactivity of the metal with SiO_2. The point of transition between reactive and unreactive interfacial behavior would tend to shift toward $\Delta H_R = 0$ eV if the heats of condensation for the metals evaporated onto SiO_2 were taken into account in calculations of ΔH_R.

Studies of Al-SiO_2 and Au-SiO_2 interfaces with Auger and photoemission spectroscopies [127, 128] have shown two distinctly different types of chemical interactions which correspond to the chemical trends for $q\phi_{Bn}$ noted in Fig. 1.13(b). The analyses indicate that aluminum reacts strongly with SiO_2, whereby oxidation-reduction products of Al_2O_3 and free silicon are detected in a $\sim$1-10 nm thick reaction layer across the Al-SiO_2 interfacial region. In contrast, gold is thought to produce a strained metal-SiO_2 interface with some indications of gold bonding to silicon atoms in a thin transition region of SiO_x to SiO_2. These results are consistent with the fact that vacuum-deposited gold adheres poorly to SiO_2 while the bond between vacuum-deposited aluminum and SiO_2 is tenacious by comparison. In this context, it is not surprising that barrier heights for even relatively unreactive Pd-SiO_2, Pt-SiO_2, and Au-SiO_2 contacts can be modified by positive or negative

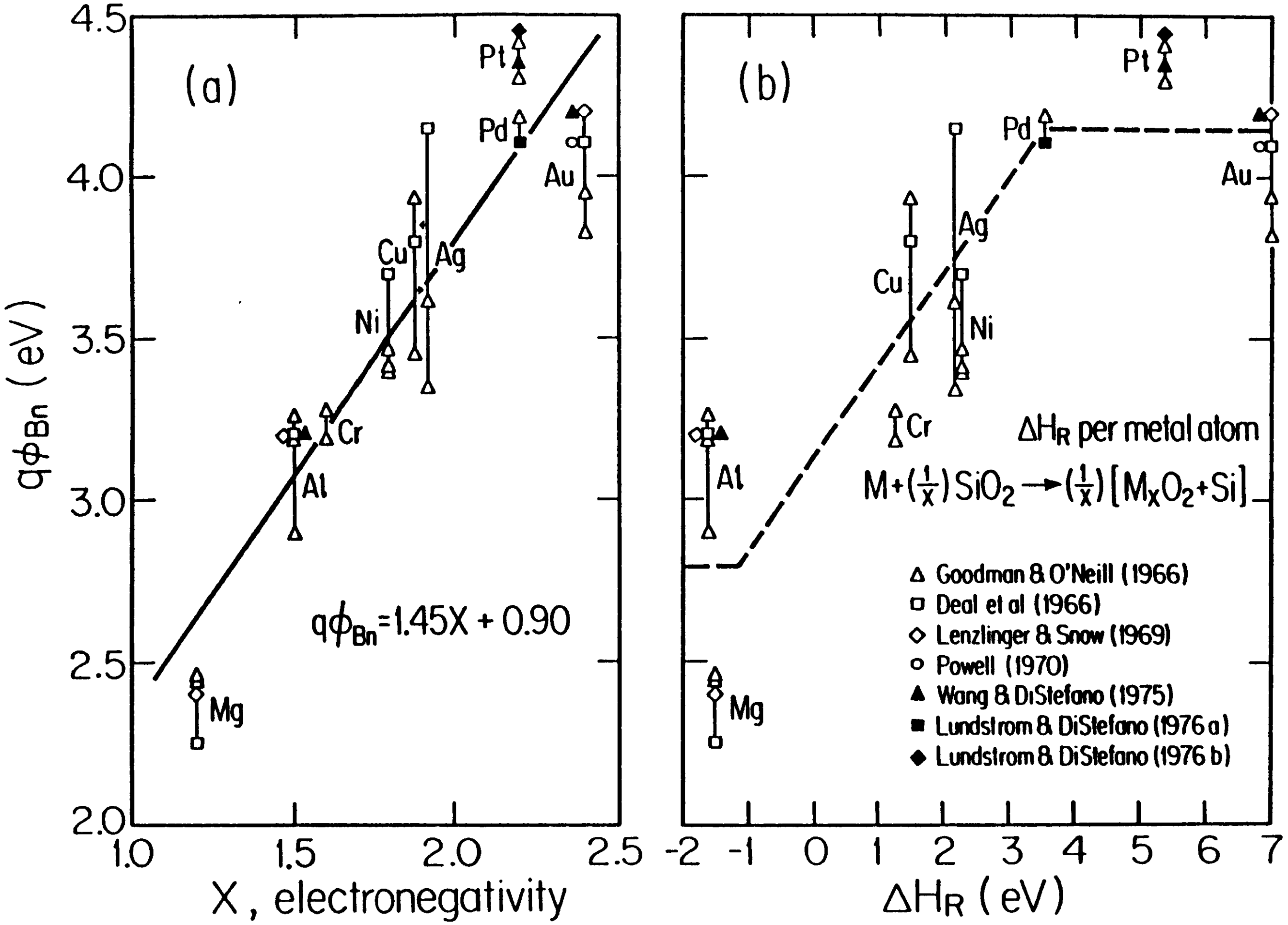

Fig. 1.13: Metal-SiO_2 contacts: (a) barrier height $q\phi_{Bn}$ vs. electronegativity and (b) $q\phi_{Bn}$ vs. enthalpy of reaction. Data for $q\phi_{Bn}$ from Refs. 36, 116-21.

interfacial dipoles depending upon processing conditions such as temperature and atmosphere [120, 121, 129]. Such effects may account for some of the scatter and nonlinear trends in the data shown in Fig. 1.13.

1.5.2. A Model for the BMD Method

A major finding of the BMD experiments in Section 1.4.1 is that each core level for SiO_2 is corrected through gold and platinum calibrants to an identical BE_F at high negative bias. An attempt to construct a unique reference to E_{VAC} by Eq. (1.7) using the vacuum work functions for the calibrants, $q\phi_{Au}=5.1$ eV and $q\phi_{Pt}=5.65$ eV, obviously leads to inconsistent values of BE_{VAC}. One response to this paradox is to question the indiscriminate application of $q\phi_M$ which are measured for clean surfaces in UHV to a situation where $q\phi_M^D$ in Eq. (1.10) is likely altered by superficial contaminants. A more pertinent explanation, however, follows directly from the above discussion of metal-insulator interfaces. The stable electronic contact observed between a calibrant and insulator in XPS over a range of appropriate negative bias is characterized by the height of the Schottky barrier $q\phi_{Bn}$ between E_F of the calibrant and E_C of the insulator at thermal equilibrium. Fortunately, values of $q\phi_{Bn}$ at metal-SiO_2 contacts [116] do not appear to be as sensitive to contamination as $q\phi_M$ [20]. Therefore, the identical BE_F scales observed for SiO_2 with gold and platinum calibrants for $-4\text{ V} \gtrsim Q \gtrsim -10$ V in Fig. 1.8 are associated with similar values of $q\phi_{Bn}$ for Au-SiO_2 and Pt-SiO_2 contacts in Fig. 1.13. Considering that the uncertainties in the measurements of BE_F (Table 1.2) and $q\phi_{Bn}$ (Fig. 1.13) are both $\sim$0.1 eV, this correspondence is nearly exact. One thus concludes that BE_{VAC} derived by Eq. (1.7) for theoretical or empirical comparisons [52, 53] represents a rather crude approximation of a binding energy reference to the vacuum level.

A revision of SB's energy-level diagram for the BMD method in Fig. 1.2 can now be proposed which accounts for the trends in BE_F above and below $Q\sim -4$ V in Fig. 1.8 for the O 1s and Si 2p core levels. Fig. 1.14(a) illustrates the electronic junction between an insulator and a gold calibrant (with the energy scales arbitrarily aligned at E_{VAC}) in the absence of an X-ray flux or slow electrons from a flood-gun. Under X-irradiation, $h\nu$, the analyzed surface develops a positive static space charge in Fig. 1.14(b). Processes which contribute to the charging and discharging electron currents, i_1 and i_2 in Eq. (1.3), also promote sufficient charge transfer across the junction to align E_F for the calibrant and insulator. However, the high concentration of holes in the insulator under positive bias causes E_C, E_V, and the core levels to bend upward relative to the common E_F. For this reason, BE_F for core levels in Fig. 1.8 are corrected via Eqs. (1.5) and (1.6) to progressively lower energies for increasing values of $Q\gtrsim -4$ V. The electronic contact between the calibrant and insulator is thus unstable in this range. When the return current i_2 is fixed by the flood-gun in Fig. 1.14(c), the tail of a Maxwellian distribution of electrons extends $\Delta E\gtrsim 1$ eV [130] above the work function of the tungsten filament, $q\phi_W$. Under these conditions, E_{VAC} of the insulator charges to the potential of the electrons emitted from the flood-gun [29]. With increasing negative bias provided by a variable potential supply, V_{Bias}, enough electrons are eventually injected into the conduction band of the insulator to bend the energy levels downward such that $q\phi_{Bn(Au)}$ is re-established for a critical value of $Q\sim -4$ V. Further increases in negative bias beyond this threshold do not alter the electronic contact at the calibrant-insulator junction for $-4\ \text{V}\lesssim Q\lesssim -10$ V as signified by the invariant BE_F of the core levels in Fig. 1.8

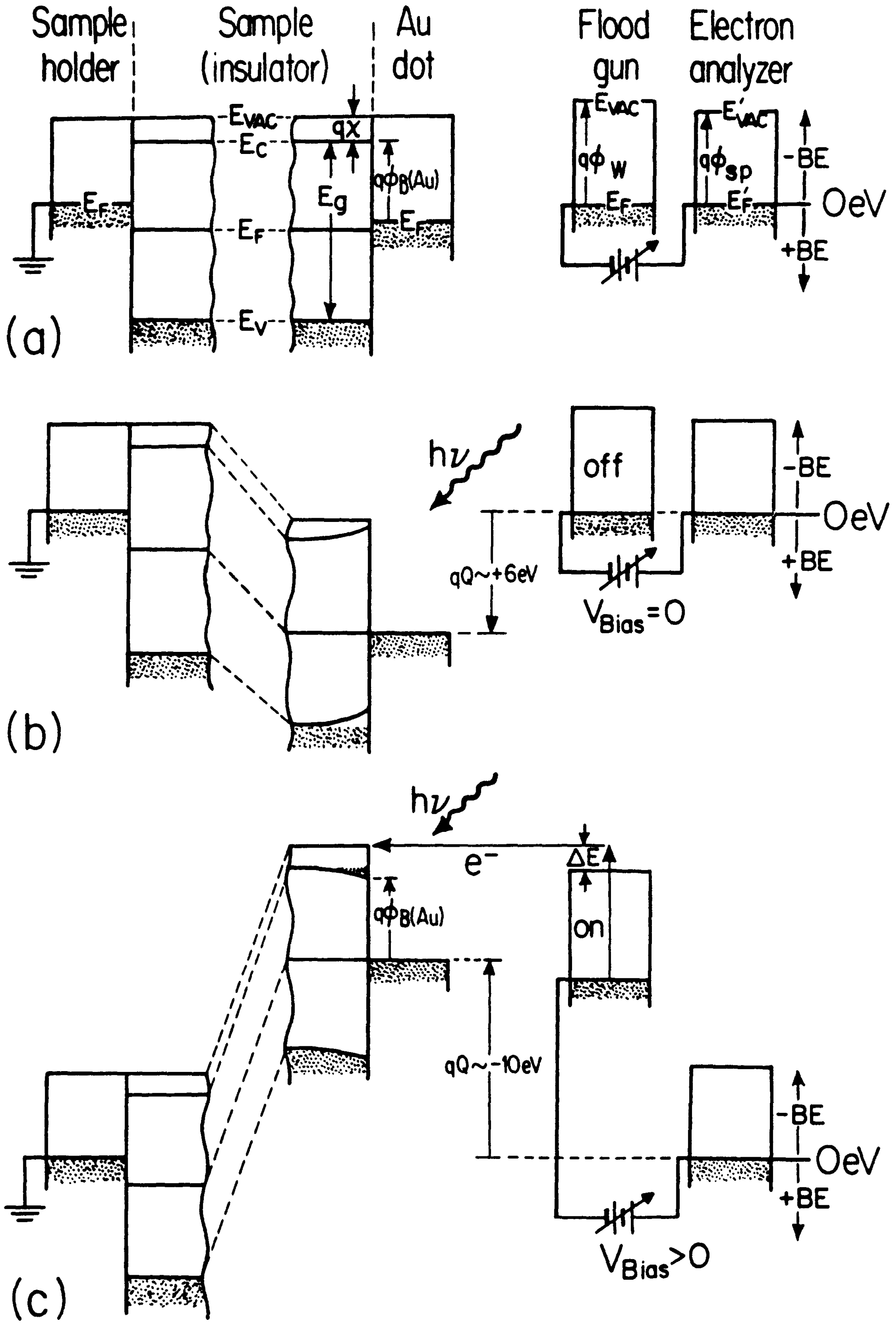

Fig. 1.14: Revised energy-level diagram for BMD method: (a) legend, (b) positive bias (Q ∿ +6 V), and (c) high negative bias (Q ∿ -10 V). Symbols are defined in text.

over this range. In other words, the electron flux from the flood-gun at high negative bias forms a virtual contact with the insulator which restores the height of the Schottky barrier between the calibrant and insulator to its value at thermal equilibrium.

The above model for the BMD method essentially maintains that for sufficient negative bias $E_{F(s)}$ of an insulator can be corrected through E_F of a calibrant metal to E'_F of the spectrometer. This premise is consistent with current knowledge of electronic contacts at metal-insulator junctions. Therefore, the relation between the energy scales for the spectrometer and sample is $BE'_F = BE_{F(s)}$. Equivalently, SB [52] stated that the insulator energies are calibrated with respect to E_F of the metal. Although this reference to $E_{F(s)}$ is somewhat arbitrary in the sense that it depends on $q\phi_{Bn}$ of a given calibrant, its physical basis is more firmly established than the reference to E_{VAC} in Eq. (1.7).

Differential charging of the SiO_2 surface by oscillations in Q is minimized under conditions of high negative bias as indicated by the equivalence in the FWHM of the Au $4f_{7/2}$ line for both the calibrant dot and the grounded metal. Since lateral gradients in Q are also likely to be small under these conditions, the FWHM of the insulator electronic levels can thus be attributed to intrinsic structural and chemical properties of the sample.

While the C 1s level accurately tracks the O 1s and Si 2p levels for SiO_2 in Fig. 1.8 over the entire range of Q, the uncertain electronic correspondence between adventitious carbon and the insulator along with other deficiencies mentioned in Section 1.2.1 militates against the use of this contaminant as a primary calibrant. The C 1s position is thus listed in Table 1.2 as a secondary reference for the SiO_2 photoemission results.

Finally, it is reasonable to expect that the BMD method is generally applicable to other dielectric materials where, in the scheme of linear interface potential theories, Kurtin et al's index S approaches the Schottky limit ~ 1.5 [109, 111-113]. In this regard, the BMD method has been successfully applied to bulk studies of multicomponent silicate glasses in Chapters 2 and 3, and polycrystalline Al_2O_3 ($S \sim 1.1$ [111]) in Appendix 1.

1.5.3. Photoemission Studies of SiO_2 Surfaces and Bulk

Although E_{VAC} or the bulk E_F for an insulating sample is not directly accessible in the current interpretation of the BMD method, the reference to $E_{F(s)}$ that is obtained for a particular calibrant is exceptionally useful when comparing results for a homologous series of samples. The utility of this approach is demonstrated by bulk studies of SiO_2 glasses and crystal in the present Chapter and alkali silicate and sodium aluminosilicate glasses in Chapters 2 and 3. Adaptation of the BMD method to vacuum-fractured surfaces in these investigations was straightforward. No difficulties were encountered with the change in sample geometry as indicated by BMD studies of vacuum-fractured surfaces of T08 fused quartz for $+6\ V \gtrsim Q \gtrsim -10$ V. For purposes of comparison, all samples were corrected through a single calibrant. Gold was a natural choice by virtue of its low chemical reactivity and ease of deposition by vacuum-evaporation. The photoemission spectra were routinely acquired at $Q \simeq -10$ V to avoid the unstable behavior at the calibrant-insulator junction observed for $Q > -4$ V in Fig. 1.8.

Earlier studies of alkali silicate and alkali phosphate glasses by XPS [15, 16, 131, 132] have clearly shown that the O 1s core level is chemically resolved into BO and NBO components, with the latter observed at lower binding energies. The geometry of the sample and CMA in the present work (see Section 1.3.1) yields an effective emission angle $\theta = 41.4°$ in Eq. (1.8) such that ∿33 % of the signal intensity from SiO_2 ($\lambda \sim 3.3$ nm) is estimated to originate from just a nanometer below the surface under analysis. Despite this appreciable surface sensitivity, no evidence that NBO's exist in detectable concentrations $\gtrsim 0.5$ atomic % ($\gtrsim 3$ % of a monolayer) [133] near vacuum-fractured surfaces of crystalline or vitreous SiO_2 was found. NBO's such as dangling singly-bonded oxygens Si-O$^\bullet$ or doubly-bonded oxygens Si=O, should be chemically distinguishable from BO's in siloxane bonds (Si-O-Si) by analogy to silicate and phosphate glasses, respectively. Core level spectra from vacuum-fractured SiO_2 surfaces are typified by those shown in Fig. 1.11 where the O 1s level consists of only a BO component. Significantly, the core level spectra from a fire-polished surface of SiO_2 glass in Fig. 1.9 closely resemble those from a vacuum-fractured surface of the same glass in Fig. 1.11. The BE_F and FWHM of the O 1s and Si 2p levels for these samples in Table 1.2 exhibit only marginal differences which suggest an underlying chemical and structural similarity.

Surfaces of SiO_2 which have been heated to $\gtrsim 800$°C are known to be virtually dehydroxylated and therefore hydrophobic [81]. Siloxane bonds at surfaces heated to >400°C have also plausibly been described as being in conformations that are less strained than is the case for surfaces heated to $\lesssim 400$°C [134, 135]. Consequently, the fire-polished surfaces examined here were not prone to gross contamination by adsorption of CO_2 or hydrocarbons in the ambient atmosphere prior to analysis. In fact, they are only efficiently rehydrated by immersion in boiling H_2O, as shown in Appendix 2. The rehydration of fire-polished surfaces is associated with a shift in BE_F for the O 1s and Si 2p core levels to lower energies with time of immersion in H_2O. It progresses at a much more rapid rate in H_2O at 100°C than at 25°C, with an ultimate decrease in the binding energy for each level of ∿1 eV.

The above comparison of photoemission results for vacuum-fractured and fire-polished surfaces of SiO_2 supports the contention of Hochstrasser and Antonini [80] that extensive surface reconstruction occurs at fracture surfaces. Within the limit of detectability for the present XPS measurements, all bonds which are broken during fracture recombine at the surface in bridging siloxane linkages. It is reasonable to assume that some of these linkages are in strained conformations to accommodate the bonding requirements of this particular reconstruction. This conjecture may account for the small differences in core level spectra between vacuum-fractured and fire-polished surfaces in Table 1.2, since the density of E'_s centers measured by ESR ($\sim 10^{12}/cm^2$) [80] is not detectable in XPS. The reconstruction suggested here excludes NBO's as a prominant surface feature at vacuum-fractured surfaces of SiO_2. It therefore disagrees with the appreciable superficial density of NBO's inferred by ELS ($\sim 10^{13}/cm^2$) [82] and the even higher density predicted by an MD simulation ($\sim 10^{14}/cm^2$) [84]. Given the thermal and chemical stability of the intrinsic surface state that was demonstrated in the ELS study, it is hard to reconcile the first discrepancy except to propose that some surface perturbation of a bridging Si-O-Si bond and <u>not</u> a Si=O bond is responsible. A likely reason for the second discrepancy is that the simulated formation of the surface does not adequately reflect the dissipative processes associated with fracture along a moving crack front. Such processes conceivably facilitate surface reconstruction by removing kinetic or topological barriers to the reformation of siloxane bonds.

The O 1s and Si 2p core levels for vacuum-fractured samples of T18, T08, and T19 SiO_2 glasses with respective bulk hydroxyl contents of ~ 8, ~ 180, and ~ 1200 ppm are characterized by identical BE_F and FWHM within the precision of the measurements as tabulated in Table 1.2. When it is considered that even the largest hydroxyl concentration is below typical bulk detection limits in XPS, this result is not surprising. Of greater interest is the finding that the core level spectra from vacuum-fractured samples of α-quartz are equivalent to those of the vitreous silicas in Table 1.2. The structures of α-quartz [136] and SiO_2 glass [137-139] are both comprised of nearly regular tetrahedra of oxygen atoms about silicon atoms which are fully connected at corners in 4-2 coordination networks. The crystal and glass have similar Si-O bond lengths of 0.161 nm and 0.162 nm, respectively. In both cases, the variation in bond lengths is negligible beyond those resulting from thermal vibrations [138-140]. The lack of long range order in the glass (ρ=2.20 g/cm^3), however, gives rise to a more open structure that is 17 % less dense than the crystal (ρ=2.65 g/cm^3).

A basic structural characteristic which distinguishes the periodic network of the crystal from the aperiodic network of the glass is the distribution of Si-O-Si angles in siloxane bonds bridging the tetrahedra. Whereas this bridging angle is constrained by periodicity in the crystal to ∿143.7°, the broader distribution of angles from ∿120° to 180° with a maximum at ∿144° in the glass leads to the generally-accepted description of its structure as being a continuous random network. The correspondence between the core level spectra for crystalline and vitreous SiO_2 implies that the covalent-ionic nature of the Si-O bond (i.e., with regard to the transfer of valence charges between silicon and oxygen atoms) does <u>not</u> change appreciably with size of the Si-O-Si angle. If the reverse were true, a broader distribution of valence charges on oxygen and silicon atoms in the glass would cause the resultant dispersion in BE_F for the O 1s and

Si 2p core levels to be manifest as an increase in FWHM relative to the crystal. The equivalence in FWHM for core levels of the crystal and glass instead suggests that similar distributions of valence charges on the constituent atoms of both materials are more closely related to the nearly identical Si-O bond lengths.

This interpretation is fully consistent with an empirical correlation of individual Si-O bond lengths with electrostatic bond strength in silicates [141, 142] and theoretical estimates of the variation in effective Mulliken atomic charges with bond length and bridging angle in SiO_2 glass [11]. However, the results presented here contradict the conclusion of an XPS study that the distribution in sizes of n-membered rings of tetrahedra (n=4, 5, 6,...) can be extracted from the Si 2p level as the result of an implicit increase in the ionic character of the Si-O bond with Si-O-Si angle [143, 144]. They are also at odds with a recent calculation of the electronic structure of α-quartz and SiO_2 glass which supports a large variation of bond lengths in the glass relative to the crystal [145]. The implications of the current photoemission results for other structural models of vitreous SiO_2 which challenge the random network model are pursued in Chapter 2.

Attention is now directed to the valence band spectrum of SiO_2 glass in Fig. 1.12(a) with reference to Table 1.2. Peaks 1, 2, and 3 of the UVB are mainly derived from nonbonding O 2p orbitals, σ bonding Si 3p - O 2p orbitals, and σ bonding Si 3s - O 2p orbitals, respectively, while the skewed peak in the LVB has primarily O 2s character [7]. A close resemblance between the three-peak structures of the UVB for vacuum-fractured SiO_2 glass in Fig. 1.12(a) and the SiO_2 film grown at 650°C in Fig. 1.12(e) is recognized, with allowance for the better instrumental resolution in the latter work. The spectral intensity between E_V at 4.8 eV and E_F=0 eV in Fig. 1.12(a) is merely an extension of the decreasing background from higher binding energies due to the bremsstrahlung from nonmonochromatic excitation in the present study. Within the precision of this measurement, there is no indication of a NBO band on the leading edges of the UVB or LVB below E_F, as compared to the valence band spectra of lithium and sodium silicates [12, 13]. The baseline widths for the UVB in Figs. 1.12(a) and (e) are 12.0 eV and 11.5 eV, respectively. This overall agreement in valence band spectra reinforces the correspondence between vacuum-fractured and fire-polished surfaces which was established above with core level spectra.

Whereas the UVB spectrum of Fischer et al [8] in Fig. 1.12(e) has generally been accepted to reflect the bulk density of states in vitreous SiO_2 [9-11], the UVB spectra of SB [52] for vacuum-milled SiO_2 glass and crystal in Figs. 1.12(c) and (d) have been controversial. Particularly troublesome is the feature at 3.5-4.0 eV whose low-energy tail increases the baseline width of the UVB from ∿12 eV to 15 eV. Griscom [7] suggested this peak is associated with surface damage and is incurred by either vacuum-milling [52] or ion-sputtering [69] solid SiO_2 surfaces. Vacuum-milling of a particulate SiO_2 is presumably less disruptive on an atomic scale since this feature is not present in the UVB spectrum of such a sample in Fig. 1.12(b). In view of the fact that this feature is also not observed for vacuum-fractured surfaces (Fig. 1.12(a)) or thermally (but fully) oxidized surfaces (Fig. 1.12(e)) [31], it is reasonably attributed to NBO's as Griscom surmised. Although the particulate SiO_2 has a nominal monolayer coverage of chemisorbed silanol groups, this coverage strongly depends upon the thermal and environmental history of the sample [81]. Lacking this critical information, one can only speculate regarding the absence of an NBO peak in Fig. 1.12(b) that can be associated with superficial silanol groups (see Appendix 2).

The O 2s orbitals of the LVB and the nonbonding O 2p orbitals at the top of the UVB have been shown to be sensitive to structural distortions in the continuous random network of vitreous SiO_2 by Ching [11]. A first-principles calculation indicated that while bond length distortions are not independent of bond angle distortions, the former have the largest effect upon the electronic structure of the glass. A larger-than-intrinsic population of such structural perturbations would explain the splitting of the nonbonding O 2p orbitals in the UVB spectra for vacuum-milled SiO_2 glass (Fig. 1.12(c)) and crystal (Fig. 1.12(d)).

Mechanical abrasion of SiO_2 surfaces is known to produce a damaged birefringent layer $\lesssim$1000 nm in thickness [146]--well in excess of the effective sampling depth in XPS of $\lesssim$10 nm. The comparison of UVB spectra in Fig. 1.12 strongly suggests that vacuum-milling of solid SiO_2 surfaces introduces NBO's and distortions in siloxane linkages that are not representative of bulk structure. Similarly, the relative and absolute positions of the O 1s and Si 2p core levels for the vacuum-milled SiO_2 glass in Fig. 1.8 may also be affected. Structural artifacts can be largely avoided by using the method of vacuum-fracture to prepare insulator surfaces for analysis. This method is more generally applicable to bulk studies of silicate glasses (especially those containing alkali or alkaline earth components) than thermal oxidation of sputtered metal films [8].

Finally, E_g for the vacuum-fractured SiO_2 glass can be estimated as $|E_F-BE_F(E_V)|$ from Table 1.2 plus $q\phi_{Bn(Au)}$ from Fig. 1.13, or 4.8 eV + 4.1 eV = 8.9 eV. This computation follows directly from the model for the BMD method given in Section 1.5.2. It is in excellent agreement with $E_g \sim 8.9$ eV as determined for vitreous SiO_2 by photoinjection and photoconductivity measurements [147]. SB's estimates of E_g from the BMD method for vacuum-milled SiO_2 glass and crystal are 7.3-5.05 eV and 7.8-5.55 eV, respectively. These rather low values for E_g are a consequence of the spurious NBO peak at 3.5-4.0 eV in UVB spectrum whose tail extends $\sim$3.0 eV into the bandgap (Figs. 1.12(b) and (c)).

1.6. Summary:

The BMD method of SB [52] is affirmed as an attractive way to overcome static and differential charging of insulators in XPS. Under conditions of high negative bias, imposed with an electron flood-gun during analysis, the height of the Schottky barrier between a metal calibrant and insulator is restored to its value at thermal equilibrium. The binding energy scale for the insulator can thus be subsequently corrected to its surface Fermi level $E_{F(s)}$ through the Fermi level of the calibrant. However, an amendment of this reference to E_{VAC} by means of the vacuum work function for the calibrant is of dubious validity. By adapting the BMD method to the analysis of vacuum-fractured surfaces, structural artifacts introduced by inappropriate means of surface preparation (including ion-sputtering and vacuum-milling) can be avoided. Accurately calibrated photoemission spectra that are indicative of bulk physicochemical properties of an insulator can thus be obtained.

The utility of this experimental approach was demonstrated in an XPS investigation of crystalline and vitreous SiO_2. A comparison of vacuum-fractured and fire-polished surfaces of SiO_2 glass lends support to a view that extensive surface reconstruction of siloxane bonds occurs at fracture surfaces. NBO's (e.g., $Si-O^{\bullet}$ or $Si=O$) were not observed in detectable concentrations $\gtrsim 0.5$ atomic % ($\gtrsim$ 3 % of a monolayer) near vacuum-fractured surfaces of SiO_2 glass or crystal. In addition, the similarity of core level spectra between several types of SiO_2 glass and α-quartz suggests that the covalent-ionic nature of the Si-O bond does not change appreciably with the Si-O-Si bridging angle. Finally, the valence band spectrum for a vacuum-fractured surface of SiO_2 glass was critically compared with earlier work in order to resolve some discrepancies in the experimental density of states for SiO_2.

REFERENCES

[1] X-ray Photoelectron Spectroscopy (XPS) is synonymous with X-ray Photoemission Spectroscopy, and is also known as Electron Spectroscopy for Chemical Analysis (ESCA).

[2] K. Siegbahn, C.N. Nordling, A. Fahlman, R. Nordberg, K. Hamrin, J. Hedman, G. Johansson, T. Bergmark, S.E. Karlsson, I. Lindgren, and B. Lindberg, ESCA: Atomic, Molecular and Solid State Structure Studied by Means of Electron Spectroscopy. Almqvist and Wiksells, Uppsala, 1967.

[3] Handbook of X-ray and Ultraviolet Photoelectron Spectroscopy. Edited by D. Briggs. Heyden, London, 1977.

[4] Photoemission in Solids I - General Principles (Topics in Applied Physics, Vol. 26). Edited by M. Cardona and L. Ley. Springer-Verlag, Berlin, 1978.

[5] V.V. Nemoshkalenko and V.G. Aleshin, Electron Spectroscopy of Crystals. Plenum, New York, 1979.

[6] Practical Surface Analysis by Auger and X-ray Photoelectron Spectroscopy. Edited by D. Briggs and M.P. Seah. Wiley, New York, 1983.

[7] D.L.Griscom, "The Electronic Structure of SiO_2: A Review of Recent Spectroscopic and Theoretical Advances", J. Non-Cryst. Solids, 24 [2] 155-234 (1977).

[8] B. Fischer, R.A. Pollak, T.H. DiStefano, and W.D. Grobman, "Electronic Structure of SiO_2, $Si_xGe_{1-x}O_2$, and GeO_2 from Photoemission Spectroscopy", Phys. Rev., B 15 [6] 3193-9 (1977).

[9] S.T. Pantelides, B. Fischer, R.A. Pollak, and T.H. DiStefano, "The Electronic Structure of SiO_2, GeO_2 and Intermediate $Si_xGe_{1-x}O_2$ Compositions: Experiment and Theory", Solid State Commun., 21 [11] 1003-6 (1977).

[10] R.B. Laughlin, J.D. Joannopoulos, and D.J. Chadi, "Bulk Electronic Structure of SiO_2", Phys. Rev., B20 [12] 5228-37 (1979).

[11] W.Y. Ching, "Theory of Amorphous SiO_2 and SiO_x.I.", Phys. Rev., B26 [12] 6610-21 (1982); "II." ibid., 6622-32.

[12] W.Y. Ching, R.A. Murray, D.J. Lam, and B.W. Veal, "Comparative Studies of Electronic Structures of Sodium Metasilicate and α and β Phases of Sodium Disilicate", Phys. Rev., B28 [8] 4724-34 (1983).

[13] W.Y. Ching, Y.P. Li, B.W. Veal, and D.J. Lam, "Electronic Structures of Lithium Metasilicate and Lithium Disilicate", Phys. Rev., B32 [2] 1203-7 (1985).

[14] Y.P. Li and W.Y. Ching, "Band Structures of All Polycrystalline Forms of Silicon Dioxide", Phys. Rev., B31 [4] 2172-9 (1985).

[15] R. Bruckner, H.-U. Chun, and H. Goretzki, "Photoelectron Spectroscopy (ESCA) on Alkali Silicate and Soda Aluminosilicate Glasses", Glastechn. Ber. 51 [1] 1-7 (1978).

[16] B.W. Veal and D.J. Lam, "XPS Study of Sodium Oxide in Amorphous SiO_2"; pp. 299-303 in The Physics of SiO_2 and Its Interfaces. Edited by S.T. Pantelides. Pergamon, New York, 1978.

[17] D.E. Eastman and W.D. Grobman, "Photoemission Energy Distributions for Au from 10 to 40 eV Using Synchrotron Radiation", Phys. Rev. Lett., 28 [20] 1327-30 (1972).

[18] P.H. Citrin and D.R. Hamann, "Measurement and Calculation of Polarization and Potential-Energy Effects on Core-Electron Binding Energies in Solids: X-ray Photoemission of Rare Gases Implanted in Noble Metals", Phys. Rev., B10 [12] 4948-63 (1974).

[19] H.B. Michaelson, "The Work Function of the Elements and Its Periodicity", J. Appl. Phys., 48 [11] 4729-33 (1977).

[20] J. Holzl and F.K. Schulte, "Work Function of Metals"; pp. 1-150 in Springer Tracts in Modern Physics (Solid Surface Physics, Vol. 85). Edited by G. Hohler. Springer-Verlag, Berlin, 1979.

[21] S. Evans, "Work Function Measurements by X-PE Spectroscopy, and Their Relevance to the Calibration of X-PE Spectra", Chem. Phys. Lett., 23 [1] 134-8 (1973).

[22] P. Ascarelli and G. Missoni, "Secondary Electron Emission and the Detection of the Vacuum Level in ESCA", J. Electron Spectrosc. Relat. Phenom., 5 417-35 (1974).

[23] H. Ibach and J.E. Rowe, "Electron Orbital Energies of Oxygen Adsorbed on Silicon Surfaces and of Silicon Dioxide", Phys. Rev., B10 [2] 710-8 (1974).

[24] J.E. Rowe, "Photoemission and Electron Energy Loss Spectroscopy of GeO_2 and SiO_2," Appl. Phys. Lett., 25 [10] 576-8 (1974).

[25] R.S. Swingle II and W.M. Riggs, "ESCA", CRC Critical Reviews in Analytical Chemistry, 5 267-321 (1975).

[26] M.F. Ebel and H. Ebel, "About the Charging Effect in X-ray Photoelectron Spectrometry," J. Electron Spectrosc. Relat. Phenom., 3 [3] 169-80 (1974).

[27] J.F. McGlip and I.G. Main, "Electrical Characteristics of an X-ray Photoelectron Spectrometer", J. Electron Spectrosc. Relat. Phenom., 6 [5] 397-409 (1975).

[28] A. Jaegle, A. Kalt, G. Nanse, and J.C. Peruchetti, J. Electron Spectrosc. Relat. Phenom., 13 [3] 175-86 (1978).

[29] R.T. Lewis and M.A. Kelly, "Binding-Energy Reference in X-ray Photoelectron Spectroscopy of Insulators", J. Electron Spectrosc. Relat. Phenom., 20 [1-2] 105-15 (1980).

[30] Compare Fig. 3.6 vs. Fig. 3.8 in Chapter 3.

[31] Compare Fig. 6 in Ref. 8 vs. Fig. 1 in Ref. 24.

[32] See Fig. 2.8 in Chapter 2.

[33] P.H. Citran and T.D. Thomas, "X-ray Photoelectron Spectroscopy of Alkali Halides", J. Chem. Phys., 57 [10] 4446-61 (1972).

[34] D.A. Huchital and R.T. McKeon, "Use of an Electron Flood Gun to Reduce Surface Charging in X-ray Photoelectron Spectroscopy", Appl. Phys. Lett., 20 [4] 158-9 (1972).

[35] A.M. Goodman, "Photoemission of Electrons from Silicon and Gold into Silicon Dioxide", Phys. Rev., 144 [2] 588-93 (1966).

[36] M. Lenzlinger and E.H. Snow, "Fowler-Nordheim Tunneling into Thermally Grown SiO_2", J. Appl. Phys., 40 [1] 278-83 (1969).

[37] Z.A. Weinburg and A. Hartstein, "Photon Assisted Tunneling from Aluminum into Silicon Dioxide", Solid State Commun., 20 [3] 179-82 (1976).

[38] F.J. Grunthaner, B.F. Lewis, N. Zamini, and J. Maserjian, "XPS Studies of Structure-Induced Radiation Effects at the Si/SiO_2 Interface", IEEE Trans. Nucl. Sci., NS-27 [6] 1640-6 (1980).

[39] S. Evans, "Energy Calibration in Photoelectron Spectroscopy"; pp. 121-51 in Ref. 3.

[40] C.D. Wagner, "Energy Calibration of Electron Spectrometers"; pp. 137-47 in Applied Surface Analysis (ASTM STP 699). Edited by T.L. Barr and L.E. Davis. American Society for Testing and Materials, 1980.

[41] N.J. Binkowski, R.F. Heitzenrater, and D.A. Stephenson, "Surface Analysis of a Treated Soda-Lime Glass", J. Am. Ceram. Soc., 59 [3-4] 153-7 (1976).

[42] T.E. Madey, C.D. Wagner, and A. Joshi, "Surface Characterization of Catalysts Using Electron Spectroscopies", J. Electron Spectrosc. Relat. Phenom., 10 [4] 359-88 (1977).

[43] P. Swift, "Adventitious Carbon - The Panacea for Energy Referencing?", Surf. Interface Anal., 4 [2] 47-51 (1982).

[44] S. Kinoshita, T. Ohta, and H. Kuroda, "Comments on the Energy Calibration in X-ray Photoelectron Spectroscopy", Bull. Chem. Soc. Japan, 49 [4] 1149-50 (1976).

[45] S. Hohiki and K. Oki, "Problems of Adventitious Carbon as an Energy Reference", J. Electron Spectrosc. Relat. Phenom., 33 [4] 375-80 (1984).

[46] P.R. Anderson and R.D. Cichy, "Fracture Device for X-ray Photoelectron Spectrometer", J. Electron Spectrosc. Relat. Phenom. 2 [5] 485-8 (1973).

[47] C.R. Ginnard and W.M. Riggs, "Gold Evaporation for Charge Correction in X-ray Photoelectron Spectroscopy", Anal. Chem., 46 [9] 1306-8 (1974).

[48] Y. Uwamino, T. Ishizuka, and H. Yamatera, "Charge Correction by Gold Deposition onto Non-Conducting Samples in X-ray Photoelectron Spectroscopy", J. Electron Spectrosc. Relat. Phenom., 23 [1] 55-62 (1981).

[49] S. Kohiki and K. Oki, "An Appraisal of Evaporated Gold as an Energy Reference in X-ray Photoelectron Spectroscopy", J. Electron Spectrosc. Relat. Phenom., 36 [1] 105-10 (1985).

[50] D. Betteridge, J.C. Carver, and D.M. Hercules, "Devaluation of the Gold Standard in X-ray Photoelectron Spectroscopy", J. Electron Spectrosc. Relat. Phenom., 2 [4] 327-34 (1973).

[51] V.I. Nefedov, Y.V. Salyn, G. Leonhardt, and R. Scheibe, "A Comparison of Different Spectrometers and Charge Corrections Used in X-ray Photoelectron Spectroscopy", J. Electron Spectrosc. Relat. Phenom., 10[2] 121-4 (1977).

[52] D.A. Stephenson and N.J. Binkowski, "X-ray Photoelectron Spectroscopy of Silica in Theory and Experiment", J. Non-Cryst. Solids, 22 [2] 399-421 (1976).

[53] M.J. Edgell, D.R. Baer, and J.E. Castle, "A Test of Biased Referencing for the XPS Analysis of Nonconducting Materials", J. Vac. Sci. Technol., A4[3] 1562-3 (1986).

[54] I. Lindau and W.E. Spicer, "The Probing Depth in Photoemission and Auger Electron Spectroscopy", J. Electron Spectrosc. Relat. Phenom., 3 [5] 409-13 (1974).

[55] M.P. Seah and W.A. Dench, "Quantitative Electron Spectroscopy of Surfaces", Surf. Interface Anal., 1 [1] 2-11 (1979).

[56] C.D. Wagner, L.E. Davis, and W.M. Riggs, "The Energy Dependence of the Electron Mean Free Path", Surf. Interface Anal., 2 [2] 53-5 (1980).

[57] C.J. Powell, "The Energy Dependence of Electron Attenuation Lengths", Surf. Interface Anal., 7 [6] 256-62 (1985).

[58] The equivalence of the IMFP from theory and the "attenuation length" from experiment has recently been challenged (see Ref. 57).

[59] D. Briggs, "X-ray Photoelectron Spectroscopy as an Analytical Technique"; pp. 153-81 in Ref. 3.

[60] M. Klasson, A. Berndtsson, J. Hedman, R. Nilsson, R. Nyholm, and C. Nordling, "Electron Escape Depth in Silicon", J. Electron Spectrosc. Relat. Phenom., 3 [6] 427-34 (1974).

[61] R. Flitsch and S.I. Raider, "Electron Mean Escape Depths from X-ray Photoelectron Spectra of Thermally Oxidized Silicon Dioxide Films on Silicon", J. Vac. Sci. Technol., 12 [1] 305-8 (1975).

[62] J.C. Ashley and V.E. Anderson, "Interaction of Low-Energy Electrons with Silicon Dioxide", J. Electron Spectrosc. Relat. Phenom., 24 [2] 127-48 (1981).

[63] H. Ibach and J.E. Rowe, "Electronic Transitions of Oxygen Adsorbed on Clean Silicon (111) and (100) Surfaces", Phys. Rev., B9 [4] 1951-7 (1974).

[64] H.R. Philipp, "Optical Properties of Non-Crystalline Si, SiO, SiO_x, and SiO_2", J. Phys. Chem. Solids, 32 [8] 1935-45 (1971).

[65] A. Koma and R. Ludeke, "Core-Electron Excitation Spectra of Si, SiO, and SiO_2", Phys. Rev. Lett., 35 [2] 107-10 (1975).

[66] R.J. Colton and J.W. Rabalais, "Mechanical Grinding Device for an Electron Spectrometer", J. Electron Spectrosc. Relat. Phenom., 7 [4] 359-63 (1975).

[67] L. Holland, The Properties of Glass Surfaces; Chapter 3. Chapman and Hall, London, 1964.

[68] H.H. Dunken, "Glass Surfaces"; pp. 1-74 in Treatise on Materials Science and Technology (Vol. 22, Glass III). Edited by M. Tomozawa and R.H. Doremus. Academic Press, New York, 1982.

[69] S.R. Nagel, J. Tauc, and B.G. Bagley, "X-ray Photoemission Study of a Soda-Lime-Silica Glass", Solid State Commun., 20 [3] 245-9 (1976).

[70] S. Hofmann and J.H. Thomas III, "An XPS Study of the Influence of Ion Sputtering on Bonding in Thermally Grown Silicon Dioxide", J. Vac. Sci. Technol., B1 [1] 43-7 (1983).

[71] T. Sasaki, M. Kawaguchi, M. Yamane, and Y. Suginohara, "On the Quantitative Analysis of O°, O^-, and O^{2-} Ions in Binary Silicate by X-ray Photoelectron Spectroscopy", J. Japan Inst. Metals, 45 [8] 790-6 (1981).

[72] See Fig. 2.10 in Chapter 2.

[73] S. Kohiki, T. Ohmura, and K. Kusao, "A New Charge-Correction Method in X-ray Photoelectron Spectroscopy", J. Electron Spectrosc. Relat. Phenom., 28 [4] 229-37 (1983).

[74] See Fig. 2.7 in Chapter 2.

[75] B.R. Lawn and T.R. Wilshaw, Fracture of Brittle Solids; Chapters 1, 4, and 7. Cambridge University Press, Cambridge, 1975.

[76] J.T. Dickinson, E.E. Donaldson, and M.K. Park, "The Emission of Electrons and Positive Ions from Fracture of Materials", J. Mater. Sci., 16 [10] 2897-908 (1981).

[77] R. Weichert and K. Schonert, "On the Temperature Rise at the Tip of a Fast Running Crack", J. Mech. Phys. Solids, 22 127-33 (1974).

[78] R. Weichert and K. Schonert, "Heat Generation at the Tip of a Moving Crack", J. Mech. Phys. Solids, 26 [3] 151-61 (1978).

[79] P.G. Simpkins and J.T. Krause, "Dynamic Response of Glass Fibers During Tensile Fracture", Proc. R. Soc. Lond., A350 [1661] 253-65 (1976).

[80] G. Hochstrasser and J.F. Antonini, "Surface States of Pristine Silica Surfaces I.", Surf. Sci., 32 644-64 (1972); "II." ibid., 665-86.

[81] R.K. Iler, The Chemistry of Silica; Chapter 6. Wiley-Interscience, New York, 1979.

[82] V.M. Bermudez and V.H. Ritz, "Investigation of the SiO_2 Surface Via Electron-Energy-Loss Spectroscopy", Phys. Rev., B20 [8] 3446-55 (1979).

[83] C.G. Pantano, J.F. Kelso, and M.J. Suscavage, "Surface Studies of Multicomponent Silicate Glasses"; pp. 1-38 in Advances in Materials Characterization (Materials Science Research, Vol. 15). Edited by D.R. Rossington, R.A. Condrate, and R.L. Snyder. Plenum, New York, 1983.

[84] S.H. Garofalini, "A Molecular Dynamics Simulation of the Vitreous Silica Surface", J. Chem. Phys., 78 [4] 2069-72 (1983).

[85] S.H. Garofalini and S.M. Levine, "Differences in the Surface Behavior of Alkali Ions in $Li_2O \cdot 3SiO_2$ and $Na_2O \cdot 3SiO_2$ Glasses", J. Am. Ceram. Soc., 68 [7] 376-9 (1985).

[86] Surface sensitivity is increased when photoemission at large angles θ in Eq. (1.8) is sampled exclusively.

[87] Perkin-Elmer, Physical Electronics Division, Eden Prairie, MN.

[88] P.W. Palmberg, "A Combined ESCA and Auger Spectrometer", J. Vac. Sci. Technol., 12 [1] 379-84 (1975).

[89] M.P. Seah, "Quantitative Auger Electron Spectroscopy and Electron Ranges", Surf. Sci., 32 703-28 (1972).

[90] J.C. Shelton, "Orientation Dependence of Overlayer Attenuation of Electrons for the Cylindrical Mirror Analyser and a Retarding Field Analyzer", J. Electron Spectrosc. Relat. Phenom., 3 [6] 417-25 (1974).

[91] VG Gas Analysis, Ltd., Cheshire, England.

[92] M.F. Koenig and J.T. Grant, "Signal-to-Noise Measurements in X-ray Photoelectron Spectroscopy", Surf. Interface Anal., 7 [5] 217-22 (1985).

[93] A.F. Carley and R.W. Joyner, "The Application of Deconvolution Methods in Electron Spectroscopy - A Review", J. Electron Spectrosc. Relat. Phenom., 16 [1-2] 1-23 (1979).

[94] M.F. Koenig and J.T. Grant, "Monochrometer Versus Deconvolution for XPS Studies Using a Kratos ES300 System", J. Electron Spectrosc. Relat. Phenom., 36 [3] 213-25 (1985).

[95] R.J. Bird and P. Swift, "Energy Calibration in Electron Spectroscopy and the Re-Determination of Some Reference Electron Binding Energies", J. Electron Spectrosc. Relat. Phenom., 21 [3] 227-40 (1980).

[96] M.T. Anthony and M.P. Seah, "XPS: Energy Calibration of Electron Spectrometers 1-", Surf. Interface Anal., 6 [3] 95-106 (1984); "2-" ibid., 107-15.

[97] Heraeus-Amersil, Inc., Sayreville, NJ.

[98] Minas Gerais, Brazil.

[99] Corning Glass Works, Corning, NY.

[100] Cabot Corp., Boston, MA.

[101] A.M. Cowley and S.M. Sze, "Surface States and Barrier Height of Metal-Semiconductor Systems", J. Appl. Phys., 36 [10] 3212-20 (1965).

[102] S.M. Sze, Physics of Semiconductor Devices; Chapters 5 and 7. Wiley-Interscience, New York, 1981.

[103] J. Bardeen, "Surface States and Rectification at a Metal Semi-conductor Contact", Phys. Rev., 71 717-27 (1947).

[104] V. Heine, "Theory of Surface States", Phys. Rev., 138 [6A] 1689-96 (1965).

[105] J.C. Inkson, "Schottky Barriers and Plasmons", J. Vac. Sci. Technol., 11 [6] 943-6 (1974).

[106] W. Schottky, Z. Phys., 118 [9-10] 539-92 (1942).

[107] J.L. Freeouf, "Schottky Barriers: Models and Tests", Surf. Sci., 132 [1-3] 233-49 (1983).

[108] C.A. Mead, "Metal-Semiconductor Surface Barriers", Solid-St. Electron., 9 1023-33 (1966).

[109] S. Kurtin, T.C. McGill, and C.A. Mead, "Fundamental Transition in the Electronic Nature of Solids", Phys. Rev. Lett., 22 [26] 1433-6 (1969).

[110] L. Pauling, The Nature of the Chemical Bond; Chapter 3. Cornell University Press, Ithaca, New York, 1960.

[111] M. Schluter, "Chemical Trends in Metal-Semiconductor Barrier Heights", Phys. Rev., B17 [12] 5044-7 (1978).

[112] M.L. Cohen, "Schottky and Bardeen Limits for Schottky Barriers", J. Vac. Sci. Technol., 16 [5] 1135-6 (1979).

[113] W. Pong and D. Paudyal, "Measurements of Interface Parameter of Metal-Insulator Interfaces", Phys. Rev., B23 [6] 3085-6 (1981).

[114] R.H. Williams, "Surface Defects on Semiconductors", Surf. Sci., 132 [1-3] 122-42 (1983).

[115] L.J. Brillson, "Advances in Understanding Metal-Semiconductor Interfaces by Surface Science Techniques", J. Phys. Chem. Solids, 44 [8] 703-33 (1983).

[116] A.M.Goodman and J.J. O'Neill, Jr., "Photoemission of Electrons from Metals into Silicon Dioxide", J. Appl. Phys., 37 [9] 3580-3 (1966).

[117] B.E. Deal, E.H. Snow, and C.A. Mead, "Barrier Energies in Metal-Silicon Dioxide-Silicon Structures", J. Phys. Chem. Solids, 27 [11-12] 1873-9 (1966).

[118] R.J. Powell, "Interface Barrier Energy Determination from Voltage Dependence of Photoinjected Currents", J. Appl. Phys., 41 [6] 2424-32 (1970).

[119] C.G. Wang and T.H. DiStefano, "Polarization Layer at Metal/Insulator Interfaces", CRC Critical Reviews in Solid State Sciences, 5 327-35 (1975).

[120] I. Lundstrom and T. DiStefano, "Influence of Hydrogen on Pt-SiO_2-Si Structures", Solid State Commun., 19 [9] 871-5 (1976).

[121] I. Lundstrom and T. DiStefano, "Hydrogen Induced Interfacial Polarization at Pd-SiO_2 Interfaces", Surf. Sci., 59 [1] 23-32 (1976).

[122] D.J. DiMaria, "The Properties of Electron and Hole Traps in Thermal Silicon Dioxide Layers Grown on Silicon"; pp. 160-78 in The Physics of SiO_2 and Its Interfaces. Edited by S.T. Pantelides. Pergamon, New York, 1978.

[123] L.J. Brillson, "Transition in Schottky Barrier Formation with Chemical Reactivity", Phys. Rev. Lett., 40 [4] 260-3 (1978).

[124] J.M. Andrews and J.C. Phillips, "Chemical Bonding and Structure of Metal-Semiconductor Interfaces", Phys. Rev. Lett., 35 [1] 56-9 (1975).

[125] T.B. Reed, Free Energy of Formation of Binary Compounds. MIT Press, Cambridge, 1971.

[126] I. Barin, O. Knacke, and O. Kubaschewski, Thermochemical Properties of Inorganic Substances (Supplement). Springer-Verlag, Berlin, 1977.

[127] Y.E. Strausser and K.S. Majumder, "Chemical Structure of the Al-SiO_2 Interface", J. Vac. Sci. Technol., 15 [2] 238-9 (1978).

[128] R.S. Bauer, R.Z. Bachrach, and L.J. Brillson, "Au and Al Interface Reactions with SiO_2", Appl. Phys. Lett., 37 [11] 1006-8 (1981).

[129] T.W. Hickmont, "Dipole Layers at the Metal-SiO_2 Interface", J. Appl. Phys., 51 [8] 4269-81 (1980).

[130] V.K. Zworykin, G.A. Morton, E.G. Ramberg, J. Hillier, and A.W. Vance, Electron Optics and the Electron Microscope; Chapter 6. Wiley, New York, 1945.

[131] R. Gresch, W. Muller-Waruth, and H. Dutz, "X-ray Photoelectron Spectroscopy of Sodium Phosphate Glasses", J. Non-Cryst. Solids, 34 [1] 127-36 (1979).

[132] R. Bruckner, H.-U. Chun, H. Goretzki, and M. Sammet, "XPS Measurements and Structural Aspects of Silicate and Phosphate Glasses", J. Non-Cryst. Solids, 42 [1-3] 49-60 (1980).

[133] Estimate of NBO detection limit is established in Chapter 3.

[134] G.J. Young, "Interaction of Water Vapor with Silica Surfaces", J. Colloid Sci., 13 [1] 67-85 (1958).

[135] G.J. Young and T.P. Bursh, "Immersion Calorimetry Studies of the Interaction of Water with Silica Surfaces", J. Colloid Sci., 15 [4] 361-9 (1960).

[136] L. Levien, C.T. Prewitt, and D.J. Weidner, "Structure and Elastic Properties of Quartz at Pressure", Am. Mineral., 65 [9-10] 920-30 (1980).

[137] R.L. Mozzi and B.E. Warren, "The Structure of Vitreous Silica", J. Appl. Cryst., 2 [4] 164-72 (1969).

[138] G.G. Wicks, Structural Studies of Amorphous Materials (Sc.D. Thesis), MIT, Cambridge, 1975.

[139] D.R. Uhlmann and G.G. Wicks, "Structural Analysis Using Fluorescence Excitation", Wiss. Ztscher. Friedrich-Schiller-Univ. Jena, Math.-Nat. R., 28 [2-3] (1979) 231-42.

[140] J.B. Bates, "Dynamics of β-Quartz Structures of Vitreous SiO_2 and BeF_2", J. Chem. Phys., 56 [5] 1910-7 (1972).

[141] W.H. Baur, "Interactomic Distance Predictions for Computer Simulation of Crystal Structures"; pp. 31-52 in Structure and Bonding in Crystals (Vol. II). Edited by M. O'Keeffe and A. Navrotsky. Academic Press, New York, 1981.

[142] W.H. Baur and T. Ohta, "The Si_5O_{16} Pentamer in Zunyite Refined and Empirical Relations for Individual Silicon-Oxygen Bonds", Acta Cryst., B38 [2] 390-401 (1982).

[143] R.N. Nucho and A. Madhukar, "Electronic Structure of α-Quartz and the Influence of Some Local Disorder: A Tight Binding Study"; pp. 60-4 in The Physics of SiO_2 and Its Interfaces. Edited by S.T. Pantelides. Pergamon, New York, 1978.

[144] F.J. Grunthaner, P.J. Grunthaner, R.P. Vasquez, B.F. Lewis, J. Maserjian, and A. Madhukar, "High-Resolution X-ray Photoelectron Spectroscopy as a Probe of Local Atomic Structure", Phys. Rev. Lett., 43 [22] 1683-6 (1979).

[145] R.P. Gupta, "Electronic Structure of Crystalline and Amorphous Silicon Dioxide", Phys. Rev., B32 [12] 8278-92 (1985).

[146] W. Primak, "The Vitreous Silica Surface: Consequences of Grinding and Polishing", Phys. Chem. Glasses, 22 [2] 43-7 (1981).

[147] T.H. DiStefano and D.E. Eastman, "The Band Edge of Amorphous SiO_2 by Photoinjection and Photoconductivity Measurements", Solid State Commun., 9 [24] 2259-61 (1971).

CHAPTER 2

STRUCTURE OF ALKALI ALUMINOSILICATE GLASSES: XPS OF ALKALI SILICATE GLASSES

2.1. INTRODUCTION

Structure-property relationships for $R_2O-Al_2O_3-SiO_2$ (RAS) glasses, where R_2O is an alkali oxide, have been extensively investigated for many years. This ongoing scientific interest has been spurred by the substantial commercial, technological, and geologic importance of glasses in these ternary systems. These relatively simple compositions also form a basis for understanding how aluminum atoms are incorporated in silicate glasses of greater chemical complexity. Despite these efforts, fundamental structural characteristics of RAS glasses, the simpler binary R_2O-SiO_2(RS) glasses, and even pure SiO_2 glass remain controversial to this day. As a salient example, one notes that although the random network theory has gained ascendency over the crystallite theory for glass structure [1, 2], the latter concept has recently been resurrected and embellished by several independent workers [3-6].

Historically, X-ray and other scattering techniques [7,8] have played a major role in elucidating the structure of silicate glasses by providing atomic coordination numbers and bond-angle distributions. One limitation of such diffraction studies is that peaks in a radial or pair distribution function represent an average of correlations in interatomic distances. Structural details such as the significantly longer Si-O bond lengths for bridging oxygens (BO's) opposed to nonbridging oxygens (NBO's) in silicate crystal structures [9-22] have not been resolved in diffraction studies of RS glasses [23-31]. Similarly, radial distribution functions of RAS glasses in the series of $xNa_2O \cdot xAl_2O_3 \cdot (1-2x)SiO_2$ where x = 0, 0.125, 0.167, and 0.250 show only a progressive shift in all peaks to larger interatomic distances as $NaAlO_2$ replaces SiO_2 [32]. Individual contributions of Si-O and Al-O correlations to the first peak in the radial distribution functions for these glasses are not distinguishable.

Although diffraction studies have shown silicon atoms to be coordinated tetrahedrally by oxygen atoms in vitreous SiO_2 and RS glasses [23-31], a second limitation is that strong Si-O, O-O, and Si-Si correlations tend to mask the weaker R-O, R-Si, and R-R correlations in RS glasses containing lithium, sodium, or potassium atoms [1, 33-35]. Hence, it is difficult to evaluate the number of oxygen atoms coordinating these lighter alkali atoms, or to assess the possibility that clustering occurs among such atoms in RS glasses. These problems are exacerbated in more complex RAS glasses. It is thus worth keeping in mind that while a prospective structural model must be consistent with the radial or pair distribution function of a glass, this is a necessary but not sufficient condition by which to judge the correctness of a given model.

X-ray photoelectron spectroscopy (XPS) has attracted considerable attention from glass scientists in recent years [36-50] due to its potential as a probe of glass structure comparable to X-ray emission spectroscopy (XES), Raman spectroscopy, nuclear magnetic resonance (NMR), and extended X-ray absorption fine structure (EXAFS). These techniques supplement and in many important ways expand upon the local structural information obtained from diffraction experiments. It has been amply demonstrated in the above work that XPS is sensitive to differences in valence charge on the constituent atoms of silicate glasses resulting from dissimilar chemical environments. In principle, this sensitivity to a "chemical shift" among oxygen atoms allows BO's and NBO's to be energetically resolved and thus the fraction of NBO's, f_{NBO}, to be determined quantitatively as a function of glass composition by analysis of the O 1s core level. In practice, however, experimental problems inherent with the XPS technique can preclude a reliable analysis as reviewed at length in Section 1.2. Briefly, an effective sampling depth $\lesssim 10$ nm for silicates requires the near surface region analyzed in XPS to have a structural and chemical integrity closely approaching that of the bulk. Static and differential charging of insulating samples such as silicate glasses can often obscure underlying physicochemical relationships of interest. Unless these difficulties are overcome by appropriate methods of sample preparation and charging compensation, spurious features can be introduced or intrinsic features suppressed in photoelectron spectra, with unfortunate consequences for a "bulk" structural analysis.

Although measurements of f_{NBO} for RS glasses [36-38, 40, 42, 43, 45, 46] by XPS have agreed well with theory (especially for mole fractions of alkali oxide $X_R \lesssim 0.30$), previous determinations of f_{NBO} for Na_2O-Al_2O_3-SiO_2 (NAS) glasses [37,41,42,44,47,50] have been in conflict with the classical model for the structural role of aluminum atoms. In essence, this model maintains that aluminum atoms are tetrahedrally coordinated with oxygen atoms and are incorporated with the concomitant elimination of NBO's as Al/R increases from zero to unity such that $f_{NBO} \to 0$ at Al/R=1.0.

The motivation for the present XPS study of RAS glasses, as typified by NAS glasses, arises from several compelling reasons. First, none of the structural models proposed as alternatives to the classical model in earlier XPS work are thought to explain satisfactorily the changes in many physical properties that have widely been reported to occur at Al/R=1.0-1.2 for series of RAS glasses with $0 \lesssim \mathrm{Al/R} \lesssim 2.0$. This evidence and the findings of structural studies by other techniques (e.g., X-ray diffraction, XES, NMR, and EXAFS) are critically reviewed in Chapter 3. Second, a parallel study by optical luminescence spectroscopy [51,52] of thallium-doped NAS glasses with constant optical basicity ($\Lambda=0.57$) has firmly supported the traditional model for compositions with $\mathrm{Al/Na} \leq 1.0$. A similar series of undoped NAS glasses is one of several series examined in the present XPS work. Third, earlier XPS investigations have primarily addressed the structure of NAS glasses with $\mathrm{Al/Na} \leq 1.0$. A rigorous structural analysis of photoemission spectra has not been attempted for glasses with $\mathrm{Al/Na} > 1.0$. Finally, an adaptation to the analysis of vacuum-fractured surfaces of a biased metal-dot (BMD) method for the charging correction of insulators in XPS has been described in Chapter 1. The use of this procedure in the current study of NAS glasses is believed to provide significant advantages over the experimental approaches of previous work. Accurately calibrated photoemission spectra that are representative of the bulk structure and chemistry of NAS glasses have thus been obtained over a broad compositional range of $0 \leq \mathrm{Al/Na} \leq 1.5$ for the purpose of a comprehensive structural analysis presented in Chapter 3.

In order to lay some groundwork for the investigation of NAS glasses, the results of an XPS study of vitreous SiO_2 and RS glasses (especially Na_2O-SiO_2(NS) glasses) are considered in this Chapter. The photoemission spectra were acquired from vacuum-fractured surfaces using the BMD method for charging correction. Insights gained here into the relations between photoemission spectra and the structural and chemical characteristics of RS glasses figure importantly in the interpretation of spectra for the more complex NAS glasses in Chapter 3. Moreover, the structural implications of these results for vitreous SiO_2 and RS glasses call into question certain assumptions of current theories [5,6] that have challenged the random network model for glass structure.

This Chapter is organized in the following manner. The random network and crystallite theories for the structure of SiO_2 and RS glasses and the findings of earlier XPS work on these glasses are reviewed in Section 2.2. The preparation of samples and procedures for data acquisition and analysis in the present XPS investigation are described in Section 2.3. Examples of spectral artifacts which illustrate the consequences of inappropriate methods for surface preparation and the confounding effects of sample charging for RS glasses are first given in Section 2.4. Photoemission results for the O 1s and Si 2p core levels of vitreous SiO_2 and RS glasses (including $Na_2O \cdot 2SiO_2$, $Li_2O \cdot 2SiO_2$, and $K_2O \cdot 2SiO_2$) which nominally reflect bulk physicochemical properties are then presented. In Section 2.5, the compatibility of these results with the tenets of the above conflicting structural models for SiO_2 and RS glasses is explored. Also, a discrepancy between the value of f_{NBO} determined in photoemission experiments and the one expected from conventional theory for RS glasses with high R_2O content is addressed. Finally, the conclusions drawn from this investigation are summarized in Section 2.6.

2.2. LITERATURE SURVEY:

2.2.1. Structural Models for SiO_2 Glass

Although the use of Zachariasen's rules [53] as structural criteria for glass formation among simple oxides has been superseded by kinetic treatments of the subject [54,55], they nonetheless render a conceptual basis for the generally-accepted description of vitreous SiO_2 as being a continuous random network. These topological rules effectively constrain the internal energy of an oxide glass to a value approaching that of a corresponding crystalline phase. For an oxide A_mO_n, they can be stated as follows: (1) an oxygen atom is linked to not more than two A atoms; (2) the number of oxygen atoms surrounding A atoms must be small (i.e., three or four); (3) the oxygen polyhedra share corners with each other, not edges or faces, and (4) for extension of the glass network in three dimensions, at least three corners of each oxygen polyhedron must be shared. If the A-O-A bridging angle between polyhedra in the glass can assume a wide distribution of values relative to the crystalline phase, the resultant structure is a aperiodic but highly-connected network that is infinitely extended in three dimensions.

Structural studies of SiO_2 glass by X-ray diffraction have given strong backing to the continuous random network theory. Vitreous SiO_2 [23,26-28] and low-pressure polymorphs of crystalline SiO_2 (e.g., α-quartz [9], α-cristobalite [10] and α-tridymite [11]) are all comprised of nearly regular tetrahedra of oxygen atoms coordinating silicon atoms with similar Si-O bond lengths of 0.161-0.162 nm. The tetrahedra are fully connected at each corner through linkages of BO's (Si-O-Si) to neighboring tetrahedra in 4-2 coordination networks of silicon and oxygen atoms. Whereas the mean of the distribution of intertetrahedral angles in SiO_2 glass ($\sim$144°)

is comparable to the crystalline polymorphs (∿144°-150°), the range of this angular distribution is significantly broader in the vitreous structure (∿120°-180°) than in any of the crystalline structures. A second distinguishing feature of the glass is the rotational freedom in the conformation of any $SiO_{4/2}$ tetrahedron about the Si-O bond that connects it with another tetrahedron. These two kinds of structural randomness along with a variation in the size of n-membered rings of tetrahedra for the glass (n=4,5,6...) [56,57] vs. the crystals (n=6) yield an aperiodic and spatially open network. While this vitreous structure is 17 % less dense than α-quartz, it is only 3 % less dense than α-tridymite.

The crystallite hypothesis [58,59], on the other hand, offers a fundamentally different view of the atomic structure in vitreous SiO_2. This theory attributes the diffuse diffraction peaks observed for SiO_2 glass, relative to the sharp peaks obtained for cristobalite, to particle-size broadening. It thus pictures the glass as being an aggregate of discrete, randomly-oriented, crystalline particles. These so-called crystallites or microcrystalline regions are believed to have individual dimensions of 1-10 nm. Regular compressive or tensile structural distortions at center of each particle are further theorized to become more arbitrary near boundaries with other particles.

In the late 1930's, Warren [60,61] made a strong rebuttal to the crystallite hypothesis in favor of the random network theory by emphasizing the structural implications of several empirical results. First, the average size of a hypothetical cristobalite crystallite, as estimated from the breadth of the main diffraction peak for SiO_2 glass, is approximately 0.8 nm. Since this dimension is close to that of a unit cell for cristobalite, the extent of a "crystallite" is incompatible with the basic premise of crystallinity in a solid--i.e., a structural unit repeats itself upon translation at regular intervals in three dimensions. Second, the absence of significant small-angle X-ray scattering for SiO_2 glass, in contrast to a particulate SiO_2 gel, indicates that if crystallites are present, they must be bonded together by a boundary phase of similar electron density. For the crystallites to be continuously bonded to each other, a relatively thick noncrystalline boundary phase is required. Thus, if crystallites ∿0.8 nm in size are postulated, they must comprise only a small volume fraction of the glass.

Recent formulations of the crystallite model for vitreous SiO_2 [3-6] are still susceptible to the criticism leveled by Warren at the original theory almost fifty years ago. In addition, Wicks [27] has attempted to fit a pair distribution function for SiO_2 glass, derived from careful X-ray diffraction measurements, with crystallite models based on various polymorphs of crystalline SiO_2. The correspondence of pair correlations calculated for crystallite structures based on β-quartz, α-cristoballite, and β-tridymite to the empirical pair distribution function was found to be inferior in each case to that of pair correlations computed for a random network structure. The arguments of Warren and Wicks thus cast serious doubt on the latest contentions that "tridymite-like regions" [3,4], "clusters" of β-cristobalite [5], or "strained mixed clusters" of different crystalline polymorphs [6] represent essential structural features of SiO_2 glass. The results of Wicks also disagree with a suggestion that vitreous SiO_2 has a defective β-quartz morphology [62].

It should be recognized that both the random network and crystallite models for vitreous SiO_2 are structural idealizations and represent extremes of atomic arrangement in a material whose chemical simplicity belies often complex physical properties [63]. Although statistical fluctuations may produce occasional regions in the glass of higher structural order than their surroundings, the preponderance of the evidence reviewed here reasonably leads to a structural description approaching the limit of the random network theory.

The crystalline cluster models of Phillips [5] and Goodman [6] are of particular interest in the present study of silicate glasses by XPS. The chemical bond between silicon and oxygen atoms is estimated to have roughly equal components of covalent and ionic bond character [64,65]. As for the covalent contribution to this bond in typical silicates, a π-bond involving Si 3d and O 2p orbitals is currently thought to impart only a few percent of double-bond character to what is primarily a single σ-bond between Si sp^3 hybrid orbitals and O 2p orbitals [65]. Although the occurrence of full Si=O double bonds in the diverse structural chemistry of silicate minerals is apparently very rare, Phillips [5] has asserted superficial Si=O bonds (i.e., silicon atoms singly bonded to two BO's and doubly bonded to an NBO) are a ubiquitous feature on internal surfaces separating β-cristobalite clusters with radii of 3.3 nm in SiO_2 glass. For clusters of this size, it was estimated that the fraction of surface molecules, $(O_{1/2})_2\text{-Si=O}$, per cluster is $\sim$0.17 and hence $f_{NBO} \sim 0.08$ since each surface molecule contributes one NBO.

Recently, Galeener and Wright [66] have given a critical appraisal of the crystalline cluster model for SiO_2 glass of Phillips. They conclude that neutron diffraction and Raman spectroscopic results for vitreous SiO_2 are incompatible with the specific cluster morphology proposed by Phillips (or variants of it on a smaller scale) and with his premise that significant concentrations of Si=O bonds exist at boundaries between clusters.

Meanwhile, Goodman [6] has proposed that vitreous SiO_2 is comprised of clusters of various crystalline polymorphs with radii $\gtrsim 1.5$ nm. Regions near boundaries between clusters are said to be strained with some interfaces of a given cluster in tension and the remaining ones under compression. The reason why structure in SiO_2 glass is only detected with a spatial extent $\lesssim 1.0$ nm by diffraction studies is ascribed by Goodman to structural distortions in the outer portions of each cluster near interfaces with adjacent clusters. This is an old argument advanced in the original crystallite theory [59] but later discounted by Warren [61].

It has been determined in Chapter 1 that photoemission spectra of core levels for α-quartz and SiO_2 glass are virtually identical. The implications of these results for the crystalline cluster models of Phillips and Goodman are explored later in the present Chapter.

2.2.2. Structural Models for R_2O-SiO_2 Glasses

Initial additions of an alkali oxide R_2O to SiO_2 cause a precipitous decrease in the viscosity of a binary RS melt. At 1300°C, an RS melt containing only 15 mol % R_2O is some 8 orders of magnitude less viscous than SiO_2 [63,67,68]. According to the random network theory of Zachariasen [53] and Warren [24,25], the incorporation of R_2O reduces the connectivity of the aperiodic silicon-oxygen network and thus lowers the activation energy for viscous flow. Diffraction studies have shown the tetrahedral coordination of silicon atoms by oxygen atoms in SiO_2 glass is maintained in RS glasses [23-31]. In contrast to SiO_2 glass, however, some of these oxygens are theoretically bonded to just one silicon (NBO's), while the others are shared between two silicons (BO's). BO's in the

Si-O-Si linkages of siloxane bonds are replaced at random throughout the network with NBO's by the reaction

$$R_2O + (\equiv Si\text{-}O\text{-}Si\equiv) \rightarrow 2(\equiv Si\text{-}O^-R^+). \tag{2.1}$$

This simple mechanism specifies a one-to-one correspondence between alkali atoms and NBO's in RS glasses. If X_{Si} and X_R are the mole fractions of SiO_2 and R_2O, the theoretical fraction of NBO's in these glasses is thus

$$f_{NBO}(\text{theo}) = \frac{2X_R}{2X_{Si}+X_R} \tag{2.2}$$

for $X_R \leq 0.67$. A better understanding of the structure of RS glasses is desirable since compositions with $0.25 \lesssim X_R \lesssim 0.33$ are characterized by $0.3 \lesssim f_{NBO}(\text{theo}) \lesssim 0.4$ and, in this sense, are analogous to more complex multicomponent silicate glasses of commercial importance.

In the conception of the random network model, alkali ions occupy voids within the not-fully-connected framework of an RS glass. The number of oxygen atoms coordinating an alkali ion increases with the size of the ion; lithium, sodium, and potassium ions are estimated to be coordinated by 4, 4-6, and 5-12 oxygens, respectively, in diffraction work on RS glasses [24,25,27,29,31]. In order to achieve charge neutrality and hence minimize the internal energy of the glass relative to the corresponding crystalline phase(s), however, the coordination shell of any alkali ion presumably contains as many NBO's as allowed by topological and configurational constraints. The basis for this statement merits further comment because it carries important implications for the atomic arrangement of RS glasses beyond those addressed by the random network theory.

From determinations of RS crystal structures [12-22] it is known that individual Si-BO bond lengths are ∿0.007 nm longer than individual Si-NBO bond lengths in any given structure as shown in Fig. 2.1. As a result, silicon-oxygen tetrahedra in RS crystals are generally more distorted than the nearly regular tetrahedra in SiO_2 polymorphs [9-11]--i.e., individual O-Si-O intra-tetrahedral angles range from ∿102° to ∿118° in RS crystals vs. ∿108° to ∿111° in SiO_2 polymorphs. Furthermore, both sets of <u>individual</u> bond lengths in Fig. 2.1 (solid lines) are found to increase markedly with the average number of NBO's bonded to a silicon atom

$$n(\mathrm{theo}) = < \frac{\mathrm{NBO}}{\mathrm{Si}} > = \frac{2X_R}{X_{Si}} , \qquad (2.3)$$

whereas the <u>average</u> Si-O bond lengths (dashed line) for these structures increase much more slowly with n(theo).

The ordering of Si-BO and Si-NBO bond lengths and their variation with n(theo) in Fig. 2.1 can be understood by Baur's extension [69-71] of the well-known electrostatic valence rule of Pauling [72,73] for bonding in complex ionic crystals. In the ionic limit of chemical bonding in silicate compounds, the bond strength, s, directed from a cation to each oxygen anion in its coordination polyhedron is given by

$$s = \frac{z}{C} , \qquad (2.4)$$

where z is the formal valence of the cation and C is its coordination number. For a stable crystal structure, Pauling's rule requires the sum of the bond strengths

$$p = \sum_i s_i = \sum_i \frac{z_i}{C_i} \qquad (2.5)$$

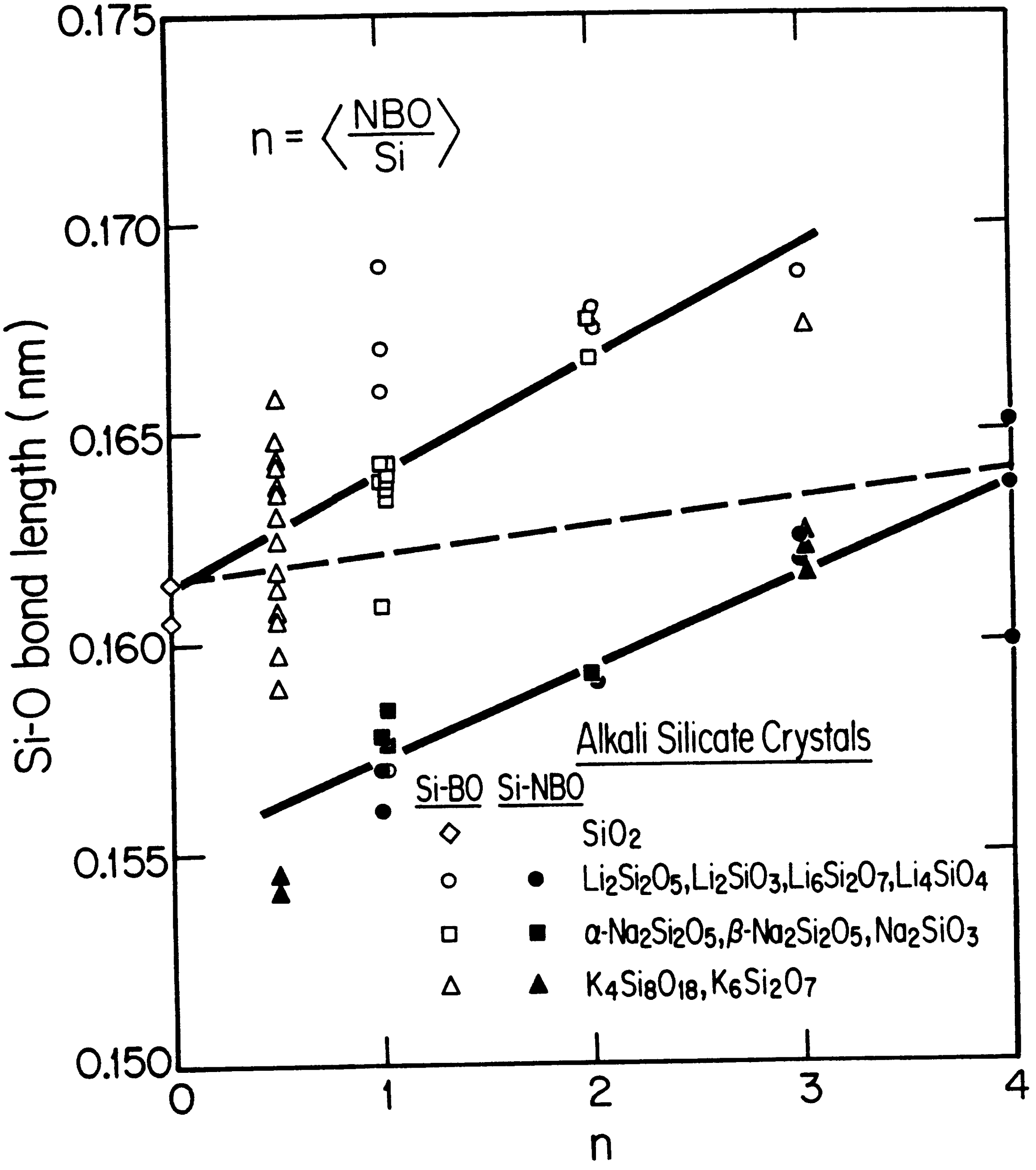

Fig 2.1: Individual Si-O bond lengths (solid lines) and average Si-O bond lengths (dashed line) for SiO_2 and RS crystals. Data obtained from Refs. 9, 12-22.

received by each oxygen anion from the i cations it coordinates be exactly or at least nearly equal to the formal valence of the anion with opposite sign (i.e., +2 for oxygen anions). In many crystal structures, however, Baur has pointed out that p for any individual anion can deviate from this value by ± 40%. The above criterion for electrostatic stability of a crystal structure is thus too stringent. Instead, only the average value of p for all anions in a basic repeating unit of structure is required to equal the formal valence of the anion with changed sign.

Of particular interest here, the deviation of p from a normalized mean value for an $SiO_{4/2}$ tetrahedron is statistically the largest contributor to the variance in individual Si-O bond lengths for silicates [70,71]; it is followed by much weaker dependences on the oxygen coordination number and Si-O-Si bridging angle. For each RS crystal structure in Fig. 2.1, $p \lesssim 2$ for NBO's in Si-NBO bonds while $p \gtrsim 2$ for BO's in Si-BO bonds. The observation that Si-BO bonds are generally longer than Si-NBO bonds within a given structure follows directly from a strong positive correlation between individual Si-O bond lengths and the sum of the bond strengths received by the oxygen anion in these bonds [69]. An effective charge balance is achieved locally for "underbonded" NBO's and "overbonded" BO's by the shortening of the Si-NBO distances and the lengthening of the Si-BO distances relative to the mean Si-O distance of ∿0.162 nm for silicates [74,75].

In order to fix these ideas, consider the schematic depictions of the bonding relationships for α-$Na_2Si_2O_5$ [18] and Na_2SiO_3 [20] shown in Fig. 2.2. Silicon atoms are tetrahedrally coordinated with oxygen atoms with n(theo)=1 in the layered silicate, α-$Na_2Si_2O_5$, and n(theo)=2 in the chain silicate,

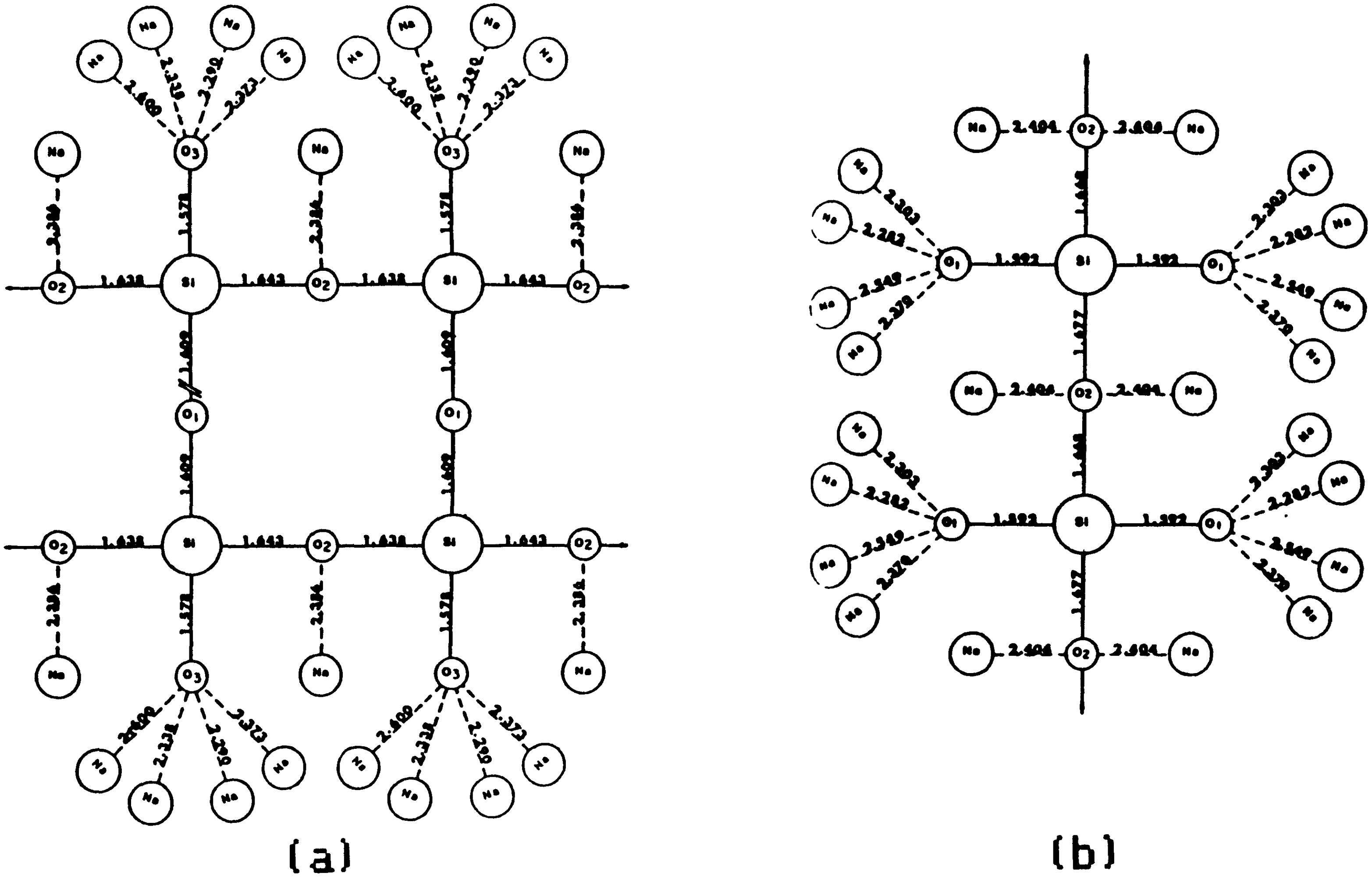

(a)

(b)

Fig. 2.2: Schematic drawings of bonding relationships in NS crystals: (a) α-$Na_2Si_2O_5$: O_1 and O_2 are BO's, O_3 is an NBO; and (b) Na_2SiO_3: O_1 is an NBO, O_2 is a BO. Figures taken from Ref. 48.

Na_2SiO_3. Sodium atoms in both crystals are coordinated by 5 oxygens, 4NBO's + 1BO, in distorted trigonal bypyramids. From Eqs. (2.4) and (2.5), this atomic arrangement yields p=1.8 for NBO's in both structures since each NBO coordinates 1 silicon and 4 sodiums atoms. In α-$Na_2Si_2O_5$, 2/3 of the BO's are shared between 2 silicons and 1 sodium, and 1/3 are bonded to only 2 silicons with p=2.2 and 2.0, respectively. For Na_2SiO_3, all BO's coordinate 2 silicons and 2 sodiums with p=2.4. The average p for all oxygen anions in a repeating unit of α-$Na_2Si_2O_5$ (2(1.8) + 2.0 + 2(2.2)/5) or Na_2SiO_3 (2(1.8) + 2.4/3) thus equals 2.0 in accord with the extended electrostatic valence rule.

Although it is only apparent for BO's in the examples given in Fig. 2.2, the sum of the bond strengths on both BO's and NBO's in RS crystal structures tends to increase with n(theo). This trend is explained for BO's by the progressively greater portion of BO's within a bonding distance of one or more alkali ions, and for NBO's by the growing ratio of NBO's to BO's in the coordination shell of an alkali ion. Therefore, individual Si-BO and Si-NBO bond lengths each increase with n(theo) in Fig. 2.1, consistent with the empirical correlation between Si-O bond lengths and p on the oxygen anion [69].

As compared to a crystalline silicate network, a much larger number of configurations is available to a vitreous silicate network. This is mainly due to the broader range of Si-O-Si intertetrahedral angles, the rotational freedom of $SiO_{4/2}$ tetrahedra about Si-O-Si linkages, and the variation in size of rings of such tetrahedra in the vitreous network. However, if the internal energy of an RS glass is to be close to that of its crystalline counterpart(s), then it is reasonable to suppose that <u>very local</u> structural distortions in the glass (i.e., the range of Si-O bond lengths and intratetrahedral angles) cannot be substantially greater than those in the crystal. The range of p on oxygen anions in the glass should thus approximate that of the crystal. For this reason, the coordination of alkali ions by NBO's is energetically favored over BO's in the glass structure. This preference imparts electrostatic stability and is subject only to topological and configurational constraints--the latter to ensure the entropy of the glass is greater than that of the crystal.

While the random network model provides a conceptually useful description of single-phase RS glasses, the above discussion suggests the coordination of alkali by oxygen atoms in these glasses is not entirely arbitrary and even bears some chemical resemblance to RS crystal structures. Support for this view is drawn from diffraction studies of RS glasses. As noted in Section 2.1, Si-BO and Si-NBO correlations are unresolved in such work. However, the average Si-O distance has been observed to increase slowly with X_R in various RS glasses [27,30]--e.g., Misawa [30] reported the Si-O distance of 0.1613 nm in SiO_2 glass increases to 0.1624 nm in $Li_2O \cdot 2SiO_2$ glass and 0.1631 nm in $Na_2O \cdot 2SiO_2$ glass. This trend is analogous to that described in Fig. 2.1 for the average Si-O bond length in RS crystal structures. Oxygen polyhedra about alkali atoms in a glass containing isolated NBO's (Si-O-R) or paired NBO's 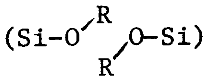 $(\text{Si-O}\overset{R}{\underset{R}{\diamond}}\text{O-Si})$ with BO's (Si-O-Si) supplying the balance of coordinating oxygen atoms can yield considerably "underbonded" NBO's ($p \lesssim 1.5$) and "overbonded" BO's ($p \gtrsim 2.5$) by the extended electrostatic valence rule. Such extremes in the sums of the bond strengths would lead to a disparity in Si-BO and Si-NBO bond lengths $\gtrsim 0.010$ nm [69-71].

Since recent diffraction work on $Na_2O \cdot P_2O_5$ glass [76] has shown P-BO and P-NBO correlations can be resolved with a separation of 0.014 nm, the lack of such empirical discrimination between Si-BO and Si-NBO correlations in RS glasses [77] implies their separation more closely approaches that of RS crystals (i.e., 0.007 nm in Fig. 2.1). It thus seems reasonable to infer atomic coordination schemes in RS glasses and crystals are similar to the extent that individual Si-O distances in a silicate network are determined by short-range considerations of charge neutrality and are independent of the long-range structure of the network. However, this correspondence is likely to be affected by the amount of entropy a vitreous network can gain for a given increase in internal energy. Interestingly, the variation in Si-O bond lengths from 0.161-0.162 nm in crystalline and vitreous SiO_2 is negligible beyond those expected from thermal vibrations [27,28,78].

Studies of $Na_2O\cdot 2SiO_2$ glass by Na EXAFS [35,79] have indicated that the sodium atoms are coordinated by 5 or 6 oxygen atoms in good agreement with diffraction results [24,29,31]. While the oxygen coordination about sodiums in the glass is similar to that of crystalline α-$Na_2Si_2O_5$ (5) [18] and β-$Na_2Si_2O_5$ (5,6) [19], neither technique can specify the ratio of NBO's to BO's in this oxygen polyhedron. Greaves et al. [35] argue, however, that clustering of NBO's around sodiums requires the clustering of sodiums about NBO's, as seen in NS crystal structures [17-20] and suggested in molecular dynamics (MD) simulations of NS glasses [33,34]. Consistent with this view, pair distribution functions derived from high-quality diffraction data for a Tl_2O-SiO_2 glass [80] (where Tl_2O is chemically analogous to R_2O) and a series of K_2O-SiO_2 (KS) glasses [27] have been interpreted in terms of clustering of the monovalent cations. Although Wicks [27] specifically modeled K-K pairing in KS glasses, his analysis does not rule out more extensive clustering of potassium ions.

For RS glasses with high R_2O content in the range of $0.30 \lesssim X_R \lesssim 0.60$ one reasonably concludes that NBO's are perhaps best represented by Si-O-$\sum_j R_j$ groupings where j alkali ions are clustered within a bonding distance of this oxygen anion. Isolated and paired NBO's probably do not exist in significant numbers over this compositional range. For RS glasses with $X_R<0.30$, however, isolated and paired NBO's might well become more important structural entities and give rise to a greater range of Si-O bond lengths. Metastable liquid-liquid immiscibility [81] leading to broad compositional regions of phase separation in Li_2O-SiO_2(LS) glasses for $0<X_{Li}<0.30$ and in Na_2O-SiO_2 (NS) glasses for $0<X_{Na}<0.20$ [82,83], conceivably results from excessively high distortions of Si-O bond lengths in single-phase topologies for these compositions. Other atomistic rationalizations of phase separation in glass systems, also employing concepts from crystal chemistry, can be found elsewhere [84,85].

In RS crystal structures with basic structural units of SiO_2 (three-dimensional network), $Si_2O_5^{-2}$ (disilicate sheets), SiO_3^{-2} (metasilicate chains or rings), $Si_2O_7^{-6}$ (pyrosilicate dimers), and SiO_4^{-4} (isolated orthosilicate tetrahedra), the number of NBO's bonded to each silica atom has uniform values of NBO/Si=0,1,2,3, and 4, respectively. If the structure of RS glasses were a completely random network, then statistical fluctuations in NBO/Si from silicon to silicon in the network about the mean value, given by n(theo) in Eq. (2.3), would be expected in vitreous analogues to the disilicate, metasilicate, and pyrosilicate crystalline compounds. Structural investigations of RS glasses by Raman spectroscopy [86,87] have suggested that such a distribution in NBO/Si occurs in disilicate and metasilicate glasses. More generally, for RS glasses with any given X_R, the width of this distribution increases with the type of alkali as K<Na<Li [86,88].

Although some interpretations of ^{29}Si NMR spectra for RS glasses favor this viewpoint [89,90], other ^{29}Si NMR studies of LS, NS, and KS glasses do not support the existence of multiple chemical states for silicon atoms in disilicate or metasilicate compositions [91-94]. As seen in the ^{29}Si magic angle spinning (MAS) NMR specrea for SiO_2 and NS glasses by Dupree et al. [92], reproduced in Fig. 2.3, silicons have single chemical states in SiO_2, $Na_2O \cdot 2SiO_2$, and $Na_2O \cdot SiO_2$, corresponding to NBO/Si=0, 1, and 2, respectively. The spectra for intermediate compositions are comprised of systematically varying contributions of silicons in two chemical states where NBO/Si=0 and 1 for $0<X_{Na}<0.33$, and NBO/Si=1 and 2 for $0.33<X_{Na}<0.50$.

While Raman spectra of RS glasses contain a potential wealth of structural information [95], the analysis of such results is rather qualitative in comparison to NMR spectra because of apparent nonlinearities or overlaps in the intensities and positions of the high frequency (800-1250 cm^{-1}) vibrational modes. These ambiguities have led to widely diverging structural interpretations for RS glasses, with one favoring the random network model [86] and another supporting a crystalline cluster model [5] which is described below.

In terms of how NBO's are distributed among silicon atoms, the NMR results in Fig. 2.3 are consistent with the notion that local atomic arrangements in RS glasses are not entirely random. However, a subtler variation in the chemical environment of each silicon site in $Na_2O \cdot 2SiO_2$ and $Na_2O \cdot SiO_2$ glasses vis-à-vis α-$Na_2Si_2O_5$ and Na_2SiO_3 crystals is indicated by the much broader width for the ^{29}Si resonance in the glasses [92,93]. The broadening of this resonance in the glasses is mainly

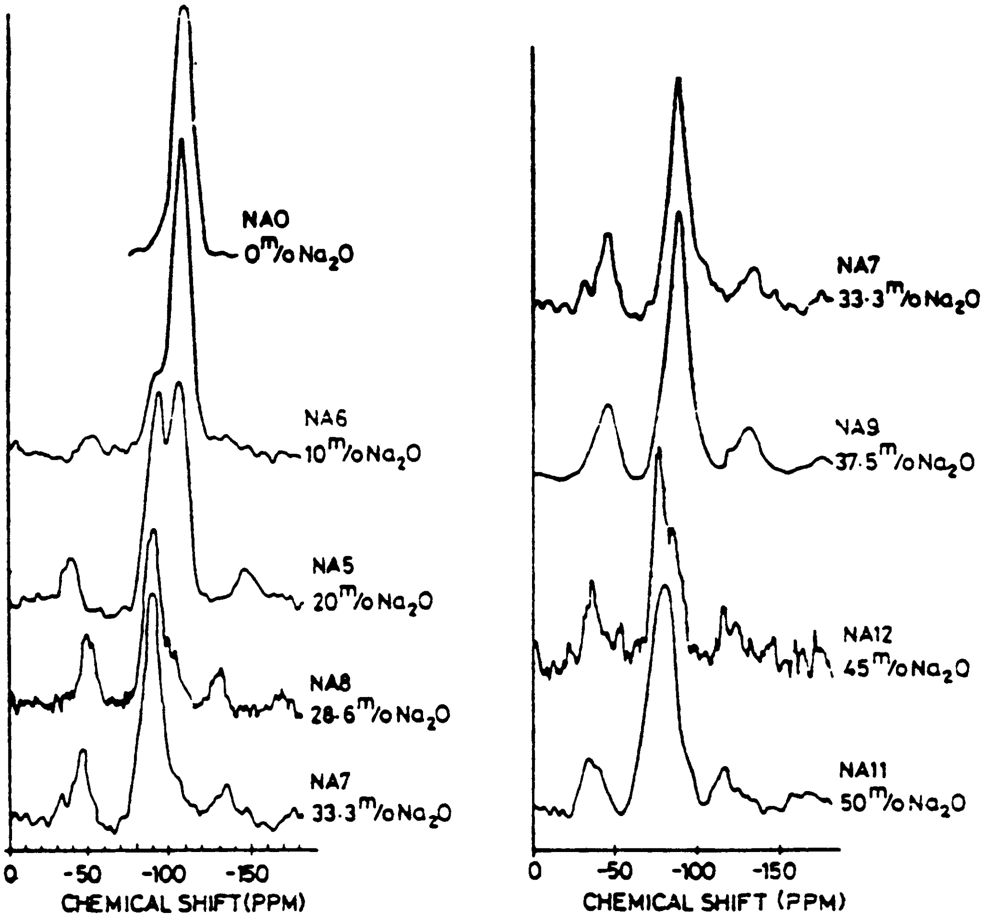

Fig. 2.3: ^{29}Si MAS NMR spectra for SiO_2 and NS glasses. Minor peaks to the left and right of the main resonances for NS glasses are spinning side bands. Figure taken from Ref. 92.

attributed to a larger distribution of Si-O-Si intertetrahedral angles [92,93,96,97]. Similar arguments, along with other kinds of structural disorder, have been used to explain the broadening of high frequency Raman lines in disilicate and metasilicate glasses relative to the corresponding crystals [86].

Whereas some similarities apparently exist between the short-range structures of RS glasses and crystals, the greater variation of the Si-O-Si intertetrahedral angle in an RS glass [27,33,34,86,92,93] results in a silicon-oxygen network without long-range periodicity. This essential characteristic of the glass is in accord with the central idea of the random network theory (see Section 2.2.1). However, constraints on the local atomic arrangements in RS glasses conceivably affect the topology of the aperiodic silicon-oxygen network on a larger scale of structure. Considering the well-defined average coordination for sodium ions in $Na_2O \cdot 2SiO_2$ glass indicated by EXAFS, Greaves et al. [35] envision a modified random network where a covalent silicon-oxygen component is intercalated by an ionic sodium-oxygen component. In agreement with the NMR results in Fig. 2.3, Yasui et al. [31] modelled $Na_2O \cdot 2SiO_2$ and $R_2O \cdot SiO_2$ glasses as convoluted sheet and unbranched chain structures, respectively. They reported a good correspondence between radial distribution functions based on such models and ones derived from diffraction measurements on the glasses. Although such propositions are interesting, they should be regarded as speculative due to a lack of uniqueness in the structural interpretation of either the EXAFS or diffraction results.

In fundamental conflict with the random network theory, the crystallite hypothesis for the structure of multicomponent glasses contends that an RS glass is an aggregate of discrete, randomly-oriented, crystalline particles of 1-10 nm is size [58,59]. According to this theory, these particles have the morphologies of the stoichiometric compounds more or less adjacent to the RS glass composition in a binary equilibrium phase diagram. Warren's criticism of the crystallite model for vitreous SiO_2 [60,61] (see Section 2.2.1) applies equally well to crystallite descriptions of multicomponent glasses. In addition, the breadth of the main diffraction peak for RS glasses approximates that of SiO_2 glass [24,25] and thus suggests the unit cells for the crystallites, if they exist, do not vary significantly in size with glass composition. Since the dimensions of unit cells among SiO_2 polymorphs and RS crystal structures can vary by a factor of 2-3 [9-22], this observation is incompatible with the crystallite model.

The crystalline cluster models for RS glasses currently advocated by Phillips [5] and Goodman [6] amount to little more than an embellishment of the ideas in the original crystallite hypothesis [58,59]. A mixture of clusters with a $Na_2Si_2O_5$ morphology becoming dominant over some progressively less distinct SiO_2 morphology is predicted in a series of NS glasses as X_{Na} increases from 0 to 0.33. Similarly, the portion of clusters with a Na_2SiO_3 morphology grows at the expense of clusters with a $Na_2Si_2O_5$ morphology as X_{Na} increases from 0.33 to 0.50.

Goodman has claimed that previous XPS studies of RS glasses are consistent with his crystalline cluster model. This assertion will be examined below in light of the present photoemission results for these glasses. At this point, however, it is instructive to review the findings of earlier XPS work on vitreous SiO_2 and RS glasses.

2.2.3. Photoemission Studies of SiO_2 and R_2O-SiO_2 Glasses

In Chapter 1, it was described how bulk physicochemical information about silicates can be reliably acquired by XPS through the analysis of vacuum-fractured surfaces and the correction of electrostatic charging effects for such dielectric samples by the BMD method. Previous photoemission studies of SiO_2 and RS glasses [36-40,42,43,45,46,48,49], although not as thorough in these experimental details as the present work, have nevertheless demonstrated the potential for evaluating f_{NBO} and elucidating other important aspects of the structural chemistry of silicate glasses. The quantitative determination of f_{NBO} for vitreous SiO_2 and RS glasses by XPS is an especially useful result because it permits a direct test of a recent crystalline cluster model for SiO_2 glass [5] and the correspondence between alkali atoms and NBO's in RS glasses assumed by Eqs. (2.1) and (2.2).

The distribution of electron density in several orthopyroxene compounds, as determined from diffraction measurements [98], indicates a larger net atomic charge resides on NBO's than on BO's in these silicate chain structures. Larger effective Mulliken atomic charges on NBO's than on BO's have also been theoretically calculated for LS and NS crystal structures [48,49]. In XPS, the disparity of valence charges on structurally distinct oxygen anions in RS crystals and glasses is manifest by the splitting of the O 1s core level into BO(Si-O-Si) and NBO($Si-O-\sum_j R_j$) components. Because a higher valence charge enables the oxygen nucleus to be screened more effectively, the ionization potential for an O 1s electron of an NBO is less than that of a BO. Therefore, NBO's have smaller binding energies than BO's in the O 1s spectral envelope, as seen in the composite spectra for SiO_2 and NS glasses of Bruckner et al. [37] which are reproduced in Fig. 2.4. Also to be noticed in these spectra, the intensity of the NBO component increases with X_{Na} relative to that of the BO component. A curve fitting analysis of O 1s spectra for such a series of RS glasses thus allows f_{NBO} to be measured as a function of glass composition.

In earlier XPS investigations of RS glasses, the fraction of NBO's from experiment, $f_{NBO}(XPS)$, has been determined by fitting the O 1s spectrum to a pair of Gaussian peaks with equal or nearly equal widths. Hence,

$$f_{NBO}(XPS) = \frac{A(NBO)}{A(BO)+A(NBO)} \quad , \qquad (2.6)$$

where A(BO) and A(NBO) are the integrated intensities of the BO and NBO component peaks. Measurements of $f_{NBO}(XPS)$ for O 1s spectra acquired from vacuum-fractured [36,37,42,43], vacuum-milled [38,46], nitrogen-fractured [40], and ion-sputtered [45] surfaces of RS glasses have been in good agreement with f_{NBO}(theo) in Eq. (2.2) for $X_R \lesssim 0.30$. However, increasingly worse agreement, with $f_{NBO}(XPS) < f_{NBO}(theo)$, has often been observed for $X_R > 0.30$ (e.g., $f_{NBO}(XPS) \sim 0.42$ vs. $f_{NBO}(theo) = 0.50$ for NS glasses with $X_{Na} = 0.40$ [38,40,42,46]).

This negative departure from theory has been attributed to the following causes. Since RS glasses with $X_R > 0.30$ are extremely hygroscopic, the exchange of protons for alkali ions near some NBO's could result in such NBO's having a chemical identity closer to BO's than to unperturbed NBO's in the O 1s spectral envelope. On the other hand, the mechanism for the incorporation of R_2O at $X_R > 0.30$ might be less efficient than the one implied by Eq. (2.1). Lastly, a disproportionate variation in the integrated intensities of the BO and NBO peaks with X_R could complicate the structural

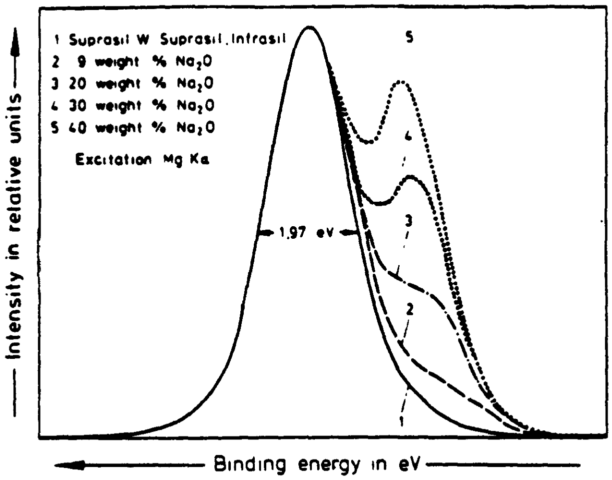

Fig. 2.4: Composite spectra of O 1s core level for vacuum-fractured SiO_2 and NS glasses. Figure reproduced from Ref. 37.

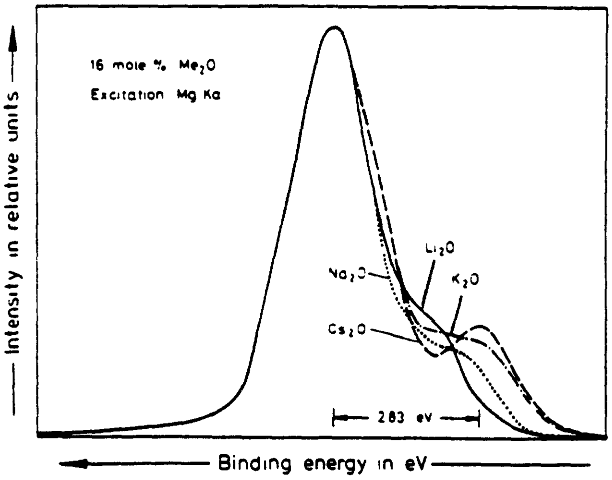

Fig. 2.5: Composite spectra of O 1s core level for vacuum-fractured RS glasses with X_R=0.16. Figure taken from Ref. 37.

interpretation of the O 1s spectra. Some insight into this problem has been gained in the present study of RS glasses and will be discussed later in the present Chapter.

While the measurements of f_{NBO}(XPS) for RS glasses from vacuum-milled, nitrogen-fractured, and ion-sputtered surfaces are comparable to those from vacuum-fractured surfaces, spectral artifacts caused by structural or chemical modifications of the surface relative to the bulk are less likely in data obtained from vacuum-fractured surfaces. Interpretation of spectra acquired from ion-sputtered surfaces of silicate glasses is particularly hazardous. As pointed out in Section 1.2.2, spectroscopic evidence purporting to establish the existence of a third chemical state for oxygen atoms (i.e., O^{2-}) in LS glasses with $X_{Li} \gtrsim 0.30$ [45] is more likely indicative of an artifact induced by ion-sputtering [99]. Another artifact, caused by hydration of an air-fractured NS glass, is demonstrated in this Chapter.

Extrapolation of XPS results [42,100] for R_2O-P_2O_5 glasses to X_R=0 suggests the O 1s core level of P_2O_5 glass can be chemically resolved into BO(P-O-P) and NBO(P=O) components with f_{NBO}=0.40 as expected theoretically. If Si=O bonds exist in vitreous SiO_2 in the abundance suggested by Phillips [5] for his crystalline cluster model (i.e., $f_{NBO} \sim 0.08$), then the O 1s level for this glass should be chemically split into BO(Si-O-Si) and NBO(Si=O) components by analogy to P_2O_5 glass. In accord with a conclusion of Chapter 1, previous XPS studies have reported no evidence for an NBO peak in the O 1s spectrum from vacuum-fractured SiO_2 glass [37,43] (e.g, see Fig. 2.4).

Systematic variations in the binding energies and widths of the O 1s and Si 2p photopeaks with composition can supply additional information about the structural chemistry of RS glasses--e.g., the energetic separation between the BO and NBO components in O 1s spectra of RS glasses has been found to decrease with X_R [38,42,43,46] and to increase at constant X_R by alkali type in order of Li<Na<K<Cs [37,42,43], as seen in Figs. 2.4 and 2.5. Such binding energy shifts reflect the interaction of alkali ions with BO's and NBO's as modulated by the ionicity of the R-O bond. However, static and differential charging of RS glasses in prior XPS work have tended to obscure the absolute nature of these shifts in binding energy and also to broaden the widths of photopeaks spuriously. In each set of composite O 1s spectra in Figs. 2.4 and 2.5, the binding energy scale has been normalized to the position of the BO peak. For the series of NS glasses in Fig. 2.4, it thus appears that the binding energy of the NBO peak increases relative to the BO peak with X_{Na}. Conversely, other equally arbitrary ways of normalizing the binding energy scale for these spectra (i.e., with respect to the Na 2s peak [38], a sodium Auger peak [38,43], or the valence band maximum [46]) indicate that the binding energy of the BO peak decreases relative to the NBO peak with X_{Na}. A conspicuous example of differential charging involving O 1s spectra of RS glasses is described later in this Chapter. Such experimental difficulties have been overcome in the present work by use of the BMD method for correction of insulator charging. This approach has afforded a clarification of the structural and chemical significance of photoemission results for RS glasses.

Finally, the O 1s and Si 2p core level spectra for α-quartz closely resemble those for SiO_2 glass, as shown in Chapter 1 [101]. Earlier XPS investigations have indicated the O 1s and valence band spectra for analogous RS crystals and glasses are also remarkably similar [36,38,48,49].

The correspondence of f_{NBO}(XPS) and the empirical density of states between these structures thus supports the idea that parallels exist between local atomic arrangements in RS crystals and glasses, as reviewed in the preceeding subsection.

2.3. EXPERIMENTAL PROCEDURES:

2.3.1. Sample Preparation

Several rods of T08 fused quartz [102] (4 mm in diameter x 20 mm) were cut from stock that was obtained commercially. The RS glasses selected for this study were outside the compositional regions of phase separation [82,83]. The glass compositions listed in Table 2.1 were prepared at the direction of Dr. P.I.K. Onorato at GTE Laboratories, Inc. in Waltham, MA. Samples were batched using 99.999% pure Li_2CO_3, Na_2CO_3, K_2CO_3, and SiO_2; heated in a platinum crucible with a lid at 1400°C for $\sim$5 hrs; and then cooled to room temperature. Several bars (4x4x20 mm) were cut under kerosene from each glass sample and stored in a dry box due to the hygroscopic nature of these compositions. Assays for some RS glasses by ICP spectroscopy or X-ray fluorescence (normalized to $X_R+X_{Si} = 1.0$) are given in Table 2.1.

2.3.2. Photoemission Measurements

The XPS data were obtained using a PHI Model 548 spectrometer [103], equipped with a non-monochromatized Mg Kα X-ray source ($h\nu = 1253.6$ eV) and a double-pass cylindrical mirror analyzer. Photoemission spectra from vacuum-fractured surfaces of SiO_2 and RS glasses were measured using experimental methods and conditions similar to those described at length in Sections 1.3.1, 1.3.2, and 1.3.4. All spectra were acquired at an apparent surface potential $Q \simeq -10$ V and corrected to Au $4f_{7/2}=84.00$ eV by the BMD method. Binding energies, BE_F, are thus referred to the surface Fermi level of the sample. Following a survey spectrum, a high resolution spectrum of the O 1s core level was obtained prior to the concurrent acquisition of high resolution spectra for the O 1s, Si 2p,

Table 2.1: SiO_2 and R_2O-SiO_2(RS) Glasses

Sample	X_R(ideal)	X_{Si}(ideal)	X_R(assay)	X_{Si}(assay)	f_{NBO}(theo)*	f_{NBO}(XPS)**
TO8[+]	0.000	1.000			0.000	0.000
NSI	0.200	0.800	0.189	0.811	0.209	0.218(0.014)
NSII	0.250	0.750			0.286	0.284(0.012)
NSIII	0.333	0.667	0.340 0.337	0.660 0.663	0.408	0.350(0.011)
NSV	0.400	0.600	0.397	0.603	0.495	0.436(0.013)
LSI	0.333	0.667			0.400	0.330(0.016)
KSI	0.333	0.667			0.400	0.355(0.014)

*from Eq. (2.2).

**mean value (standard deviation) from Eq. (2.6).

[+] fused quartz[102].

X_R and X_{Si} are the mole fractions of R_2O and SiO_2, respectively.

(Li 1s, Na 1s, or K 2p), and C 1s levels. A final survey spectrum completed an analysis. At least two fracture surfaces for each glass composition were examined to assure the reproducibility of these measurements. In one instance, spectra were measured from an air-fractured surface of an NS glass (NSV in Table 2.1) for comparison with spectra from a vacuum-fractured surface. The air-fractured glass was exposed to the ambient atmosphere for ∿15 sec.

Refinement of the core level spectra was accomplished by the methods of deconvolution, smoothing, and background subtraction which are detailed in Section 1.3.1. Photopeak energies and full widths at half maximum (FWHM) were also computed as in Section 1.3.1 for the Si 2p and (Li 1s, Na 1s, or K $2p_{3/2}$) levels using a nonlinear least squares fitting analysis. The O 1s spectral envelopes for vacuum-fractured samples were fit to two peaks without constraints on intensity, FWHM, or mixture of Gaussian and Lorentzian peak shapes for either component. Binding energies for these two peaks were allowed to vary within overlapping 3 eV windows. As a check on the algorithm employed to reduce the Mg $K\alpha_2$ contribution of the source linewidth, the FWHM of the O 1s components for SiO_2 glass and a series of NS glasses were determined with and without spectral deconvolution.

2.4. RESULTS AND ANALYSIS:

2.4.1. Spectral Artifacts

Survey spectra for vacuum-fractured and air-fractured surfaces of glass NSV are presented in Fig. 2.6. While no evidence of carbon contamination is detected initially for the vacuum-fractured glass in Fig. 2.6(a), significant contamination is indicated for the air-fractured glass in Fig. 2.6(b) by the prominent C 1s photopeak and C KVV Auger lines. The C 1s signal from the vacuum-fractured surface increased only very slowly with time under X-irradiation to a level of $\lesssim 1$ atomic % after several hours.

A rather striking chemical modification of the air-fractured glass is made apparent by high resolution spectra of the O 1s core level shown in Fig. 2.7 for the vacuum-fractured and air-fractured surfaces. In the case of the vacuum-fractured glass in Fig. 2.7(a), the BO and NBO components of the O 1s spectral envelope are well resolved and closely fit by two nearly Gaussian peaks BO and NBO1 with FWHM of $\underset{\sim}{\sim}1.55$ eV and $\underset{\sim}{\sim}1.30$ eV, respectively. In contrast, both the relative intensity of the NBO component and the resolution between the BO and NBO components of the O 1s envelope are greatly reduced for the air-fractured glass in Fig. 2.7(b). It is suggested that this spectrum may be reasonably fit by three Gaussian peaks BO, NBO1, and NBO2 with FWHM constrained to $\underset{\sim}{\sim}1.55$, 1.30 and 1.30 eV, respectively. A characteristic of this particular fit is that f_{NBO}(XPS) in Fig. 2.7(b) is very similar to that in Fig. 2.7(a).

The rationale for the analysis in Fig. 2.7(b) is that hydration of the air-fractured glass causes a partial exchange of protons for sodium ions in the near-surface region of the sample. Thus, a portion of NBO's

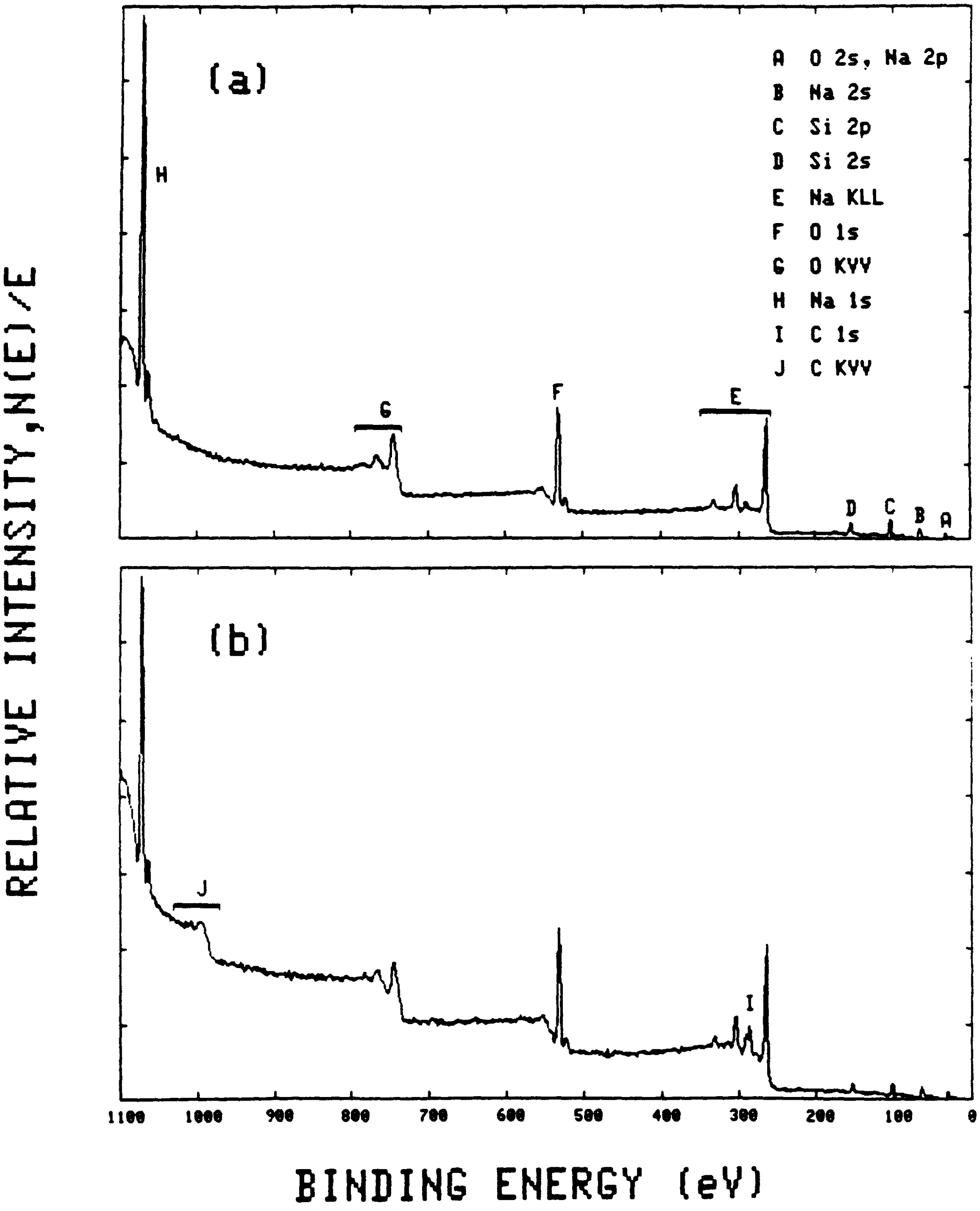

Fig. 2.6: NS glass with X_{Na}=0.40 (NSV): (a) survey spectrum of vacuum-fractured surface and (b) survey spectrum of air-fractured surface.

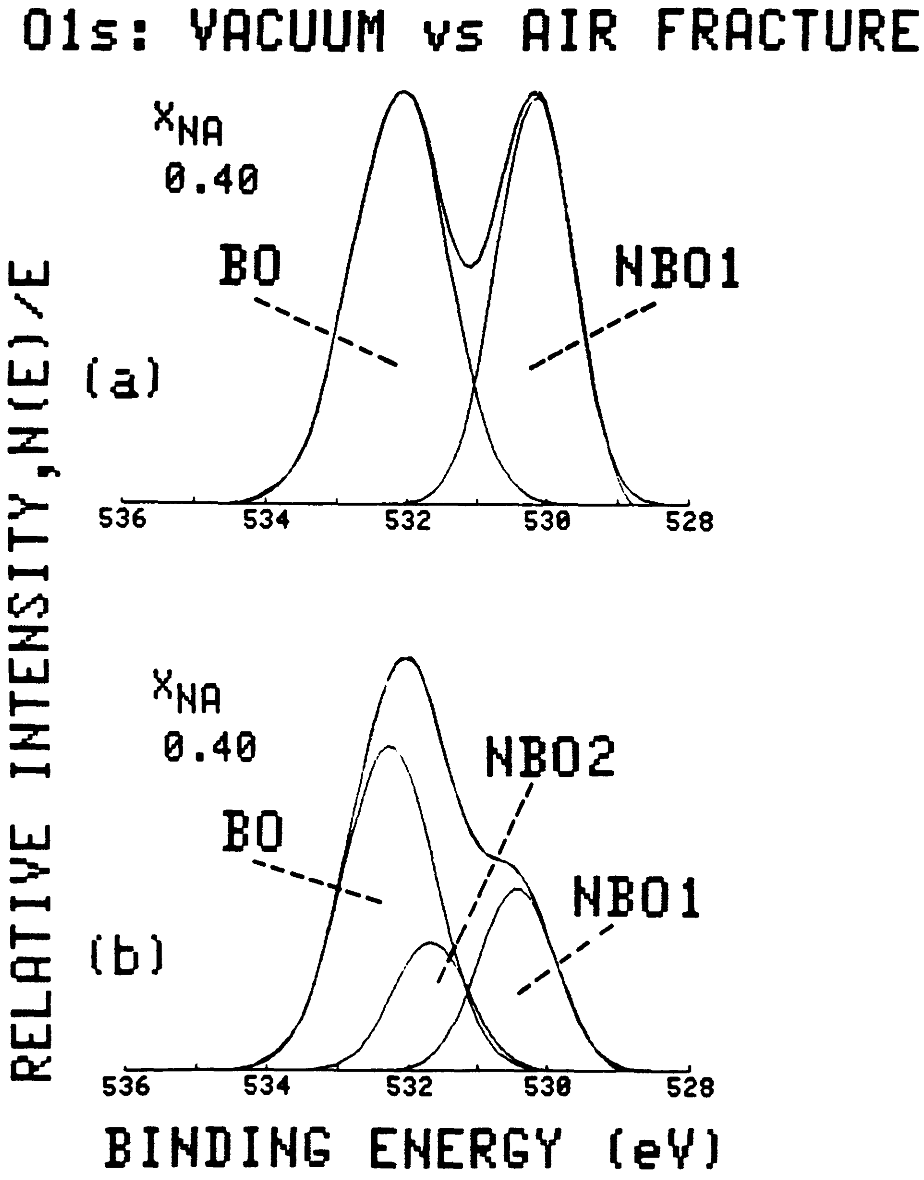

Fig. 2.7: NS glass with X_{Na}=0.40 (NSV): (a) O 1s core level for vacuum-fractured glass, f_{NBO}(XPS)≈0.44; and (b) O 1s core level for air-fractured glass, f_{NBO}(XPS)≈0.45. The experimental spectrum, component peaks, and sum of the component peaks are shown in both cases.

is converted from NBO1 (Si-O-$\sum_j Na_j$) to NBO2(Si-OH). The decrease of electron density on NBO2 relative to NBO1 results in the NBO2 chemical state having a binding energy intermediate to those of the BO and NBO1 states. While this analysis is by no means unique, it provides a logical explanation for the pronounced differences in the O 1s spectra of Fig. 2.7. However, the intent of this exercise is more to emphasize the advantage of preparing and analyzing fracture surfaces of reactive or hygroscopic glasses in situ under ultra-high vacuum conditions when the experimental objective is to investigate bulk physicochemical properties. With less stringent methods of surface preparation (including vacuum-milling, nitrogen-fracturing, and ion-sputtering), there is a considerably greater risk of encountering spectral artifacts as exemplified by Fig. 2.7(b).

The FWHM's computed for the BO and NBO components of O 1s spectra from vacuum-fractured surfaces of SiO_2 glass and several NS glasses are plotted versus X_{Na} in Fig. 2.8. The width of the BO peak for NS glasses is significantly broader than that of vitreous SiO_2. In addition, the width of the NBO peak is substantially narrower than that of the BO peak for the NS glasses. Analogous trends in the raw and deconvoluted data attest to the appropriateness of the algorithm used for spectral deconvolution. In comparison to the raw spectra, the deconvoluted spectra are fit by peaks ∿20 % narrower and more nearly Gaussian in shape (>97 % Gaussian).

Smets and Lommen [43] also acquired O 1s spectra from vacuum-fractured surfaces of NS glasses, but made no attempt to compensate for electrostatic charging effects. The spectra (without deconvolution) were fit by constraining the FWHM of the BO and NBO peaks to be equal for a given glass composition and by fixing the peak shapes as completely Gaussian [44].

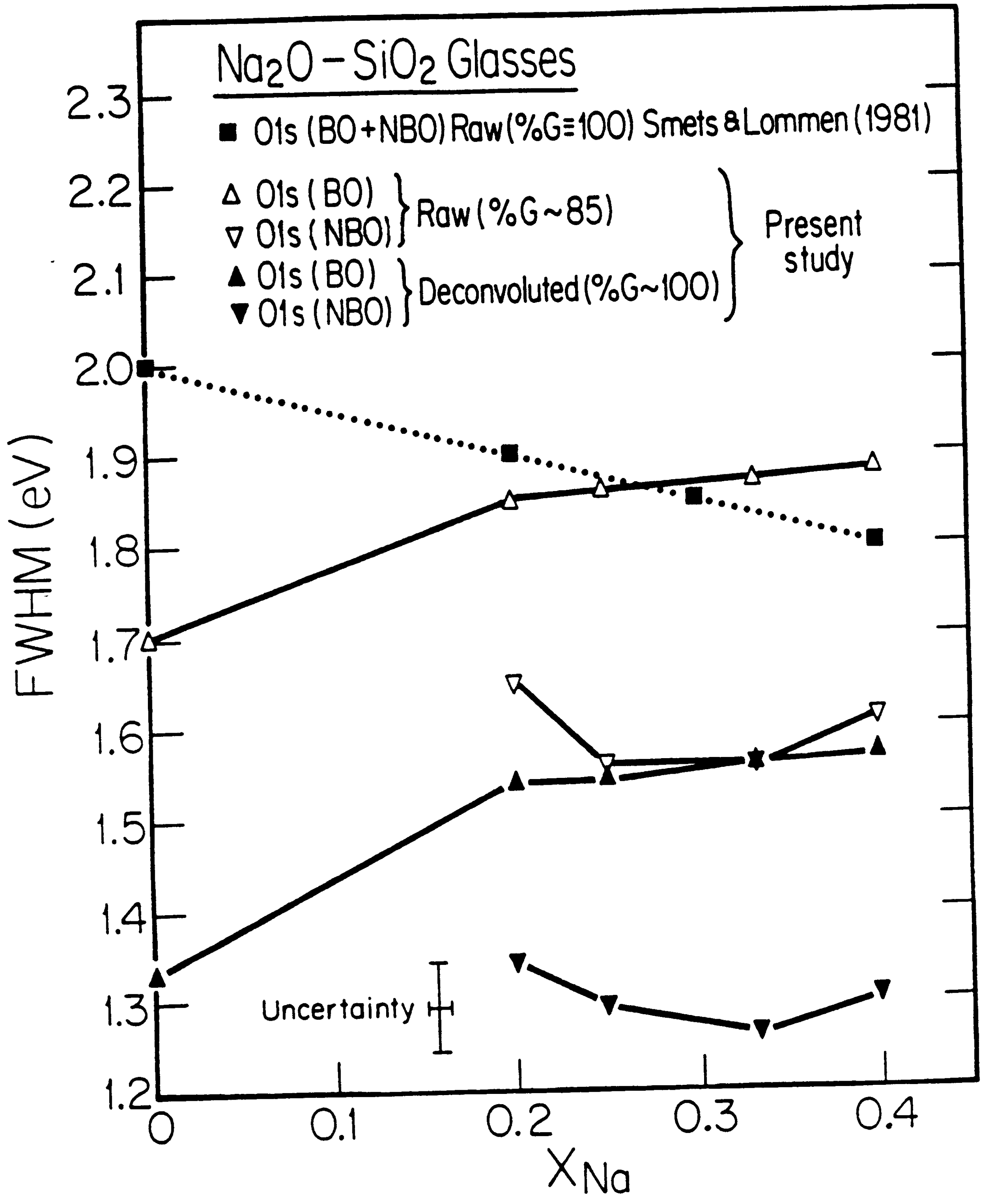

Fig. 2.8: Widths for BO and NBO components of the O 1s core level for SiO_2 and NS glasses. Data of Smets and Lommen [43] are shown for comparison. % G refers to the percentage of Gaussian character in the peak shape.

Curiously, Smets and Lommen's peak widths are seen to decrease with X_{Na} in Fig. 2.8. This trend would be expected if differential charging across the analyzed surface contributed to the apparent peak width, since the severity of this charging effect decreases with increasing sample conductivity.

As discussed in Section 1.5.2, the use of the BMD method for charging correction in the present study not only calibrates the binding energy scale for a glass relative to its surface Fermi level, but also acts to minimize peak broadening caused by differential charging. For this reason, the variation in FWHM for the BO and NBO peaks with X_{Na} observed in the present study is believed to reflect more realistically the bulk physicochemical nature of these glasses. The distinct widths for the BO and NBO components of NS glasses (Fig. 2.8) also provided input values for the FWHM assigned to the BO, NBO1, and NBO2 peaks in the analysis of the O 1s envelope in Fig. 2.7(b).

2.4.2. Core Level Spectra for SiO_2 and R_2O-SiO_2 Glasses

In Fig. 2.9, typical O 1s spectra from vacuum-fractures surfaces of SiO_2 and NS glasses are displayed. The spectrum for vitreous SiO_2 is comprised of only a BO component. NBO's are not observed for SiO_2 glass in detectable concentrations of $f_{NBO} \gtrsim 0.010$ (atomic % $\gtrsim 0.5$) [104]. For the NS glasses, however, BO and NBO components of the O 1s envelope are well resolved and closely fit by two nearly Gaussian peaks. The NBO peak has a lower binding energy and a narrower width than the BO peak. Decidedly inferior fits were obtained when the peak widths were constrained such that FWHM(BO) $\equiv$ FWHM(NBO) for any given glass composition.

Representative O 1s spectra from vacuum-fractured surfaces of $Li_2O \cdot 2SiO_2$, $Na_2O \cdot 2SiO_2$, and $K_2O \cdot 2SiO_2$ glasses are compared in Fig. 2.10.

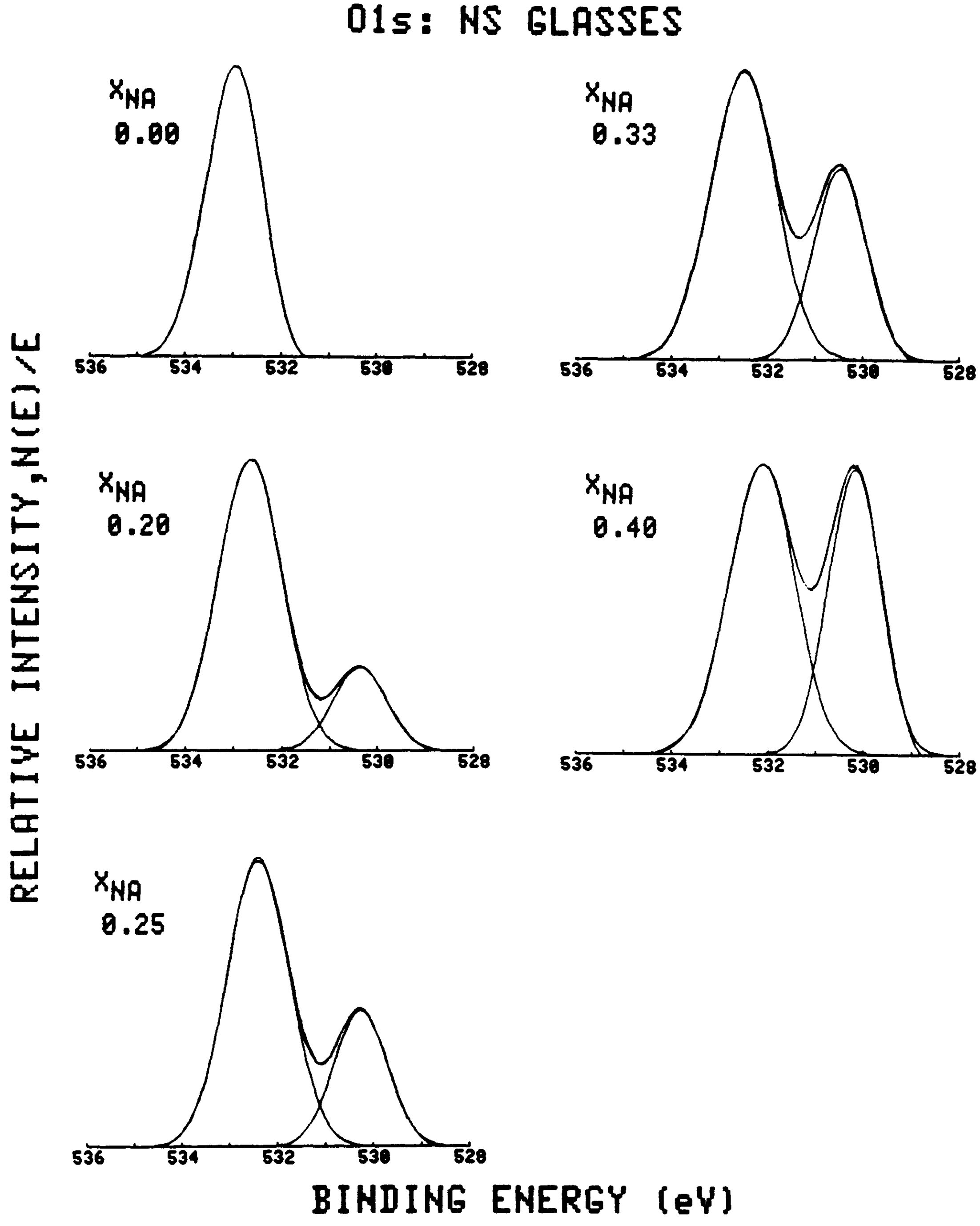

Fig. 2.9: O 1s core level for vacuum-fractured SiO_2 glass (T08) and NS glasses (NSI, NSII, NSIII, and NSV). The experimental spectrum, component peaks, and sum of the component peaks are shown for each NS glass. The sum of each two-component fit is nearly indistinguishable from the experimental spectrum.

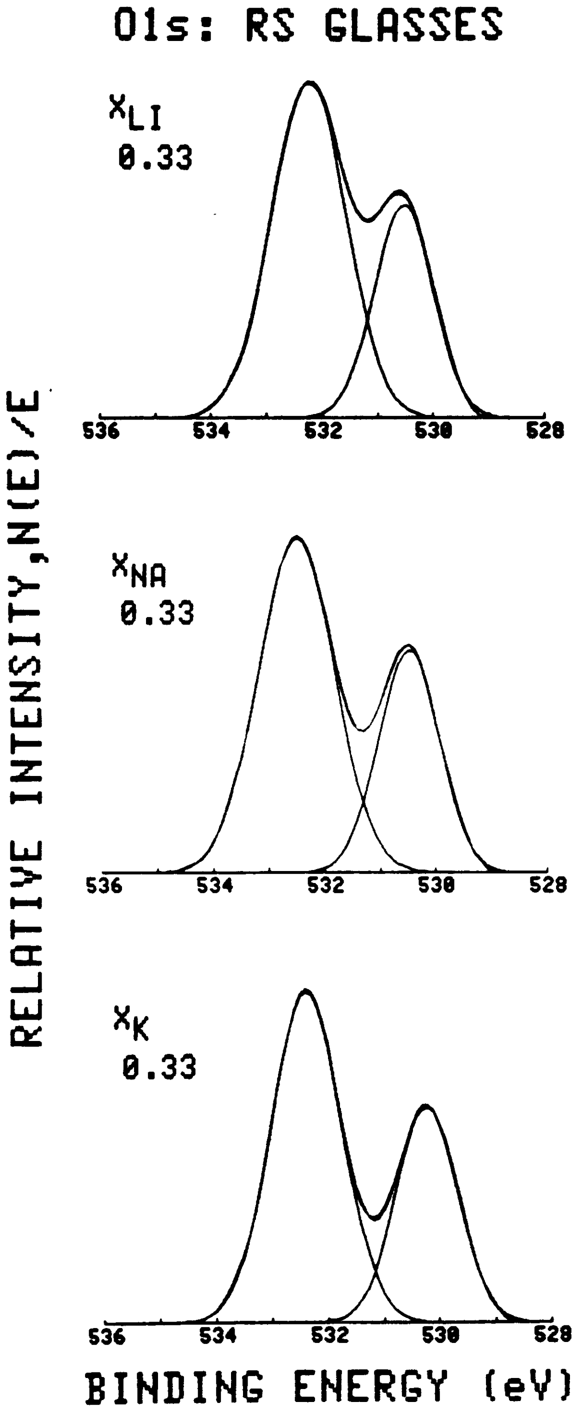

Fig. 2.10: O 1s core level for vacuum-fractured RS glasses with X_R=0.33 (LSI, NSIII, AND KSI). The experimental spectrum, component peaks, and sum of the component peaks are shown in each case. The sum of each two-component fit closely approximates the experimental spectrum.

The BO and NBO components of the O 1s enveloped are progressively better resolved in the following order according to alkali type as Li<Na<K. Once again, these components are well fit by two nearly Gaussian peaks with the NBO peak having a lesser binding energy and smaller width than the BO peak for each disilicate glass.

From the analyses of the O 1s spectra in Figs. 2.9 and 2.10, f_{NBO}(XPS) has been determined for each composition and is listed together with f_{NBO}(theo) in Table 2.1. Excellent agreement between experiment and theory is obtained for glasses with $X_R<0.30$ (T08, NSI, and NSII). However, f_{NBO}(XPS) is significantly smaller than f_{NBO}(theo) for glasses with $X_R>0.30$ (NSIII, NSV, LSI, and KSI). These results thus reproduce the findings of several earlier XPS studies of SiO_2 and RS glasses [38,40,42,46].

Binding energies for the BO and NBO components of the O 1s level and the Si 2p level for SiO_2 and RS glasses are graphed vs. n(theo) in Fig.2.11. For the NS glases, BE_F of the BO component decreases with n(theo) toward that of the NBO component, whereas BE_F of the NBO component is invariant at 530.30 eV (standard deviation $\sigma \simeq 0.15$ eV) for $0.5 \lesssim$ n(theo) $\lesssim 1.5$. The BE_F of the Si 2p level appears to decrease at almost twice the rate with n(theo) as the BO component. In addition, the binding energy of the Na 1s level (not shown in Fig. 2.11) is constant at 1072.00 eV ($\sigma \simeq$ 0.15 eV) for $0.5 \lesssim$ n(theo) $\lesssim 1.5$. In comparing the $R_2O \cdot 2SiO_2$ glasses at n(theo) = 1.0 in Fig. 2.11, there is some indication that BE_F of the NBO component shifts downward in energy relative to that of the BO component according to alkali type. The size of this shift increases in the order of Li<Na<K. The BE_F of the Si 2p level does not change significantly among the disilicate glasses.

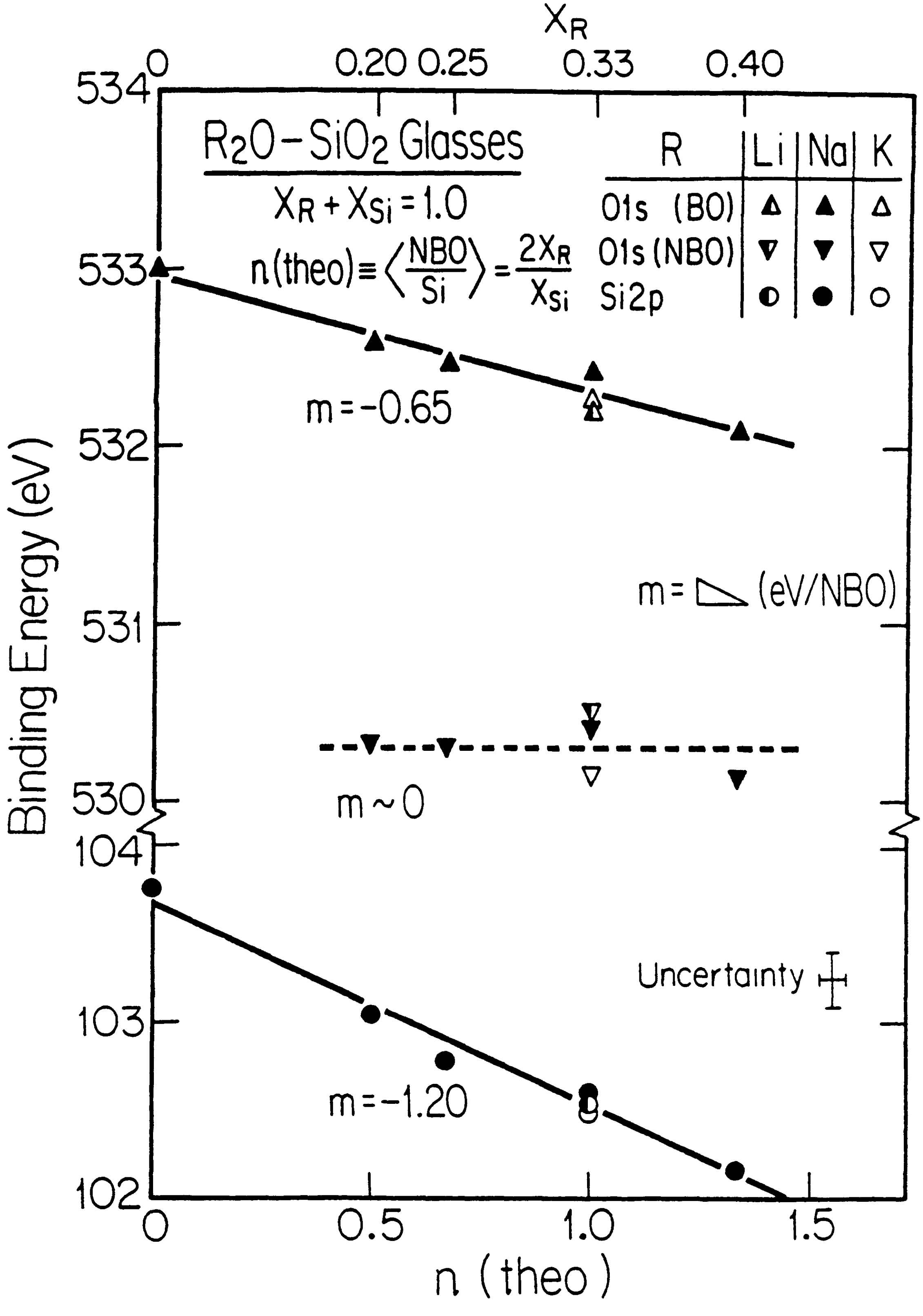

Fig. 2.11: BE_F for O 1s and Si 2p photopeaks of SiO_2 and RS glasses vs. n(theo).

Finally, the peak widths for the BO and NBO components of the O 1s level and the Si 2p level for SiO_2 and RS glasses are graphed vs. n(theo) in Fig. 2.12. The FWHM of the BO component for vitreous SiO_2 is 1.33 eV ($\sigma \simeq 0.02$ eV) [101]. The FWHM's of the BO and NBO peaks for the NS glasses are invariant at 1.55 eV and 1.30 eV ($\sigma \simeq 0.05$ eV), respectively, for $0.5 \lesssim$ n(theo) $\lesssim 1.5$. In contrast, the FWHM of the Si 2p peak first broadens from ∼ 1.40 eV for vitreous SiO_2 to a maximum of ∼1.85 eV at n(theo) = 0.5, and then narrows to a local minimum of ∼1.60 eV at n(theo)=1.0. The FWHM of the Na 1s peak (not shown in Fig. 2.12) is constant at 1.84 eV ($\sigma \simeq 0.05$ eV) for $0.5 \lesssim$ n(theo)$\lesssim 1.5$. The FWHM's of the BO and NBO components of the O 1s level and the Si 2p level for the $Li_2O \cdot 2SiO_2$ and $K_2O \cdot 2SiO_2$ glasses are very close to those for the $Na_2O \cdot 2SiO_2$ glass at n(theo) = 1.0 in Fig. 2.12.

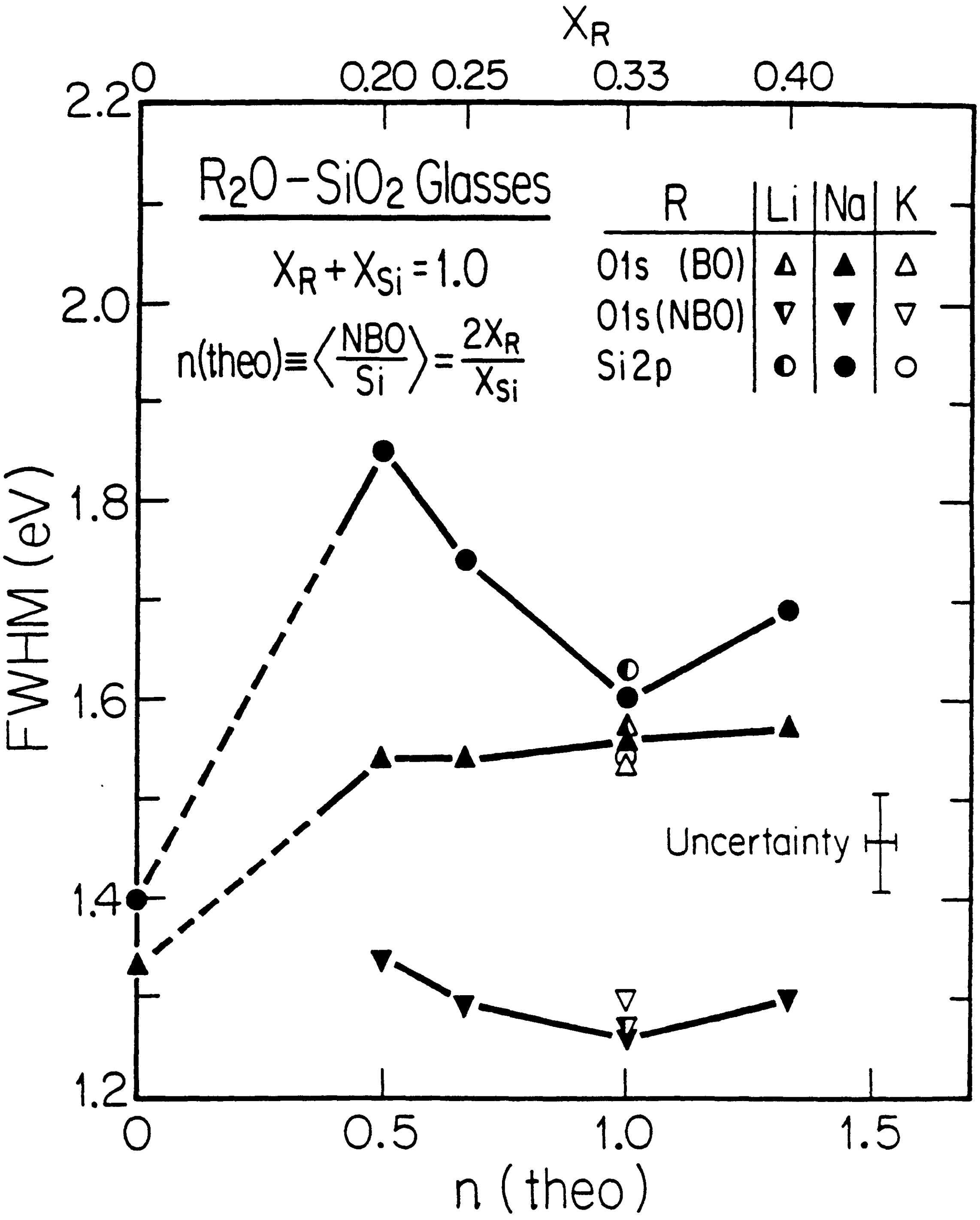

Fig. 2.12: Widths for O 1s and Si 2p photopeaks of SiO_2 and RS glasses vs. n(theo).

2.5. DISCUSSION:

2.5.1. SiO_2 Glass

Recently, the random network model for vitreous SiO_2 has been challenged anew by structural models descended from the original crystallite hypothesis. It is argued here that photoemission results for crystalline and vitreous SiO_2 from this and earlier work are in disagreement with key provisions of the crystalline cluster models by Phillips [5] and Goodman [6] for the structure of SiO_2 glass.

The current XPS study confirms and amplifies a previous finding for vitreous SiO_2 that NBO's are not present in detectable concentrations--i.e., $f_{NBO}(XPS) < 0.010$. This empirical result contradicts Phillips' estimate that $f_{NBO} \sim 0.08$ in SiO_2 glass due to superficial Si=O bonds on internal surfaces separating crystalline clusters with radii ∿ 3 nm. A critical cluster size can be calculated above which the decreasing surface-to-volume ratio of this aggregate morphology would yield $f_{NBO} \to 0$ in agreement with photoemission measurements. If R = the radius of a cluster, ΔR = the thickness for the layer of surface molecules, $(O_{1/2})_2 - Si = O$, and $\bar{v}$ = the average volume of a surface or interior molecule, then

$$f_{NBO} \sim \frac{4\pi R^2 \Delta R\, \bar{v}}{2(\frac{4}{3}\pi R^3)\, \bar{v}} = \frac{3\Delta R}{2R} \; . \qquad (2.7)$$

The factor of 2 in the denominator accounts for a contribution of one NBO by each surface molecule. With $\Delta R = 0.2$ nm, this approximation gives $f_{NBO} \sim 0.10$, 0.03, and 0.01 for R = 3, 10, and 30 nm, respectively. Therefore, the average cluster size must be at least an order of magnitude larger than originally proposed by Phillips if this structural model is to agree with f_{NBO}(XPS) for SiO_2 glass. The existence of crystalline clusters with dimensions on the scale of tens of nanometers would be evident in the widths of X-ray diffraction peaks. Such peak widths are, however, inconsistent with crystallites anything like 10 nm in size. The XPS data combined with X-ray diffraction results thus inveigh against this cluster model in favor of the random network theory.

According to the cluster model of Goodman for vitreous SiO_2, interfacial regions between clusters with radii $\gtrsim$ 1.5 nm are distorted relative to a periodic atomic arrangement within each cluster. A first-principles calculation has concluded the effective Mulliken atomic charges on oxygen and silicon atoms in SiO_2 glass are much more strongly dependent on Si-O bond length than on Si-O-Si intertetrahedral angle [57]. If Goodman's premise is realistic, then interfacial strains would produce a broader distribution in Si-O bond lengths with a presumably wider variation of valence charges on oxygen and silicon atoms for SiO_2 glass than for α-quartz. From the vantage of XPS, one would thus expect such differences in the chemical bonding between crystalline and vitreous SiO_2 to be denoted in core level spectra by broader photopeaks for the glass. In Chapter 1, it was established that BE_F and FWHM of the O 1s and Si 2p levels for vacuum-fractured α-quartz and SiO_2 glass are <u>not</u> significantly different [101]. These results suggest the covalent-ionic nature of the Si-O bond does not change appreciably with the Si-O-Si bridging angle and concur with other evidence indicating the deviation in Si-O bond lengths from 0.161 - 0.162 nm in both crystalline <u>and</u> vitreous SiO_2 is limited to thermal oscillations [27,28,78]. The equally narrow distribution of Si-O bond lengths for α-quartz and SiO_2 glass, inferred from photoemission spectra, is therefore contrary to expectations for Goodman's structural model. The argument against expanding the cluster size above some critical dimension whereby strained siloxane bonds (Si-O-Si) are not empirically observable is analogous to the one given above for Phillips's model. Once again, the random network model appears to be a more appropriate structural description for SiO_2 glass.

2.5.2. R_2O-SiO_2 Glasses

A structural interpretation of photoemission spectra for RS glasses is now presented which focuses on how the random silicon-oxygen network of vitreous SiO_2 is modified by substantial additions of R_2O. An understanding of the way in which physicochemical properties of relatively simple, single-phase RS glasses are revealed in XPS is essential to the interpretation of photoemission spectra for NAS glasses in Chapter 3. This discussion concludes with some comments on the compatibility of the present XPS results and the crystalline cluster models of Phillips [5] and Goodman [6] for RS glasses.

While gratifying agreement between f_{NBO}(XPS) and f_{NBO}(theo) is seen in Table 2.1 for RS glasses with $X_R<0.30$, f_{NBO}(XPS) is considerably smaller than f_{NBO}(theo) for $X_R>0.30$. Hydration of the glasses with $X_R>0.30$ before or during the time O 1s spectra were acquired from vacuum-fractured surfaces is apparently not a major cause of this discrepancy. Attempts to refit these spectra by the method employed for the spectrum of the air-fractured NS glass in Fig. 2.7(b) did not yield any sensible indication for the presence of an NBO2 peak. Furthermore, f_{NBO}(XPS) for $Li_2O\cdot 2SiO_2$, $Na_2O\cdot 2SiO_2$, and $K_2O\cdot 2SiO_2$ glasses are equivalent within experimental uncertainty (Table 2.1) even though susceptibility of these glasses to hydrolytic attack substantially increases with alkali type as Li<Na<K [105] Also, f_{NBO}(XPS) for these vacuum-fractured glasses were virtually constant in measurements conducted over several hours. Finally, a preliminary XPS study [106] of a vacuum-fractured surface of $PbO \cdot SiO_2$ glass yielded f_{NBO}(XPS) = 0.54 vs. f_{NBO}(theo) = 0.67 despite the far greater chemical durability of this composition relative to any of the RS glasses examined here.

Although it is not immediately obvious for α-$Na_2Si_2O_5$ and $NaSiO_3$ in Fig. 2.2, a one-to-one correspondence between alkali atoms and NBO's exists in these NS crystal structures. Based on the concepts reviewed in Section 2.2.2, one reasonably expects that a similar atomic correspondence characterizes the incorporation of Na_2O in analogous NS glasses. Earlier XPS work [36,38] has indicated f_{NBO}(XPS) for the disilicate crystal and glass are nearly identical, but smaller than theoretically expected (i.e., f_{NBO}(XPS)$\simeq$ 0.33 vs. f_{NBO}(theo) = 0.40). This result thus implies the disagreement of f_{NBO}(XPS) with f_{NBO}(theo) for RS glasses at X_R>0.30 is also not due to some less efficient mechanism for the incorporation of R_2O than supposed by Eq. (2.1).

Other explanations for this disagreement are a nonlinearity in the relative contributions of BO and NBO to the O 1s spectral envelope at X_R>0.30, as inferred by Ching et al. [49], or a surface reconstruction (see Section 1.2.2) where alkali ions locally segregate to a vacuum-fractured surface, as simulated by Garofalini and Levine [107]. However, the invariant f_{NBO}(XPS) determined here for $R_2O \cdot 2SiO_2$ glasses (Table 2.1) are not in accord with specific chemical trends proposed by Ching et al. that A(BO)/A(NBO) is larger for $Na_2O \cdot 2SiO_2$ glass than for $Li_2O \cdot 2SiO_2$ glass or by Garofalini and Levine that surface segregation increases in the order of Li<<Na<K for $R_2O \cdot 3SiO_2$ glasses.

An interesting possibility is that the strain energy dissipated locally during fracture of brittle solids such as silicate glasses generates sufficient thermal energy [108,109] to alter the composition and chemical bonding of the near-surface region in the following way. During and after fracture of silicate glasses in vacuum, the emission of electrons, ions, neutral particles, and photons has been detected from the freshly formed surfaces [110]. It is plausible that alkali species could be preferentially ejected from the surface of an RS glass formed by fracture with the concomitant conversion of some portion of the NBO's originally present near this surface into BO's. A comparison of vacuum-fractured and fire-polished surfaces of SiO_2 glass in Chapter 1 supports the view that the fracture process is sufficiently energetic to allow for extensive reconstruction of siloxane bonds near the fracture surface.

While the last mechanism is consistent with the general finding of XPS studies on RS glasses with high R_2O content that $f_{NBO}(XPS) < f_{NBO}(theo)$, it does not answer the key question of why this discrepancy is not observed for compositions with $X_R \lesssim 0.30$. Additional work is necessary before the difference between $f_{NBO}(XPS)$ and $f_{NBO}(theo)$ for RS glasses with $X_R > 0.30$ can be fully understood. Angle-resolved photoemission measurements of vacuum-fractured surfaces of RS glasses whereby $f_{NBO}(XPS)$ can be determined as a function of depth below the fracture surface would be particularly beneficial in this regard.

The close correspondence between f_{NBO}(XPS) and f_{NBO}(theo) for NS glasses with $X_{Na} \lesssim 0.30$ obtained here and elsewhere [38,40,42,46] is encouraging for the study of NAS glasses in Chapter 3. According to the classical model for the structure of NAS glasses, the compositions chosen for that study have $0 \leq f_{NBO}$(theo)≤ 0.25. This range of f_{NBO}(theo) for the NAS glasses is well within the one observed for NS glasses, $0 \leq f_{NBO}$(theo)<0.35, where f_{NBO}(XPS) conforms to theory. An unambiguous test of the classical model for these NAS glasses by XPS is thus thought to be feasible.

For the O 1s core level of NS glasses in Fig. 2.11, BE_F of the BO component decreases relative to that of the NBO component and thus indicates that a successively higher average valence charge resides on BO's with increasing n(theo) or X_{Na}. Meanwhile, the constancy of BE_F for the NBO component suggests the valence charge on NBO's does not change appreciably over the range of NS glass compositions examined in this work. Extrapolation of the data in Fig. 2.11 shows that binding energies for the BO component would approach those of the NBO component as n(theo)→ 4.0, (i.e., the orthosilicate composition where f_{NBO}(theo)=1.00). These trends can be understood from the viewpoint that certain similarities exist between the local atomic arrangements of RS crystals and glasses (see Section 2.2.2).

Structural and chemical environments for NBO's in $Na_2Si_3O_7$, α-$Na_2Si_2O_5$, β-$Na_2Si_2O_5$, and Na_2SiO_3 crystals with n(theo)≤ 2 [17-20] are not substantially different, as depicted for α-$Na_2Si_2O_5$ and Na_2SiO_3 in Fig. 2.2. However, the environment of BO's is increasingly perturbed in the sequence of SiO_2, α-$Na_2Si_2O_5$, and $NaSiO_3$ by the growing portion of BO's within a bonding distance of one or more sodium ions. Atomic coordination schemes for BO's and NBO's in NS glasses which are similar to those found in NS crystals would explain the variation of BE_F for the BO and NBO components of the O 1s level in Fig. 2.11. Elements of this argument have been used before to describe the decreasing energetic separation between the BO and NBO components of the O 1s level for RS glasses with X_R [42,43].

In the case of the $R_2O \cdot 2SiO_2$ glasses at n(theo) = 1.0 in Fig. 2.11, the progressively lower BE_F for the NBO component in the sequence of Li>Na>K indicates the valence charge associated with NBO's increases with the ionicity [64] of the R-O bond (i.e., Li-O<Na-O<K-O). If more alkali ions coordinate NBO's than BO's in RS glasses, as happens in RS crystals, then one would expect the binding energy of the NBO component to shift relative to the BO component for this series of disilicate glasses, as suggested in Fig. 2.11. The connection between the ionicity of the R-O bond and the energetic separation of the BO and NBO components of the O 1s level for analogous RS glasses has previously be recognized [37,42,43].

For RS crystals with $n(\text{theo}) \leq 2.0$, BO's within a bonding distance of one or more alkali ions have greater bond strength sums p and hence longer Si-BO bond lengths than unperturbed BO's (see Section 2.2.2). Since NBO's have more regular structural and chemical environments than BO's in such structures (e.g., see Fig. 2.2), the distribution of Si-NBO distances is consequently narrower than the distribution of Si-BO distances, as indicated in Fig. 2.1. By analogy to these RS crystal structures, it is proposed the larger FWHM of the BO component vis-a-vis the NBO component for all RS glasses in Fig. 2.12 reflects a broader distribution of Si-BO distances than Si-NBO distances. The relative uniformity of the Si-NBO bond lengths in RS glasses is further indicated by the similarity in FWHM for the NBO component in RS glasses and the BO peak for SiO_2 glass in Fig. 2.12 (see Section 2.5.1).

Attention is now directed to the Si 2p core level of NS glasses. The comparatively rapid decrease of BE_F in Fig. 2.11 and the maximum and minimum in FWHM at n(theo)=0.5 and 1.0, respectively, in Fig. 2.12 for the Si 2p photopeak strongly suggest that silicon atoms occur in different chemical states. These energetically distinct states reflect a sequential increase of valence charge corresponding to the number of NBO's bonded to a silicon atom. They are distributed according to composition approximately as follows: NBO/Si=0 for $X_{Na}=0$, NBO/Si=0 and 1 for $0<X_{Na}<0.33$, NBO/Si=1 for $X_{Na}=0.33$, and NBO/Si=1 and 2 for $0.33<X_{Na}<0.50$. Although these bonding states are unresolved in Si 2p photoemission spectra of this study, the situation is rather analogous to the systematic changes in the ^{29}Si MAS NMR spectra for NS glasses in Fig. 2.3. In Fig. 2.12, therefore, the maximum in FWHM at n(theo)=0.5 indicates about equal numbers of silicons with NBO/Si=0 and NBO/Si=1 exist in $Na_2O \cdot 4SiO_2$ glass while the minimum in FWHM at n(theo)=1.0 signifies nearly all silicons have NBO/Si=1 in $Na_2O \cdot 2SiO_2$ glass. Also, the $Li_2O \cdot 2SiO_2$ and $K_2O \cdot 2SiO_2$ glasses appear similar to the $Na_2O \cdot 2SiO_2$ glass in this regard, since no significant differences in BE_F or FWHM for the Si 2p level of the $R_2O \cdot 2SiO_2$ glasses are seen in Figs. 2.11 and 2.12 at n(theo)=1.0.

The invariance of BE_F and FWHM for the Na 1s core level over the range of NS glasses considered here mirrors the behavior for the NBO component of the O 1s level. Thus, the valence charge on sodium atoms in these glasses, like NBO's, must not vary appreciably with composition. If NS glasses have atomic coordination schemes which are similar to those in NS crystals, then the regularity of the structural and chemical environments for sodium ions in NS crystals with $n(theo) \leq 2$ [17-20] would account for the constant binding energies and widths of the Na 1s photopeak for the glasses.

The above observations about the structural chemistry of RS glasses have been derived from photoemission results for a limited number of compositions. Additional data, obtained by methods comparable to those used here, for a series of more closely spaced KS glass compositions over a range of $0 \leq X_K \leq 0.50$ would be particularly interesting. Aside from corroborating the physicochemical trends deduced in the present study for NS glasses, photoemission data for KS glasses would provide insight into the way smaller additions of R_2O are accommodated by the silicon-oxygen network than could be assessed here for NS glasses because of phase separation in the range of $0 < X_{Na} < 0.20$

Finally, the interpretation of XPS results for RS glasses given here is based upon the premise that local atomic arrangements in RS glasses resemble those in RS crystals. The correspondence in coordination chemistry between these structures imparts electrostatic stability to the random silicon-oxygen network of the glass. It thus enables the internal energy of the glass to be similar to that of its crystalline counterpart(s). Consequently, glass formation is controlled by kinetic factors [54,55]. However, aspects of this interpretation could be construed as support for the crystalline cluster models of Phillips and Goodman. It must be emphasized that other empirical and theoretical evidence [27,33,34,86,92,93] indicates RS glasses are essentially distinguished from RS crystals by a broader distribution of Si-O-Si bridging angles. This structural characteristic of RS glasses is more in keeping with the central idea of the random network model. Furthermore, evidence which demonstrates the existence of specific structural features predicted by the crystalline cluster models (i.e., Si=O bonds or strained siloxane bonds at cluster interfaces) is not discerned in photoemission spectra for RS glasses.

Instead, the results of this study are quite reasonably explained in the context of the random network model. The same conclusion was reached for vitreous SiO_2 in the preceeding subsection.

2.6. SUMMARY:

Photoemission results for vitreous SiO_2 are incompatible with underlying assumptions of recent crystalline cluster models for glass structure. Si=O bonds or strained siloxane bonds are not observed in detectable concentrations for SiO_2 glass. A lower limit on the cluster radius required to obtain consistency with this empirical result is estimated and found unreasonably large ($\gtrsim$ 30 nm). One concludes the random network model remains the most appropriate structural description for vitreous SiO_2.

Photoemission spectra of the O 1s, Si 2p, and alkali core levels for RS glasses (including $Na_2O \cdot 2SiO_2$, $Li_2O \cdot 2SiO_2$, and $K_2O \cdot 2SiO_2$) have been obtained from vacuum-fractured surfaces and corrected for electrostatic charging effects by the BMD method. In accord with earlier work, the present XPS study of RS glasses has shown that f_{NBO}(XPS) agrees with conventional theory for the incorporation of R_2O in a vitreous silicon-oxygen network for $X_R<0.30$, but departs negatively from this theory for $X_R>0.30$. While additional work is required to resolve this discrepancy for RS glasses with high R_2O content, hydration of these glasses or the possibility of a less efficient mechanism for the incorporation of R_2O are discounted as being significant factors. Instead, a specific surface reconstruction at vacuum-fractured surfaces is proposed as a more likely explanation for this inconsistency. Nonetheless, the results of this study also indicate that an unambiguous structural analysis of NAS glasses by XPS in Chapter 3 is feasible.

Trends in the binding energies and widths of the O 1s, Si 2p and Na 1s photopeaks in NS glasses support the view that local atomic arrangements in RS glasses are similar to those in RS crystals. In the absence of any empirical evidence to the contrary, the photoemission results for RS glasses are best understood in the context of the random network model.

REFERENCES

[1] E.A. Porai-Koshits, "The Structure of Glass", J. Non-Cryst. Solids, 25[1-3] 87-128 (1977).

[2] A.R. Cooper, "W.H. Zachariasen - The Melody Lingers On", J. Non-Cryst. Solids, 49[1-3] 1-17 (1982).

[3] J.H. Konnert and J. Karle, "Tridymite-like Structure in SiO_2 Glass", Nature Phys. Sci., 236 92-4 (1972).

[4] J.H. Konnert, J. Karle, and G.A. Ferguson, "Crystalline Ordering in Silica and Germania Glasses", Science, 179 [4069] 177-9 (1973).

[5] J.C. Phillips, "Spectroscopic and Morphological Structure of Tetrahedral Oxide Glasses"; pp. 93-171 in Solid State Physics (Advances in Research and Applications, Vol. 37). Edited by H. Ehernreich, D. Turnbull, and F. Seitz. Academic, New York, 1982.

[6] C.H.L. Goodman, "The Structure and Properties of Glass and the Strained Mixed Cluster Model", Phys. Chem. Glasses, 26[1] 1-10 (1985).

[7] A.C. Wright, "The Structure of Amorphous Solids by X-Ray and Neutron Diffraction"; pp. 1-84 in Advances in Structure Research by Diffraction Methods (Vol. 5). Edited by W. Hoppe and R. Mason. Pergamon, Oxford, 1974.

[8] A.C. Wright and A.J. Leadbetter, "Diffraction Studies of Glass Structure", Phys. Chem. Glasses, 17[5] 122-45 (1976).

[9] L. Levien, C.T. Prewitt, and D.J. Weidner, "Structure and Elastic Properties of Quartz at Pressure", Am. Mineral., 65[9-10] 920-30 (1980).

[10] W.A. Dollase, "Reinvestigation of the Structure of Low Cristobalite", Z. Kristallogr., 121[5] 369-77 (1965).

[11] W.H. Baur, "Silicon-Oxygen Bond Lengths, Bridging Angles Si-O-Si and Synthetic Low Tridymite", Acta Cryst., B33[8] 2615-9 (1977).

[12] F. Liebau, Acta Cryst. 14 389-95 (1961).

[13] H. Vollenkle, "Refinement of Crystal Structure for Li_2SiO_3 and Li_2GeO_3", Z. Kristallogr., 154[1-2] 77-81 (1981).

[14] H. Vollenkle, A. Wittmann, and H. Nowotny, "The Crystal Structure of $Li_6(Si_2O_7)$", Mh. Chem., 100[1] 295-303 (1969).

[15] H. Vollenkle, A. Whittmann, and H. Nowotny", The Crystal Structure of Li_4SiO_4", Mh. Chem., 99[4] 1360-71 (1968).

[16] D. Tranqui, R.D. Shannon, H.-Y. Chen, S. Iijima, and W.H. Baur, "Crystal Structure of Ordered Li_4SiO_4", Acta Cryst. B35[11] 2479-87 (1979).

[17] P.B. Jamieson, "Crystal Structure of $Na_2Si_3O_7$: A New Type of Silicate Sheet", Nature, 214 794-6 (1967).

[18] A.K. Pant and D.W.J. Cruickshank, "The Crystal Structure of α-$Na_2Si_2O_5$", Acta Cryst., B24[2] 13-9 (1968).

[19] A.K. Pant, "A Reconsideration of the Structure of β-$Na_2Si_2O_5$", Acta Cryst., B24[7] 1077-83 (1968).

[20] W.C. McDonald and D.W.J. Cruickshank, "A Reinvestigation of the Structure of Sodium Metasilicate, Na_2SiO_3", Acta Cryst., 22 37-43 (1967).

[21] H. Schweinsberg and F. Liebau, "The Crystal Structure of $K_4(Si_8O_{18})$", Acta Cryst., B30[9] 2206-13 (1974).

[22] M. Jansen, "The Structure of Potassium Disilicate", Z. Kristallogr., 160[1-2] 127-33 (1982).

[23] B.E. Warren, H. Krutter, and O. Morningstar, "Fourier Analysis of X-ray Patterns of Vitreous SiO_2 and B_2O_3", J. Am. Ceram. Soc., 19[7] 202-6 (1936).

[24] B.E. Warren and J. Biscoe, "Fourier Analysis of X-ray Patterns of Soda-Silica Glass", J. Am. Ceram. Soc., 21[7] 259-65 (1938).

[25] J. Biscoe, M.A.A. Druesne, and B.E. Warren, "X-ray Study of Potash-Silica Glass", J. Am. Ceram. Soc., 24[3] 100-2 (1941).

[26] R.L. Mozzi and B.E. Warren, "The Structure of Vitreous Silica", J. Appl. Cryst., 2[4] 164-72 (1969).

[27] G.G. Wicks, Structural Studies of Amorphous Materials (Sc.D. Thesis), MIT, Cambridge, 1975.

[28] D.R. Uhlmann and G.G. Wicks, "Structural Analysis Using Fluorescence Excitation", Wiss. Ztscher. Friedrich-Schiller-Univ. Jena, Math.-Nat. R., 28[2-3] 231-42 (1979).

[29] Y. Waseda and H. Soito, "The Structure of Molten Alkali Metal Silicates", Trans. Iron Steel Inst., Japan, 17[2] 82-91 (1977).

[30] M. Misawa, D.L. Price, and K. Suzuki, "The Short-Range Structure of Alkali Disilicate Glasses by Pulsed Neutron Total Scattering", J. Non-Cryst. Solids, 37[1] 85-97 (1980).

[31] I. Yasui, H. Hasegawa, and M. Imaoka, "X-ray Diffraction Study of the Structure of Silicate Glasses. Part 1. Alkali Metasilicate Glasses", Phys. Chem. Glasses, 24[3] 65-71 (1983); "Part 2. Alkali Disilicate Glasses", ibid., 72-8.

[32] M. Taylor and G.E. Brown, "Structure of Mineral Glasses - I. The Feldspar Glasses $NaAlSi_3O_8$, $KAlSi_3O_8$, $CaAl_2Si_2O_8$", Geochimica et Cosmochimica Acta, 43[1] 61-75 (1979); "II. The SiO_2-$NaAlSiO_4$ Join" ibid., [9] 1467-73.

[33] T.F. Soules, "A Molecular Dynamic Calculation of the Structure of Sodium Silicate Glasses", J. Chem. Phys., 71[11] 4570-8 (1979).

[34] S.K. Mitra and R.W. Hockney, "Molecular Dynamics Simulation of the Structure of Soda Silica", Phil. Mag., B48[2] 151-67 (1983).

[35] G.N. Greaves, A. Fontaine, P. Lagarde, D. Raoux, and S.J. Gurman, "Local Structure of Silicate Glasses", Nature 293[5834] 611-6 (1981).

[36] P.R. Anderson, "X-ray Photoelectron Spectroscopy of Sodium-Silicate Glasses", Am. Chem. Soc. Meeting, New York, 1973.

[37] R. Bruckner, H.-U. Chun, and H. Goretzki, "Photoelectron Spectroscopy (ESCA) on Alkali Silicate and Soda Aluminosilicate Glasses", Glastechn. Ber. 51[1] 1-7 (1978).

[38] B.W. Veal and D.J. Lam, "XPS Study of Sodium Oxide in Amorphous SiO_2", pp. 299-303 in The Physics of SiO_2 and Its Interfaces. Edited by S.T. Pantelides. Pergamon, New York, 1978.

[39] Y. Kaneko, "Application of Photoelectron Spectroscopy to Glasses", Yogyo-Kyokai-Shi, 86[7] 330-3 (1978).

[40] J.S. Jen and M.R. Kalinowski, "An ESCA Study of the Bridging to Non-Bridging Oxygen Ratio in Sodium Silicate Glass and the Correlations to Glass Density and Refractive Index", J. Non-Cryst. Solids, 38-39 21-6 (1980).

[41] D.J. Lam, A.P. Paulikas, and B.W. Veal, "X-ray Photoemission Spectroscopy Studies of Soda Aluminosilicate Glasses", J. Non-Cryst. Solids, 42[1-3] 41-8 (1980).

[42] R. Bruckner, H.-U. Chun, H. Goretzki, and M. Sammet, "XPS Measurements and Structural Aspects of Silicate and Phosphate Glasses", J. Non-Cryst. Solids, 42[1-3] 49-60 (1980).

[43] B.M.J. Smets and T.P.A. Lommen, "The Structure of Germanosilicate Glasses, Studied by X-ray Photoelectron Spectroscopy", J. Non-Cryst. Solids, 46[1] 21-32 (1981).

[44] B.M.J. Smets and T.P.A. Lommen, "The Incorporation of Aluminum Oxide and Boron Oxide in Sodium Silicate Glasses, Studied by X-ray Photoelectron Spectroscopy", Phys. Chem. Glasses, 22[6] 158-62 (1981).

[45] T. Sasaki, M. Kawaguchi, M. Yamane, and Y. Suginohara," On the Quantitative Analysis of O°, O^-, and O^{2-} Ions in Binary Silicate by X-ray Photoelectron Spectroscopy", J. Japan Inst. Metals, 45[8] 790-6 (1981).

[46] B.W. Veal, D.J. Lam, A.P. Paulikas, and W.Y. Ching, "XPS Study of CaO in Sodium Silicate Glasses", J. Non-Cryst. Solids, 49[1-3] 309-20 (1982).

[47] Y. Kaneko, H. Nakamura, M. Yamane, K. Mizoguchi, and Y. Suginohara, "Photoelectron Spectra of Silicate Glasses Containing Trivalent Cations", Yogyo-Kyokai-Shi 91[7] 321-4 (1983).

[48] W.Y. Ching, R.A. Murray, D.J. Lam, and B.W. Veal, "Comparative Studies of Electronic Structures of Sodium Metasilicate and α and β Phases of Sodium Disilicate", Phys. Rev., B28[8] 4724-34 (1983).

[49] W.Y. Ching, Y.P. Li, B.W. Veal, and D.J. Lam, "Electronic Structures of Lithium Metasilicate and Lithium Disilicate", Phys. Rev., B32[2] 1203-7 (1985).

[50] H. Wakabayashi, R. Terai, and H. Yamanaka, "Effects of Trivalent Oxides on Electrical Conductivity in Alkali Silicate Glasses", Yogyo-Kyokai-Shi, 93[4] 209-16 (1985).

[51] M.N. Alexander, P.I.K. Onorato, C.W. Struck, J.R. Rozen, G.W. Tasker, and D.R. Uhlmann, "Structure of Alkali (Alumino) Silicate Glasses. I. Tl^+ Luminescence and the Nonbridging Oxygen Issue", J. Non-Cryst. Solids, 79[1,2] 127-54 (1986).

[52] M.N. Alexander, P.I.K. Onorato, C.W. Struck, G.W. Tasker, and D.R. Uhlmann, "Structure of Alkali (Alumino) Silicate Glasses. II. Luminescence of Tl^+-doped Sodium Aluminosilicates", J. Non-Cryst. Solids, in press.

[53] W.H. Zachariasen, "The Atomic Arrangement in Glass", J. Am. Chem. Soc., 54[10] 3841-51 (1932).

[54] D. Turnbull, "Under What Conditions Can a Glass Be Formed?", Contemp. Phys., 10[5] 473-88 (1969).

[55] D.R. Uhlmann and H. Yinnon, "The Formation of Glasses", pp. 1-47 in Glass: Science and Technology (Glass-Forming Systems, Vol. 1). Edited by D.R. Uhlmann and N.J. Kreidl. Academic, New York, 1983.

[56] R.J. Bell and P. Dean, "The Structure of Vitreous Silica: Validity of the Random Network Theory", Phil. Mag., 25 1381-98 (1972).

[57] W.Y. Ching, "Theory of Amorphous SiO_2 and SiO_x. I. Atomic Structural Models", Phys. Rev., B26[12] 6610-21 (1982); "II. Electron States in an Intrinsic Glass", ibid., 6622-32.

[58] J.T. Randell, H.P. Rooksby, and B.S. Cooper, "The Structure of Glasses; The Evidence of X-ray Diffraction", J. Soc. Glass Technol., 14 219-29 (1930).

[59] N. Valenkov and E. Porai-Koshits, "X-ray Investigation of the Glassy State", Z. Kristallogr. 95[3,4] 195-229 (1936).

[60] B.E. Warren, "X-ray Determination of the Structure of Liquids and Glass", J. Appl. Phys., 8[10] 645-54 (1937).

[61] B.E. Warren and J. Biscoe, "The Structure of SiO_2 Glasses by X-ray Diffraction Studies", J. Am. Ceram. Soc., 21[2] 49-54 (1938).

[62] A.H. Narten, "Diffraction Pattern and Structure of Noncrystalline BeF_2 and SiO_2 at 25°C", J. Chem. Phys., 56[5] 1905-9 (1972).

[63] R. Bruckner, "Properties and Structure of Vitreous Silica. I", J. Non-Cryst. Solids, 5 123-75 (1970); "II" ibid., 177-216 (1971).

[64] L. Pauling, The Nature of the Chemical Bond; Chapter 3. Cornell University Press, Ithaca, New York, 1960.

[65] F. Liebau, Structural Chemistry of Silicates; Chapter 3. Springer-Verlag, Berlin, 1985.

[66] F.L. Galeener and A.C. Wright, "The J.C. Phillips Model for Vitreous SiO_2: A Critical Appraisal", Solid State Commun. 57[8] 677-82 (1986).

[67] K. Endell and H. Hellbrugge, Angew. Chem., 53[25-26] 271-3 (1940).

[68] J. O'M.Bockris, J.D. MacKenzie, and J.A. Kitchener, "Viscous Flow in Silica and Binary Liquid Silicates", Trans. Faraday Soc., 51 1734-48 (1955).

[69] W.H. Baur, "Bond Length Variation and Distorted Coordination Polyhedra in Inorganic Crystals"; pp. 129-55 in Transactions of the American Crystallographic Association (Vol. 6). Edited by W.R. Busing. 1970.

[70] W.H. Baur, "Interatomic Distance Predictions for Computer Simulation of Crystal Structures"; pp. 31-52 in Structure and Bonding in Crystals (Vol.II). Edited by M. O'Keeffe and A. Navrotsky. Academic Press, New York, 1981.

[71] W.H. Baur and T. Ohta, "The Si_5O_{16} Pentamer in Zunyite Refined and Empirical Relations for Individual Silicon-Oxygen Bonds", Acta Cryst., B38[2] 390-401 (1982).

[72] L. Pauling, "The Principles Determining the Structure of Complex Ionic Crystals", J. Am. Chem. Soc., 51[4] 1010-26 (1929).

[73] L. Pauling, The Nature of the Chemical Bond; Chapter 13. Cornell University Press, Ithaca, New York, 1960.

[74] I.D. Brown and R.D. Shannon, "Empirical Bond-Strength-Bond-Length Curves for Oxides", Acta Cryst., A29[4] 266-82 (1973).

[75] I.D. Brown, "Predicting Bond Lengths in Inorganic Crystals", Acta Cryst., B33[5] 1305-10 (1977).

[76] K. Suzuki and M. Ueno, "Experimental Discrimination between Bridging and Nonbridging Oxygen-Phosphorous Bonds in $P_2O_5 \cdot Na_2O$ Glass by Pulsed Neutron Total Scattering", J. de Physique, 46[12] C8-(261-5) (1985).

[77] Compare Ref. 30 vs. Ref. 76. In both studies, radial distribution functions are derived from measurements by neutron diffraction of the structure factor S(Q) up to very high values of the scattering vector $Q = 4\pi \sin\theta/\lambda \sim 400\ nm^{-1}$.

[78] J.B. Bates, "Dynamics of β-Quartz Structures of Vitreous SiO_2 and BeF_2", J. Chem. Phys., 56[5] 1910-7 (1972).

[79] D.A. McKeown, G.A. Waychunas, and G.E. Brown, Jr., "EXAFS and XANES Study of The Local Coordination Environment of Sodium in a Series of Silica-Rich Glasses", J. Non-Cryst. Solids, 74[2-3] 325-48 (1985).

[80] H.D. Blair and M.E. Milberg, "Structure of Thallium Silicate Glass", J. Am. Ceram. Soc., 57[6] 257-60 (1974).

[81] D.R. Uhlmann and A.G. Kolbeck, "Phase Separation and the Revolution in Concepts of Glass Structure", Phys. Chem. Glasses, 17[5] 146-58 (1976).

[82] R.J. Charles, "Metastable Liquid Immiscibility in Alkali Metal Oxide-Silica Systems", J. Am. Ceram. Soc., 49[2] 55-62 (1966).

[83] R.J. Charles, "Activities in Li_2O-, Na_2O-, and K_2O-SiO_2 Solutions", J. Am. Ceram. Soc., 50[12] 631-41 (1967).

[84] B.E.Warren and A.G. Pincus, "Atomic Consideration of Immiscibility in Glass Systems", J. Am. Ceram. Soc., 23[10] 301-4 (1940).

[85] F. Liebau, "The Influence of Cation Properties on the Conformation of Silicate and Phosphate Anions"; pp. 197-232 in Structure and Bonding in Crystals (Vol.II). Edited by M.O. O'Keeffe and A. Navrotsky. Academic Press, New York, 1981.

[86] S. A. Brawer and W.B. White, "Raman Spectroscopic Investigation of the structure of Silicate Glasses. I. The Binary Alkali Silicates", J. Chem. Phys. 63[6] 2421-32 (1975).

[87] T. Furukawa, K.E. Fox, and W.B. White, "Raman Spectroscopic Investigation of the Structure of Silicate Glasses. III. Raman Intensities and Structural Units in Sodium Silicate Glasses", J. Chem. Phys., 75[7] 3226-37 (1981).

[88] D.W. Matson, S.K. Sharma, and J.A. Philpotts, "The Structure of High-Silica Alkali-Silicate Glasses. A Raman Spectroscopic Investigation", J. Non-Cryst. Solids, 58[2,3] 323-52 (1983).

[89] C.M. Schramm, B.H.W.S. de Jong, and V.E. Parziale, "^{29}Si Magic Angle Spinning NMR Study on Local Silicon Environments in Armorphous and Crystalline Lithium Silicates", J. Am. Chem. Soc., 106[16] 4396-402 (1984).

[90] J.B. Murdoch, J.F. Stebbins, and I.S.E. Carmichael, "High-Resolution ^{29}SiNMR Study of Silicate and Aluminosilicate Glasses: The Effect of Network-Modifying Cations", Am. Mineral., 70[3,4] 332-43 (1985).

[91] I.A. Harris, Jr. and P.J. Bray, "Si^{29}NMR Spectra of Glasses and Polycrystalline Compounds in the System K_2O-SiO_2", Phys. Chem. Glasses, 21[4] 156-9 (1980).

[92] R. Dupree, D. Holland, P.M. McMilland, and R.F. Pettifer, "The Structure of Soda-Silica Glasses: A MAS NMR Study", J. Non-Cryst. Solids, 68 [2,3] 399-410 (1984).

[93] A.-R. Grimmer, M. Magi, M. Hahnert, H. Stade, A. Samoson, W. Wieker, and E. Lippmaa, "High Resolution Solid-State ^{29}Si Nuclear Magnetic Resonance Spectroscopic Studies of Binary Alkali Silicate Glasses", Phys. Chem. Glasses, 25[4] 105-9 (1984).

[94] R. Dupree, D. Holland, and D.S. Williams, "The Structure of Binary Alkali Silicate Glasses", J. Non-Cryst.Solids, 81[1-2] 185-200 (1986).

[95] P. McMillan, "Structural Studies of Silicate Glasses and Melts-Applications and Limitations of Raman Spectroscopy", Am. Mineral., 69[7,8] 622-44 (1984).

[96] J.V. Smith and C.S. Blackwell, "Nuclear Magnetic Resonance of Silica Polymorphs", Nature, 303[5914] 223-5 (1983).

[97] E. Dupree and R.F. Pettifer, "Determination of the Si-O-Si Bond Angle Distribution in Vitreous Silica by Magic Angle Spinning NMR", Nature, 308[5959] 523-5 (1984).

[98] S. Sasaki, Y. Takeuchi, K. Fujimo, and S. Akimoto, "Electron-Density Distributions of Three Orthopyroxenes, $Mg_2Si_2O_6$, $Co_2Si_2O_6$, and $Fe_2Si_2O_6$", Z. Kristallogr., 158[3,4] 279-97 (1982).

[99] Compare Fig. 1.5 in Chapter 1 and Fig. 2.10 in Chapter 2.

[100] R. Gresch, W. Muller-Waruth, and H. Dutz, "X-ray Photoelectron Spectroscopy of Sodium Phosphate Glasses", J. Non-Cryst. Solids, 34[1] 127-36 (1979).

[101] See Table 1.2 in Chapter 1.

[102] Heraeus-Amersil, Inc., Sayreville, N.J.

[103] Perkin-Elmer, Physical Electronics Division, Eden Prairie, MN.

[104] Estimate of NBO detection limit is established in Chapter 3.

[105] L.L. Hench, "Characterization of Glass Corrosion and Durability", J. Non-Cryst. Solids, 19, 27-39 (1975).

[106] G.W. Tasker, unpublished data.

[107] S.H. Garofalini and S.M. Levine, "Differences in the Surface Behavior of Alkali Ions in $Li_2O \cdot 3SiO_2$ and $Na_2O \cdot 3SiO_2$ Glasses", J. Am. Ceram. Soc., 68[7] 376-9 (1985).

[108] R. Weichert and K. Schonert, "On the Temperature Rise at the Tip of a Fast Running Crack", J. Mech. Phys. Solids, 22, 127-33 (1974).

[109] R. Weichert and K. Schonert, "Heat Generation at the Tip of a Moving Crack", J. Mech. Phys. Solids, 26[3] 151-61 (1978).

[110] J.T. Dickinson, E.E. Donaldson, and M.K. Park, "The Emission of Electrons and Positive Ions from Fracture of Materials", J. Mater. Sci., 16[10] 2897-908 (1981).

CHAPTER 3

STRUCTURE OF ALKALI ALUMINOSILICATE GLASSES: XPS OF SODIUM ALUMINOSILICATE GLASSES

3.1. INTRODUCTION :

The structural role of aluminum atoms in R_2O-Al_2O_3-SiO_2 (RAS) glasses, where R_2O is an alkali oxide, has long been a subject of scientific interest and debate. Apart from the commercial, technological, and geologic importance of RAS glasses themselves, the addition of Al_2O_3 in small amounts to other silicate glass compositions is known to improve chemical durability, to suppress phase separation, and to limit devitrification [1]. Substantial conflicts exist, however, among models describing the structural and chemical environments of aluminum atoms in RAS glasses not only for $Al/R>1.0$ but also for $Al/R\leq1.0$. Much of this controversy originates from the observation that aluminum atoms typically exhibit oxygen coordination numbers of 4 and 6 in crystalline aluminosilicate compounds [2-7].

The cation-to-anion radius ratio for aluminum octahedrally coordinated by oxygen is $\sim$0.4 [8]. This value is near the critical ratio of 0.414 which, in a hard sphere approximation for ions, marks the transition from stable tetrahedral to stable octahedral coordination of anions about a central cation [9]. Accordingly, aluminum atoms in aluminosilicate crystals are commonly found in tetrahedral (Al^{IV}) groups--e.g., albite ($NaAlSi_3O_8$) [2] and nepheline ($NaAlSiO_4$) [3]; in octahedral (Al^{VI}) groups--e.g., jadeite ($NaAlSi_2O_6$) [4] and kyanite (Al_2SiO_5) [5]; or, in both Al^{IV} and Al^{VI} coordinations at different lattice sites--e.g., mullite ($Al_6Si_2O_{13}$) [6] and sillimanite (Al_2SiO_5) [7]. While much more rare in occurrence, aluminum atoms have also been observed in hexahedral (Al^{V}) groups--e.g., andulusite (Al_2SiO_5) [10]. Since aluminum atoms can display multiple oxygen coordinations in aluminosilicate crystals, a similar flexibility in coordination schemes has often been hypothesized for RAS glasses.

Structural models for RAS glasses have mostly been advanced in the past as ad hoc rationalizations of changes in various physical properties with glass composition (e.g., density vs. Al/R). In glasses with $Al/R \leq 1.0$, Al^{IV} groups are generally accepted to substitute isomorphically for $SiO_{4/2}$ tetrahedra with the aluminum atoms acting as network formers. However, some models maintain that a fraction of the aluminums reside in Al^{VI} sites with structural roles of either network formers or network modifiers. For glasses with $Al/R > 1.0$, the structural conceptions are often more complex. If the aluminums in excess of alkali atoms exist in Al^{IV} sites, they are believed to act as network formers; but, aluminums in Al^{VI} groups have been suggested to function either as network formers, network modifiers, or as interstitial charge compensators.

Considering the implications of the above models for the bonding of oxygen atoms in RAS glasses, it is apparent that the relative numbers of bridging oxygens (BO's) and nonbridging oxygens (NBO's) are affected by the mechanism for incorporation of aluminum atoms. Therefore, an empirical knowledge of how the fraction of NBO's, f_{NBO}, varies in a series of RAS glasses over $0 \lesssim Al/R \lesssim 1.5$ would, in theory, clarify the structure of these glasses.

As discussed in Chapter 2, determinations of f_{NBO} for R_2O-SiO_2 (RS) glasses [11-18] by X-ray photoelectron spectroscopy (XPS) have agreed reasonably well with theory (especially for mole fractions of alkali oxide $X_R \lesssim 0.30$). However, previous XPS measurements of f_{NBO} for RAS glasses, as typified by Na_2O-Al_2O_3-SiO_2 (NAS) glasses [12,14,19-22], have been controversial. Two different dependencies of f_{NBO} on Al/Na have been reported; but neither can adequately account for the maximum, minimum, or discontinuity in many physical properties which occur at Al/R=1.0-1.2.

In the present Chapter, photoemission spectra for three series of NAS glasses are considered for the purpose of amending what are viewed as discrepant structural interpretations in prior XPS work. The compositions selected for this study are the following: (1) constant optical basicity ($\Lambda=0.57$) with $0\leq Al/Na\leq 1.5$; (2) constant mole fraction SiO_2 ($X_{Si}=0.67$) with $0\leq Al/Na\leq 1.5$; and (3) Al/Na=1.0 including vitreous analogues to albite (Ab), jadeite (Jd), and nepheline (Ne). Spectra for these glasses were acquired from vacuum-fractured surfaces and corrected for electrostatic charging effects by the biased metal-dot (BMD) method, as described in Chapter 1. An analysis of these spectra was facilitated using insights gained in Chapter 2 into the way physicochemical characteristics of simpler Na_2O-SiO_2 (NS) glasses are reflected in XPS results. This experimental and analytical approach has afforded a better understanding of the structural role of aluminum atoms in RAS glasses below and above the equivalence point of Al/R=1.0. Furthermore, the conclusions of this XPS study fully support the structural interpretation of a parallel study by optical luminescence spectroscopy [23,24] of thallium-doped NAS glasses with constant optical basicity ($\Lambda=0.57$) for $0.42\leq Al/Na\leq 1.1$.

This Chapter proceeds according to the following plan. In Section 3.2, models and structural studies of RAS glasses are first reviewed and then conclusions of prior XPS investigations on NAS glasses are described. The preparation of samples and procedures for data acquisition and analysis in the present XPS study are given in Section 3.3. In Section 3.4, curve fitting analyses of individual O 1s spectra for some 20 different NAS compositions are first presented. Additional photoemission results for the O 1s, Si 2p, Al 2p, and Na 1s core levels of these glasses are then described. The Section concludes with a test of structural models for RAS glasses in two compositional regions, Al/Na$\leq$1.0 and Al/Na$>$1.0. The compatibility of the present XPS results with various structural models for RAS glasses is discussed in Section 3.5. Also, some observations are made regarding the generality of the structural conclusions of this work and their implications for theories about glass structure and structure-property relationships. Finally, the principal findings of this investigation are summarized in Section 3.6.

3.2. LITERATURE SURVEY:

3.2.1. Structural Models for R_2O-Al_2O_3-SiO_2 Glasses

The classical model for the structure of RAS glasses with $Al/R \leq 1.0$ holds that all silicon and aluminum atoms are tetrahedrally coordinated with oxygen atoms and act as network formers. The Al^{IV} groups are fully connected through BO's to neighboring tetrahedral centers; whereas some portion of the Si^{IV} groups are not fully connected for $Al/R<1.0$ due to NBO's associated with the latter. Alkali ions are thought to occupy the following two types of sites: those of network modifiers ($\equiv Si\text{-}O^-R^+$) which break up the connectivity of the random aluminosilicate network by creating NBO's bonded to silicon atoms, and those of charge compensators for Al^{IV} groups,

$$R_2O + Al_2O_3 \rightarrow 2R^+(AlO_{4/2})^-, \tag{3.1}$$

which maintain local charge neutrality. Thus, starting with an RS glass (e.g., $R_2O{\cdot}3SiO_2$) and systematically increasing the ratio of Al/R, BO's are formed with the concomitant elimination of NBO's up to the equivalence point of $Al/R=1.0$. At that composition, NBO's no longer exist in the glass structure and all tetrahedral centers are fully connected by BO's in a continuous random network. According to the classical model, if X_{Si}, X_{Al}, and X_R are the mole fractions of SiO_2, Al_2O_3, and R_2O, the theoretical fraction of NBO's in glasses with $Al/R \leq 1.0$ and $X_{Si} \gtrsim 0.50$ is given by

$$f_{NBO}(\text{theo}) = \frac{2X_R - 2X_{Al}}{2X_{Si} + 3X_{Al} + X_R}; \tag{3.2}$$

and the average number of NBO's bonded to a silicon atom can be computed by

$$n(\text{theo}) = < \frac{NBO}{Si} > = \frac{2X_R - 2X_{Al}}{X_{Si}}. \tag{3.3}$$

For RAS glasses, one reasonably expects the compositional dependencies of many physical properties to be strongly correlated with variations in f_{NBO}. A large body of published data supports the traditional model by showing that an extremum or discontinuity in some property, measured for a series of glasses with $0 \lesssim Al/R \lesssim 2.0$, occurs at Al/R=1.0-1.2 [23-42]. Typical results for density vs. Al/Na of Day and Rindone [28] and viscosity isokoms near the glass transition range vs. Al/Na of Taylor and Rindone [34] for two series of NAS glasses are reproduced in Fig. 3.1. As Al/Na increases from zero to unity, the densities for both series of glasses in Fig. 3.1(b) decrease to a minimum. This indicates the formation of a progressively more open glass structure with increasing Al_2O_3 content. Over the same range of Al/Na, the viscosity isokoms for these glasses in Figs. 3.1(c) and (d) increase slowly at first and then quite sharply as the equivalence point is approached. These trends in the densities and viscosity isokoms are explained by the classical model as manifestations of a gradual replacement of NBO's by BO's in the glasses with increasing Al/Na such that $f_{NBO} \to 0$ at Al/Na=1.0.

Observations that many physical properties have extrema or discontinuities at Al/R=1.1-1.2 rather than exactly at Al/R=1.0 (cf Figs. 3.1(b) vs. (c) and (d)), while some properties also have extrema at $0.3 \lesssim Al/R \lesssim 0.5$ have prompted several modifications to the traditional model. Values of Al/R where various physical properties of RAS glasses have been reported to display extrema or discontinuities are summarized in Table 3.1.

The alternative theories [38-40, 43] propose that a large fraction of aluminum atoms are incorporated in Al^{VI} groups at small Al/R with the ratio of octahedral-to-tetrahedral sites, Al^{VI}/Al^{IV}, decreasing at larger

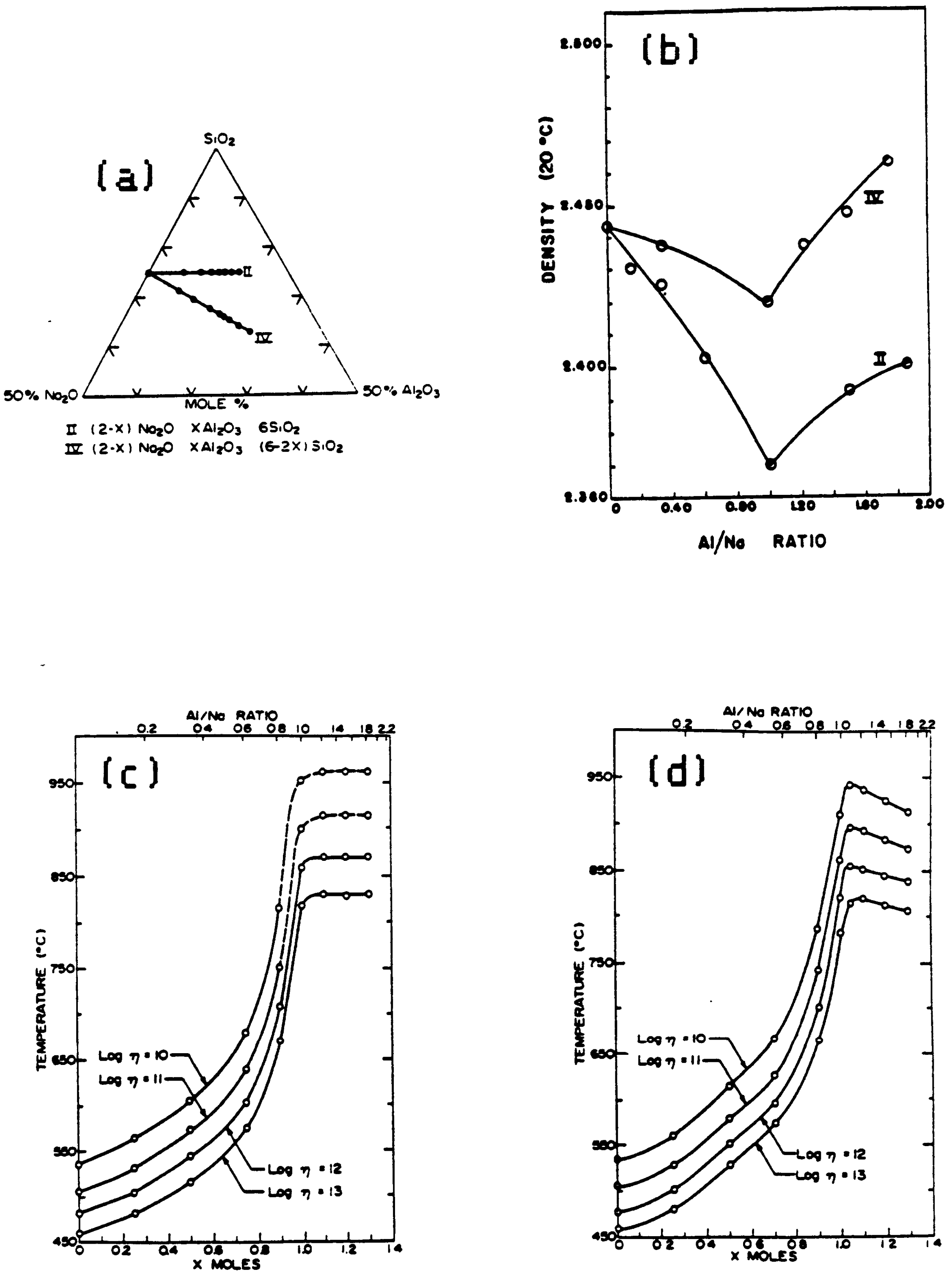

Fig. 3.1: Variation of selected physical properties of NAS glasses: (a) compositional lines; (b) density vs. Al/Na for Series II and IV; (c) viscosity isokom temperatures vs. Al/Na for Series II; and (d) viscosity isokom temperatures vs. Al/Na for Series IV. Figures taken from Refs. 28 and 34.

Table 3.1: Variation in Physical Properties of RAS Glasses with $0 \le Al/R \le 2.0$

Property	Al/R		
	Maximum	Minimum	Discontinuity
density	-	1.0(a,c)[28], ≥1.0(a)[36], 1.2(a)[39]	1.0(a)[41]
refractive index	-	1.0(a)[25], 1.0(a)[28] 1.1(a)[38], 1.2(a)[39], 1.0(a)[41]	1.0(b)[25], 1.0(b)[27] 1.0(b,c)[28], 1.1(b)[38]
viscosity (T_g or 10^{10}-10^{13} poise isokom temperature)	1.1(c)[23], 1.2(a)[34] 1.1(c)[34], 1.1(a,b)[38], 1.2(a)[39]	-	-
activation energy, ionic conductivity	0.2(b*)[26],0.3(c)[33], 0.2(b*)[35],0.5(a)[39], 0.4(b*)[42]	1.0(b)[26], 1.0(a)[32], 1.0(c)[33], 1.0(b)[35], 1.2(a)[39]	-
activation energy, alkali diffusion	0.3(c)[33]	1.0(a)[30], 1.0(c)[33]	-
activation energy, helium permeation	-	1.0(a)[36], ≥ 1.0(a)[37]	-

---

(a) series of glasses with $X_{Si} \approx$ constant
(b) series of glasses with $X_R \approx$ constant
(c) other
* near compositional transition from two-phase to single-phase morphology
[ ] reference

Al/R. Several workers [38,42,43] assert aluminums in Al^{VI} coordination act as network modifiers,

$$Al_2O_3 + 3(\equiv Si\text{-}O\text{-}Si\equiv) \rightarrow 2(\equiv Si\text{-}O^-)_3Al^{3+} \ . \qquad (3.4)$$

Here, each aluminum atom is presumedly associated with three NBO's and an equal number of neutral BO's shared between neighboring Si^{IV} and Al^{IV} sites. Yoldas [43] has concluded that mainly Al^{VI} groups exist for $Al/(Na+2Ca) \lesssim 0.01$ in his study of small additions of Al_2O_3 to a Na_2O-CaO-SiO_2 glass. Shelby and Piguet [38,42] suggest that Al^{VI} groups are present in RAS glasses for all Al/R, although Al^{VI}/Al^{IV} and hence f_{NBO} pass through a minimum at Al/R=1.1-1.2.

In contrast, Hunold and Bruckner [39,40] imply aluminums in Al^{VI} coordination function essentially as network formers,

$$3R_2O + Al_2O_3 \rightarrow 2R_3^+ (AlO_{6/2})^{-3}, \qquad (3.5)$$

but indicate the Al^{VI}-O bond is weaker than the Al^{IV}-O bond. In this role, however, an Al^{VI} group is three times more efficient than an Al^{IV} group in converting alkali ions from network modifiers to charge compensators (cf Eq. (3.5) vs. Eq. (3.1)). One thus expects $f_{NBO} \rightarrow 0$ at some Al/R<1.0. Beyond that point, additional aluminum atoms are said to enter the glass structure such that Al^{VI}/Al^{IV} is at a minimum for $Al/R \sim 1.2$. However, mechanisms by which Al^{IV} and Al^{VI} groups can be accommodated with local charge neutrality being preserved in the absence of available alkali ions are not specified by Hunold and Bruckner. Stoichiometrically feasible mechanisms for the incorporation of excess aluminums in glasses with Al/R>1.0 are described below.

The measurements by Hunold and Bruckner [39,40] of various physical properties in the series of glasses $(0.33-x)Na_2O \cdot xAl_2O_3 \cdot 0.67SiO_2$ seem to give strong support to models advocating a major structural change at Al/R=1.1-1.2, since most of their results exhibit distinct maxima, minima, or discontinuities at Al/Na$\sim$1.2 (Table 3.1). However, a comparison of data from other sources [25,28,36] for the density and refractive index of the Jd glass at Al/Na=1.0 suggests an error in chemical analysis may be responsible for the extrema or discontinuities appearing to occur at Al/Na$\sim$1.2 rather than closer to the equivalence point.

While many workers accept the classical model as an appropriate description for the structure of RAS glasses with Al/R$\leq$1.0 [23,24,26-35,37,41], no concensus exists about the atomic arrangement of glasses with Al/R>1.0. Most structural models adhere to a view that some if not all aluminum atoms in excess of alkali atoms are accommodated in Al^{VI} groups. Isard [26] and Klonkowski [41] envision the role of aluminums in Al^{VI} groups as network modifiers (see Eq. (3.4)) which introduce NBO's and thus reduce the connectivity of the aluminosilicate network. On the contrary, Taylor and Rindone [34] suppose one of every four aluminums in excess of alkali occupy Al^{VI} sites as an interstitial (i.e., non-bonded) charge compensator for three neighboring Al^{IV} groups which function as network formers,

$$2Al_2O_3 \rightarrow Al^{+3}\ (AlO_{4/2})_3^- \ . \qquad (3.6)$$

This bonding arrangement is depicted in Fig. 3.2(a). In its favor, this configuration is electrostatically balanced and maintains the continuity of the network in correspondence with the asymmetry of the viscosity isokoms about Al/Na=1.0 for the NAS glasses in Figs. 1.1(c) and (d). However, the notion that aluminum atoms can function as charge compensators

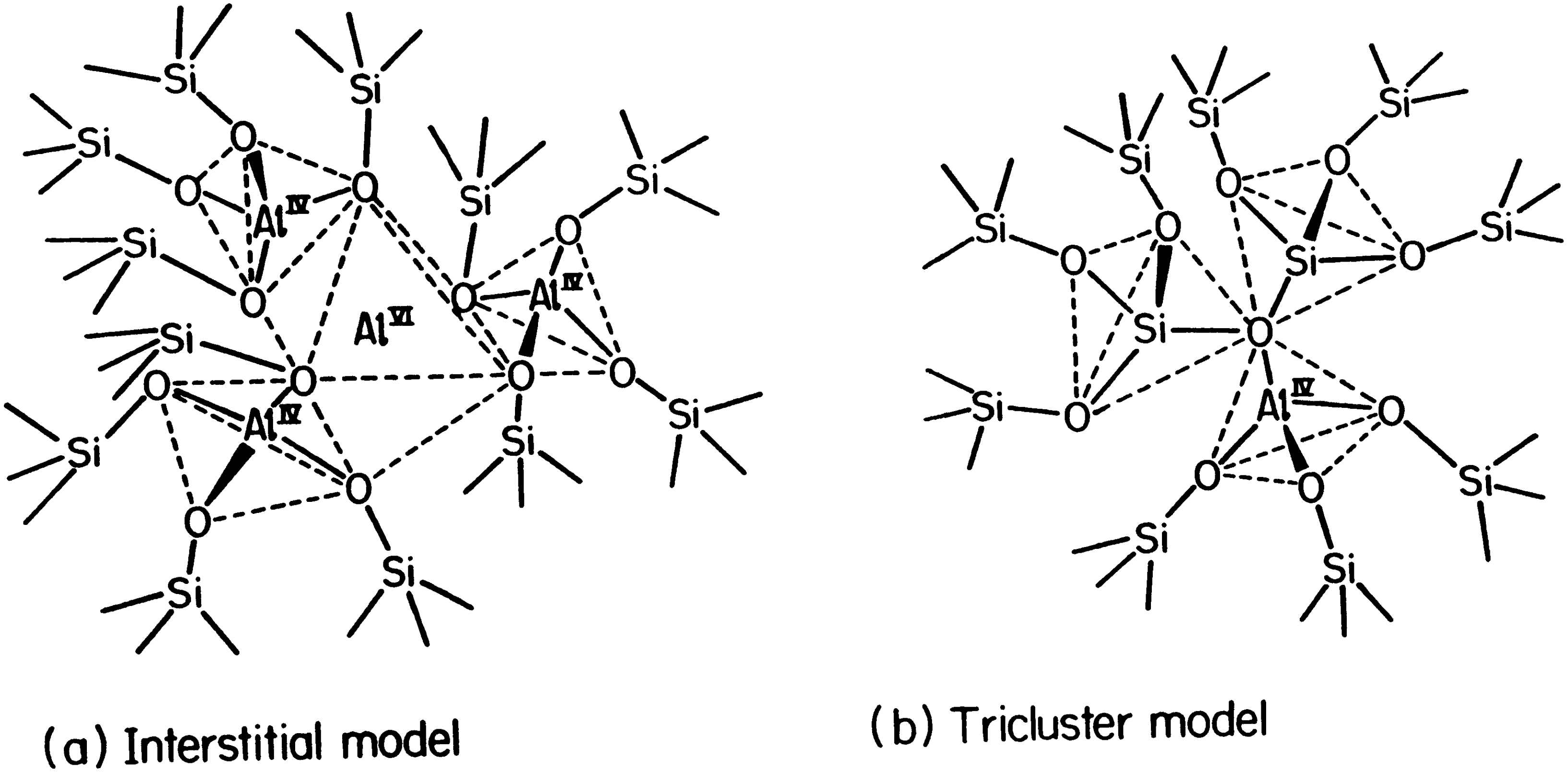

(a) Interstitial model

(b) Tricluster model

Fig. 3.2: Bonding configurations proposed for all glasses with Al/Na>1.0:
(a) interstitial model of Taylor and Rindone [34], and
(b) tricluster model of Lacy [44].

or network modifiers in addition to being capable network formers presumes the chemical nature of such atoms is amphoteric to an extent that is probably unrealistic.

Although Lacy [44] does not rule out the possibility of aluminum atoms in Al^{VI} sites acting as network formers for Al/R<1 (see Eq. (3.5)), he reasons that such sites are unlikely to exist at Al/R>1 primarily because of constraints on stoichiometry. Moreover, he argues that prohibitive oxygen packing densities inveigh against aluminums existing as interstitial cations in either Al^{IV} or Al^{VI} sites (e.g., see Fig. 3.2(a)). Instead, Lacy proposes that aluminums are incorporated at Al/R>1 in "triclusters" of one Al^{IV} group and two Si^{IV} groups,

$$4SiO_2 + Al_2O_3 \rightarrow 2(AlSi_2O_{5.5}), \qquad (3.7)$$

where one oxygen is common to the three tetrahedra. This bonding arrangement is illustrated in Fig. 3.2(b). Electrostatic stability is attained in this configuration since the formation of a pair of triclusters conserves one oxygen relative to the oxygen demand of a 4-2 coordination network. The average sum of the bond strengths for all oxygen anions coordinating the aluminum (2.75 + 3(1.75)/4) in Fig. 3.2(b) thus equals 2.0 in accord with the extended electrostatic valence rule (see Section 2.2.2). Furthermore, triclusters confer a higher oxygen packing density (15 oxygens about each Al^{IV} and Si^{IV} group in a tricluster) than the 4-2 coordination network at Al/R=1.0 of the classical model (12 oxygens about every Al^{IV} and Si^{IV} group) while maintaining the full connectivity of the network at Al/R>1.0. These structural characteristics are consistent with the increase in densities in Fig. 3.1(b) and the invariant or slowly changing viscosity isokoms in Figs. 3.1(c) and (d) for the NAS glasses as Al/Na increases above unity.

Studies by X-ray diffraction [45] for the series of glasses $xNa_2O \cdot xAl_2O_3 \cdot (1-2x)SiO_2$ where x=0, 0.125, 0.167, and 0.250 show that the first correlation in the radial distribution function shifts in the order of 0.162, 0.163, 0.164, and 0.167 nm as $NaAlO_2$ replaces SiO_2. This trend is explained by a progressive substitution of Al^{IV} groups for Si^{IV} groups, where individual Si^{IV}-O and Al^{IV}-O correlations at ∿0.162 nm and ∿0.175 nm are not resolved. There is no evidence of an Al^{VI}-O correlation at ∿0.190 nm in any of these NAS glasses with Al/Na=1.0 in agreement with the traditional model for the structure of RAS glasses.

In X-ray emission spectroscopy (XES), $\Delta 2\theta$ for the Al Kα emission line from oxide systems measured relative to aluminum metal primarily corresponds to the mean Al-O distance of Al groups [46]. With a suitable choice of standards, however, an indication of the average coordination number for aluminum atoms can be deduced with this technique. The results of XES investigations [28,47-51] for various series of NAS glasses are gathered in a plot of $\Delta 2\theta$ vs. Al/Na for Fig. 3.3. Aside from the early study of Day and Rindone [28], a significant shift in $\Delta 2\theta$ is not observed from the values recorded for the Al^{IV} standard, microcline ($KAlSi_3O_8$), in glass compositions on either side of Al/Na=1.0. Day and Rindone and later Taylor and Rindone [34] were led to conclude that at least some aluminum atoms occupy Al^{VI} sites in compositions with Al/Na>1.0 on the basis of the shift in their data [28] toward the position of the Al^{VI} standard, corundum (Al_2O_3). However, the more recent studies indicate that only Al^{IV} groups are present in glasses over the range of $0.5 \lesssim Al/Na \lesssim 2.0$. The majority

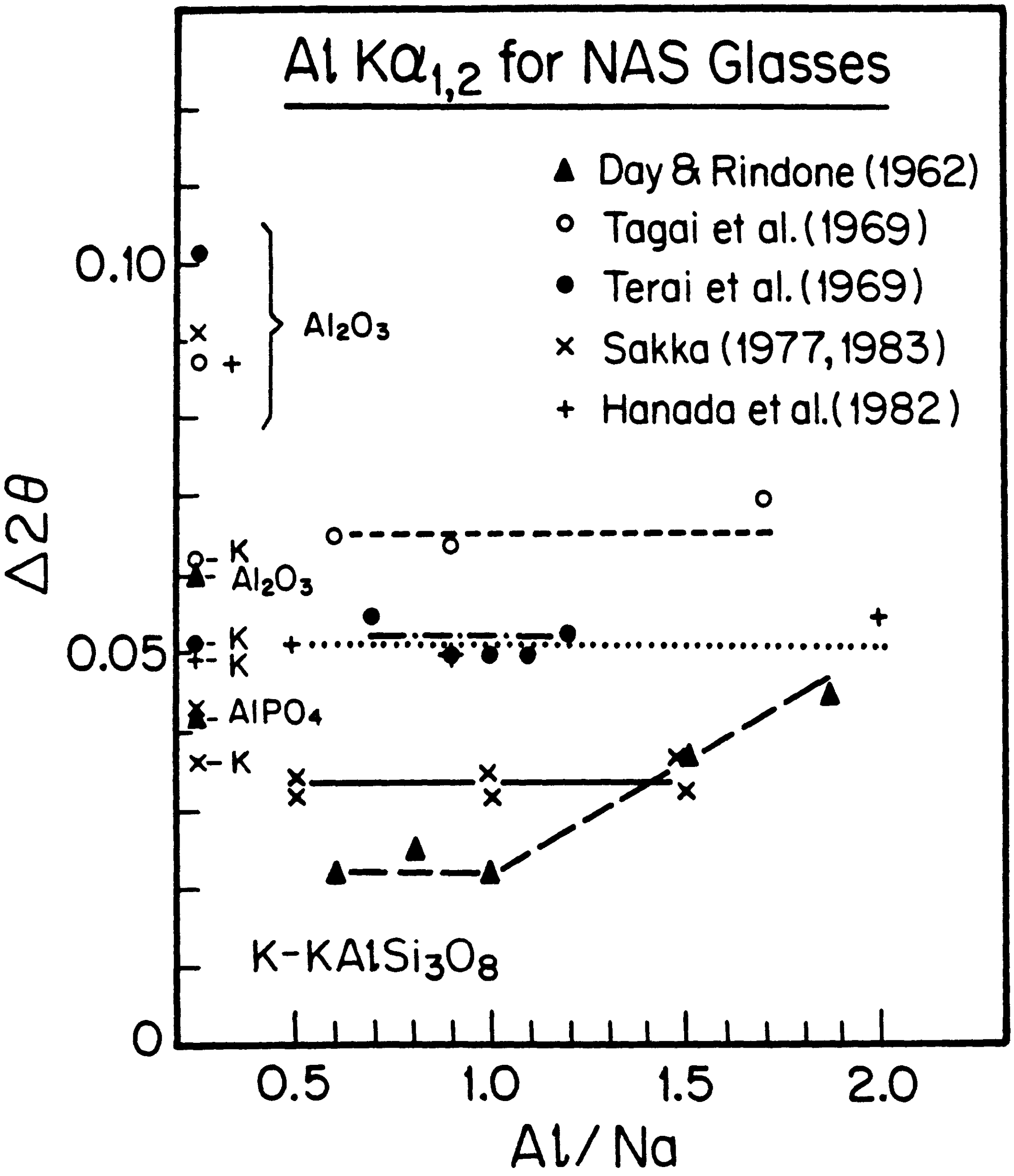

Fig. 3.3: Al Kα-XES results for various series of NAS glasses. Data from Refs. 28 and 47-51.

of the data in Fig. 3.3, thus tends to support the classical model for Al/R$\leq$1.0 and Lacy's tricluster model for Al/R>1.0. Finally, Hanada et al. [51] did report a sizable shift in Δ 2θ for glasses with substantially larger values of Al/Na than considered in Fig. 3.3. The detection of Al^{VI} groups in highly aluminous compositions could be expected for reasons developed later in this Chapter.

The structural role of aluminum atoms in RAS glasses has been extensively investigated by Raman spectroscopy [52-59]. For NAS glasses with Al/Na<0.2, Brawer and White [52] proposed that aluminum atoms reside in both Al^{IV} and Al^{VI} groups as network formers and modifiers, respectively, where Al^{VI}/Al^{IV} is a function of glass composition. To the contrary, the general opinion of later work [53-59] is that aluminums enter the glass structure according to the classical model for Al/Na$\leq$1.0. One finds the interpretation of Raman spectra is complicated by an ongoing argument [53-56, 59] over structural assignments for the high frequency (800-1250 cm^{-1}) vibrational modes. Moreover, structural inferences are often derived from speculative fitting analyses of complex spectral envelopes. In view of these limitations, information about atomic arrangement of RAS glasses from Raman studies is rather qualitative at present; and therefore many interpretations based on such data should be regarded as conjectural.

In nuclear magnetic resonance (NMR), an atomic nucleus with a non-zero spin serves as a sensitive probe of the local structural environment for the atom. While ^{27}Al magic angle spinning (MAS) NMR can distinguish between Al^{IV} and Al^{VI} sites in crystalline aluminosilicates [60, 61], difficulties arise when this technique is applied to RAS glasses. Except for compositions with small Al/R, ^{27}Al MAS NMR does not sample all aluminum nuclei due to an apparent increase in the fraction of aluminum atoms with distorted coordination polyhedra at larger Al/R [61, 62]. For NAS glasses with small Al/R, virtually all aluminums are indicated to have Al^{IV} coordination [62,63]. In RAS glasses with Al/R=1.0, the fraction of aluminums which do contribute to a narrowed MAS resonance also have Al^{IV} coordination [61,62]. Although the presence or absence of Al^{VI} groups at Al/R=1.0 cannot be established by ^{27}Al MAS NMR, the existence of only Al^{IV} groups at small Al/R is antagonistic to several structural models [38-40, 43] which suggest Al^{VI}/Al^{IV} is at a maximum for such compositions.

X-ray absorption near edge structure (XANES) and extended X-ray absorption fine structure (EXAFS) have recently been used by McKeown et al. [64,65] to elucidate the oxygen coordinations of aluminum and sodium atoms in NAS glasses. Al-XANES spectra for aluminosilicate crystals and a series of NAS glasses ($X_{Si}=0.75$) with Al/Na=0.28, 1.00, 1.26, and 1.61 are reproduced in Fig. 3.4. Whereas the crystalline standards containing Al^{VI} groups (sillimanite, jadeite, and corundum) have two edge maxima at 1568 eV and 1572 eV, the standards with only Al^{IV} groups (nepheline and albite) exhibit just one edge maximum at 1566 eV, as seen in Fig. 3.4(a). Each NAS glass in Fig. 3.4(b) has a single edge maximum near 1566 eV. Other spectra for Jd glass and Ne glass were similar to that of Ab glass in Fig. 3.4(b). Al-EXAFS results for Jd glass, Ab glass, and the glass with Al/Na=1.61 yielded Al-O distances close to 0.177 nm. From this compelling evidence, McKeown et al. concluded that the aluminum atoms are present in Al^{IV} coordination for all NAS glasses characterized in their study. These findings are therefore in accord with the classical model of RAS glasses for $Al/R\leq1.0$ and with the tricluster model for Al/R>1.0. A comparison

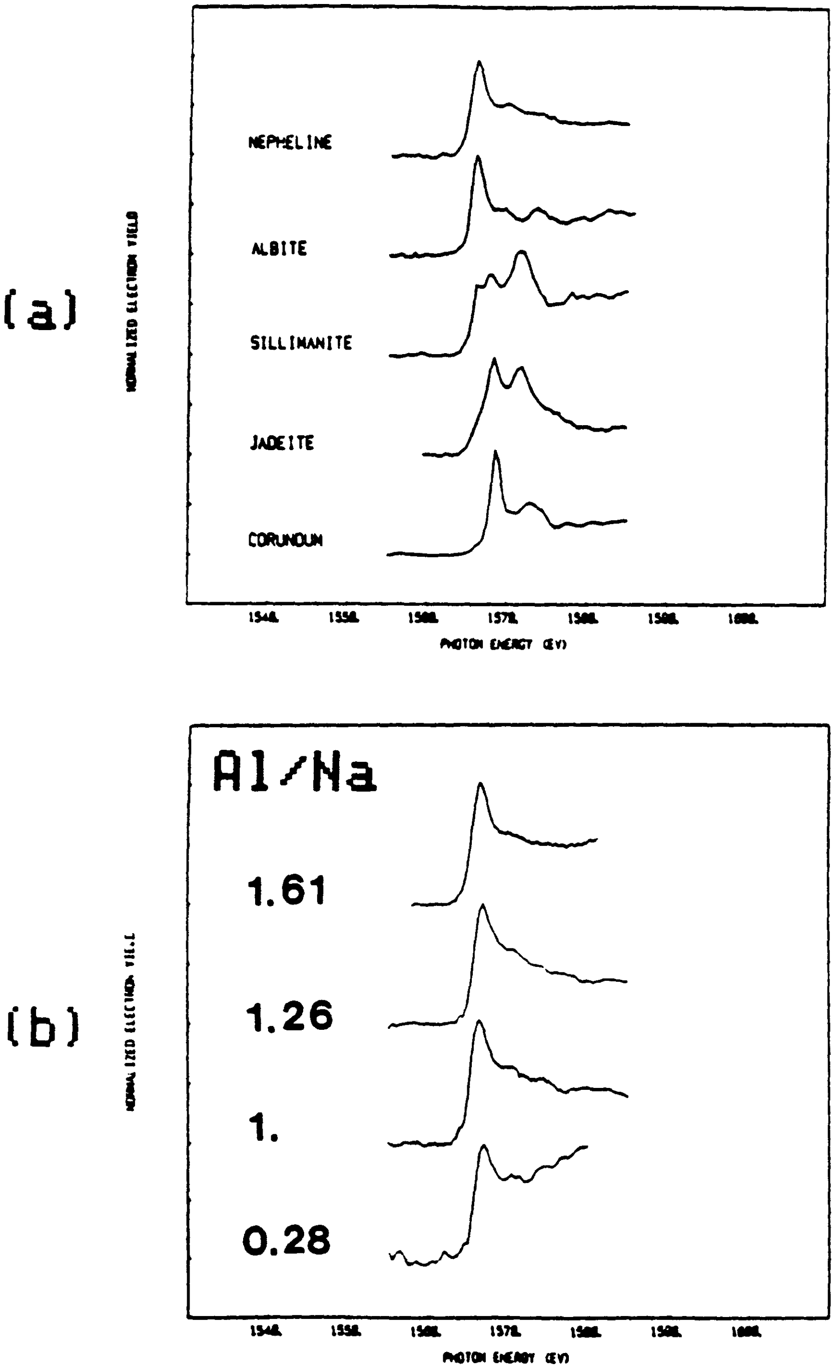

Fig. 3.4: Al-XANES results: (a) for aluminosilicate crystalline compounds, and (b) for NAS glasses with X_{Si}=0.75. Figures taken from Ref. 65.

of Na-XANES and Na-EXAFS spectra for the series of NAS glasses (X_{Si}=0.75), crystalline and vitreous nepheline, and $Na_2O\cdot 2SiO_2$ glass suggested that little if any variation occurs in the number of oxygen atoms (∿5-7) coordinating sodium atoms among these samples.

Optical luminescence spectra for a series of thallium-doped NAS glasses with constant optical basicity (Λ=0.57) have been measured in a study by Alexander et al. [23,24] which compliments the present XPS investigation of similar but undoped glasses. In that work, it was reasonably assumed that thallium ions, as optically active structural probes, are analogous to sodium ions in NAS glasses. The luminescence results indicate that thallium ions reside in both modifier sites ($\equiv Si\text{-}O^{-}Tl^{+}$) and charge compensator sites ($Tl^{+}(AlO_{4/2})^{-}$) for Al/Na<1.0. Furthermore, the ratio of ($\equiv Si\text{-}O^{-}Tl^{+}$)/($Tl^{+}(AlO_{4/2})^{-}$) sites is found to decrease systematically with Al/Na to zero at the equivalence point. For Al/Na≥1.0, thallium ions are only present unperturbed charge compensator sites. These results thus provide additional support for the traditional model of RAS glasses with Al/Na≤1.0; and, they imply that thallium (and alkali) ions are not greatly affected by the incorporation of excess aluminum atoms above the equivalence point.

In addition, a molecular dynamics (MD) simulation of NAS glasses [66] suggests that aluminum atoms prefer Al^{IV} sites for 0<Al/Na≤2.0; and oxygen atoms show an increased tendency for bonding to three tetrahedral centers for Al/Na>1.0. These results can also be interpreted in terms of the traditional model for Al/R≤1.0 and the tricluster model for Al/R>1.0.

Finally, the chemical nature of oxygen bridges between aluminum and silicon polyhedral centers in RAS glasses is another important structural consideration. According to the aluminum avoidance principle [67], Al^{IV}-O-Al^{IV} linkages are electrostatically unstable such that the reaction,

$$(\equiv Si\text{-}O\text{-}Si\equiv) + (\equiv Al\text{-}O\text{-}Al\equiv) \rightarrow 2(\equiv Al\text{-}O\text{-}Si\equiv), \qquad (3.8)$$

is favored. While the generality of this concept has been questioned [61,68], a study by ^{29}Si MAS NMR [69] of the series of glasses $xNa_2O \cdot xAl_2O_3 \cdot (1-2x)SiO_2$ where x = 0, 0.125, 0.167, and 0.250 has concluded that the aluminum avoidance rule is largely obeyed for these compositions.

From this review of structural studies on RAS glasses by X-ray diffraction, XES, Raman spectroscopy, NMR, XANES, EXAFS, optical luminescence spectroscopy, and MD, it is clear that the evidence weighs heavily in favor of the classical model for $Al/R \leq 1.0$ and it is not inconsistent with Lacy's tricluster model for $Al/R > 1.0$. However, previous XPS investigations of NAS glasses have produced structural interpretations which are in substantial disagreement with these models--most obviously for compositions with $Al/Na \leq 1.0$. The methods and conclusions of these photoemission studies are described in the following subsection.

3.2.2. Photoemission Studies of Na_2O-Al_2O_3-SiO_2 Glasses

The series of NAS glass compositions examined in earlier XPS studies [12,14,19-21] are given in Fig. 3.5. Consider first the composite sets of O 1s core level spectra of Bruckner et al. [12,14] (BCGS) and Smets and Lommen [20] (SL) for vacuum-fractured glasses which are reproduced in Fig. 3.6. Binding energies for each set of spectra were arbitrarily normalized to the position of the main component, the "bridging oxygen peak". This BO component was said to contain unresolved contributions from bridging (Si-O-Si), (Al-O-Si), and (Al-O-Al) bonds in order of decreasing binding energy. An NBO ($Si\text{-}O\text{-}\Sigma_j Na_j$) component is partially resolved at binding

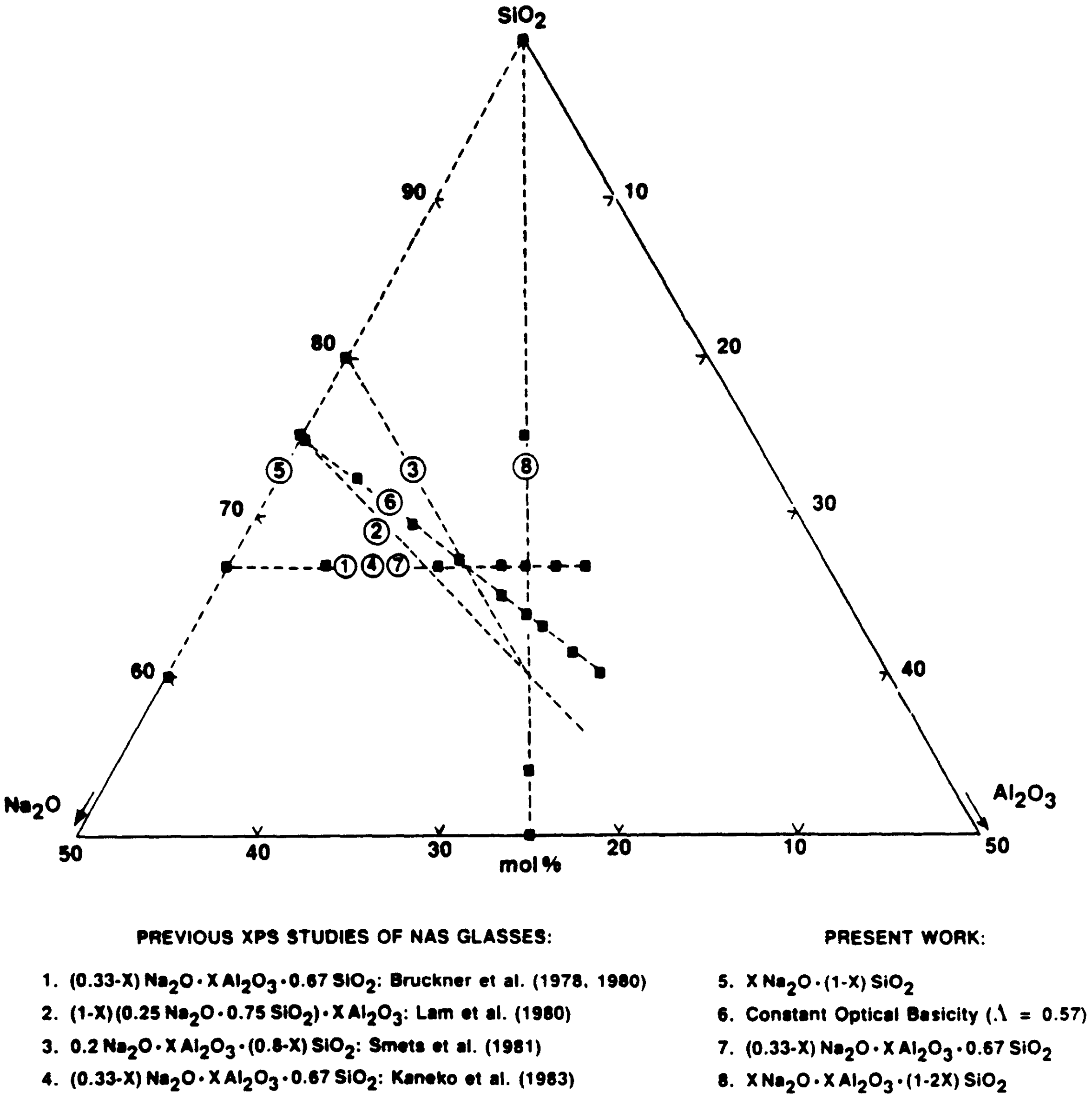

Fig. 3.5: Compositional lines of earlier and present XPS studies of NAS glasses. Batch compositions of present work are indicated by solid squares.

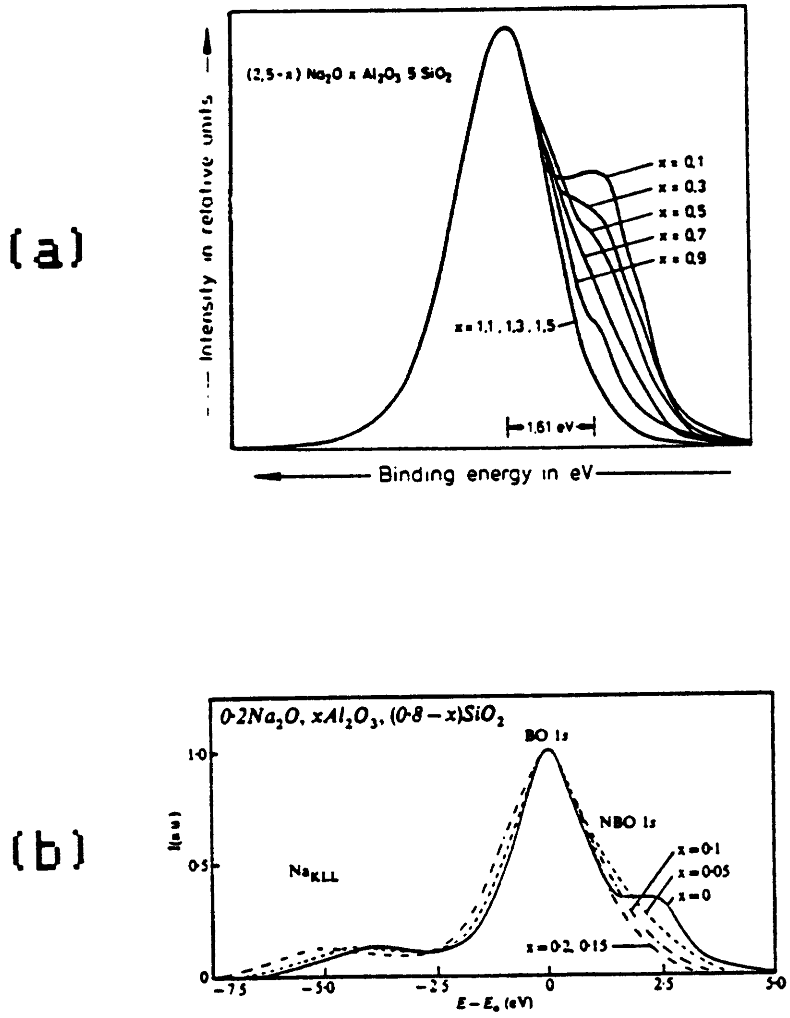

Fig. 3.6: Composite spectra of O 1s core level for vacuum-fractured NAS glasses: (a) Bruckner et al. [12] with Mg Kα excitation, and (b) Smets and Lommen [20] with Al Kα excitation.

energies ~ 2 eV lower than the BO component. SL reported that the width of the "BO peak" broadens and the energy separation between the BO and NBO components decreases with increasing Al/Na. Interestingly, the intensity of the NBO peak apparently decreases to zero at $Al/Na<1.0$ for both series of glasses in Figs. 3.6(a) and (b). By fitting each O 1s spectral envelope with a pair of Gaussian peaks having equal widths in an extension of the method successfully applied to RS glasses (see Section 2.2.3), the fraction of NBO's from experiment, $f_{NBO}(XPS)$, was evaluated for the NAS glasses. BCGS and SL concluded that $f_{NBO}(XPS) \rightarrow 0$ at $Al/Na = 0.67$ and 0.75, respectively, rather than at unity as theoretically expected from the classical model for RAS glass structure (see Eq. (3.2)). They asserted that their XPS results support an alternative model, also advanced by Hunold and Bruckner [39,40], where some fraction of the aluminum atoms exist in Al^{VI} groups as network formers for $Al/Na \leq 1.0$. Since these Al^{VI} groups are more efficient than Al^{IV} groups in converting alkali ions from network modifiers to charge compensators (cf Eq.(3.5) vs. Eq. (3.1)) , this model predicts $f_{NBO} \rightarrow 0$ below the equivalence point in accord with the XPS findings. BCGS also commented that systematic changes in the shape of O 1s spectra with increasing Al_2O_3 content cease at $Al/Na=0.67$ (Fig. 3.6(a)). While no firm conclusions were drawn about the structure of glasses with $Al/Na>1.0$, BCGS speculated about the existence of Al^{VI} groups for such compositions.

Kaneko et al. [21] examined NAS glasses similar in composition to those of BCGS, but analyzed surfaces prepared by ion sputtering rather than by vacuum fracture. Changes in the shape of the O 1s envelope with

Al/Na were thought to be consistent with the results of BCGS and SL. Wakabayashi et al. [22] (not indicated in Fig. 3.5) recently investigated vacuum-fractured NAS glasses from the same series as SL. An analysis of the O 1s spectra by fitting to a pair of Lorentzian peaks yielded a variation in f_{NBO}(XPS) with Al/Na similar to that obtained by SL.

In contrast to the interpretation of BCGS [12,14] and SL [20], Lam et al. [19] (LPV) claimed that f_{NBO}(XPS) is virtually independent of Al/Na on the basis of a residual analysis for O 1s spectra acquired from vacuum-milled glasses. Difference spectra were generated by subtracting the spectrum for $Na_2O \cdot 3SiO_2$ glass from spectra for a series of NAS glasses with successively greater additions of Al_2O_3. The O 1s envelopes for the NS and each NAS glass were scaled to the position and intensity of a nearby sodium Auger peak (due to Al $K\alpha_1$ excitation). This analysis was indicated to show that for successive additions of Al_2O_3 to the $Na_2O \cdot 3SiO_2$ base glass, (Si-O-Si) siloxane bonds of the starting matrix are destroyed and (Al-O-Si) bonds are created, but NBO's are unaffected by this process. Supposedly, $(AlO_{4/2})^-$ tetrahedra are charge compensated by a transfer of valence charge from sodium ions to the aluminosilicate network without the elimination of NBO's as Al/Na becomes greater. LPV also reported that the width of the Si 2p photopeak is substantially reduced whereas the widths of the Al 2p and Na 2s photopeaks broaden only slightly if at all as Al/Na changes from 0 to 1.33. Over the same range, binding energies of the Na 2s core level were found to increase ∿0.8 eV relative to the Si 2p level, whereas the energetic separation between the Al 2p and Si 2p levels did not vary significantly with Al/Na except possibly beyond the equivalence point.

Similar trends in binding energies were indicated by SL in their latter study of a different series of NAS glasses. In addition, they identified a large positive shift in the energy of the sodium Auger peak relative to the position of the NBO peak in the O 1s spectrum (Fig. 3.6(b)) as Al/Na increases from zero. LPV attribute the shift of the sodium signal to a redistribution of valence charge from the sodium ions to the aluminosilicate network with increasing Al/Na. On the contrary, SL suggest the effect is caused by the gradual replacement of modifier sites ($\equiv$Si-O^-Na^+) with charge compensator sites ($Na^+(AlO_{4/2})^-$ or $Na_3^+(AlO_{6/2})^{-3}$) having greater ionic character than the modifier sites.

It has been recounted above that earlier photoemission studies have produced two remarkably dissimilar interpretations for the structure of NAS glasses. Neither of these structural scenarios, however, can plausibly explain the occurrence of a maximum, minimum, or discontinuity in many physical properties at Al/Na=1.0-1.2 (e.g., see Fig. 3.1). Furthermore, they are in basic disagreement with findings from other structural investigations of RAS glasses reviewed in the preceeding subsection. This divergence of opinion is well demonstrated by comparing the compositional dependencies for f_{NBO} from the XPS studies of BCGS [12,14], SL [20], and LPV [19] with that inferred from the optical luminescence work of Alexander et al. [23, 24].

In Chapter 2, it was established for NS glasses that f_{NBO}(XPS) conforms to theory over the range of $0 \leq f_{NBO}(\text{theo}) < 0.35$. Therefore, the above controversial XPS results for NAS glasses are not likely ascribable to some inherent deficiency of this technique. A motivation for the present reexamination of NAS glasses by XPS was the desire to reconcile the conflicting structural interpretations for compositions with $Al/Na \leq 1.0$ of prior photoemission studies with the strong support given to the classical model by the optical luminescence work. Another was to gain a better understanding of how aluminum atoms are structurally incorporated in glasses with Al/Na>1.0 than has been achieved previously in XPS studies.

3.3. EXPERIMENTAL PROCEDURES:

3.3.1. Sample Preparation

The three series of NAS glasses chosen for this investigation are indicated in Fig. 3.5. They are described as follows: (1) constant optical basicity ($\Lambda=0.57$) with $0 \leq Al/Na \leq 1.5$; (2) constant mole fraction SiO_2($X_{Si}=0.67$) with $0 \leq Al/Na \leq 1.5$; and (3) $Al/Na=1.0$ with $0.33 \leq Al/Si \leq 1.0$. All compositions are outside known regions of phase separation [70-73] in the SiO_2-rich corner of the NAS ternary system. The glass compositions listed in Table 3.2 were prepared at the direction of Dr. P.I.K. Onorato at GTE Labs, Inc. in Waltham, MA. Samples were batched using 99.999% pure Na_2CO_3, $NaAlO_2$, Al_2O_3 and SiO_2; heated in a platinum crucible with a lid at 1400-1630°C for 5-30 hrs; then transferred to a furnace at 1100°C and slowly cooled to room temperature. Several bars (4x4x20 mm) were cut under kerosene from each glass sample. Hygroscopic samples with low Al_2O_3 contents were stored in a dry box. Assays for most of the NAS glasses by ICP spectroscopy or X-ray fluorescence (normalized to $X_{Na}+X_{Al}+X_{Si}=1.0$) are given in Table 3.2.

The NAS glasses with $\Lambda=0.57$ examined here are similar to a series investigated by Alexander et al. [23,24] with optical luminescence spectroscopy in related work, but were prepared without thallium doping. A discussion of the concept of optical basicity and the way in which lines of glass compositions with constant optical basicity are calculated can be found in the papers by Alexander et al.

3.3.2. Photoemission Measurements

The XPS data were obtained using a PHI Model 548 spectrometer [74], equipped with a non-monochromatized Mg Kα X-ray source ($h\nu=1253.6$ eV) and

Table 3.2(a): $Na_2O-Al_2O_3-SiO_2$ (NAS) Glasses (Λ=0.57)

Sample	Al/Na(ideal)	X_{Na}(ideal)	X_{Al}(ideal)	X_{Si}(ideal)	X_{Na}(assay)	X_{Al}(assay)	X_{Si}(assay)
NSII	0.00	0.250	-	0.750		-	
NASXXX	0.02	0.248	0.005	0.748			
NASII	0.19	0.232	0.045	0.723	0.247 0.240 0.231	0.043 0.048 0.045	0.710 0.713 0.724
NASIII	0.42	0.216	0.090	0.694	0.221 0.212	0.084 0.082	0.695 0.706
NASVII	0.63	0.202	0.127	0.671	0.202 0.197 0.187	0.125 0.125 0.118	0.672 0.678 0.695
NASXXII	0.85	0.189	0.161	0.650	0.197 0.187	0.164 0.166	0.639 0.646
NASV	1.00	0.181	0.181	0.638	0.170 0.191	0.185 0.193	0.646 0.616
NASXII	1.10	0.176	0.194	0.630	0.181	0.193	0.626
NASXX	1.30	0.168	0.218	0.614	0.165	0.228	0.607
NASXXVIII	1.50	0.160	0.239	0.601	0.158	0.240	0.602

Table 3.2(b): Na_2O-Al_2O_3-SiO_2 (NAS) Glasses (X_{Si}=0.67)

Sample	Al/Na(ideal)	X_{Na}(ideal)	X_{Al}(ideal)	X_{Si}(ideal)	X_{Na}(assay)	X_{Al}(assay)	X_{Si}(assay)
NSIII	0.00	0.333	-	0.667	0.340 0.337	-	0.660 0.663
NASXXIX	0.20	0.277	0.055	0.667			
NASXXIV	0.55	0.215	0.118	0.667	0.218 0.220	0.118 0.138	0.664 0.642
NASXXIII	0.85	0.180	0.153	0.667	0.182 0.186	0.163 0.169	0.655 0.645
NASXXV	1.00	0.167	0.167	0.667	0.165 0.172 0.163	0.171 0.166 0.177	0.664 0.662 0.660
NASXXXI	1.30	0.145	0.188	0.667	0.141	0.223	0.636
NASXXXII	1.50	0.133	0.200	0.667	0.150	0.227	0.623

Table 3.2(c): Na_2O-Al_2O_3-SiO_2 (NAS) Glasses (Al/Na=1.0)

Sample	Al/Si(ideal)	X_{Na}(ideal)	X_{Al}(ideal)	X_{Si}(ideal)	X_{Na}(assay)	X_{Al}(assay)	X_{Si}(assay)
NASXXVI	0.33	0.125	0.125	0.750	0.128	0.130	0.742
NASXXV	0.50	0.167	0.167	0.667	0.165	0.171	0.664
					0.172	0.166	0.662
					0.163	0.177	0.660
NASV	0.57	0.181	0.181	0.638	0.170	0.185	0.646
					0.191	0.193	0.616
NASXIII	0.85	0.230	0.230	0.540			
NASXXVII	1.00	0.250	0.250	0.500	0.248	0.256	0.496

X_{Na}, X_{Al}, and X_{Si} are the mole fractions of Na_2O, Al_2O_3, and SiO_2, respectively a double-pass cylindrical mirror analyzer. Photoemission spectra from vacuum-fractured surfaces of the NAS glasses were measured using experimental methods and conditions similar to those described at length in Sections 1.3.1., 1.3.2., and 1.3.4. All spectra were acquired at an apparent surface potential $Q \simeq -10$ V and corrected to Au $4f_{7/2}=84.00$ eV by the BMD method. Binding energies, BE_F, are thus referenced to the surface Fermi level of the sample. After a survey spectrum, a high-resolution spectrum of the O 1s core level was obtained prior to the concurrent acquisition of high-resolution spectra for the O 1s, Si 2p, Al 2p, Na 1s, and C 1s levels. Whereas signal-to-noise ratios [75] $\sim$100 for the raw O 1s, Si 2p, and Na 1s data were typically attained, the much poorer quality of the Al 2p data for glasses with $Al/Na \lesssim 0.5$ limited their usefulness. A final survey spectrum completed an analysis. At least two fracture surfaces for each glass composition were examined to assure the reproducibility of the measurements.

Refinement of the core level spectra was accomplished by the methods of deconvolution, smoothing, and background subtraction which are detailed in Section 1.3.1. Photopeak energies and full widths at half maximum (FWHM) were also computed as in Section 1.3.1. for the Si 2p, Al 2p, and Na 1s levels using a nonlinear least squares fitting analysis. The O 1s spectra envelopes were fit to as many as three distinct Gaussian peaks without constraints on intensity for any component. Binding energies for each peak were allowed to vary within overlapping 3 eV windows. However, the FWHM of each component was appropriately constrained in this analysis as described in the next Section.

3.4. RESULTS AND ANALYSIS:

3.4.1. Core Level Spectra for Na_2O-Al_2O_3-SiO_2 Glasses

Representative survey spectra from vacuum-fractured surfaces of two compositions, NASVII and NASXXVIII, in the series of NAS glasses with $\Lambda=0.57$ are shown in Fig. 3.7. Negligible carbon contamination is initially detected for these surfaces [76]. The C 1s signal at $\sim$285 eV increased only very slowly with time under X-irradiation to a level of $\lesssim 1$ atomic % after several hours.

Composite sets of O 1s core level spectra for two series of NAS glasses, $\Lambda=0.57$ and $X_{Si}=0.67$, in the compositional range of $0 \leq Al/Na \leq 1.0$ are displayed in Fig. 3.8. In contrast to the normalized energy scales for the spectra of BCGS [12,14] and SL [20] in Fig. 3.6, the BE_F scales for the spectra in Fig. 3.8 give a more realistic depiction of how the shape of the O 1s envelope changes as a function of Al/Na. As can be seen in the composite O 1s spectra for the glasses with $\Lambda=0.57$ in Fig. 3.8(a), the intensity of the NBO peak (i.e., the component with the lowest binding energy) decreases up to Al/Na=1.0 relative to the scaled intensity of the main "BO peak". Also, the "BO peak" broadens and shifts to lower binding energy by about 1 eV with increasing Al/Na. Similar trends are found in the composite O 1s spectra for the glasses with $X_{Si}=0.67$ in Fig. 3.8(b). The systematic variations in spectral shape along both lines of compositions with Al/Na, however, practically cease at the equivalence point. A much slower evolution in the shape of the O 1s envelope occurs in each series for glasses with Al/Na>1.0 (not shown in Fig. 3.8). Aspects of this behavior have been observed in earlier work [12,14,19-21]; but the significance was not fully appreciated. Better insight into the atomic arrangement of NAS glasses

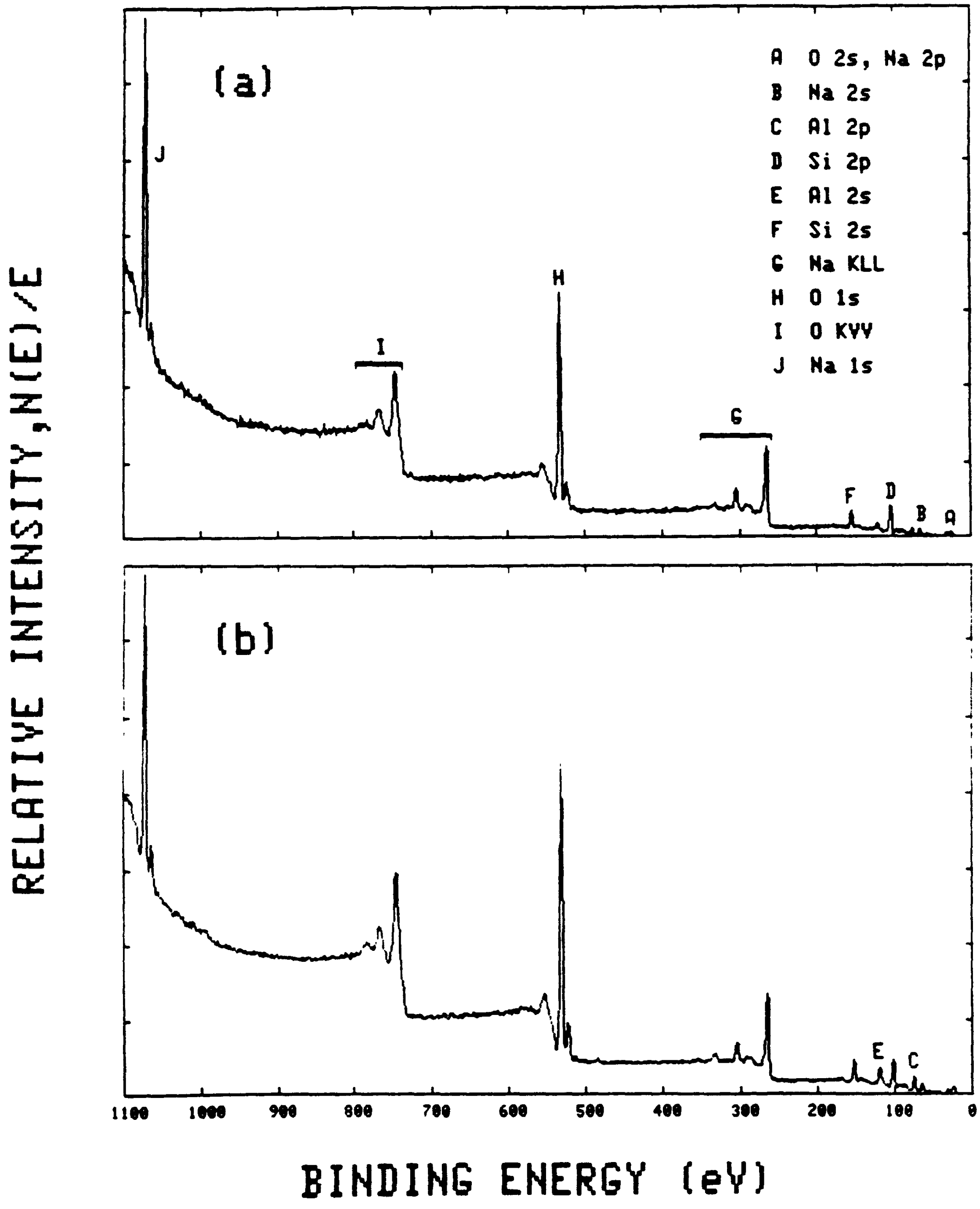

Fig. 3.7: Survey spectra of vacuum-fractured NAS glasses with $\Lambda=0.57$: (a) Al/Na=0.63 (NASVII), and (b) Al/Na=1.50(NASXXVIII).

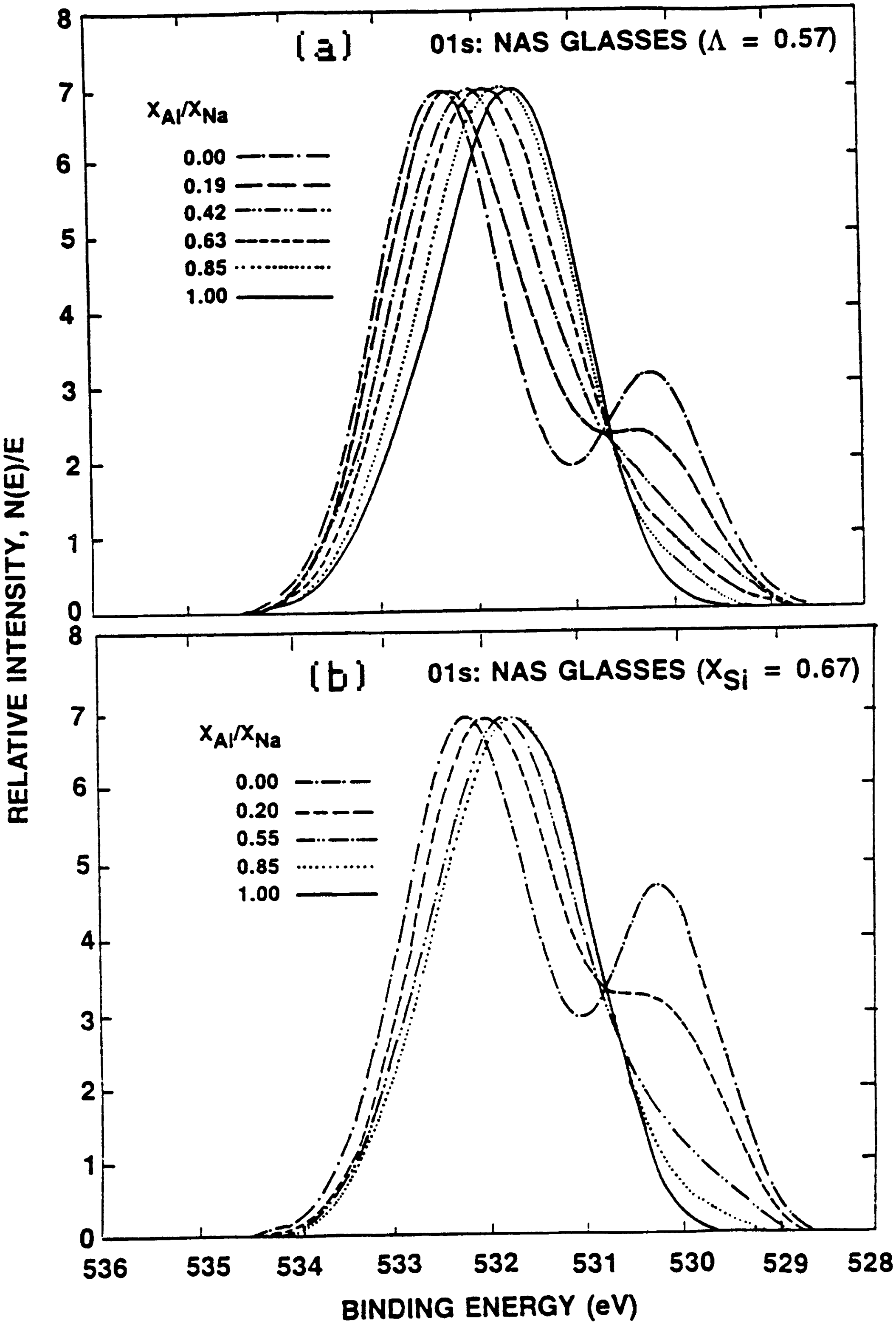

Fig. 3.8: Composite spectra of O 1s core level for vacuum-fractured NAS glasses: (a) Λ=0.57, and (b) X_{Si}=0.67.

can be realized if one hypothesizes that the "BO peak" is complex and can therefore be characterized by two energetically distinct components in a curve-fitting analysis.

The case of NAS glasses with $Al/Na \leq 1.0$ is addressed first with the assumption that the classical structural model (see Section 3.2.1.) is valid. The O 1s spectra for compositions with $Al/Na < 1.0$ should then be generally comprised of three oxygen chemical states, BO1, BO2, and NBO, as defined in Table 3.3. Whereas the BO1 and NBO bonding states correspond to those which are well resolved in analyses of O 1s spectra for NS glasses in Chapter 2 [77], the BO2 state is an Al^{IV}-O-Si^{IV} linkage with a sodium ion nearby for charge compensation (see Eq. (3.1)). In accordance with the aluminum avoidance principle (see Eq. (3.8)), Al^{IV}-O-Al^{IV} bridges are presumed not to exist. The valence charge on oxygen anions in the chemical states given in Table 3.3 is expected to increase in the order of BO1<BO2<NBO; hence, binding energies for these states should decrease in the sequence of $BE_F(BO1) > BE_F(BO2) > BE_F(NBO)$.

In the analysis of each O 1s spectrum, the FWHM's of <u>three</u> Gaussian peaks representing these three chemical states are constrained to the values indicated in Table 3.3 with FWHM(BO1)≡FWHM(BO2). The peak widths assigned here to the different oxygen chemical states in NAS glasses with $Al/Na \leq 1.0$ are believed to be reasonable fitting parameters. They approximate the peak widths determined in Section 2.4.2. for the BO and NBO components of O 1s spectra for the series NS glasses in Fig. 3.5. For those compositions, the BO and NBO peaks were found to have FWHM(BO)≃1.55 eV and FWHM(NBO)≃1.30 eV in a curve fitting analysis without constraints on peak energies, intensities, shapes, <u>or</u> widths.

Table 3.3: O 1s Chemical States for NAS Glasses with $0 \le \mathrm{Al/Na} \le 1.0$

	Chemical State	FWHM (eV)
BO1	$\mathrm{Si{-}O{-}Si}$	1.50 ± 0.05
BO2	$\mathrm{Al{-}\underset{\underset{\displaystyle Na}{|}}{O}{-}Si}$	1.50 ± 0.05
NBO	$\mathrm{Si{-}O{-}}\sum_{j} \mathrm{Na}_{j}$	1.30

Note: BO2's do not exist at Al/Na=0. NBO's are not present at Al/Na=1.0. All silicon and aluminum atoms are coordinated by four oxygen atoms.

Attention is now directed to the case of NAS glasses with Al/Na>1.0. For the analysis of these compositions, it is assumed that Lacy's tricluster model [44] (see Section 3.2.1.) provides a satisfactory structural description. The O 1s spectra of glasses with Al/Na>1.0 should then be composed of four oxygen chemical states, BO1, BO2, BO3, and BO4, as identified in Table 3.4. Whereas the BO1 and BO2 bonding states are identical to those postulated above for glasses with $Al/Na\leq 1.0$, the BO3 and BO4 states are associated with the incorporation of aluminum atoms in excess of sodium atoms within tricluster configurations (Fig. 3.2(b)). From the standpoint of the extended electrostatic valence rule (see Sections 2.2.2. and 3.2.1.), the BO3 state is an "underbonded" Al^{IV}-O-Si^{IV} linkage without a sodium ion available for charge compensation and the BO4 state is an "overbonded" bridging oxygen connecting an Al^{IV} group and a pair of Si^{IV} groups. Once again, the aluminum avoidance rule is invoked to exclude Al^{IV}-O-Al^{IV} bridges from the set of possible bonding states. This assumption is still plausible for the compositions with $1.0<Al/Na\leq 1.5$ as will be indicated later in this Chapter. The valence charge on oxygen atoms in the chemical states listed in Table 3.4 is presumed to increase in the sequence of BO1∿BO3<BO2∿BO4. In order to make the analysis tractable, it is further assumed that the binding energies for these states have a two-fold degeneracy and therefore decrease in the order of $BE_F(BO1)=BE_F(BO3)>BE_F(BO2)=BE_F(BO4)$.

In the analysis of each O 1s spectrum for glasses with Al/Na>1, the FWHM's of <u>two</u> Gaussian peaks representing these four chemical states are constrained to the values given in Table 3.4 with FWHM(BO1+BO3)≡FWHM(BO2+BO4). Although they are arbitrary to some extent, these fitting parameters were chosen in correspondence with the peak widths assigned to the distinct BO1

Table 3.4: O 1s Chemical States for NAS Glasses with $1.0 \leq Al/Na \leq 1.5$

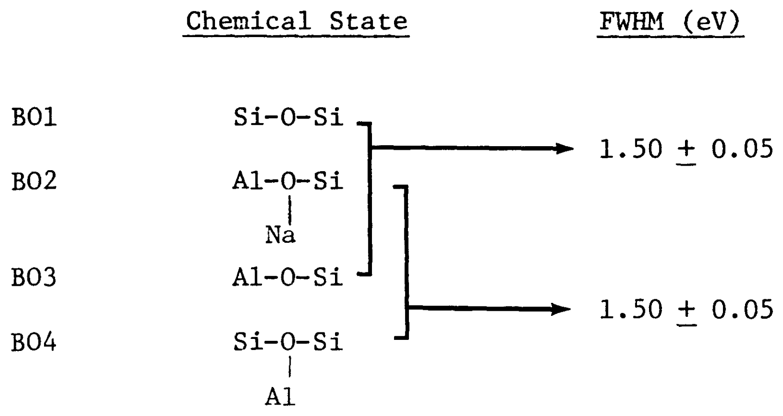

Note: BO3's and BO4's do not exist at Al/Na=1.0. All silicon and aluminum atoms are coordinated by four oxygen atoms.

and BO2 bonding states in glasses with $Al/Na \leq 1.0$ (Table 3.3).

Using the procedures outlined above and in Section 3.3.2., the individual fits obtained to O 1s spectra for the series of NAS glasses with $\Lambda=0.57$ are presented in Fig. 3.9. Particular attention is called to the fact that as Al/Na goes from zero to unity, the empirical fraction of NBO's,

$$f_{NBO}(XPS) = \frac{A(NBO)}{A(BO1) + A(BO2) + A(NBO)} \qquad (3.9)$$

where A(BO1), A(BO2), and A(NBO) are the integrated intensities of the BO1, BO2, and NBO component peaks, decreases to zero <u>at the equivalence point</u>. Also, the ratio of the bridging oxygen peaks,

$$r(XPS) = \frac{A(BO2)}{A(BO1)}, \qquad (3.10)$$

rapidly increases over the same compositional range. While the fit to the O 1s spectrum for the glass NASXXX (not included in Fig. 3.9) is consistent with the above trends, this particular analysis is rather sensitive to the peak widths selected for the BO1 and BO2 components on account of the low Al_2O_3 content for this composition (Table 3.2). As Al/Na rises above unity in Fig. 3.9, the ratio of the compound bridging oxygen peaks,

$$r'(XPS) = \frac{A(BO2+BO4)}{A(BO1+BO3)} \qquad (3.11)$$

where A(BO1+BO3) and A(BO2+BO4) are the integrated intensities of the BO1+BO3 and BO2+BO4 component peaks, increases very slowly in comparison to the pronounced variation in r(XPS) for compositions below the equivalence point. For glasses with $Al/Na>1.0$ there is <u>no</u> indication of an NBO component on the low energy side of each O 1s envelope.

Individual fits computed to O 1s spectra for the series of NAS glasses with $X_{Si}=0.67$ are shown in Fig. 3.10. The description of the structural

Fig. 3.9: O 1s core level spectra for vacuum-fractured NAS glasses with Λ=0.57 (NSII, NASII, NASIII, NASVII, NASXXII, NASV, NASXII, NASXX, and NASXXVIII). The experimental spectrum, component peaks, and sum of the component peaks are shown for each composition. The sum of each multi-component fit is nearly indistinguishable from the experimental spectrum.

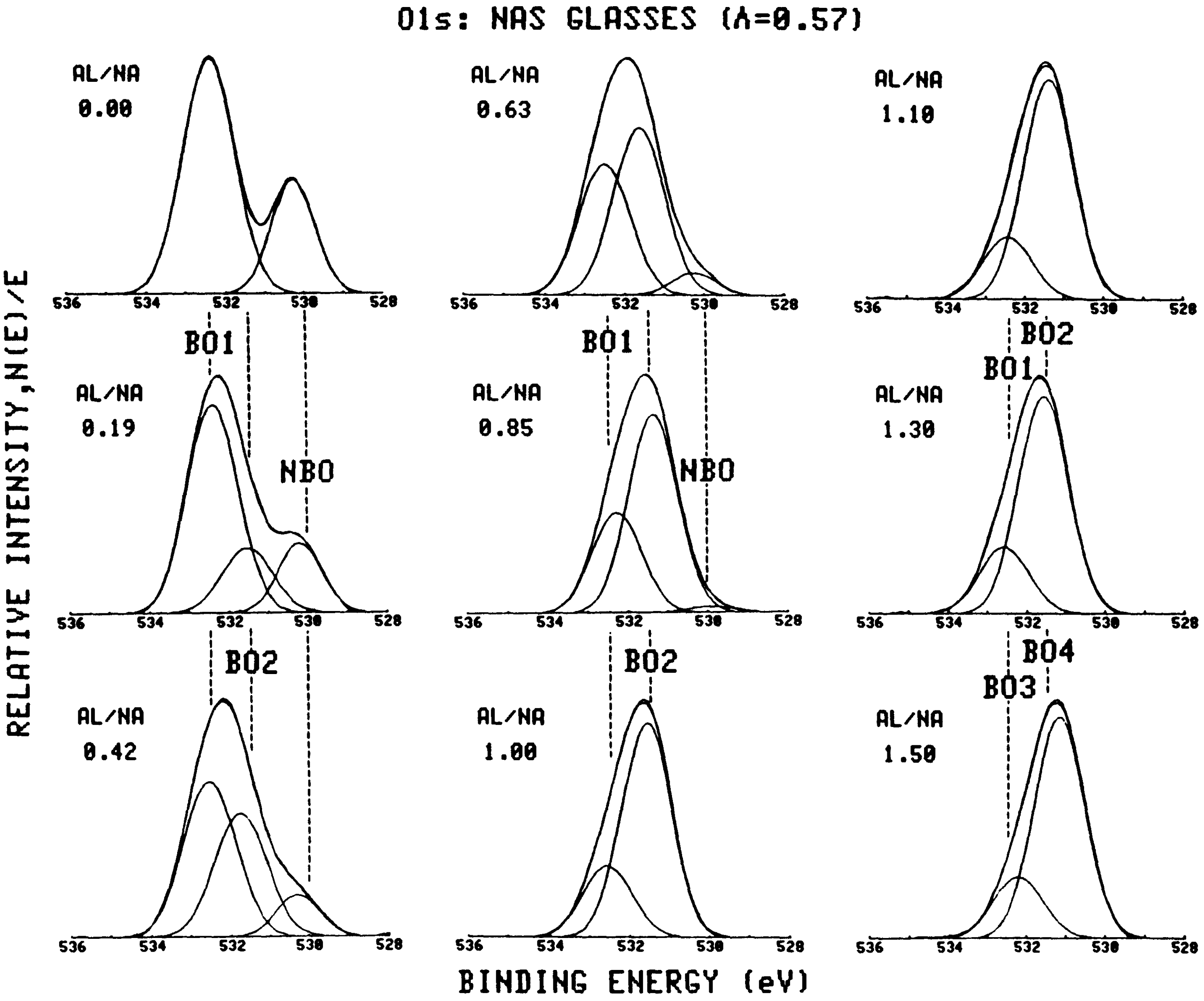
O1s: NAS GLASSES (Λ=0.57)
RELATIVE INTENSITY, N(E)/E
BINDING ENERGY (eV)
AL/NA 0.00
AL/NA 0.19
AL/NA 0.42
AL/NA 0.63
AL/NA 0.85
AL/NA 1.00
AL/NA 1.10
AL/NA 1.30
AL/NA 1.50
536
534
532
530
528
BO1
BO2
NBO
BO3
BO4

Fig. 3.10: O 1s core level spectra for vacuum-fractured NAS glasses with X_{Si}=0.67(NSIII, NASXXIX, NASXXIV, NASXXIII, NASXXV, NASXXXI, and NASXXXII). The experimental spectrum, component peaks, and sum of the component peaks are shown for each composition. The sum of each multi-component fit is nearly indistinguishable from the experimental spectrum.

O1s: NAS GLASSES (X_{Si}=0.67)

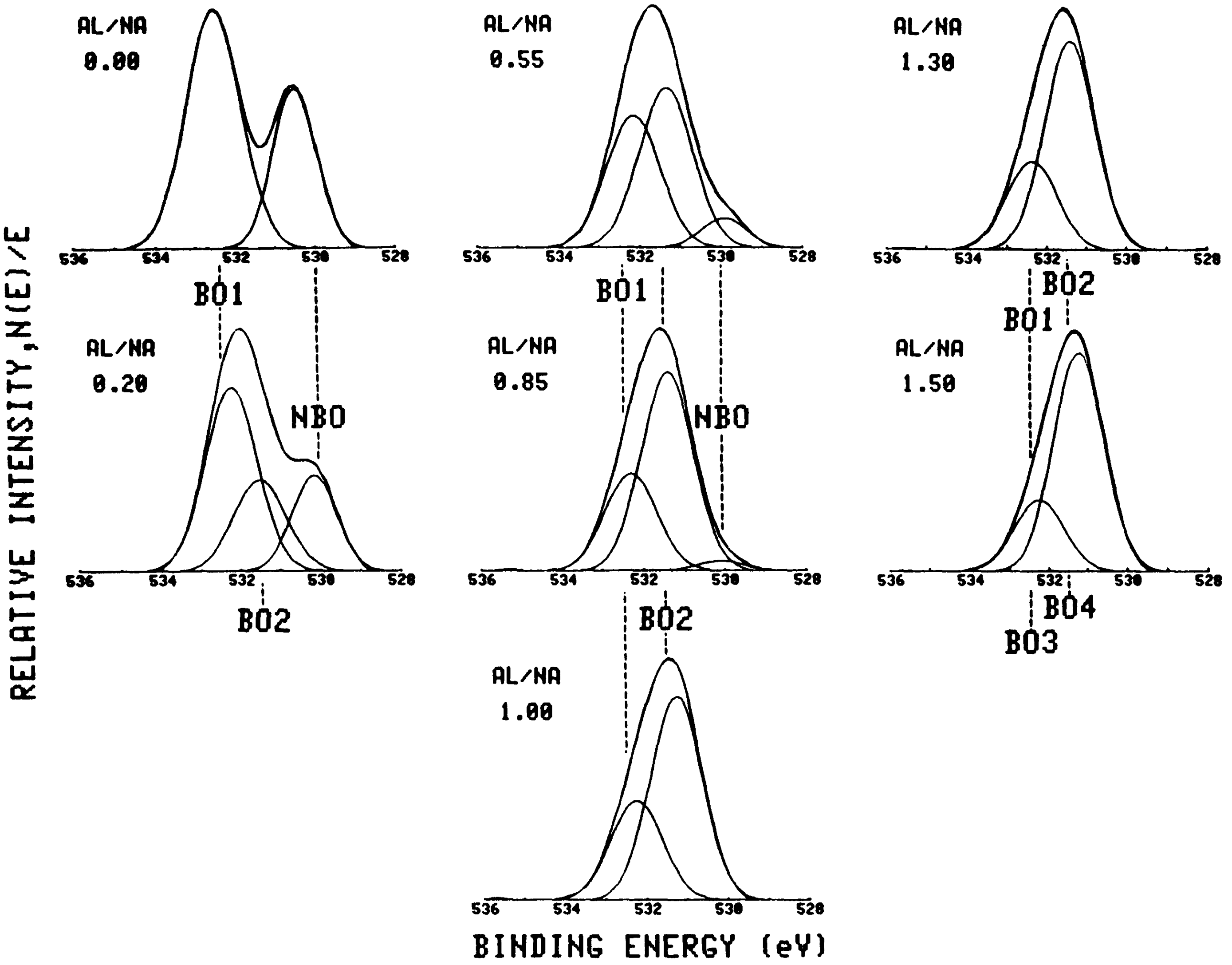

trends with increasing Al/Na in Fig. 3.10 is similar to that given for the series of glasses with Λ=0.57 in Fig. 3.9. While f_{NBO}(XPS) decreases to zero at Al/Na=1.0, r(XPS) markedly increases up to that composition. Beyond the equivalence point, r'(XPS) grows at a much slower rate. For glasses with Al/Na>1.0, there is again no evidence for an NBO component on the low energy side of each O 1s envelope.

Finally, the individual fits obtained to O 1s spectra for Ab glass, Jd glass, and Ne glass from the series of compositions with Al/Na=1.0 are exhibited in Fig. 3.11. As Al/Si goes from 0.33 to 1.0, r(XPS) is seen to increase for these compositions. While there is no suggestion of an NBO component in any of these spectra at low binding energies, the fit to the O 1s spectrum of the Ne glass was judged inadequate when the fitting parameters in Table 3.3 were employed for the analysis. If the aluminum avoidance principle was strictly obeyed for this composition, then the O 1s envelope would be characterized by a single BO2 component under the assumptions of the traditional structural model. However, the FWHM of the experimental spectrum is greater than the range of widths assigned to the BO2 bonding state (Table 3.3) with success in the above analyses of the other lines of compositions. A better fit to the spectrum for Ne glass was computed, as indicated in Fig. 3.11, by allowing for the existence of a new chemical state, BO5(Al-O-Al), in addition to BO1 and BO2 states. This new state is an Al^{IV}-O-Al^{IV} linkage and its presence denotes a partial breakdown of the aluminum avoidance rule. The FWHM of the Gaussian peak representing the BO5 state was set equal to the FWHM's of the BO1 and BO2 states for this analysis. The fit to the O 1s spectrum for the glass NASXIII (not shown in Fig. 3.11) was also improved by including a small BO5 component. However, O 1s spectra for the more SiO_2-rich glasses in

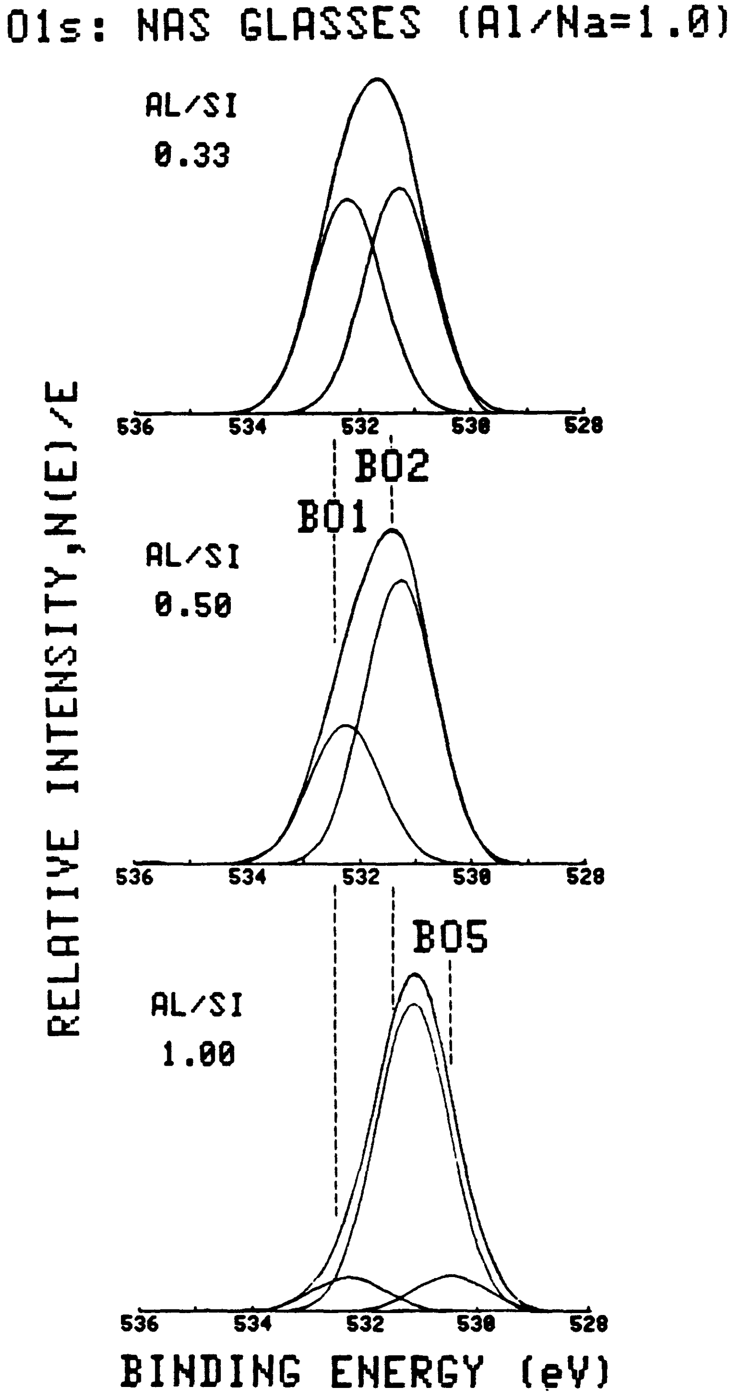

Fig. 3.11: O 1s core level spectra for vacuum-fractured NAS glasses with Al/Na=1.0 (NASXXVI, NASXXV, and NASXXVII). The experimental spectrum, component peaks, and sum of the component peaks are shown for each composition. The sum of each multi-component fit is nearly indistinguishable from the experimental spectrum.

the series with Al/Na=1.0 (Table 3.2) are well described by only BO1 and BO2 components.

For the various NAS glass compositions examined in this work, the binding energies of the BO1(+BO3), BO2(+BO4), BO5 and NBO components to the O 1s spectra are virtually constant and have mean values of 532.36, 531.43, 530.55, and 530.19 eV, respectively, (standard deviations $\sigma \simeq 0.15$ eV). The BE_F of the NBO peak for NAS glasses is not significantly different from the value of 530.30 eV determined for the NBO peak of NS glasses in Section 2.4.2.

Attention is called to the relative energetic positions of the Na 1s, O 1s, Si 2p, and Al 2p core levels in Fig. 3.7. In Fig. 3.12, differences in BE_F between the Na 1s core level and the BO2(+BO4) component of the O 1s envelope, between the BO2(+BO4) component and the Si 2p level, and between the Si 2p and Al 2p levels are plotted vs. Al/Na for the three series of NAS glasses. As Al/Na varies from 0.2 to 1.5 for the glasses with $\Lambda=0.57$ and $X_{Si}=0.67$, the binding energy of the Na 1s line first increases by ∿0.8 eV up to Al/Na=1.0, but then levels off above the equivalence point in relation to the BE_F of the BO2(+BO4) line. Also, the energy of the Na 1s line increases by ∿0.6 eV as Al/Na goes from zero to unity and then becomes constant for Al/Na$\geq$1.0 relative to the BE_F of the BO1(+BO3) line (not indicated in Fig. 3.12). Meanwhile, the binding energy of the Si 2p line is invariant within experimental uncertainty in relation to the BE_F of the BO2(+BO4) line for $0.2\leq$Al/Na≤ 1.5. Although the energetic separation of the Si 2p and Al 2p levels does not change appreciably with Al/Na up to the equivalence point, a decreasing separation between these levels with Al/Na beyond unity is suggested by the data. This indicates the binding energy of the Al 2p level increases relative to the BE_F of the Si 2p level

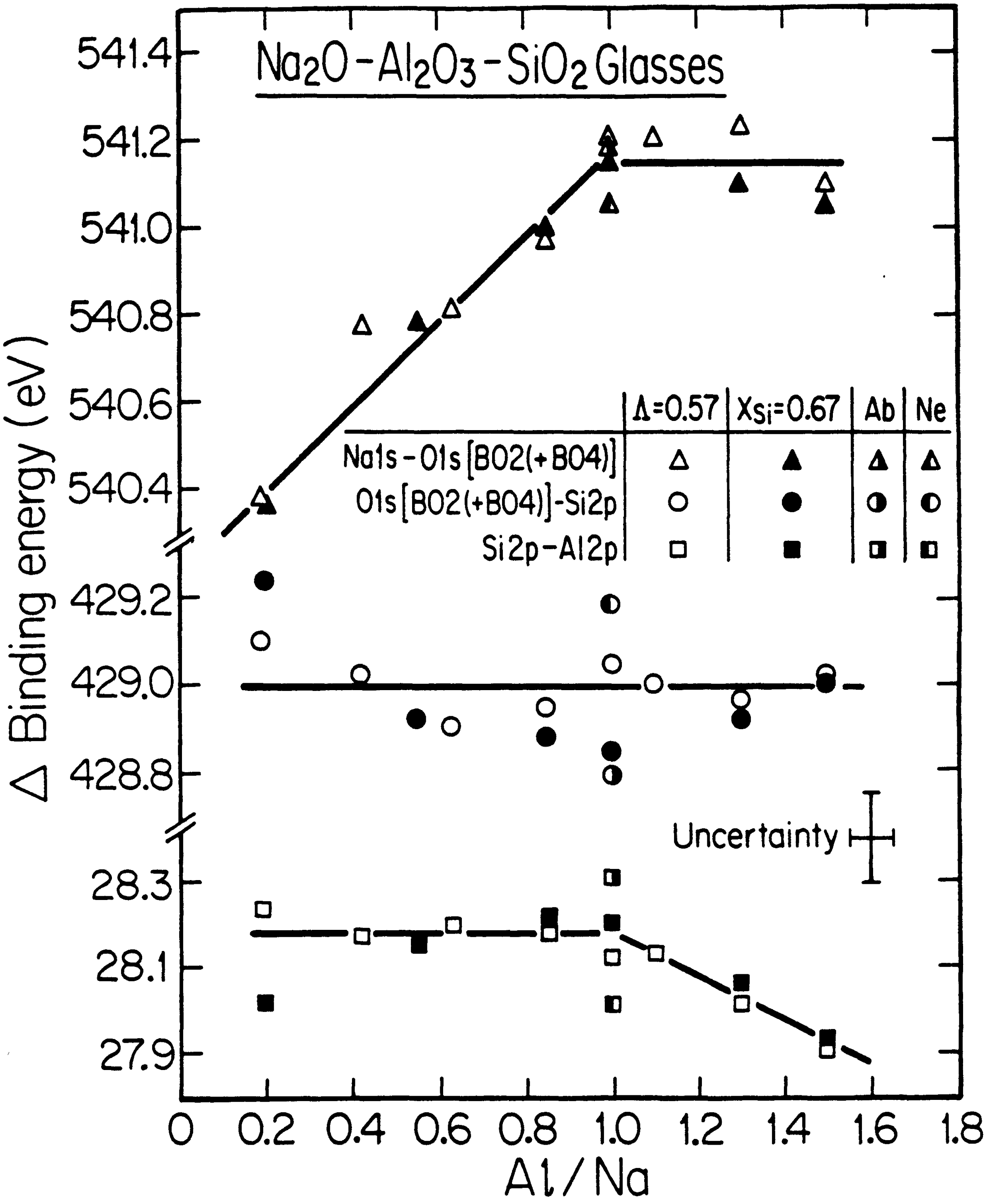

Fig. 3.12: Differences in binding energy between the Na 1s, O 1s, Si 2p, and Al 2p core levels of NAS glasses vs. Al/Na.

with Al/Na above the equivalence point. LPV [19] also found some evidence of this trend in their XPS work. As Al/Si rises from 0.33 to 1.0 for the glasses with Al/Na=1.0, the binding energy of the Na 1s line does not vary substantially with respect to the BO2 line; however, the binding energy of the Si 2p line apparently decreases with respect to the BO2 and Al 2p lines.

The peak widths for the BO1, BO2, and NBO components of the O 1s level and the Si 2p level for NAS glasses with $Al/Na\leq 1.0$ along the compositional lines of $\Lambda=0.57$ and $X_{Si}=0.67$ are graphed vs. n(theo) in Fig. 3.13. The FWHM's of the BO1, BO2, and NBO components yielding the best fit to each O 1s envelope fall within the ranges prescribed for these compositions in Table 3.3 with FWHM(BO1) $\equiv$ FWHM(BO2). In contrast to the nearly constant widths for the BO1 and BO2 components with n(theo), the FWHM of the Si 2p photopeak first broadens from ∿1.53 eV at n(theo)=0 (i.e., Al/Na=1.0) to ∿1.75 eV at n(theo)=0.5, and then narrows to ∿1.60 eV at n(theo)=1.0 as Al/Na decreases along both lines of composition. LPV [19] also reported a large variation in the width of the Si 2p photopeak with Al/Na in their study. The trends in the data of Fig. 3.13 are very similar to those measured for NS glasses in Chapter 2 [78]. For all NAS glasses with $Al/Na\geq 1.0$ investigated in this study, the width of the Si 2p peak is constant at 1.53 eV ($\sigma\simeq 0.05$ eV).

Finally, the FWHM of the Al 2p photopeak increases marginally from ∿1.40 eV to ∿1.55 eV above the equivalence point as Al/Na goes from 0.5 to 1.5 in the NAS glasses of this study. Measurements of FWHM for the Al 2p level in glasses with Al/Na<0.5 were unreliable because of poor signal quality. The FWHM of the Na 1s peak is invariant at 1.81 eV ($\sigma\simeq 0.05$ eV) for

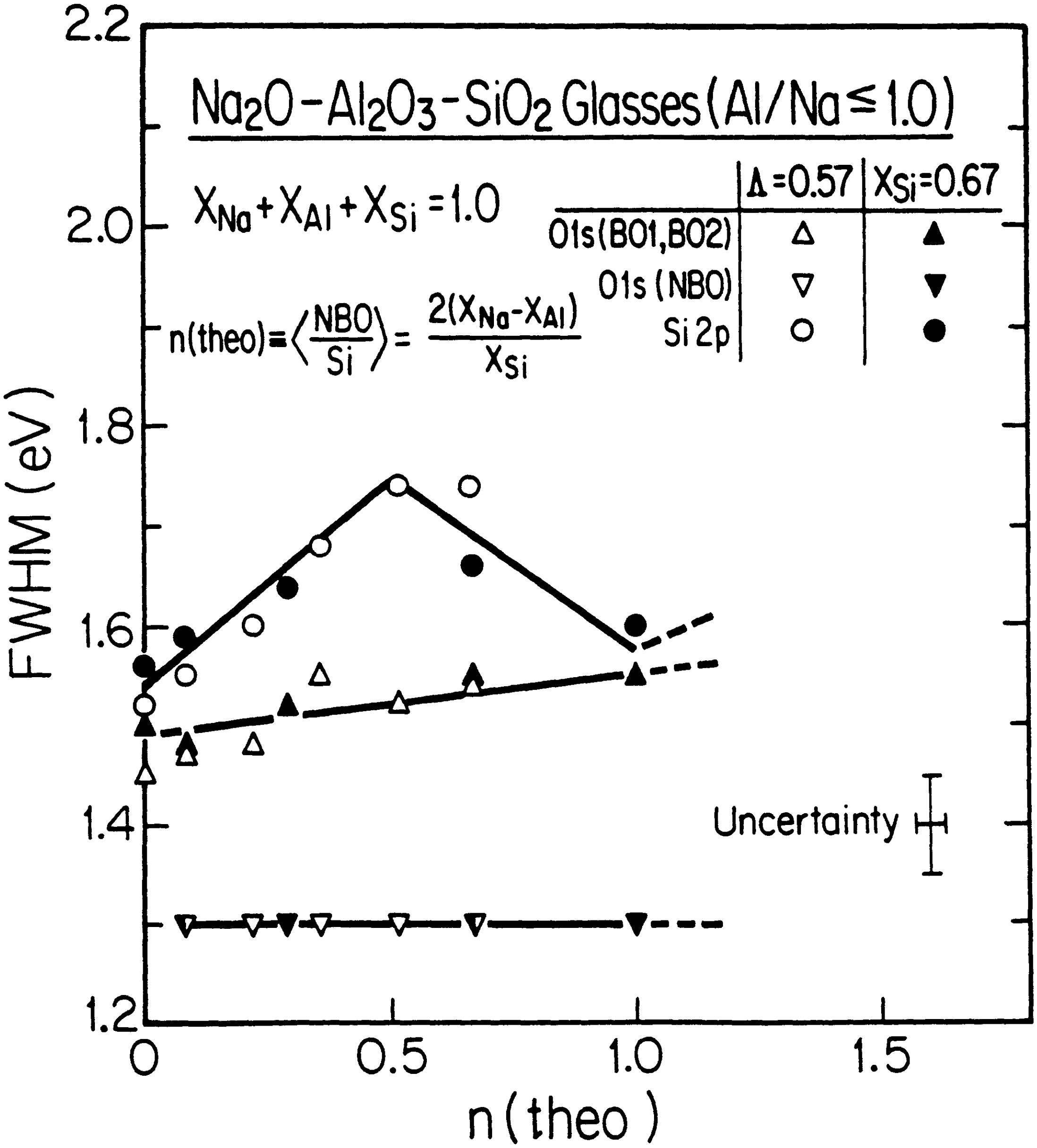

Fig. 3.13: Widths for O 1s and Si 2p photopeaks of NAS glasses with Λ=0.57 and X_{Si}=0.67 for Al/Na$\leq$1.0 vs. n(theo).

all of the NAS glasses. This is not significantly different from the width of 1.84 eV found for the Na 1s peak of NS glasses in Section 2.4.2.

3.4.2. Test of Structural Models for $Na_2O-Al_2O_3-SiO_2$ Glasses

The qualitative trends in the analysis of O 1s spectra for NAS glasses with $0 \leq Al/Na \leq 1.0$ described in the preceeding subsection for Figs. 3.9-3.11 can be quantified in strong support for the classical structural model. In addition, XPS results for glasses with $1.0 < Al/Na \leq 1.5$ can be shown to provide at least permissive evidence in favor of Lacy's tricluster model [44] for the incorporation of excess aluminums in compositions with $Al/Na > 1.0$. A test of the traditional model is considered first in which f_{NBO}(XPS) and r(XPS) are compared with theoretical predictions. This is followed by a comparison of r'(XPS) with expectations from the tricluster model.

In Fig.3.14, a plot of f_{NBO}(XPS) vs. f_{NBO}(theo) is displayed for the two series of NAS glasses with $\Lambda = 0.57$ and $X_{Si}=0.67$. Results for NS glasses obtained in Chapter 2 [79] are also included in Fig. 3.14. For each NAS glass, f_{NBO}(theo) was calculated using the assayed composition if available (Table 3.2). With the exception of NS glasses where $f_{NBO}(theo) \gtrsim 0.35$ (including the glass NSIII for which Al/Na=0 in the NAS series with $X_{Si}=0.67$), f_{NBO}(XPS) agrees with f_{NBO}(theo) within experimental uncertainty over the compositional range of $0 \leq Al/Na \leq 1.0$. These findings are in striking contrast to the conclusion of LPV [19] that f_{NBO}(XPS) is nearly independent of Al/Na for glass compositions similar to the series with $\Lambda=0.57$ of the present study (Fig. 3.5).

Attention is now focussed on glasses NASXXII (Fig. 3.9) and NASXXIII (Fig. 3.10) with Al/Na=0.85. These glasses are within the range of

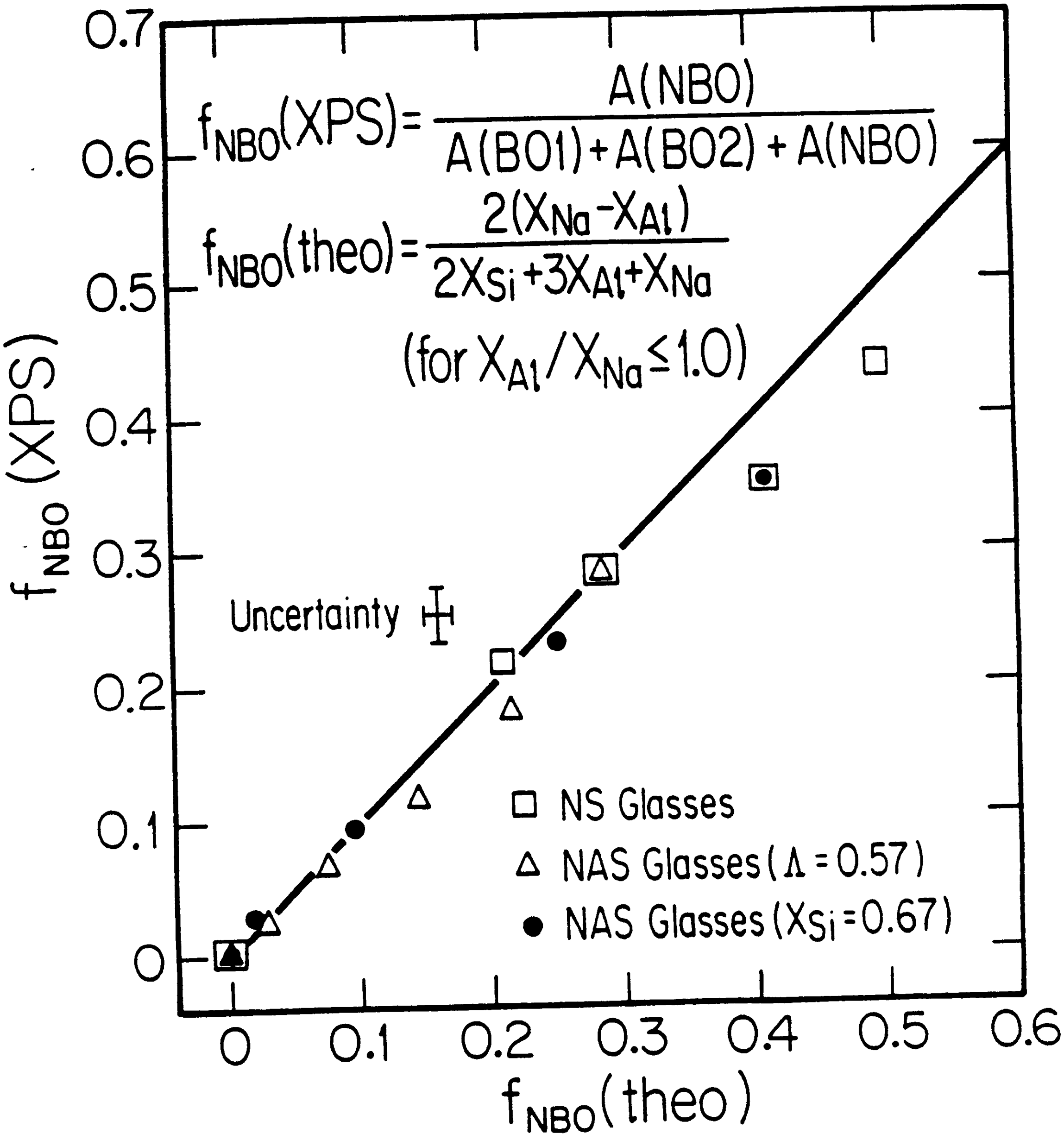

Fig. 3.14: Test of classical model for NAS glasses with Al/Na≤1.0: f_{NBO}(XPS) vs. f_{NBO}(theo).

$0.7 \lesssim Al/Na < 1.0$ where BCGS [12,14] and SL [20] claimed $f_{NBO}(XPS)=0$ for similar compositions (Fig. 3.5) in conflict with the classical model. In the current work, however, it has been determined that $f_{NBO}(XPS)=0.022$ vs. $f_{NBO}(theo)=0.028$ for NASXXII and $f_{NBO}(XPS)=0.028$ vs. $f_{NBO}(theo)=0.018$ for NASXXIII in accord with the classical model. From the analyses of these glasses, it is estimated the detectability limit for NBO's under the experimental conditions of this work is $f_{NBO} \gtrsim 0.010$ (atomic % $\gtrsim 0.5$).

Three assumptions have been made in deriving a theoretical relation for the ratio of chemical states, BO2/BO1, according to the traditional model for glasses with $Al/Na \leq 1.0$:

1. All silicon and aluminum atoms are tetrahedrally coordinated by oxygen atoms. One sodium ion acts as a charge compensator for each Al^{IV} group $(Na^{+}(AlO_{4/2})^{-})$.
2. All sodiums in excess of aluminums act as network modifiers $(\equiv Si\text{-}O^{-}Na^{+})$ and form NBO's bonded to silicon atoms only.
3. The aluminum avoidance principle is obeyed (i.e., (Al-O-Al) bonds do not exist).

With these assumptions about the nature of chemical bonding in NAS glasses for $Al/Na \leq 1.0$ and $X_{Si} \gtrsim 0.50$, a calculation of the network algebra leads to the relation

$$r(theo) = \frac{BO2}{BO1} = \frac{8X_{Al}}{2X_{Si} - 3X_{Al} - X_{Na}} \, . \tag{3.12}$$

A graph of r(XPS) vs. r(theo) is presented in Fig. 3.15 for the three series of NAS glasses in this study. Using the assayed compositions when possible (Table 3.2) to compute r(theo), the correlation between r(XPS) and r(theo) is excellent for the range of $0 \leq Al/Na \leq 1.0$. Data for glasses NASXIII

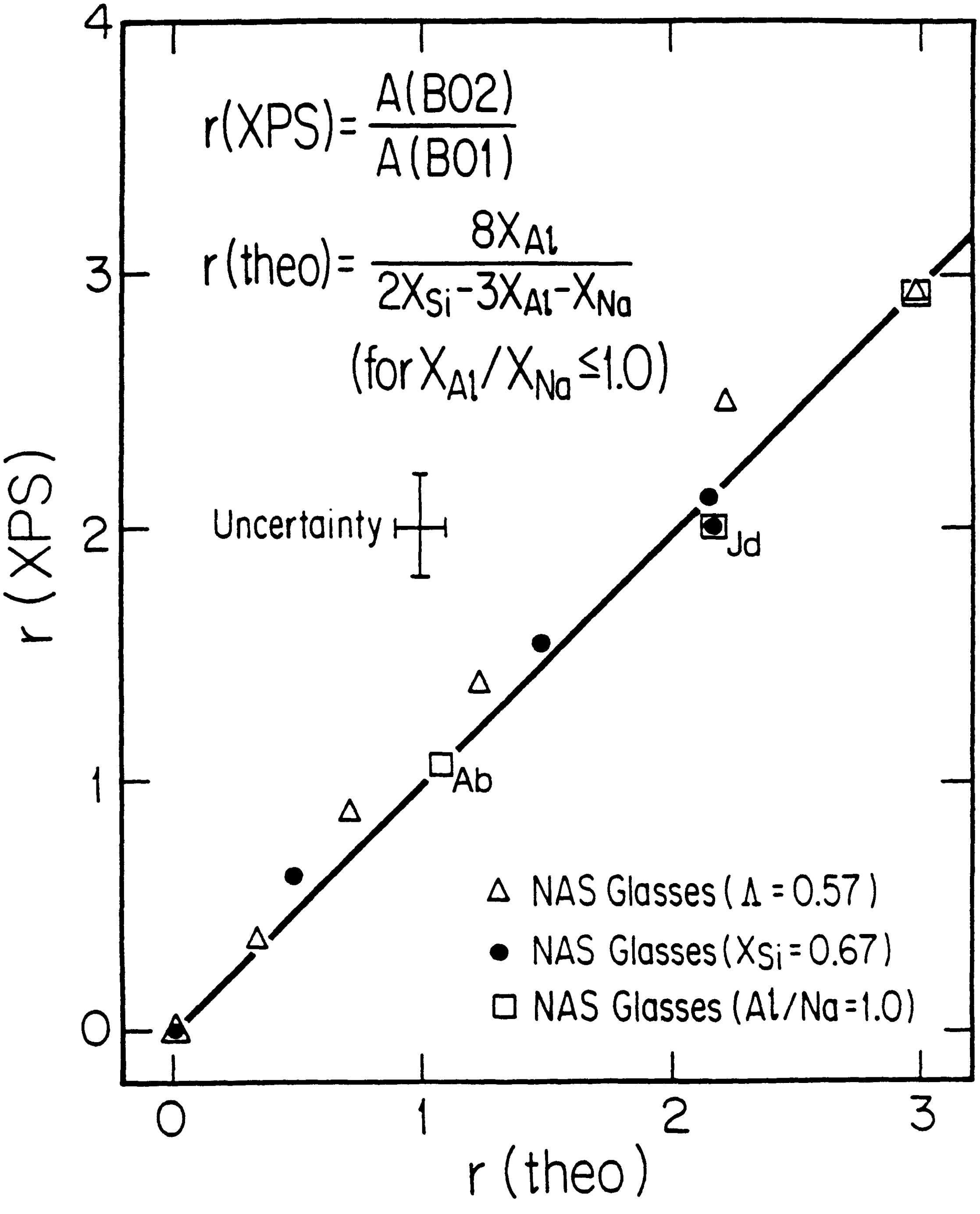

Fig. 3.15: Test of classical model for NAS glasses with Al/Na$\leq$1.0: r(XPS) vs. r(theo).

(r(theo)=12) and NASXXVII (r(theo)=∞) in the series of glasses with Al/Na=1.0 were excluded from consideration in Fig. 3.15 since the aluminum avoidance rule is apparently violated for these compositions with much larger values or r(theo).

A theoretical relation for the ratio of chemical states, BO2+BO4/BO1+BO3, in glasses with Al/Na>1.0 according to the tricluster model has been derived under the following assumptions:

1. Aluminum atoms up to the number of sodium ions are tetrahedrally coordinated by oxygen atoms with one sodium for each Al^{IV} group acting as a charge compensator ($Na^{+}(AlO_{4/2})^{-}$). All silicon atoms are tetrahedrally coordinated by oxygens.
2. All aluminums in excess of sodiums are also tetrahedrally coordinated by oxygens, but one oxygen is bonded to a pair of silicon atoms in a tricluster configuration ($AlSi_2O_{5.5}$).
3. The aluminum avoidance principle is obeyed (i.e., (Al-O-Al) bonds do not exist).

The network algebra with these assumptions for NAS glasses with $Al/Na \geq 1.0$ and $X_{Si} \gtrsim 0.50$ yields the relation

$$r'(\text{theo}) = \frac{BO2+BO4}{BO1+BO3} = \frac{X_{Al}+3X_{Na}}{X_{Si}-X_{Al}-X_{Na}}, \tag{3.13}$$

where r'(theo)=r(theo) at Al/Na=1.0. A plot of r'(XPS) vs. r'(theo) is shown in Fig. 3.16 for the two series of NAS glasses with $\Lambda=0.57$ and $X_{Si}=0.67$. For r'(theo) calculated from the assayed compositions (Table 3.2), there is good agreement between r'(XPS) and r'(theo) over the range of $1.0 \leq Al/Na \leq 1.5$.

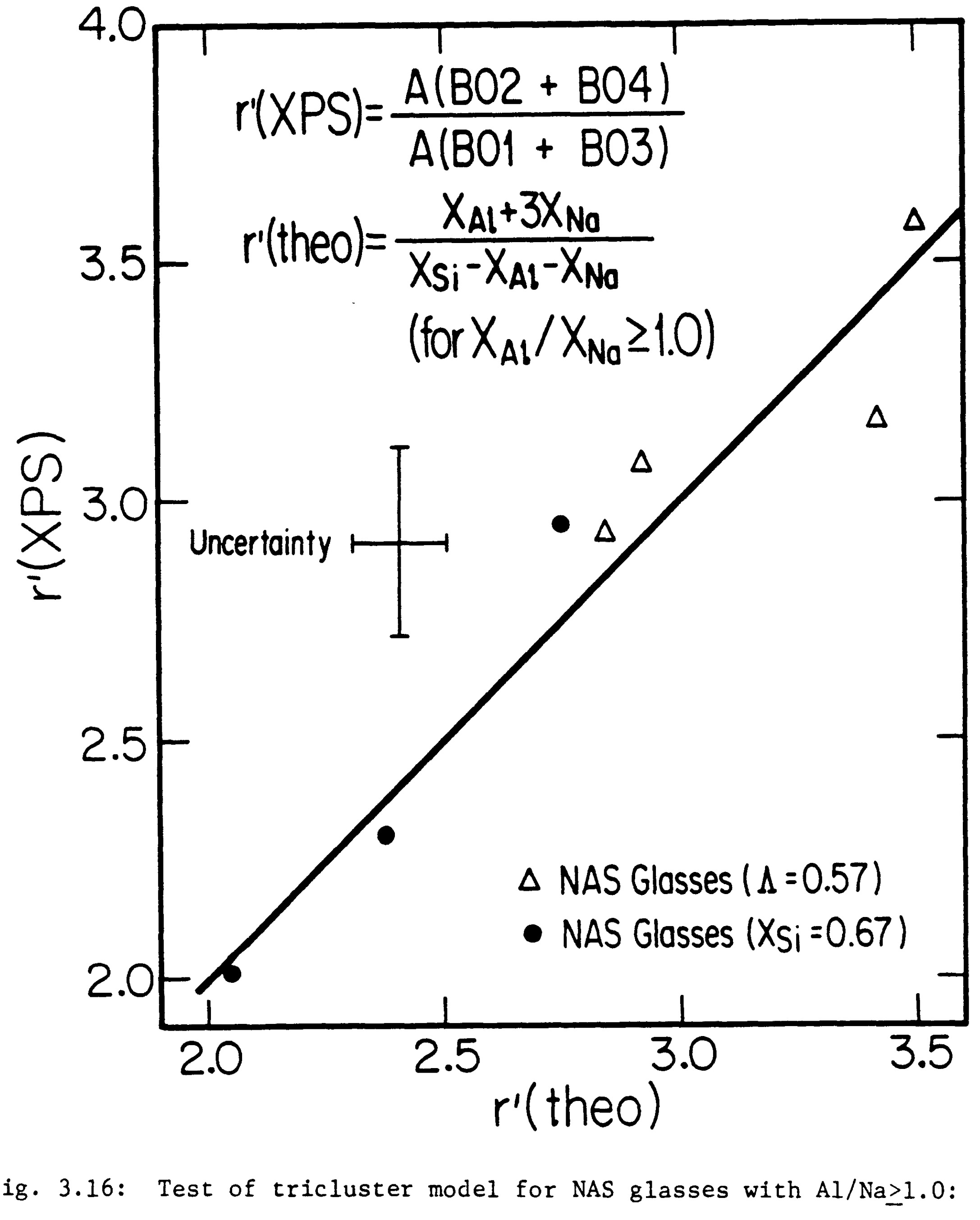

Fig. 3.16: Test of tricluster model for NAS glasses with Al/Na≥1.0: r'(XPS) vs.r'(theo).

In contrast, an algebraic relation for Taylor and Rindone's interstitial model [34] (see Section 3.2.1.) of accommodating excess aluminums in glasses with Al/Na>1.0 does not provide an adequate description of the photoemission spectra. For this model, the ratio of Al^{IV}-O-Si^{IV} linkages that are charge compensated by either sodium ions or interstitial aluminum ions (see Eqs. (3.1) and (3.6)) to Si^{IV}-O-Si^{IV} bridges is given by

$$r^*(\text{theo}) = \frac{6X_{Al}+2X_{Na}}{2X_{Si}-3X_{Al}-X_{Na}}, \qquad (3.14)$$

where the aluminum avoidance rule is again assumed to be valid. With increasing Al/Na above the equivalence point along the series of NAS glasses with Λ=0.57 and X_{Si}=0.67, r*(theo) increases more rapidly than r'(theo) and therefore diverges from the empirical ratio of the bridging oxygens, r*(XPS), which is numerically equivalent to r'(XPS). For the glass NASXXVIIIwith Al/Na=1.5 in the series of Λ=0.57, r'(theo)=3.5 by the tricluster model compares much better with r'(XPS)=r*(XPS)=3.6 than does r*(theo)=5.4 by the interstitial model.

3.5. DISCUSSION:

3.5.1. Glasses with $0 \leq Al/Na \leq 1.0$

The analyses of O 1s spectra for NAS glasses with $0 \leq Al/Na \leq 1.0$ in this investigation give persuasive support to the classical structural picture. The parameters f_{NBO}(XPS) and r(XPS) are generally found to characterize O 1s spectral envelopes along three different lines of composition. The large variation of these parameters with composition in Figs. 3.14 and 3.15 closely conforms to theoretical predictions based on the traditional model for NAS glass structure (see Section 3.4.2).

The progressive decrease in the intensity of the NBO peak with increasing Al/Na up to the equivalence point in the composite sets of O 1s spectra for the series of glasses with $\Lambda=0.57$ and $X_{Si}=0.67$ in Figs. 3.8(a) and (b) corresponds to the determination that f_{NBO}(XPS) monotonically decreases to zero at Al/Na=1.0 in the analyses of individual O 1s spectra in Figs. 3.9 and 3.10. Furthermore, the ∿1 eV shift of the "BO peak" to lower binding energy and the changing slope on the high-energy side of the "BO peak" with increasing Al/Na in Figs. 3.8(a) and (b) can also be understood from the analyses in Figs. 3.9 and 3.10 where the BO1 and BO2 states are found to maintain a separation of ∿1 eV in binding energy while r(XPS) increases from zero at Al/Na=0 to values substantially greater than unity at Al/Na=1.0.

The only departure from the assumptions for the classical model (see Section 3.4.2) is indicated in the series of glasses with Al/Na=1.0. As Al/Si goes from 0.33 to 1.0 in this series, the aluminum avoidance rule appears to break down somewhere in the range of $0.57<Al/Si<0.85$. By the above assumptions, this would not be expected until $Al/Si>1.0$.

However, since the integrated intensities of the BO1, BO2, and BO5 components to the O 1s spectrum for Ne glass in Fig. 3.11 increase as A(BO1) ≃ A(BO5) << A(BO2), it is concluded that the aluminum avoidance principle is still largely obeyed even for the least SiO_2-rich composition of this series.

For the lines of composition with $\Lambda=0.57$ and $X_{Si}=0.67$ in Fig. 3.12, the pronounced increase in the binding energy of the Na 1s level relative to the BE_F of the BO2 component of the O 1s envelope as Al/Na varies from 0.2 to 1.0 is explained by the progressive replacement of modifier sites ($\equiv$ Si-O^-Na^+) with charge compensator sites associated <u>exclusively</u> with Al^{IV} groups ($Na^+(AlO_{4/2})^-$). More valence charge is withdrawn from sodium ions as charge compensators than as network modifiers resulting in higher binding energies for Na 1s level with increasing Al/Na. The abrupt end of this relative shift in the position of the Na 1s level <u>at the equivalence point</u> signifies that all modifier sites are not replaced by charge compensator sites until Al/Na=1.0 in agreement with the traditional model. The same conclusion was reached in the study by optical luminescence spectroscopy [23,24] of thallium-doped NAS glasses with $\Lambda=0.57$ where modifier sites ($\equiv$Si-O^-Tl^+) are not completely removed in favor of charge compensator sites ($Tl^+(AlO_{4/2})^-$) as Al/Na increases below the equivalence point until Al/Na=1.0.

For the line of composition with Al/Na=1.0 in Fig. 3.12, the decrease in the binding energy of the Si 2p level relative to the BE_F of both the BO2 and Al 2p levels as Al/Si goes from 0.33 to 1.0 reflects a systematic replacement of oxygen atoms in the BO1 chemical state tetrahedrally coordinating silicon atoms with those in the BO2 state. Since the valence charge on oxygens in the BO2 bonding state is greater than that for the BO1 state, a relaxation in the valence charge distribution towards silicons as r(XPS) increases with Al/Si results in a lower binding energy for the Si 2p level. Also, since the aluminum avoidance rule remains largely valid at Al/Si=1.0 in this series of glasses, any shift in the binding energy of the Al 2p level due to a minor replacement of oxygens in the BO2 chemical state tetrahedrally coordinating aluminum atoms with those in the BO5 state would be small in comparison to the shift of the Si 2p level.

The variation in the FWHM of the Si 2p photopeak over $0 \leq n(\text{theo}) \leq 1.0$ in Fig. 3.13 for glasses with $Al/Na \leq 1.0$ on the compositional lines of $\Lambda=0.57$ and $X_{Si}=0.67$ suggests silicon atoms exist in energetically distinct chemical states. Similar to the case of NS glasses (see Section 2.5.2), these states correspond to the number of NBO's bonded to a silicon atom. As Al/Na increases below the equivalence point, the minimum peak width inferred at n(theo)=1.0 implies that almost all silicons have NBO/Si=1; the maximum peak width at n(theo)=0.5 indicates the number of silicons with NBO/Si=0 and NBO/Si=1 are nearly equal; and the minimum peak width at n(theo)=0 signifies NBO/Si=0 for all silicons at Al/Na=1.0. This interpretation justifies the assumption in the calculation of r(theo) by the classical model (see Section 3.4.2) that for glasses with $Al/Na<1.0$ all sodium atoms in excess of aluminum atoms create NBO's bonded to silicon atoms only.

As Al/Na goes from zero to unity along the series of glasses with $\Lambda=0.57$ and $X_{Si}=0.67$, that FWHM of the Na 1s photopeak is constant despite the complete replacement of modifier sites by charge compensator sites. This result is somewhat surprising in view of the variation in

FWHM of the Si 2p photopeak with n(theo) (Fig. 3.13). However, the rather broad width of the Na 1s line in comparison to the Si 2p or Al 2p lines and its invariance with Al/Na may be an indication that the number of oxygen atoms in distorted coordination polyhedra about sodium atoms varies little as oxygens in the BO2 chemical state replace those in the NBO state up to Al/Na=1.0.

The conclusions about the structure of NAS glasses with $0 \leq Al/Na \leq 1.0$ from the present XPS study are in gratifying agreement with structural information obtained by other techniques including X-ray diffraction, XES, NMR, XANES, EXAFS, and optical luminescence spectroscopy as reviewed in Section 3.2.1. There is little convincing structural evidence to support the suggestions of several workers that at least some fraction of the aluminum atoms in RAS glasses with $Al/R \leq 1.0$ occur in Al^{VI} groups either as network modifiers [38,42,43,52] or as network formers [12,14,20,39,40]. Instead, the consensus of most structural studies upholds the classical model as the best description of the atomic arrangement for these compositions.

In light of the strong support given to the traditional model of NAS glasses with $Al/Na \leq 1.0$ in this XPS investigation, several criticisms are directed toward what are viewed here as discrepant structural interpretations in earlier photoemission work (see Section 3.2.2). Without an adequate method of correction for electrostatic charging of insulators in XPS, BCGS [12,14] and SL [20] chose to normalize the binding energy scales for their respective O 1s spectra to the position of the "BO peak". Although this procedure is commonly used to display spectra of dielectric samples, it tends to obscure underlying energetic and structural relationships of interest. This point is demonstrated by comparing the composite sets of O 1s spectra of BGCS and SL in Fig. 3.6 to those of the current study in Fig. 3.8. The BE_F scales for the spectra in Fig. 3.8 were obtained using the BMD method of charging correction and more clearly indicate the evolution in the shape of the O 1s envelope with Al/Na. The systematic changes in the O 1s spectra of Fig. 3.8 in turn suggested the appropriateness of a <u>three-component</u> fitting analysis with reasonable constraints on the FWHM's of the BO1, BO2, and NBO peaks that was employed here for glasses with $Al/Na \leq 1.0$ in Figs. 3.9-3.11 (see Section 3.4.1).

In contrast to the methods of this study, BGCS and SL elected to use a <u>two-component</u> fitting analysis for their O 1s spectra with the constraint of $FWHM(BO) \equiv FWHM(NBO)$. The O 1s envelopes of the two glasses with Al/Na=0.85 in the present work have approximately Gaussian peak shapes (Figs. 3.8-3.10). If the fitting parameters of BGCS and SL are applied to these spectra, they are roughly characterized by a single broad ($FWHM \simeq 1.85$ eV) Gaussian peak. With the presumption that this component represents the unresolved contributions of bridging (Si-O-Si), (Al-O-Si), and (Al-O-Al) bonds <u>only</u>, one now can see how BCGS and SL might have come to the incorrect conclusion that $f_{NBO}(XPS) \rightarrow 0$ at $Al/Na \simeq 0.7$.

The lack of uniqueness in a nonlinear least squares fit of a complex spectral envelope to multiple component peaks is a disturbing problem. Stephenson and Binkowski [80] have remarked that structural inferences extracted from such analyses without <u>à priori</u> information regarding the expected intensity ratios or widths of the component peaks are all too often unreliable. For this reason, peak widths for the three-component fitting analysis used in the current study of NAS glasses with Al/Na$\leq$1.0 were constrained in accordance with insights gained from experience with simpler NS glasses in Chapter 2. As indicated above, this analysis of NAS glasses provides a logical explanation for the markedly changing shape of the O 1s envelope with Al/Na up to the equivalence point and strong evidence for the classical model which compliments and reinforces the findings of structural studies by other techniques. Moreover, an analysis of the O 1s spectrum obtained in a preliminary study [81] of a vacuum-fractured natural Ab crystal [82] yielded r(XPS)=1.03 vs. r(theo)=1.00. This result agrees well with that obtained for Ab glass (Fig. 3.15) and thus offers additional support for the appropriateness of the fitting analysis employed here.

In principle, a residual analysis of O 1s spectra for NAS glasses like the one of LPV [19] should produce conclusions compatible with those from a curve fitting analysis about glass structure. In practice, however, the relative energetic alignment of each pair of NAS and NS O 1s spectra prior to subtraction is critically important. LPV decided to scale the position of their O 1s envelopes relative to that of a nearby sodium Auger line. Significantly, SL [20] reported the energetic separation between a sodium Auger peak and the NBO component of the O 1s spectrum increases even more rapidly with Al/Na below the equivalence point than the shift of the Na 1s peak relative to the BO2 component of the O 1s envelope in the present study (Fig. 3.12). From the standpoint of the current structural interpretation, the positions of BO1, BO2, and NBO bonding states of an NAS glass would become increasingly misaligned in relation to the BO and NBO states of the NS glass as Al/Na increases up to unity by following the scaling procedure of LPV. Serious questions can therefore be raised regarding the propriety of the difference spectra generated by LPV. Moreover, there is a possibility that structural artifacts are represented in their analysis since the photoemission spectra were acquired from vacuum-milled surfaces (see Section 1.2.2). These objections thus undermine the basis for LPV's anomalous conclusion that f_{NBO}(XPS) is virtually independent of Al/Na.

3.5.2. Glasses with $1.0<Al/Na\leq1.5$

The analyses of O 1s spectra for NAS glasses with $1.0<Al/Na\leq1.5$ in this study are consistent with Lacy's mechanism [44] for the incorporation of aluminum atoms in excess of sodium atoms. The parameter r'(XPS) is generally found to describe O 1s spectral envelopes for glasses of the series $\Lambda=0.57$ and $X_{Si}=0.67$ above the equivalence point. Although the range of r'(XPS) for these compositions is rather small in Fig. 3.16, this parameter corresponds well to theoretical estimates based on the tricluster model for NAS glasses with $Al/Na\geq1.0$ (see Section 3.4.2). In contrast, the analyses of the O 1s spectra in Figs. 3.9 and 3.10 disagree with theoretical predictions derived for the interstitial model of Taylor and Rindone [34] for the accommodation of excess aluminums in NAS glasses with $Al/Na>1.0$.

Opposed to the sharp increase in the binding energy of the Na 1s level relative to the BE_F of the BO2 component of the O 1s envelope as Al/Na increases below the equivalence point in Fig. 3.12, the energetic separation between the Na 1s level and the BO2+BO4 component is constant for $Al/Na\geq1.0$ in the series of glasses with $\Lambda=0.57$ and $X_{Si}=0.67$. The inflection at Al/Na=1.0 indicates that sodium ions are not greatly affected by the incorporation of excess aluminum atoms in compositions above the equivalence point. A similar conclusion was drawn from optical luminescence results [23,24] for thallium-doped NAS glasses with $\Lambda=0.57$ at $Al/Na \geq 1.0$. These observations are not inconsistent with the formation of tricluster configurations in glasses with $Al/Na>1.0$.

Whereas the energetic separation between the Si 2p and Al 2p levels is invariant up to the equivalence point, there is some suggestion in Fig. 3.12 that the binding energy of the Al 2p level increases relative to the BE_F of the Si 2p level at $Al/Na>1.0$ in the glasses with $\Lambda=0.57$ and $X_{Si}=0.67$. In the bonding arrangement of a tricluster, an Al^{IV} group contains three oxygen atoms in the "underbonded" BO3 chemical state and one oxygen in the "overbonded" BO4 state (see Section 3.2.1 and 3.4.1). A relaxation in the valence charge distribution from these aluminums towards the "underbonded" oxygens in their coordination shell conceivably results in a higher binding energy for the Al 2p level with increasing Al/Na above the equivalence point.

The invariance in the FWHM of the Si 2p photopeak for all NAS glasses with $Al/Na \geq 1.0$ is understood to mean $NBO/Si=0$ for all silicon atoms in each of these compositions. The small increase in the FWHM of the Al 2p photopeak for NAS glasses with $Al/Na>1.0$ may indicate the occurrence of two energetically distinct chemical states for aluminum atoms: the first in Al^{IV} groups for which sodiums ions are available as charge compensators, and the second in Al^{IV} groups within tricluster configurations.

The conclusions for the atomic arrangement of NAS glasses with $1.0<Al/Na \leq 1.5$ from this XPS study are in accord with structural details provided by other techniques including XES, XANES, EXAFS, and optical

luminescence spectroscopy as described in Section 3.2.1. There is little compelling structural evidence to support the conventional idea that a significant fraction of the aluminum atoms in RAS glasses with $1.0<\mathrm{Al/R}\lesssim 2.0$ exist in Al$^{\mathrm{VI}}$ groups either as network modifiers [26,38,41,42], interstitial charge compensators [34], or as network formers (though weaker than Al$^{\mathrm{IV}}$ groups) [39,40]. On the contrary, most structural investigations have given results which are better explained by the tricluster model for these compositions.

One reservation about the existence of tricluster configurations in RAS glasses with $\mathrm{Al/R}>1.0$ comes from the observation that such a bonding arrangement violates Zachariasen's rules for the bonding topology of multicomponent oxide glasses [83]--i.e., one oxygen atom is shared among *three* tetrahedral centers (two Si$^{\mathrm{IV}}$ groups and an Al$^{\mathrm{IV}}$ group). However, analogous bonding arrangements are not unknown in aluminosilicate crystals [5-7,44]--e.g., sillimanite exhibits an oxygen atom shared by Si$^{\mathrm{IV}}$, Al$^{\mathrm{IV}}$, and Al$^{\mathrm{VI}}$ groups. In addition, triclusters are structurally stable with regard to the extended electrostatic valence rule (see Sections 2.2.2 and 3.2.1). It follows that tricluster configurations in RAS glasses with $\mathrm{Al/R}>1.0$ allow for the formation of continuous single-phase glasses (within limits to be explored in the next subsection) having fully connected aluminosilicate networks by relaxing the rigid structural constraints of the 4-2 coordination network found in RAS glasses with $\mathrm{Al/R}=1.0$.

More serious objections can be raised about an underlying assumption for the parameter r'(XPS) that was introduced here in the interpretation of O 1s photoemission spectra for NAS glasses with $1.0<\mathrm{Al/Na}\leq 1.5$.

While the ranking of valence charges thought to exist on oxygen anions in the BO1, BO2, BO3, and BO4 chemical states is plausible (see Section 3.4.1), the assumption that the binding energies for these states exhibit a two-fold degeneracy is somewhat tenuous. An empirical determination by diffraction methods of the distribution in electron density among oxygen anions of an aluminosilicate crystal containing bonding arrangements similar to tricluster configurations (e.g., sillimanite) could provide some means for assessing the validity of this simplifying approximation. Also, a first-principles calculation of the effective Mulliken atomic charges on oxygen atoms in BO1 and BO3 vs. BO2 and BO4 bonding states for an NAS glass with triclusters at $Al/Na>1.0$ would be useful in this regard.

Although the tricluster model provides a reasonable explanation for the slowly evolving shape of the O 1s envelope with Al/Na for NAS compositions with $Al/Na\geq 1.0$ in Figs. 3.9 and 3.10, some concern about the uniqueness of this interpretation is warranted (especially in view of the above comments). Peak widths for the <u>two-component</u> fitting analysis of these O 1s spectra were constrained in a way, however, that is natural extension of the <u>three-component</u> fitting analysis applied to O 1s spectra for NAS compositions with $Al/Na\leq 1.0$. Despite the limitations of the two-component fitting analysis for glasses with $Al/Na>1.0$, permissive evidence for the tricluster model has been demonstrated which is consistent with results from structural studies by other techniques.

3.5.3. Additional Implications for Glass Structure

For glasses in the NAS ternary system with $X_{Si}\gtrsim 0.50$ it has been shown that the integrated intensities of various BO and NBO components of the O 1s spectral envelope are directly related to glass composition in a predictable and rather general manner within two adjacent compositional regions: $0 \leq Al/Na \leq 1.0$ and $1.0 < Al/Na \leq 1.5$. If one accepts the classical model and tricluster models as satisfactory descriptions for the atomic arrangement of glasses in these respective regions, then lines of constant f_{NBO}(theo) in Fig. 3.17 and constant r(theo) and r'(theo) in Fig. 3.18 can be mapped for the SiO_2-rich corner of the NAS system. Areas of phase separation (L+L) [70-73] and the series of compositions with $\Lambda = 0.57$ are indicated in these ternary diagrams. Inspection of Fig. 3.18 makes clear the nature of the pronounced variation in r(XPS) for $Al/Na \leq 1.0$ versus the slow change in r'(XPS) for $Al/Na \geq 1.0$ in Fig. 3.9 for this line of glass compositions.

In Fig. 3.18, a compositional line is drawn which shows where BO1 → 0 for the ratio of chemical states

$$r''(\text{theo}) = \frac{BO2+BO3+BO4}{BO1} = \frac{8X_{Al}}{2X_{Si}-5X_{Al}+X_{Na}} \qquad (3.15)$$

under the assumptions of the tricluster model for NAS glasses with $Al/Na > 1.0$ (see Section 3.4.2). The line $r'' = \infty$ thus defines the extent of the region above the equivalence point within which the aluminum avoidance principle is valid in theory. It extends from the Ne composition to a binary SiO_2-Al_2O_3 composition with $X_{Al} = 0.286$. Interestingly, the latter composition coincides with the center of a broad metastable miscibility gap between $X_{Al} \simeq 0.12$ and 0.43 as determined by Jantzen et al. [73]. In a modification of their structural rationale for phase separation, it is suggested here that substantial violation of the aluminum avoidance rule

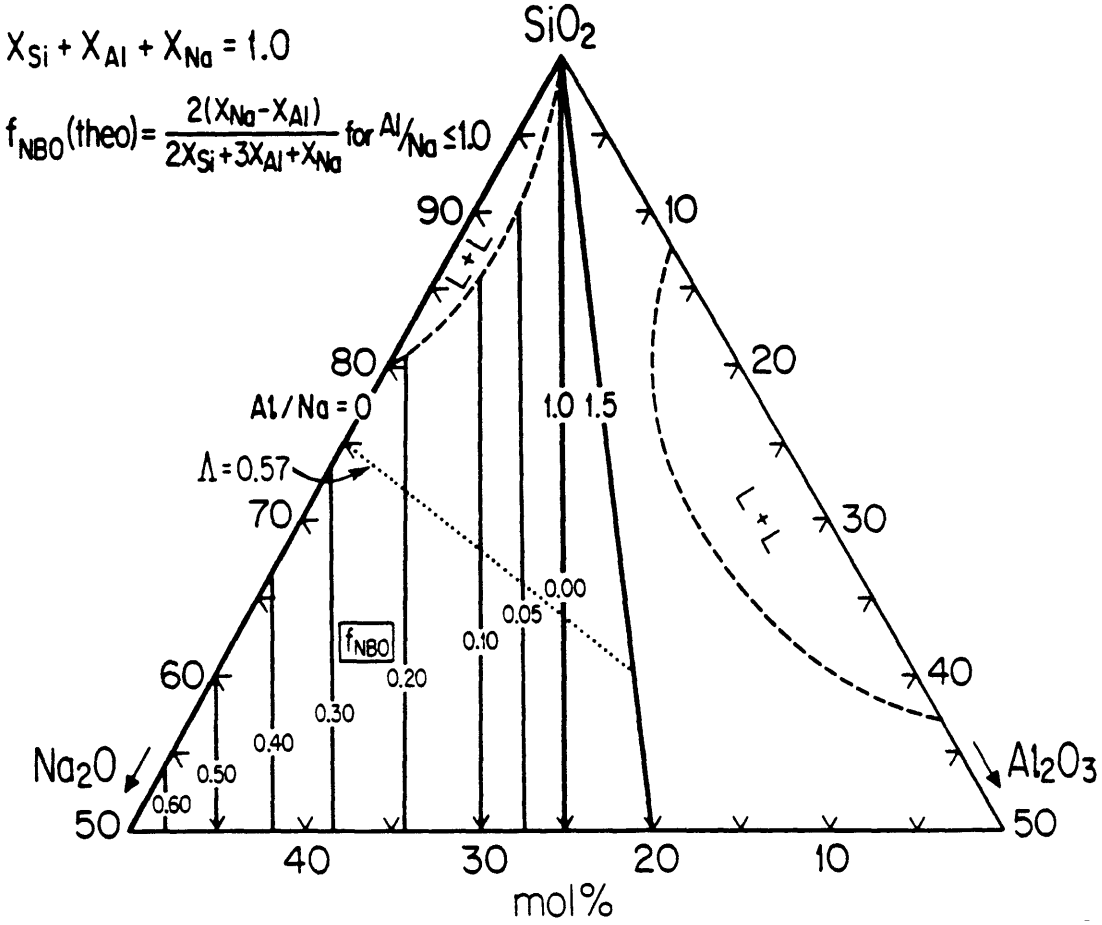

Fig. 3.17: Lines of constant f_{NBO}(theo)=NBO/BO1+BO2+NBO for NAS glasses with $X_{Si} \geq 0.50$.

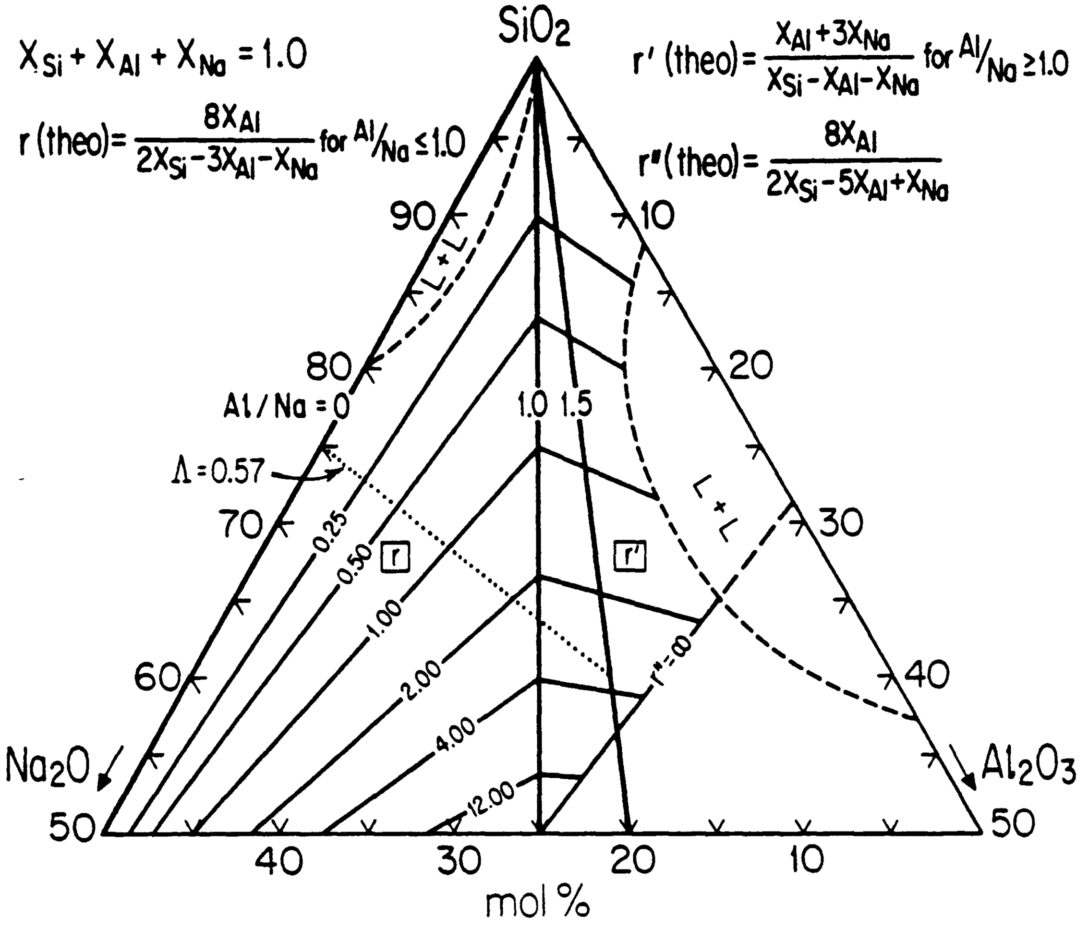

Fig. 3.18: Lines of constant r(theo)=BO2/BO1, constant r'(theo)= BO2+BO4/BO1+BO3, and r"(theo)=BO2+BO3+BO4/BO1=∞ for NAS glasses with $X_{Si} \geq 0.50$.

provides more of an impetus for this process rather than the mere presence of oxygen atoms in the "overbonded" BO4 chemical state. More generally, for NAS glasses with Al_2O_3 contents greater than those demarked by $r''=\infty$ in Fig. 3.18, the incorporation of oxygens in the BO5 state conceivably destabilizes the aluminosilicate network based on Al^{IV} and Si^{IV} groups and thus leads to the incorporation of Al^{VI} groups as seen in the XES results of Hanada et al. [51].

Along the series of NAS glasses with Al/Na=1.0, the XPS results of this study indicate that a small fraction of oxygen atoms exist in the BO5 bonding state for glasses with $X_{Si}=0.50$ and 0.54 near the compositional line $r''=\infty$. It is shown in Fig. 3.18 that the extent of the series of glasses with $\Lambda=0.57$ above the equivalence point falls well short of the compositional line $r''=\infty$. It therefore seems reasonable to expect that the aluminum avoidance principle holds for even the most aluminous compositions (Al/Na=1.5) in the two series of glasses with $\Lambda=0.57$ and $X_{Si}=0.67$ as was assumed for the spectral analysis in Section 3.4.1.

According to the crystallite hypothesis [84,85] and the more recent crystalline cluster models of Phillips [86] and Goodman [87] for glass structure (see Sections 2.2.1 and 2.2.2), vitreous silicates are viewed as aggregates of discrete, randomly-oriented, crystalline particles of 1-10 nm in size. For a ternary glass, these particles supposedly have morphologies of the stoichiometric compounds forming the compatibility triangle associated with the glass composition as determined from an equilibrium phase diagram. While certain similarities exist between the short-range structure of glasses and crystalline compounds of the NAS ternary system (e.g., the commonality of Si^{IV} and Al^{IV} groups), the preponderance of structural evidence indicates that Al^{VI} groups do not exist in jadeite-like bonding arrangements for glasses with $Al/Na \leq 1.0$ (see Section 3.5.1) or in jadeite-, mullite-, or corundum-like bonding configurations for glasses with $1.0 < Al/Na \lesssim 2.0$ (see Section 3.5.2). This observation thus argues against the crystallite or crystalline cluster models as valid structural descriptions for NAS glasses. Instead, the systematic variation of the structural parameters f_{NBO}, r, and r' with composition in Figs. 3.17 and 3.18, as projected from the photoemission results of the present study, are better viewed in the context of the random network model for glass structure (see Sections 2.2.1 and 2.2.2).

While a full rationalization of structure-property relationships for RAS glasses is beyond the scope of this Thesis, the transition from the classical model for $0 \leq Al/R \leq 1.0$ to the tricluster model for $Al/R > 1.0$ is thought to provide a reasonable basis for future work attempting to understand in detail the variation of physical properties at $Al/R = 1.0$-1.2 (Table 3.1). In particular, the compositional dependences of f_{NBO}, r, and r' in Figs. 3.17 and 3.18 conceivably hold important keys to explaining why some properties mostly exhibit extrema or discontinuities at $Al/R = 1.0$ (e.g., density in Fig. 3.1(b)) while others tend to display such features at $Al/R = 1.1$-1.2 (e.g., viscosity in Figs. 3.1(c) and (d)) in series of RAS glasses with $0 \leq Al/R \leq 2.0$.

Aside from resolving controversies generated by earlier XPS studies of NAS glasses, the experimental methods and analytical approach described in this Chapter also offer a firm foundation for future structural investigations of other RAS glasses (R=Li,K, etc.), MO-Al_2O_3-SiO_2 glasses (M=Mg, Ca, etc.), and R_2O-A_2O_3-SiO_2 glasses (A=B, Ga, In). Finally, one can readily appreciate how the structural and chemical information from this photoemission work on NAS glasses would be highly relevant to the understanding of heterogeneous catalysis at aluminosilicate surfaces.

3.6. SUMMARY:

Photoemission spectra of the O 1s, Si 2p, Al 2p, and Na 1s core levels for three series of NAS glasses (Λ =0.57, X_{Si}=0.67, and Al/Na=1.0) have been acquired from vacuum-fractured surfaces and corrected for electrostatic charging effects by the BMD method. The integrated intensities of the various BO and NBO components of the O 1s spectra are shown to be directly related to glass composition in a predictable and rather general way within two adjacent compositional regions: $0 \leq Al/Na \leq 1.0$ and $1.0 < Al/Na \leq 1.5$. In marked contrast to several previous XPS studies of NAS glasses, a curve fitting analysis of the O 1s spectra for glasses with $0 \leq Al/Na \leq 1.0$ gives strong support to tne classical structural model for the incorporation of aluminum atoms. Along the series of compositions with Al/Na=1.0, this analysis also indicates the aluminum avoidance principle begins to break down in the range of $0.57 < Al/Si < 0.85$. A curve fitting analysis for O 1s spectra of glasses with $1.0 < Al/Na \leq 1.5$ is consistent with Lacy's tricluster model for the accommodation of aluminum atoms in excess of sodium atoms. Finally, trends in the binding energies and widths of O 1s, Si 2p, Al 2p, and Na 1s photopeaks provide collateral support for the above structural conclusions about NAS glasses.

This work demonstrates the ability of XPS to supply quantitative information about the structural chemistry of complex (i.e., ternary) silicate glass systems. Such information not only compliments and reinforces the findings of structural studies by other techniques, but also has potential for yielding uniquely clarifying insights into how the variation of many physical properties of glasses with composition can be correlated to structural changes.

REFERENCES

[1] N.J. Kreidl, "Inorganic Glass-Forming Systems"; pp. 105-299 in Glass: Science and Technology (Glass-Forming Systems, Vol. 1). Edited by D.R. Uhlmann and N.J. Kreidl. Academic, New York, 1983.

[2] G.E. Harlow and G.E. Brown, Jr., "Low Albite: An X-ray and Neutron Diffraction Study", Am. Mineral., 65[9,10] 986-95 (1980).

[3] G. Donnay, J.F. Schairer, and J.D.H. Donnay, "Nepheline Solid Solutions", Mineral. Mag., 32 [245] 93-109 (1959).

[4] M. Cameron, S. Sueno, C.T. Prewitt, and J.J. Papike, "High-Temperature Crystal Chemistry of Acmite, Diopside, Hedenbergite, Jadeite, Spodumene, and Ureyite", Am. Mineral., 58 [7,8] 594-618 (1973).

[5] C.W. Burnham, "Refinement of the Crystal Structure of Kyanite", Z. Kristallogr., 118 [5,6] 337-60 (1963).

[6] R. Sadanaga, M. Tokonami, and Y. Takeuchi, "The Structure of Mullite, $2Al_2O_3\cdot SiO_2$, and Relationship with the Structures of Sillimanite and Andalusite", Acta. Cryst., 15 65-8 (1962).

[7] C.W. Burnham, "Refinement of the Crystal Structure of Sillimanite", Z. Kristallogr., 118 [1,2] 127-48 (1963).

[8] R.D. Shannon and C.T. Prewitt, "Effective Ionic Radii in Oxides and Fluorides", Acta Cryst., B25 [8] 925-46 (1969).

[9] L. Pauling, The Nature of the Chemical Bond; Chapter 13. Cornell University Press, Ithaca, New York, 1960.

[10] C.W. Burnham and M.J. Buerger, "Refinement of the Crystal Structure of Andalusite", Z. Kristallogr., 115 [3,4] 269-90 (1961).

[11] P.R. Anderson, "X-ray Photoelectron Spectroscopy of Sodium-Silicate Glasses", Am. Chem. Soc. Meeting, New York, 1973.

[12] R. Bruckner, H.-U. Chun, and H. Goretzki, "Photoelectron Spectroscopy (ESCA) on Alkali Silicate and Soda Aluminosilicate Glasses", Glastechn. Ber. 51[1] 1-7 (1978).

[13] B.W. Veal and D.J. Lam, "XPS Study of Sodium Oxide in Amorphous SiO_2"; pp. 299-303 in The Physics of SiO_2 and Its Interfaces. Edited by S.T. Pantelides. Pergamon, New York, 1978.

[14] R. Bruckner, H.-U. Chun, H. Goretzki, and M. Sammet, "XPS Measurements and Structural Aspects of Silicate and Phosphate Glasses", J. Non-Cryst. Solids, 42 [1-3] 49-60 (1980).

[15] J.S. Jen and M.R. Kalinowski, "An ESCA Study of the Bridging to Non-Bridging Oxygen Ratio in Sodium Silicate Glass and the Correlations to Glass Density and Refractive Index", J. Non-Cryst. Solids, 38-39 21-6 (1980).

[16] B.M.J. Smets and T.P.A. Lommen, "The Structure of Germanosilicate Glasses, Studied by X-ray Photoelectron Spectroscopy", J. Non-Cryst. Solids, 46 [1] 21-32 (1981).

[17] T. Sasaki, M. Kawaguchi, M. Yamane, and Y. Suginohara, "On the Quantitative Analysis of O°, O^{-}, and O^{2-} Ions in Binary Silicate by X-ray Photoelectron Spectroscopy", J. Japan Inst. Metals, 45 [8] 790-6 (1981).

[18] B.W. Veal, D.J. Lam, A.P. Paulikas, and W.Y. Ching, "XPS Study of CaO in Sodium Silicate Glasses", J. Non-Cryst. Solids, 49 [1-3] 309-20 (1982).

[19] D.J. Lam, A.P. Paulikas, and B.W. Veal, "X-ray Photoemission Spectroscopy Studies of Soda Aluminosilicate Glasses", J. Non-Cryst. Solids, 42 [1-3] 41-8 (1980).

[20] B.M.J. Smets and T.P.A. Lommen, "The Incorporation of Aluminum Oxide and Boron Oxide in Sodium Silicate Glasses, Studied by X-ray Photoelectron Spectroscopy," Phys. Chem. Glasses, 22 [6] 158-62 (1981).

[21] Y. Kaneko, H. Nakamura, M. Yamane, K. Mizoguchi, and Y. Suginohara, "Photoelectron Spectra of Silicate Glasses Containing Trivalent Cations", Yogyo-Kyokai-Shi, 91 [7] 321-4 (1983).

[22] H. Wakabayashi, R. Terai, and H. Yamanaka, "Effects of Trivalent Oxides on Electrical Conductivity in Alkali Silicate Glasses", Yogyo-Kyokai-Shi, 93 [4] 209-16 (1985).

[23] M.N. Alexander, P.I.K. Onorato, C.W. Struck, J.R. Rozen, G.W. Tasker, and D.R. Uhlmann, "Structure of Alkali (Alumino) Silicate Glasses. I. Tl^{+} Luminescence and the Nonbridging Oxygen Issue", J. Non-Cryst. Solids, 79 [1,2] 137-54 (1986).

[24] M.N. Alexander, P.I.K. Onorato, C.W. Struck, G.W. Tasker, and D.R. Uhlmann, "Structure of Alkali (Alumino) Silicate Glasses. II. Luminescence of Tl^{+}-doped Sodium Aluminosilicates", J. Non-Cryst. Solids, in press.

[25] J.F. Schairer and N.L. Bowen, "The System Na_2O-Al_2O_3-SiO_2", Am. J. Sci., 254 [3] 129-95 (1956).

[26] J.O. Isard, "Electrical Conduction in Aluminosilicate Glasses", J. Soc. Glass Technol., 43 [211] 113-23T (1959).

[27] E.I. Galant, "Refractive Index and Coordination Transformation in Aluminoborosilicate Glasses"; pp. 451-3 in The Structure of Glass (Vol. 2). Edited by E.A. Porai-Koshits. Consultants Bureau, New York, 1960.

[28] D.E. Day and G.E. Rindone, "Properties of Soda Aluminosilicate Glasses: I,", J. Am. Ceram. Soc., 45 [10] 489-96 (1962); "II", ibid., 496-504; "III", ibid., [12] 579-81.

[29] P.W.L. Grahm and G.E. Rindone, "Properties of Soda Aluminosilicate Glasses: IV,", J. Am. Ceram. Soc., 47 [1] 19-24 (1964).

[30] E.L. Williams and R.W. Heckman, "Sodium Diffusion in Soda-Lime-Aluminosilicate Glasses", Phys. Chem. Glasses, 5 [6] 166-71 (1964).

[31] E.F. Riebling, "Structure of Sodium Aluminosilicate Melts Containing at Least 50 mole % SiO_2 at 1500°C", J. Chem. Phys., 44 [8] 2857-65 (1966).

[32] R.W. Heckman, J.A. Ringlien, and E.L. Williams, "Sodium Diffusion and Electrical Conductivity in Sodium-Aluminosilicate and Sodium-Calcium-Aluminosilicate Glasses", Phys. Chem. Glasses, 8 [4] 145-50 (1967).

[33] R. Terai, "Self-diffusion of Sodium Ions and Electrical Conductivity in Sodium Aluminosilicate Glasses", Phys. Chem. Glasses, 10 [4] 146-52 (1969).

[34] T.D. Taylor and G.E. Rindone, "Properties of Soda Aluminosilicate Glasses: V,", J. Am. Ceram. Soc., 53 [12] 692-95 (1970).

[35] W.C. La Course, "Structural Influences on Diffusion in Glass -- The Mixed Site Effect", J. Non-Cryst. Solids, 21 [3] 431-4 (1976).

[36] J.E. Shelby and R.J. Eagan, "Helium Migration in Sodium Aluminosilicate Glasses", J. Am. Ceram. Soc., 59 [9-10] 420-5 (1976).

[37] J.E. Shelby, "Helium Migration in Lithium Aluminosilicate Glasses", J. Appl. Phys., 48 [4] 1497-1502 (1977).

[38] J.E. Shelby, "Viscosity and Thermal Expansion of Lithium Aluminosilicate Glasses", J. Appl. Phys., 49 [12] 5885-91 (1978).

[39] K. Hunold and R. Bruckner, "Physical Properties and Structural Details of Sodium Aluminosilicate Glasses and Melts", Glastechn. Ber., 53 [6] 149-61 (1980).

[40] K. Hunold and R. Bruckner, "Chemical Diffusion of Sodium and Aluminum Ions in Sodium Aluminosilicate Melts", Glastechn. Ber., 53 [8] 207-19 (1980).

[41] A. Klonkowski, "The Structure of Sodium Aluminosilicate Glass", Phys. and Chem. Glasses, 24 [6] 166-71 (1983).

[42] J.L. Piguet and J.E. Shelby, "Electrical Conductivity of Lithium Aluminosilicate, Galliosilicate, and Alumino/Galliosilicate Glasses", Adv. Ceram. Mater., 1 [2] 192-7 (1986).

[43] B.E. Yoldas, "The Nature of the Coexistence of Four- and Six-co-ordinated Al^{3+} in Glass", Phys. Chem. Glasses, 12 [1] 28-32 (1971).

[44] E.D. Lacy, "Aluminum in Glasses and Melts", Phys. Chem. Glasses, 4 [6] 234-8 (1963).

[45] M. Taylor and G.E. Brown, "Structure of Mineral Glasses - I. The Feldspar Glasses $NaAlSi_3O_8$, $KAlSi_3O_8$, $CaAl_2Si_2O_8$", Geochimica et Cosmochimica Acta, 43 [1] 61-75 (1979); "II. The SiO_2-$NaAlSiO_4$ Join" ibid., [9] 1467-73.

[46] R.W. Wardle and G.W. Brindley, "The Dependence of the Wavelength of AlKα Radiation from Alumino-Silicates on the Al-O Distance", Am. Mineral., 56 [11,12] 2123-8 (1971).

[47] H. Tagai, T. Iwai, and Y. Mori, The Seventh Meeting on Basic Science of Ceramics, Tokyo, 1969.

[48] R. Terai, S. Kuroda, and T. Ueno, Daikoshi-Kiho, 20 172 (1969).

[49] S. Sakka, "Study on the Coordination Number of Aluminum Ions in Alumino-silicate Glasses by Means of AlKα Fluorescence X-ray Spectra", Yogyo-Kyokai-Shi, 85 [4] 168-73 (1977).

[50] S. Sakka, Science of Glass and Amorphous Materials; Chapter 6. Uchida-Rokakuho-Shinsha, Tokyo, 1983.(in Japanese).

[51] T. Hanada, T. Aikawa, and N. Soga, "Coordination of Aluminum in Amorphous Sodium Aluminosilicate Films", J. Non-Cryst. Solids, 50 [3] 397-405 (1982).

[52] S.A. Brawer and W.B. White, "Raman Spectroscopic Investigation of the Structure of Silicate Glasses (II). Soda-Alkaline Earth-Alumina Ternary and Quartenary Glasses", J. Non-Cryst. Solids, 23 [2] 261-78 (1977).

[53] B.O. Mysen, D. Virgo, and I. Kushiro, "The Structural Role of Aluminum in Silicate Melts - a Raman Spectrographic Study at 1 Atmosphere", Am. Mineral., 66 [7,8] 678-701 (1981).

[54] P. McMillan, B. Piriou, and A. Navrotsky, "A Raman Spectroscopic Study of Glasses along the Joins Silica-Calcium Aluminate, Silica-Sodium Aluminate, and Silica-Potassium Aluminate", Geochim. Cosmochim. Acta, 46 [11] 2021-37 (1982).

[55] F. Seifert, B.O. Mysen, and D. Virgo, "Three-dimensional Network Structure of Quenched Melts (Glasses) in the Systems SiO_2-$NaAlO_2$, SiO_2-$CaAl_2O_4$, and SiO_2-$MgAl_2O_4$", Am. Mineral., 67 [7,8] 696-717 (1982).

[56] P. McMillan and B. Piriou, "Raman Spectroscopic Studies of Silicate and Related Glass Structure - A Review", Bull. Mineral., 106 [1,2] 57-75 (1983).

[57] W.B. White and D.G. Minser, "Raman Spectra and Structure of Natural Glasses", J. Non-Cryst. Solids, 67 [1-3] 45-59 (1984).

[58] D.A. McKeown, F.L. Galeener, and G.E. Brown, Jr., "Raman Studies of Al Coordination in Silica-rich Sodium Aluminosilicate Glasses and Some Related Minerals", J. Non-Cryst. Solids, 68 [2,3] 361-78 (1984).

[59] B.O. Mysen, D. Virgo, and F.A. Seifert, "Relationships between Properties and Structure of Aluminosilicate Melts", Am. Mineral., 70 [1,2] 88-105 (1985).

[60] D. Muller, W. Gessner, H.J. Behrens, and G. Scheler, "Determination of the Aluminum Coordination in Aluminum-Oxygen Compounds by Solid-State High-Resolution ^{27}Al NMR", Chem. Phys. Lett., 79 [1] 59-62 (1981).

[61] B.H.W.S. de Jong, C.M. Schramm, and V.E. Parziale, "Polymerization of Silicate and Aluminate Tetrahedra in Glasses, Melts, and Aqueous Solutions - IV.", Geochim. Cosmochim. Acta, 47 [7] 1223-36 (1983).

[62] E. Hallas, U. Haubenreiber, M. Hahnert, and D. Muller, "NMR Investigations of Na_2O-Al_2O_3-SiO_2 Glasses by Using the Chemical Shift of ^{27}Al Nuclei", Glastechn. Ber., 56 [3] 63-70 (1983).

[63] J.M. Thomas, J. Klinowski, P.A. Wright, and R. Roy, "Probing the Environment of Al Atoms in Noncrystalline Solids: Al_2O_3-SiO_2 Gels, Soda Glass, and Mullite Precursors", Angew. Chem. Int. Ed. Engl., 22 [8] 614-6 (1983).

[64] D.A. McKeown, G.A. Waychunas, and G.E. Brown, Jr., "EXAFS and XANES Study of The Local Coordination Environment of Sodium in a Series of Silica-Rich Glasses", J. Non-Cryst. Solids, 74 [2,3] 325-48 (1985).

[65] D.A. McKeown, G.A. Waychunas, and G.E. Brown, Jr., "EXAFS Study of the Coordination Environment of Aluminum in a Series of Silica-Rich Glasses", J. Non-Cryst. Solids, 74 [2,3] 349-71 (1985).

[66] T.F. Soules, "Molecular Dynamic Calculations of Glass Structure and Diffusion in Glass" J. Non-Cryst. Solids, 49 [1-3] 29-52 (1982).

[67] W. Loewenstein, "The Distribution of Aluminum in the Tetrahedra of Silicates and Aluminates", Am. Mineral., 39 [1,2] 92-6 (1954).

[68] A. Navrotsky, G. Peraudeau, P. McMillan, and J.-P. Coutures, "A Thermochemical Study of Glasses and Crystals along the Joins Silica-Calcium Aluminate and Silica-Sodium Aluminate", Geochim. Cosmochim. Acta, 46 [11] 2039-47 (1982).

[69] J.B. Murdoch, J.F. Stebbins, and I.S.E. Carmichael, "High-Resolution ^{29}Si NMR Study of Silicate and Aluminosilicate Glasses: The Effect of Network-Modifying Cations", Am. Mineral., 70 [3,4] 332-43 (1985).

[70] R.J. Charles, "Metastable Liquid Immiscibility in Alkali Metal Oxide-Silica Systems", J. Am. Ceram. Soc., 49 [2] 55-62 (1966).

[71] R.J. Charles, "Activities in Li_2O-, Na_2O-, and K_2O-SiO_2 Solutions", J. Am. Ceram. Soc., 50 [12] 631-41 (1967).

[72] B.G. Varshal, "Liquation Phenomena and the Structure of Glasses in Three-Component Aluminosilicate Systems", Fizika i Khimiya Stekla, 1 [1] 47-51 (1975).

[73] C.M. Jantzen, D. Schwahn, J. Schetten, and H. Herman, "The SiO_2-Al_2O_3 System. Part 1.", Phys. Chem. Glasses, 22 [5] 122-37 (1981); "Part 2." ibid., 138-44.

[74] Perkin-Elmer, Physical Electronics Division, Eden Prairie, MN.

[75] M.F. Koenig and J.T. Grant, "Signal-to-Noise Measurements in X-ray Photoelectron Spectroscopy", Surf. Interface Anal., 7 [5] 217-22 (1985).

[76] Compare Fig. 3.7 in Chapter 3 with Fig. 2.6(b) in Chapter 2.

[77] See Fig. 2.9 in Chapter 2.

[78] Compare Fig. 3.13 in Chapter 3 vs. Fig. 2.12 in Chapter 2.

[79] See Table 2.1 in Chapter 2.

[80] D.A. Stephenson and N.J. Binkowski, "X-ray Photoelectron Spectroscopy of Silica in Theory and Experiment", J. Non-Cryst. Solids, 22 [2] 399-421 (1976).

[81] G.W. Tasker, unpublished data.

[82] Amelia County, Virginia.

[83] W.H. Zachariasen, "The Atomic Arrangement in Glass", J. Am. Chem. Soc., 54 [10] 3841-51 (1932).

[84] J.T. Randell, H.P. Rooksby, and B.S. Cooper, "The Structure of Glasses; The Evidence of X-ray Diffraction", J. Soc. Glass Technol., 14 219-29 (1930).

[85] N. Valenkov and E. Poray-Koshits, "X-ray Investigation of the Glassy State", Z. Kristallogr. 95 [3,4] 195-229 (1936).

[86] J.C. Phillips, "Spectroscopic and Morphological Structure of Tetrahedral Oxide Glasses"; pp. 93-171 in Solid State Physics (Advances in Research and Applications, Vol. 37). Edited by H. Ehernreich, D. Turnbull, and F. Seitz. Academic, New York, 1982.

[87] C.H.L. Goodman, "The Structure and Properties of Glass and the Strained Mixed Cluster Model", Phys. Chem. Glasses, 26 [1] 1-10 (1985).

CHAPTER 4

CONCLUSIONS

1. Adaptation of the biased metal-dot (BMD) method to the analysis of vacuum-fractured surfaces of insulators in XPS yields the following benefits:

   a. Experimental difficulties associated with static and differential charging of insulators are largely eliminated.

   b. The binding energy scale for an insulating sample is referred to its surface Fermi level, consistent with Schottky barrier formation at metal-insulator interfaces.

   c. Information can be obtained about the bulk structure and chemistry of an insulator. Artifacts associated with surface preparation by ion-sputtering or vacuum-milling techniques are avoided.

2. The similarity of O 1s and Si 2p core level spectra acquired from vacuum-fractured and fire-polished surfaces of SiO_2 glass lends support to a view that extensive surface reconstruction of siloxane bonds (Si-O-Si) occurs at fracture surfaces. Nonbridging oxygens (e.g., Si-O· or Si=O) are not observed in detectable concentrations $\gtrsim 0.5$ atomic % ($\gtrsim$ 3% of a monolayer) near vacuum-fractured surfaces.

3. The O 1s and Si 2p lines for several types of SiO_2 glass (T18, T08, and T19) are not significantly different in binding energy or width from the O 1s and Si 2p lines of α-quartz. Since the range of the Si-O-Si bridging angle is considerably larger in vitreous SiO_2 than in crystalline

SiO_2, this result suggests the covalent-ionic nature of the Si-O bond (i.e., in regard to the transfer of valence charge between silicon and oxygen atoms) does not change appreciably with bridging angle.

4. The O 1s spectral envelopes for α-quartz and SiO_2 glass are characterized by single bridging oxygen components of equal width. Si=O bonds or strained siloxane bonds are not observed in detectable concentrations for SiO_2 glass. These XPS results call into question the assertions of recent crystalline cluster models for glass structure. A lower limit on the cluster radius required to obtain consistency with f_{NBO}(XPS) → 0 is estimated and found unreasonably large ($\gtrsim$30 nm). One concludes the random network model remains the most appropriate structural description for vitreous SiO_2.

5. In accord with earlier work, an analysis of O 1s spectra for R_2O-SiO_2 glasses has shown f_{NBO}(XPS) agrees with conventional theory for the accommodation of alkali atoms in a vitreous silicon-oxygen network for $X_R<0.30$, but departs negatively from this theory for $X_R>0.30$. Hydration of these glasses or the possibility of a less efficient mechanism for the incorporation of alkali are discounted as being significant factors behind this discrepancy.

6. Trends in the binding energies and widths of the O 1s, Si 2p, and Na 1s photopeaks for a series of Na_2O-SiO_2 glasses support a contention that while single-phase R_2O-SiO_2 glasses do not exhibit any long-range order, chemical details of the short-range atomic structure bear a close resemblance to those in R_2O-SiO_2 crystals. In the absence of any empirical evidence to the contrary, the photoemission results for R_2O-SiO_2 glasses are best understood in the context of the random

network model for glass structure.

7. The proportions of various bridging and nonbridging oxygen components of O 1s spectra for three series of $Na_2O-Al_2O_3-SiO_2$ glasses are demonstrated to be directly related to glass composition in a predictable and rather general way within two adjacent compositional regions: $0 \leq Al/Na \leq 1.0$ and $1.0 < Al/Na \leq 1.5$.

8. In contrast to prior XPS studies, an analysis of O 1s spectra for $Na_2O-Al_2O_3-SiO_2$ glasses with $0 \leq Al/Na \leq 1.0$ gives strong support to the classical model for incorporation of aluminum atoms in tetrahedral sites as network formers. The present work clearly shows that $f_{NBO}(XPS) \rightarrow 0$ at $Al/Na = 1.0$ as the equivalence point is approached from below along two series of compositions with $\Lambda = 0.57$ and $X_{Si} = 0.67$. This analysis also suggests the aluminum avoidance principle begins to break down in the range of $0.57 < Al/Si < 0.85$ as Al/Si goes from 0.33 to 1.0 in the series of compositions with $Al/Na = 1.0$.

9. An analysis of O 1s spectra for $Na_2O-Al_2O_3-SiO_2$ glasses with $1.0 < Al/Na \leq 1.5$ is consistent with Lacy's tricluster model for the incorporation of aluminum atoms in excess of sodium atoms in tetrahedral sites as network formers.

10. Trends in the binding energies and widths of the O 1s, Si 2p, Al 2p, and Na 1s photopeaks for $Na_2O-Al_2O_3-SiO_2$ glasses lend collateral support to the classical model for $Al/Na \leq 1.0$ and the tricluster model for $Al/Na > 1.0$.

CHAPTER 5

SUGGESTIONS FOR FUTURE WORK

1. Employ angle-resolved photoemission spectroscopy to further characterize vacuum-fractured versus fire-polished surfaces of vitreous SiO_2. The enhanced surface sensitivity that is achievable with this method would allow surface reconstruction and relaxation accompanying fracture and thermal activation to be studied in greater detail than was possible in this Thesis. Extension of this experimental approach to the study of R_2O-SiO_2 (RS) glasses (R = Li, Na, K, etc.) would likely give important insight into the discrepancy between the fraction of nonbridging oxygens that is expected from conventional theory and the significantly smaller value that has often been reported in XPS studies of RS glasses with high alkali content.

2. Provisions for hydrating a sample under well-controlled conditions in an auxiliary chamber connected by a feedthrough to the XPS chamber and for heating the sample during photoemission measurements would enable the investigation of hydration and dehydration phenomena at glass surfaces. A better understanding of weathering and aqueous corrosion of glasses would be a practical benefit of such work.

3. An XPS study of K_2O-SiO_2(KS) glasses using the experimental procedures described in this Thesis is desirable. Important information about the structural chemistry of RS glasses with low alkali content (i.e., below the range of $0.2 \leq X_{Na} \leq 0.4$ for Na_2O-SiO_2(NS) glasses examined in the present study) could thus be obtained without the complication of phase separation. Furthermore, the photoemission results for KS glasses would provide a means for corroborating general structural conclusions for RS glasses advanced here.

4. On the basis structural information about $Na_2O-Al_2O_3-SiO_2$(NAS) glasses obtained in the present photoemission work and the results of prior structural studies by other techniques, a detailed rationalization of structure-property relationships for $R_2O-Al_2O_3-SiO_2$(RAS) glasses now appears feasible. Such efforts might eventually yield models which are capable of quantitatively predicting the variation of physical properties for RAS glasses as a function of composition.

5. The experimental methods and interpretational approach of the present study of NAS glasses have provided a firm foundation for future XPS studies of other RAS glasses (R = Li, K, etc.), $MO-Al_2O_3-SiO_2$ glasses (M = Mg, Ca, etc.), and $R_2O-A_2O_3-SiO_2$ glasses (A = B, Ga, In). Photoemission data for RAS glasses other than NAS glasses would be especially useful for the modeling of structure-property relationships proposed above.

APPENDIX 1

XPS of Polycrystalline Al_2O_3

Photoemission spectra have also been acquired from vacuum-fractured surfaces of Lucalox brand polycrystalline Al_2O_3 [1]. The experimental details and procedures for this work are similar to those described in Sections 1.3.1, 1.3.2, and 1.3.4. Spectra for the O 1s and Al 2p core levels were collected from six samples; the spectrum of the valence band (40-0 eV) was recorded for two of these samples. All spectra were obtained at an apparent surface potential $Q \simeq -10$ V and corrected to Au $4f_{7/2}=84.00$ eV by the BMD method.

Typical spectra of the O 1s and Al 2p core levels are presented in Fig. A1.1. In contrast to the symmetric and nearly Gaussian shape of the Al 2p line in Fig. A1.1(b), the O 1s line in Fig. A1.1(a) is distinctly asymmetric with a tail skewed to higher binding energies. Binding energies for the main component of the O 1s spectrum and the Al 2p spectrum are 531.61 eV (standard deviation $\sigma \simeq 0.15$ eV) and 75.12 eV ($\sigma \simeq 0.15$ eV), respectively.

The fracture mode for these polycrystalline samples was intergranular. In survey spectra (1100-0 eV), the presence of some calcium impurity was indicated by the detection of weak Ca 2p doublet lines. Calcium is a common impurity in polycrystalline Al_2O_3 and is known to segregate at grain boundaries. While the asymmetry of the O 1s line in Fig. A1.1(a) may be related to the calcium impurity, it might also arise from surface reconstruction during fracture. Additional work is needed to clarify this issue.

Valence band spectra from two vacuum-fractured surfaces which have been overlayed to emphasize the reproducibility of these measurements are shown in Fig. A1.2. The upper valence band (UVB) exhibits two peaks at 6.70 and 10.70 eV and has a baseline width of 10.0 eV. The lower valence band (LVB) consists of one peak at 23.50 eV with a distinct shoulder at higher binding energies.

A more detailed discussion of these results and a critical comparison with earlier work will be given elsewhere [2].

[1] General Electric Co., Schenectady, NY.

[2] R.H. French and G.W. Tasker, "X-ray Photoelectron Spectroscopy of Al_2O_3", to be published.

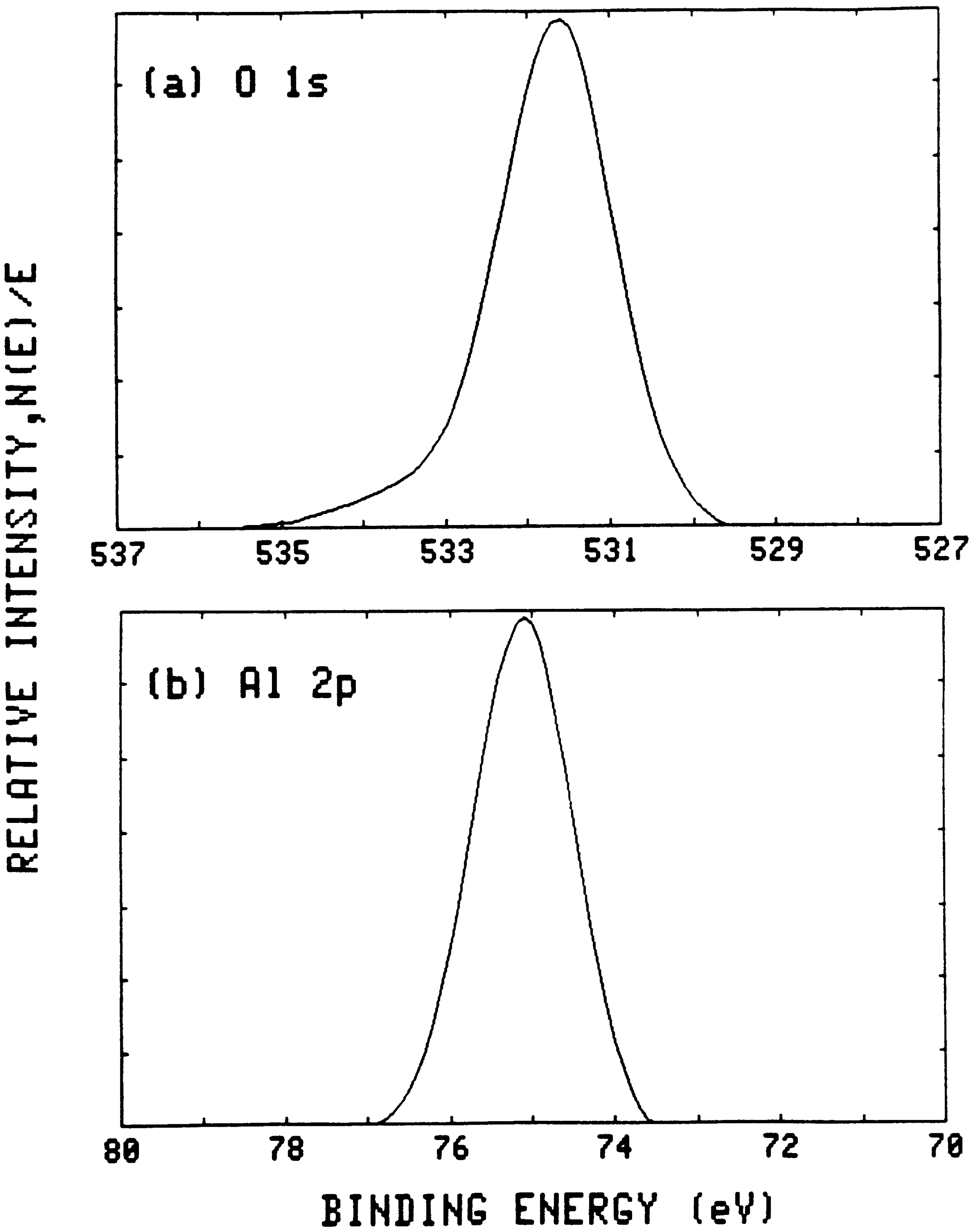

Fig. A1.1: Vacuum-fractured Lucalox brand polycrystalline Al_2O_3: (a) O 1s and (b) Al 2p core levels.

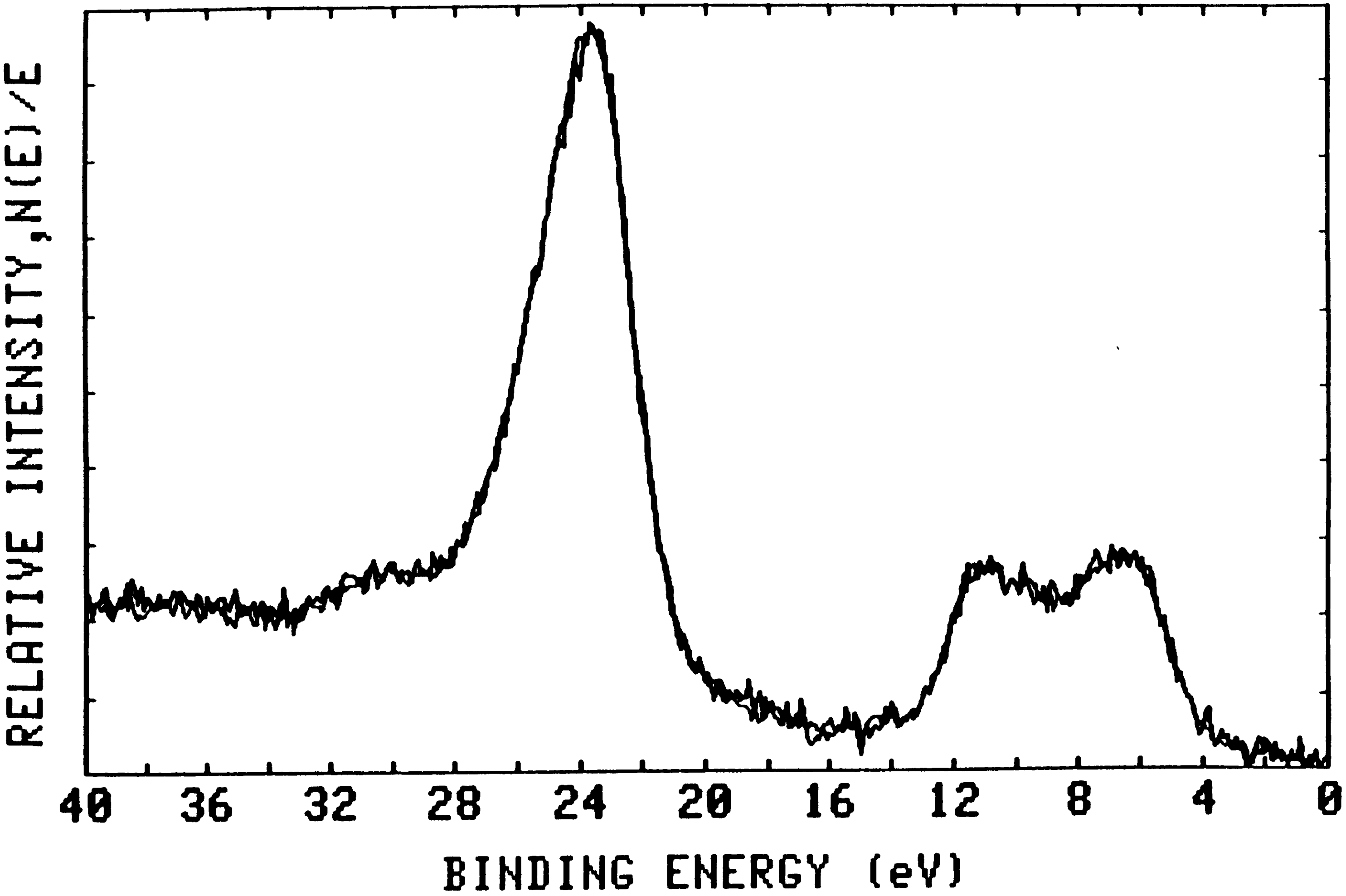

Fig. A1.2: Valence band spectrum for vacuum-fractured Lucalox brand polycrystalline Al_2O_3.

APPENDIX 2

Hydration of Fire-polished Surfaces of Fused Quartz

Data are reported here for a study of the kinetics of hydration for fire-polished surfaces of T08 fused quartz [1] by XPS. Fire-polished surfaces of fused quartz plates, prepared as described in Section 1.3.3, were subsequently hydrated under two conditions of differing severity: immersion in 18 $M\Omega$ H_2O at 25°C versus 100°C. The variation of the binding energies for the O 1s, Si 2p, and C 1s photopeaks from their initial values for a fire-polished surface as a function of time at the two temperatures of hydration are presented in Fig. A2.1. Sets of spectra for each hydration time were acquired at an apparent surface potential $Q \simeq -10$ V and corrected to Au $4f_{7/2} = 84.00$ eV by the BMD method (see Section 1.3.3). These experiments were conducted using one sample for the study at 25°C and two samples for the study at 100°C. In contrast, fire-polished samples which were exposed to the prevailing humidity of the laboratory atmosphere showed little if any change in the binding energies of the core levels over time intervals comparable to those in Fig. A2.1 (i.e., $\sim$1000 min).

Surfaces of SiO_2 which have been heated to $\gtrsim$800°C are known to be virtually dehydroxylated and therefore hydrophobic [2]. Consequently, the fire-polished surfaces examined before hydration treatments in H_2O were remarkably free of contamination due to adsorption of CO_2 or hydrocarbons from the ambient laboratory atmosphere. Such surfaces are only efficiently rehydrated by immersion in boiling H_2O, as indicated in Fig. A2.1. The rehydration of fire-polished fused quartz surfaces is seen to be associated with a shift in the binding energies of the O 1s and Si 2p core levels to lower energies with time of immersion in H_2O. This process proceeds at a much more rapid rate in H_2O at 100°C than at 25°C with an ultimate decrease in binding energy for each level of $\sim$1 eV.

While the C 1s photopeak from surface contamination does not exhibit a significant shift in binding energy in Fig. A2.1, its intensity (relative to the O 1s and Si 2p lines) increases markedly with time of hydration. With increasing time of hydration, the fire-polished SiO_2 surface apparently undergoes a transformation from one that is hydrophobic without many sites for adsorption of carbonaceous species to one that is fully hydroxylated with abundant sites for adsorption of such contaminants.

The widths of the O 1s and Si 2p photopeaks were both observed to broaden with the duration and severity of the hydration treatment--e.g., the FWHM of the O 1s line increased from 1.29 eV for the fire-polished surface to 1.46 eV and 1.65 eV after 5 min and 750 min, respectively, in boiling H_2O. However, a nonbridging oxygen component associated with the formation of hydroxyl bonds (Si-OH) could not be clearly distinguished from the bridging oxygen component for siloxane bonds (Si-O-Si) in the O 1s spectral envelope of any hydrated sample. A curve fitting analysis of the O 1s spectrum for samples hydrated under the conditions of these experiments is likely complicated by the adsorption of oxygen-containing carbonaceous species from the laboratory atmosphere [3]. Studies of the hydration kinetics under better-controlled conditions (e.g., in a reaction chamber connected to the XPS test chamber by a vacuum feed-through) are thus required for better understanding of the interaction of H_2O with SiO_2 surfaces.

[1] Heraeus-Amersil, Inc., Sayreville, NJ.

[2] R.K. Iler, The Chemistry of SiO_2; Chapter 6. Wiley-Interscience, New York, 1979.

[3] O. Puglisi, A. Torrisi, and G. Marletta, "XPS Investigation of the Effects Induced by Silanization on Real Glass Surfaces", J. Non-Cryst. Solids, 68 [2,3] 219-30 (1984).

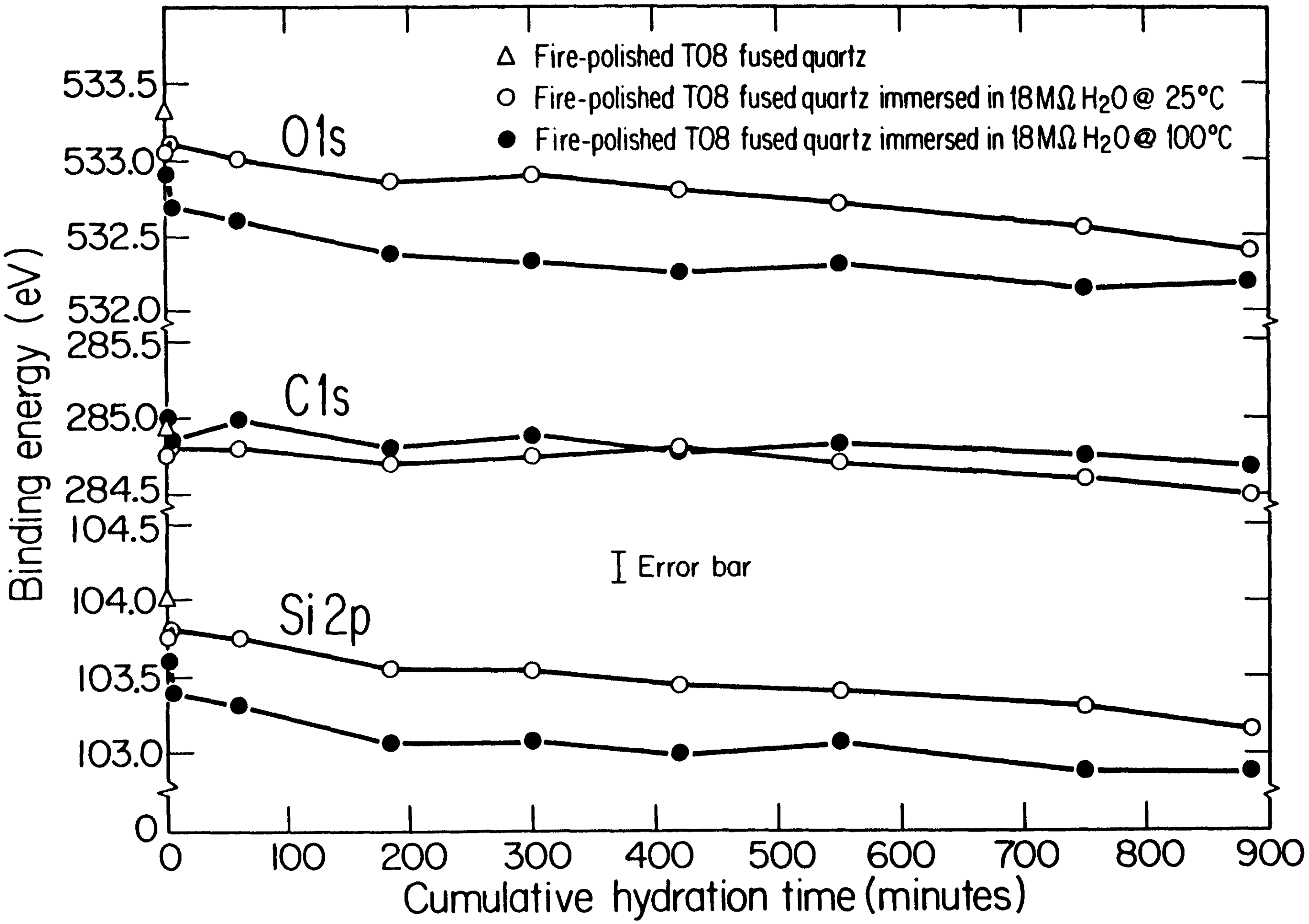

Fig. A2.1: BE_F for O 1s, Si 2p, and C 1s core levels of fire-polished T08 fused quartz vs. time of hydration.

BIOGRAPHICAL NOTE

The author was born in Washington, D.C. on 8 November 1950. He attended Richard Montomery High School in Rockville, MD. In September 1968, he entered the Pennsylvania State University and graduated from that institution in June 1972 with a B.S. in Ceramic Science. From 1972 to 1976, he was employed by Bell Laboratories in Murray Hill, NJ where he contributed to the development of the Modified Chemical Vapor Deposition (MCVD) process for the production of glass fiber optical waveguides. In September 1976, he entered M.I.T. to pursue a Ph.D. in Ceramics with Professor Donald R. Uhlmann as his advisor. In October 1986, he began work at Galileo Electro-Optics in Sturbridge, MA. Including anticipated publications from his doctoral thesis, he has authored or co-authored 20 scientific papers. He is also the co-inventor of two U.S. patents.